The University of Nottingham

Carbon Nanotube Based Composites for Electricity Storage in Supercapacitors

Shengwen Zhang, MSc, BEng

Thesis submitted to the University of Nottingham
for the degree of Doctor of Philosophy

September 2009

BEST COPY

AVAILABLE

Variable print quality

Education is what remains after one has forgotten everything he learned in school.

ALBERT EINSTEIN

ABSTRACT

In the context of fossil-fuel shortage and climate change, the production, conversion, storage and distribution of energy have become the focus of today's world. Supercapacitors, with their unique energy and power density specifications, cover the application gap between batteries and conventional capacitors and hence making valuable contributions in energy storage and distribution.

Caron nanotubes (CNTs), with their unique aspect ratio and other distinctive physical, electrochemical and electronic properties have been chosen to enhance traditional electrode materials for supercapacitors, i.e. conducting polymer and transition metal oxides. Polypyrrole/CNTs (PPy/CNTs), polyaniline/CNTs (PAni/CNTs) and manganese oxides/CNTs (MnO_x/CNTs) nanocomposites have been synthesised through chemical redox reaction in aqueous solutions. The nanocomposites have been characterised with scanning electron microscopy (SEM), transition electron microscopy (TEM), BET nitrogen surface adsorption, X-Ray diffraction (XRD), thermogravimetric analysis (TGA), infrared and X-ray photoelectron spectroscopy (XPS) to examine and to select the appropriate candidates as electrode materials.

Electrochemical characterisations, i.e. cyclic voltammetry (CV) and electrochemical impedance spectroscopy (EIS), have been conducted with the selected nano-composites in a classic three-electrode compartment cell. Desirable capacitive behaviour, with long-term cycling stability, has been identified within appropriate potential windows for each of the nanocomposites.

Asymmetric and symmetric supercapacitor prototypes have been constructed with the nanocomposites synthesised and characterised in this work. Carbon materials, due to their higher hydrogen overpotential in aqueous systems, have been proved to be good negative electrode materials in this study. Excellent specific capacitances of 1.2 F cm^{-2}, 0.83 F cm^{-2} and 0.96 F cm^{-2} have been achieved with PAni/CNTs, PPy/CNTs and MnO_x/CNTs electrodes respectively. Supercapacitor-stacks with multiplied cell voltage have been constructed with both symmetric and asymmetric prototype cells. Therefore, it has been confirmed that

desirable cell voltage and capacitance can be achieved by connecting appropriate individual cells in parallel and in series to cater the requirements of the end-users.

Last but not least, the prototype cells have been fitted with equivalent circuits to gain an insight into the resistive and capacitive contributions from each component. Suggestion for improvement has been given based on the simulation results of the prototype cells.

Affirmation

The work reported in this thesis is solely the work of the author and has not been published elsewhere except for the following publications.

X.B. Jin, W.Z. Zhou, S.W. Zhang, G.Z.Chen, **Nanoscale Microelectrochemical Cells on Carbon Nanotubes**, Small, Volume 3 (2007), Issue 9, 1513 - 1517

C. Peng, S.W. Zhang, D. Jewell, G.Z. Chen, **Carbon nanotube and conducting polymer composites for supercapacitors**, Progress in Natural Science, Volume 18 (2008), Issue 7, 777-788

M.J. Bleda-Martínez, C. Peng, S.W. Zhang, G.Z. Chen, E. Morallón, D. Cazorla-Amorósa, **Electrochemical Methods to Enhance the Capacitance in Activated Carbon/Polyaniline Composites**, Journal of The Electrochemical Society, Volume 155 (2008), Issue 9, A672-A678

K.C. Ng, S.W. Zhang, G.Z. Chen, **An Asymmetrical Supercapacitor Based on CNTs/SnO$_2$ and CNTs/MnO2 Nanocomposites**, ECS Transactions, Volume 16 (2008), Issue 1, 153-162

S.W. Zhang, G.Z. Chen, **Manganese Oxide based materials for supercapacitors**, Energy Materials, (2009) Article in Press

K.C. Ng, S.W. Zhang, C. Peng, G.Z. Chen, **Individual and Bipolarly Stacked Asymmetrical Aqueous Supercapacitors of CNTs/SnO$_2$ and CNTs/MnO$_2$ Nanocomposites**, Journal of The Electrochemical Society, Volume 156 (2009), issue 11, A846-A853

S.W. Zhang, C. Peng, K.C. Ng, G.Z. Chen, **MnO$_x$/CNTs Nanocomposites for Aqueous Supercapacitor Stack**, ElectroChimica Acta Proceeding (ISEE'CAP 09 Symposium), submitted manuscript.

Acknowledgement

Table of Content

Chapter 8 Prototype Supercapacitors

Chapter 9 Equivalent Circuits for Prototype Cells

Chapter 10 Conclusions

List of Figures

List of Tables

1. Background of Research

1.1. Energy Consumption and Strategy

In the context of fossil-fuel shortage and climate change, the production, conversion, storage and distribution of energy have become the focus of today's world. The global oil supply is estimated to peak around 2020 (DTI, 2006). On the other hand, US Department of Energy (DOE) has predicted a steady 36% increase of international energy consumption between 2010 and 2030 (as seen in Fig.1.1.) (EIA, 2008).
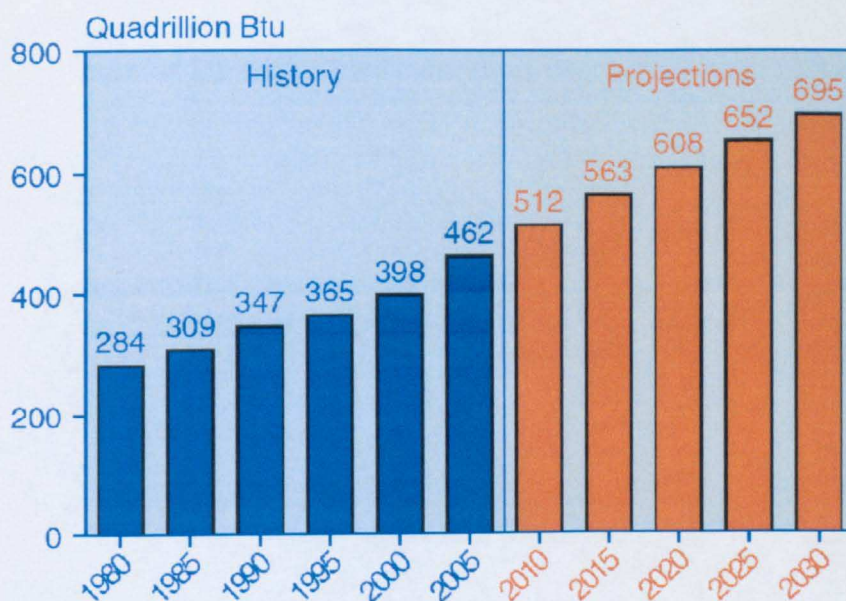
Fig. 1.1. USA EIA world marketed energy consumption and projections (1980 – 2030) (EIA, 2008).

Despite of the international agreement and commitment to cut the carbon emission (Protocol, 1990) (UN, 2007), the global carbon emission is expected to double between 2005-2030 (as depicted in Fig.1.2.) (EIA, 2008). With the growing concerns of carbon reduction and clean energy, to deliver reliable energy supply without producing excessive carbon emission has become a crucial requirement. Therefore, one of most challenging issues facing the energy industry is to achieve a successful transformation in

which sustainable and renewable energy sources with enhanced energy efficiency and lower carbon emission shall replace traditional fossil fuels. Under mounting pressure, new energy strategies, including microgeneration system (Industry, 2006), nuclear power and renewable energy, have been developed to meet the growing energy demands and tackle the climate change at the same time (Industry, 2007).
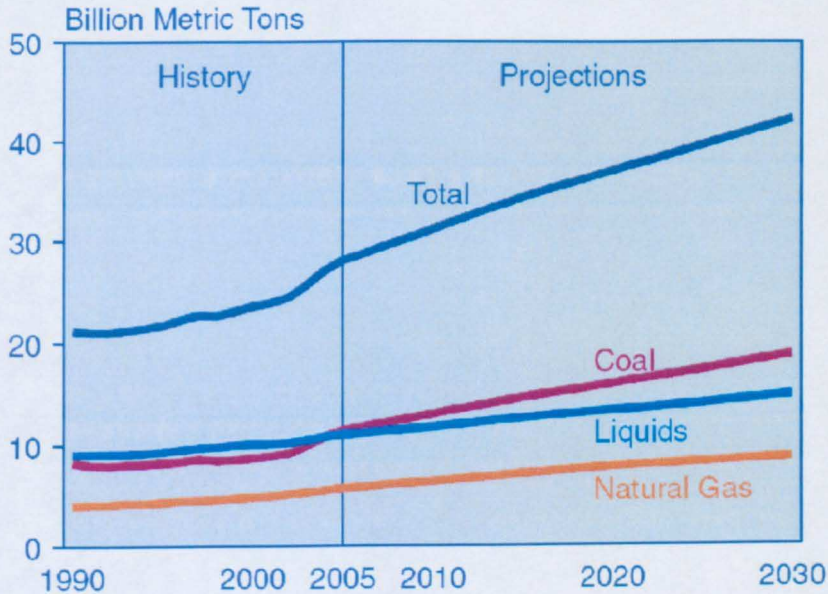
Fig. 1.2. World energy-related carbon dioxide emission by fuel type 1990 - 2030 (EIA, 2008).

1.2. Energy Storage System

With the development of renewable energy and microgeneration (Hall, 2008), competent energy storage systems, which facilitates the transmission network as well as the individual end users at different levels, have become increasingly important. Typically, a good energy storage system can effectively smooth the energy supply from renewable energy sources that do not produce constant levels of power (e.g. wind and solar) (POST, 2008). In addition, these energy storage systems help to expand the capacity of distribution networks to remote area in an economical way. Also, they make it possible to integrate large quantities of microgeneration and enhance the distribution network (POST, 2008).

Different technologies have been applied to develop such energy store
systems (Price, 2005), as categorised in Table 1.1 (Swanbarton, 2004).
As depicted in Fig. 1.3, these energy storage technologies, with their
unique parameters and applications, are at different stages of
development (Swanbarton, 2004). One thing for certain is that the future
development strategies for energy storage technologies will be aiming
at green energy storage with excellent energy efficiency.

Electrical	Capacitor and Supercapacitor
	Superconducting Magnetic Energy Storage (SMES)
Mechanical	Pumped Hydro
	Compressed Air Energy Storage (CAES)
	Flywheels
Electro-chemical	Batteries, Flow Batteries, Advanced Batteries
Chemical	Electrolyser/H_2/FC or ICE
	Other Chemical
Thermal	Hot water, Stream, Ice
	Ceramics, Molten Salt

Table 1.1. Energy storage system (Swanbarton, 2004).
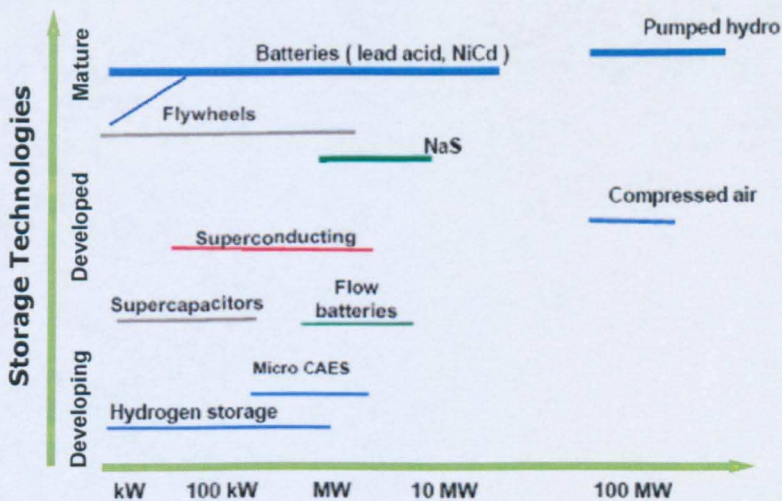
Fig. 1.3. Technical capability and commercial availability of energy
storage systems (Swanbarton, 2004).

2. Electrochemical Capacitors

2.1. Definition and Applications

Supercapacitors, or more scientifically termed as 'electrochemical capacitors', are capacitors with a large specific-value. This type of devise exhibits 20 to 10^6 times greater capacitance than conventional capacitors (Sarangapani et al., 1996) and delivers a pulsed high power 10~100 greater than batteries. Originated from Becker's research in 1950s (Becker, 1957), it is one of the most extensively studied energy-storage systems for applications in hybrid vehicles and portable electronic devices in the last decade.

As shown in Ragone plot in Fig.1.4, supercapacitors have a certain specific energy and specific power range which conveniently fills in the gap between batteries and conventional capacitors. This gap covers several orders of magnitude for both specific energy and specific power. Thus, the existence of electrochemical capacitor is believed to be of significant importance for energy-storage systems. Particularly in the cases where the ratio of stored energy to available power is unfavourable for batteries and conventional capacitors, and the devices have to be over-dimensioned due to either the power or energy demands (Kötz and Carlen, 2000).

Typical applications for supercapacitors are those demanding energy for a duration in the time range between 0.01 S and 100 S (Kötz and Carlen, 2000), e.g. levelling peak/valley usage of electric energy, emergency power backup systems, accelerating electric cars in town areas, etc. (Hughes et al., 2002).
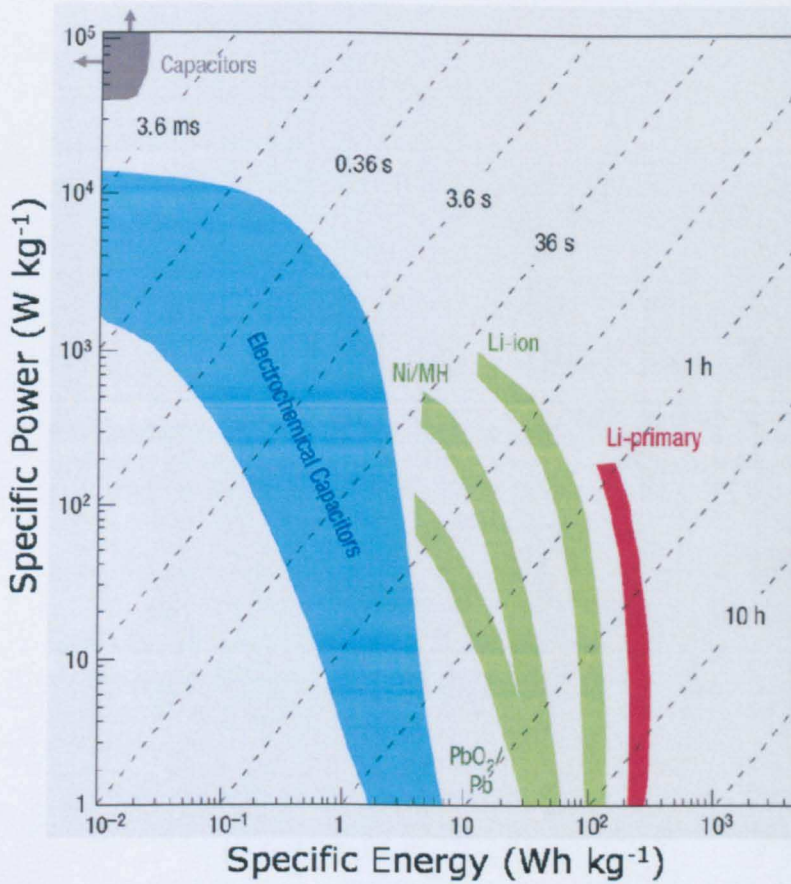
Fig. 1.4. Ragone plot for various energy storage and conversion devices
(Simon and Gogotsi, 2008).

The most distinct benefits of supercapacitors over batteries have been
identified (Kötz and Carlen, 2000). In short, supercapacitors have high
rates of charge-discharge with very little degradation over thousands
of cycles. Also, their excellent reversibility and high cycle efficiency
make them compatible with battery systems, although the later have the
well-established techniques over the years.

2.2. Challenges in Developing Electrode Materials

In the field of energy storage, energy density and power density are two
main parameters. The total energy stored is:

$$W = i \int V \, dt \qquad\qquad \text{Eq. 1.1.}$$

For a supercapacitor, the capacitance is derived from:

$$C = \frac{Q}{V} \qquad\qquad \text{Eq. 1.2.}$$

Therefore, the mass specific energy density for a supercapacitor is defined as:

$$\frac{W}{m} = \frac{1}{m} \times i \int V \, dt = \frac{1}{m} \times \frac{iVt}{2} = \frac{1}{2m} \times CV^2 \qquad \text{Eq. 1.3.}$$

Where m is the mass of electrode material.

Combining Eq. 1.2 and Eq. 1.3, specific mass power density of a supercapacitor is:

$$P = \frac{E}{t} = \frac{1}{m} \times \frac{1}{t} \times \frac{CV^2}{2} = \frac{1}{m} \times \frac{iV}{2} \qquad \text{Eq. 1.4.}$$

Alternatively, for a supercapacitor with effective series resistance of R, the mass power density can be determined in a constant current charge-discharge as:

$$\frac{P}{m} = \frac{1}{4Rm} V^2 \qquad\qquad \text{Eq. 1.5.}$$

From Eq.1.3 and Eq.1.5, it is clearly demonstrated that a high operating cell voltage (V) and low effective series resistance (R) are genuinely desirable to achieve high energy and power density. Besides, it is essential for an eligible electrode material to exhibit distinctive capacitive behaviour (C) over a wide potential (V) during the electrode processes and reasonable material density (mass per unit volume). Therefore, in spite of the intensive researches carried out since 1957, only three categories of materials, namely carbon, conducting polymer and metal oxides, remained.

The development of the electrochemical capacitors is defined by the evolution of the electrode materials and the cell configuration. Fig. 1.5 and Fig. 1.6 illustrate the development in materials and the cell design of supercapacitors.
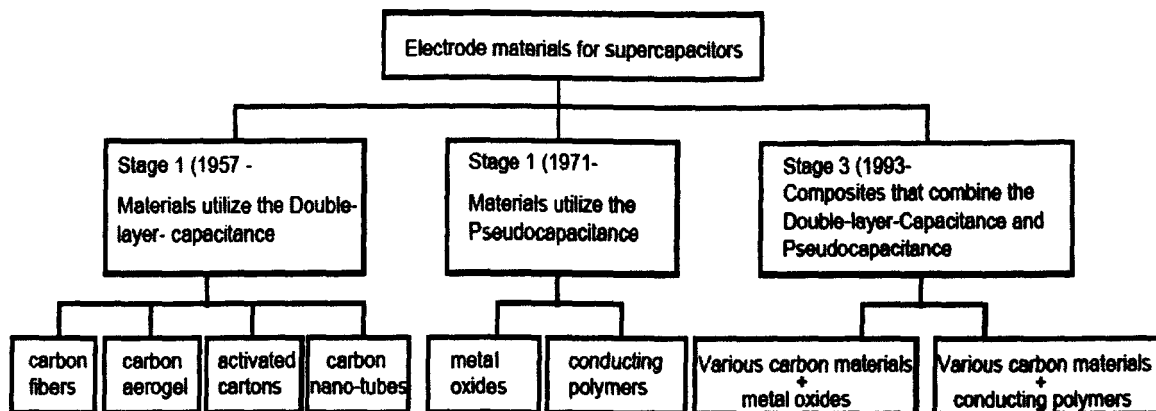
Fig. 1. 5. Development of electrode materials in the application of

supercapacitors (Peng et al., 2008).
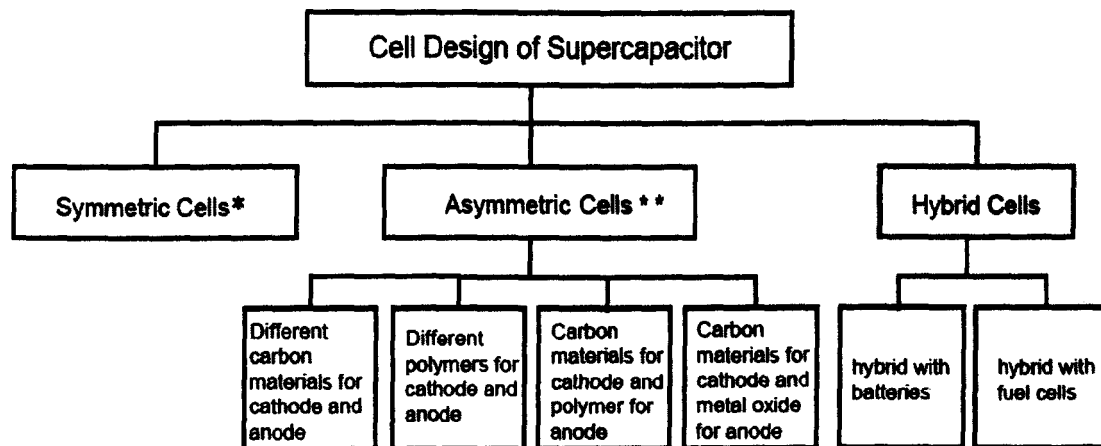
* Symmetric Cells: use same amount of identical materials for both cathode and anode;
** Asymmetric Cells: use different types or amount of materials for cathode and anode;

Fig. 1. 6. Cell design for supercapacitors (Peng et al., 2008).

3. Research Aims and Objectives

This research aims to enhance the electrochemical properties of the

existing electrode materials for supercapacitors, i.e. conducting

polymers and manganese oxides (MnO_x), by incorporating carbon nanotubes

(CNTs) through chemical synthesis. The main objectives of this study are

presented as below.

●   Synthesise a series of carbon nanotubes based nanocomposites,

including PAni/CNTs, PPy/CNTs, MnO_x/CNTs, through in-situ chemical

synthesis.

- Characterise these CNTs based nanocomposites by various material analytical techniques, including scanning electron microscope (SEM), transmission electron microscopy (TEM), Fourier transform infra-red (FT-IR), BET nitrogen adsorption-desorption isotherms, Thermogravimetric Analysis (TGA), X-ray diffraction (XRD), and X-ray Photoelectron Spectroscopy (XPS).

- Load these CNT based nanocomposites into trenched electrodes and characterise electrochemical performance of the composites in a three-electrode cell by different electrochemical methods, including cyclic voltammetry (CV), electrochemical impedance spectrometry (EIS), and galvanostatic charge-discharge.

- Build supercapacitor prototypes with the composites which exhibit outstanding properties into symmetrical and asymmetrical prototype cells. Test the cell performance and explore the possibility of extending the operating voltage by building cell stacks.

- Model the impedance performance of the prototype cells with equivalent circuits, aiming to understand the electrochemical systems within the cells.

4. Scope of this Thesis

This thesis explains the chemical synthesis of composites, general and electrochemical characterisations, the fabrication of supercapacitor prototypes and the electrochemical performance of the cells.

Chapter 2 reviews the existing literature discussing the origin of capacitance and development in electrode materials and cell configuration for supercapacitors. Chapter 3 introduces the general strategy, the specifications of the experiment details, and the general and electrochemical analytical techniques applied in this study. The details

of pre-treatments and the chemical synthesis of the CNT based composites, including PAni/CNT, PPy/CNT and MnO_x/CNT, are described in Chapter 4. General characterisations of the composites synthesised, including morphology, porosity, crystallinity, thermal stability and composition analysis, are presented in Chapter 5. In Chapter 6, the fabrication of composites into electrodes, i.e. trenched electrodes, sol-casting and pressed pellets, are described. Chapter 7 explores the electrochemical behaviours of the composites with various electrochemical methods, e.g. cyclic voltammetry, AC impedance and chronopotentiometry. Important parameters determining the capacitive performance, including potential window, scan rate, cyclic stability and the effect of electrolytes were examined to ensure an optimum performance of the composites. The electrochemical performances of symmetrical and asymmetrical prototype cells are studied in Chapter 8. Moreover, cell stacks are successfully constructed with both the symmetrical and asymmetrical cells to achieve higher operating voltage. Equivalent circuits of the prototype cell are proposed to model the electrochemical system in Chapter 9, aiming to understand and to improve the performance of the prototype cells. Finally, the findings from this study are summarised in Chapter 10 to conclude this thesis.

1. Energy Storage of Supercapacitors

1.1. Introduction

Capacitance is a measure of the amount of electric charge stored for a

given electric potential (Conway et al., 1997):

$$C = \frac{\Delta q}{\Delta v}$$ Eq. 2.1.

There are two types of supercapacitors, classified by the nature of the

energy storage: 'double layer' type and 'Pseudocapacitance' type (Conway,

1999). The charge storage mechanisms of these two processes are

intrinsically different, as will be described in detail in the following

sections. However, in most of the cases, double layer capacitance and

pseudocapacitance co-exist. For instance, about 1-5 % of the total

capacitance from a double-layer carbon capacitors was from the

contribution of pseudocapacitance, due to their surface

oxygen-functionalities (Conway et al., 1997). On the other hand,

pseudocapacitive devices always exhibit some electrostatic double-layer

capacitance which is proportional to their electrochemically accessible

interfacial areas (about 5-10 %) (Conway et al., 1997).

1.2. Double Layer Capacitance

Double layer capacitance is non-faradaic in nature, it utilises the

capacitance associated with electrode double layer charging-discharging

process in which electrons and ions only accumulate on each side of the

electrode/electrolyte. Double layer capacitance arises from the

potential-dependence of the surface density of electrostatically stored

charges. The concept and model of the double layer are credited to the

work of Von Helmholtz on the interfaces of colloidal suspensions and are

subsequently extended to surfaces of metal electrodes (Bard and Faulkner,

2001). In such systems, accumulation of anions or cations develop at the

solution side of the interface (as shown in Fig. 2.1), in response to positive or negative electric polarisation of the electrode.

In the cases when the accumulation of charges (Δq) of opposite signs takes place across the interface to an extent which is dependent on the potential change (ΔV) of the electrode, the capacitance arises. As expressed in Eq. 2.1: $C=\Delta q/\Delta V$.
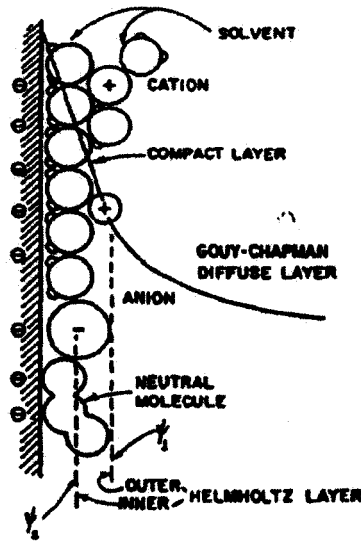
Fig. 2.1. General representation of the structure of the double layer (Conway et al., 1997).

Fig.2.1 illustrates the different regions for adsorption of hydrated cations and less hydrated anions, together with solvent molecules and adsorbed neutral molecules in a double-layer structure. In theory, double layer capacitance (C_{dl}) can be quantified by (Conway, 1999):

$$C_{dl} = \frac{\varepsilon A}{4\pi t} \qquad \text{Eq. 2.2.}$$

In Eq.2.2, ε is the dielectric constant, A is the surface area of the electrode, and t is the electrical double-layer thickness. Large interfacial capacities of several tens of F g^{-1} of active electrode material can be achieved with material of high surface area, e.g. carbon powders, carbon fibres and carbon felts.

1.3. The Band Theory and Origin of Pseudocapacitance

Pseudocapacitance is associated with electrosorption processes or surface redox reactions. Pseudocapacitance is Faradaic in origin, viz. its electrode processes involve electron-transfer across the electrode/electrolyte interface (Conway, 1999). In this sense, pseudocapacitive processes are similar to the processes in battery charging and discharging. However, pseudocapacitance only arises on account of a special relation that originates between the extent of charge acceptance (Δq) and the change of potential (ΔV), due to thermodynamic reasons (Conway, 1999). The capacitance formed is hence defined as:

$$C = \frac{Q}{E} = \frac{dq\,/dt}{dE\,/dt} \qquad\qquad \text{Eq. 2.3.}$$

Fig. 2.2 (a) illustrates this ideal pseudocapacitive process at different scan rates. Typical materials with pseudocapacitive behaviour are semiconducting redox active materials, including transition metal oxides and electrically conducting polymers. According to Bard (Bard and Faulkner, 2001), for the thin layer of a redox active material that is chemically bonded to the surface of an electrode and undergoes the reversible electron transfer reaction ($R \rightleftarrows O + ne^-$), the current-potential plot is typically bell-shaped with the peak potential determined by the redox potential of the material, as represented in Fig. 2.2.(b). In this situation, the current response towards the potential change is quantified as (Bard and Faulkner, 2001):

$$i = \frac{n^2 F^2 A \Gamma_t v \exp\left[\left(E - E^\circ\right)\dfrac{nF}{RT}\right]}{RT\left\{1 + \exp\left[\left(E - E^\circ\right)\dfrac{nF}{RT}\right]\right\}} \qquad\qquad \text{Eq. 2.4.}$$

In Eq.2.4, n is the number of electrons transferred between the reduced and oxidised sites; Γ_t ($= \Gamma_o + \Gamma_r$) is the total surface covered by the reduced and oxidized sites; A, the area of electrode; the potential scan rate. Assuming that $n = 1$, $A = 1$ cm^2, $\Gamma_t = 0.05$, $T = 300$ K, the simulated current response from Eq. 2.4 at three different scan rates are presented

in Fig. 2.2.(b).
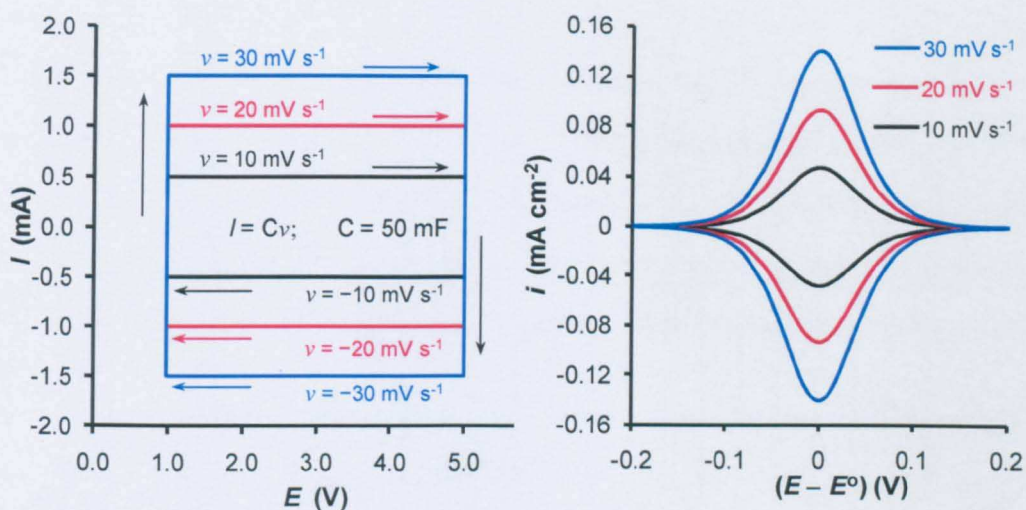
Fig. 2.2. Comparison of current responses at different scan rates of (a) delocalised capacitive electron transfer; (b) ideal localised reversible charge transfer reaction in thin redox active coating on electrode.

Clearly, the electrode processes represented by Fig. 2.2(b) differ significantly from the rectangular shaped capacitive processes shown in Fig. 2.2 (a). The reason for this difference can be explained with localised and delocalised valence electrons in these two different Faradaic processes.

Basically, the electron transfer processes in the classic chemically modified electrodes take place in very well separated redox active sites which are non-interactive with each other. In other words, these localised redox active sites are equal or fairly close to each other in energy state, and hence accept or donate electrons at specific potentials or in very confined potential ranges, leading to peak-shaped figure in cyclic voltammetry (CV). However, if these redox active sites are closely located in the surface layer of the electrode and hence are interactive with each other, a broad range or band of energy states can form with negligibly small differences between the neighbouring states (Zhang and Chen, 2009).

Such situation corresponds to that in semiconductors, including most transition metal oxides, and is also comparable with electron delocalisation in conjugated chemical bonds, as in conducting polymers, resulting from overlapping electron orbits between neighbouring atoms. Consequently, electron transfer into each energy state in this broad band becomes continuous over a wide range of potentials, which is responsible for the constant current flow and hence the rectangular shaped graph in CV.
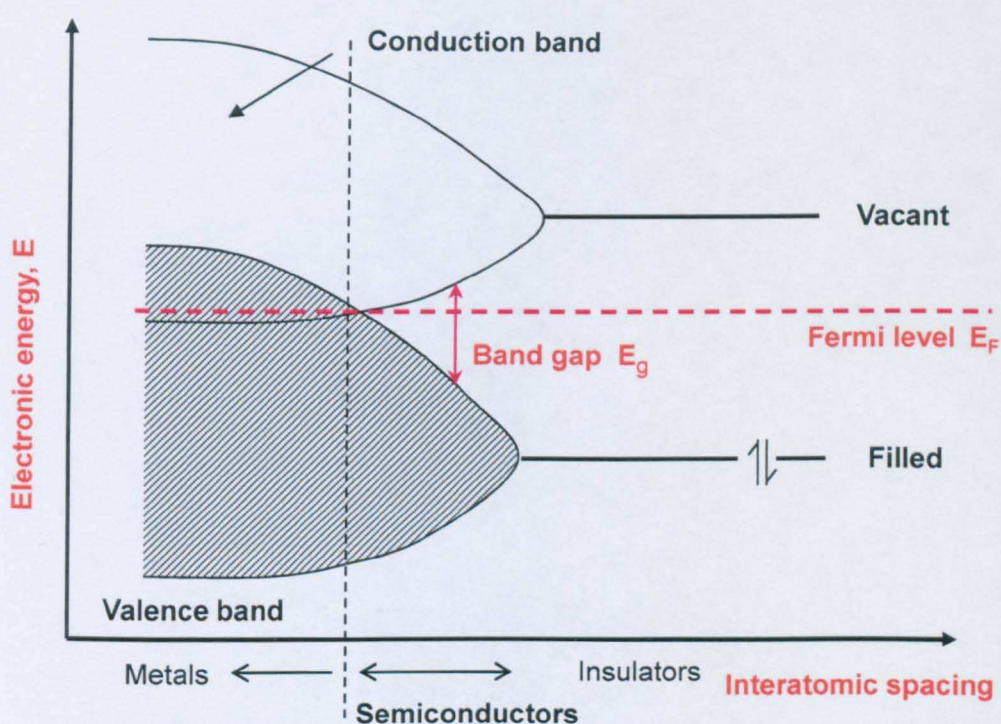
Fig. 2.3. A schematic illustration of the Band Theory (Bard and Faulkner, 2001).

The above analysis is derived from the band theory (Bard and Faulkner, 2001), as qualitatively illustrated in Fig. 2.3. With large interatomic spacing (far right hand side of Fig.2.3), electron energy states exist as isolated molecules and insulators. This is the case for classic chemically modified electrodes in which the redox active sites are well separated and only support localised electron transfer from the electrode substrate to each of the redox active sites, but no electron conduction

between any neighbouring sites. The energy levels of the filled and vacant

states are singular, corresponding to a fixed potential for electron

transfer. On the other hand, free electron mobility in response to an

electric field is expected for metals, because of their continuous

electron energy states from the filled valence band to vacant conduction

band (as shown in the far left hand side of Fig. 2.3) In Band Theory,

semi-conductors are featured by the separated filled valence band and

the vacant conduction band. The energy gap between the lowest vacant and

highest valence levels, E_g, is characteristic to each semiconductor. In

a sufficiently high and increasing electric field, continuous excitation

of electrons from the valence band to the conduction band occurs. This

process produces free moving, or so-called 'delocalised electrons' in

the conduction band as well as mobile 'holes' in the valence band (Bard

and Faulkner, 2001), leading to the continuous charge accumulation upon

the application of the increasing potential, and hence the

pseudocapacitive current.

Fig. 2.3 also shows the Fermi level, E_F, where the probability of occupancy

of the energy state by electrons is 0.5 (Bard and Faulkner, 2001). At

any other energy levels, E, the probability of occupancy is governed by

the Fermi function, $f(E)$, as given below:

$$\blacksquare$$ Eq. 2.5.

where x is Boltzmann constant, T is the absolute temperature. From the

Fermi function, it can be easily deducted that for the energies much lower

than the Fermi level, the occupancy is practically 1, and for energies

much higher than the Fermi level, the occupancy is 0 (Bard and Faulkner,

2001). Neither of these two situations can facilitate the mobility of

electrons. Only for the energy states within a few xT of E_F have

intermediate occupancy which can contribute to the electrons mobility.

Thus the potential range within which the capacitive behaviour occurs is restricted.

More explanations on the energy-storage mechanisms and the origin of the pseudocapacitance for each individual material will be given in the following sections.

2. Carbon Materials

2.1. Electrochemical Performance of Carbon Materials

Carbon, in their various forms, is a type of versatile electrode material for supercapacitors in both aqueous and non-aqueous systems (Conway, 1999, Frackowiak and Beguin, 2001). The charge is stored through adsorption of electrolyte ions on its large surface area, defined as 'double layer capacitance'. These carbon materials mainly utilise the non-faradaic double-layer capacitance arose from their high surface area and their advantageous pore accessibility. Hence, supercapacitors with carbon electrodes are also called electric double layer capacitors (EDLC). Currently, most of the commercial supercapacitors on the market are EDLC type, due to the abundance of carbon material and the availability of manufacturing technologies.

Both aqueous and non-aqueous electrolytes have been used in carbon based supercapacitors. Aqueous electrolytes are more conductive with low viscosity. Also, they are environmentally friendly comparing to non-aqueous electrolytes. However, it normally has a limited operating potential window of 1.2 V due to the decomposition of water. Carbon based capacitors have extremely high cyclability with negligible decrease in performance, owing to the nature of its charge storage mechanism,

Capacitance of 20 – 200 F/g (Vix-Guterl et al., 2005) and 20 to 35 uF/cm^2

(Conway, 1999) could be reached with carbon materials after appropriate

treatments with hot nitrogen (Phillips et al., 1998), hydrogen (Luiz et

al., 2004) are applied to optimise the pore size, surface area, stability

and conductivity.

2.2. Different Forms of Carbon as Electrode Materials

2.2.1. Activated Carbons

The activated carbons (AC) for supercapacitor applications are obtained

by carbonisation of carbon-rich organic precursors in inert atmosphere

with subsequent selective oxidation in CO_2, water vapour or KOH to increase

the specific surface area and pore volume (Simon and Gogotsi, 2008). The

BET surface areas of ACs ranges from 500 to 3000 m^2 g^{-1}, arises from a

complex interconnected network of internal pores (Pandolfo and Hollenkamp,

2006). In addition, the ACs are expected to meet other requirements,

including high temperature stability and controlled pore structure

(Pandolfo and Hollenkamp, 2006), to be considered as adequate electrode

materials for supercapacitors. Despite of these requirements, one of the

most competitive properties of activated carbon is its low cost (Fischer

et al., 1997). Fig.2.4 shows the typical capacitive behaviour of AC in

three electrolyte systems: aqueous, organic and ionic liquid (IL)
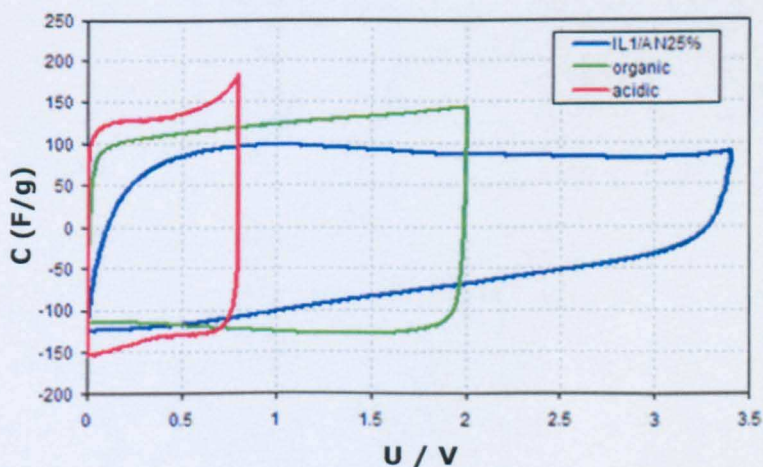
Fig. 2.4. Capacitance characteristics of activated carbon in three

electrolytic media (scan rate: 5 mV / s) (Frackowiak, 2007).

Surface area, pore size and pore distribution have been proved to have fundamental influence on the capacitance of the carbon material (Endo et al., 2001, Song et al., 2000, Fuertes et al., 2004). Although generally higher surface area leads to higher capacitance, the relation between these two is far more complicated. Beyond certain point, e.g. 2000 m^2 g^{-1}, the increase of surface area will not result in the increase of capacitance (Pandolfo and Hollenkamp, 2006). Various theories have been proposed aiming to explain the actual relationship between surface area and capacitance. Some claimed that the increase of surface area beyond a certain extent could cause decrease of electric conductivity of carbon materials (Frackowiak and Beguin, 2001) and the electronic properties strongly affect the capacitive behaviour of carbon materials (Kastening et al., 1997). Some suggested that the capacitance is strongly related with mesopore surface area, rather than the total BET surface area (Li et al., 2002). Some more recent research proposes that pore size, in fact, is the controlling parameter in determining the capacitance and the optimum adsorption capacitance can be achieved by matching pore size to the ion size of the electrolyte, with the pore size slightly larger than the ion size (Lin et al., 2009). Further investigations are still required to identify the favourable pore structures that can reach the balance among the electric conductivity, ionic conductivity and capacitance. Before an accurate simulation model come into existence, it is necessary to extend the investigations to each individual electrolyte system, as the pore accessibility is determined by the ion size of the electrolyte as well as the pore structure of the carbon material (Largeot et al., 2008), and theses investigations are highly time-consuming. In addition, the treatments involved in optimising the carbon materials could result in significant cost increase, which limits its applications in market.

2.2.2. Aerogel and Xerogel

Carbon aerogel is composed of interconnected colloidal like carbon particles or polymeric chains, synthesised by the pyrolysis of organic aerogels, e.g. resorcinol and formaldehyde (Pröbstle et al., 2003). Carbon aerogels obtained from a precursor prepared by a conventional drying instead of the supercritical method in CO_2 are called xerogels (Lin et al., 1999). Their macroscopic properties, including density, pore size and form (shape/size) can be controlled by varying the condition of sol-gel process (Pandolfo and Hollenkamp, 2006). Carbon aerogels, in their optimised conditions, are more conductive than most activated carbons (Pandolfo and Hollenkamp, 2006). However, their cost is a major drawback (Li et al., 2002).

The capacitance of carbon aerogels originates from the high double layer capacitance associated with their large specific surface area and high electrical conductivity (Fischer et al., 1997). The high surface area per unit volume permits the energy stored to be released rapidly, leading to high power densities (Mayer et al., 1993).

In addition, by doping active materials (e.g. ruthenium nanoparticles) (Miller et al., 1997, Lin et al., 1999) into the carbon aerogel, the capacitive performance can be greatly enhanced. As presented in Fig.2.5, the chemical vapour impregnation of ruthenium into carbon aerogel led to a 117 % increase in specific capacitance in aqueous electrolyte (Miller et al., 1997).
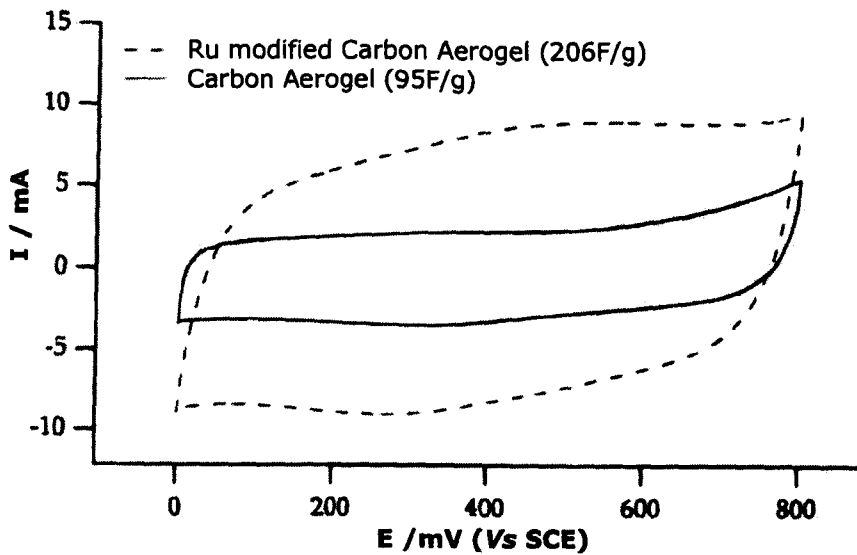
Fig. 2.5. CV of Ru/carbon aerogel composite in 1.0 M H_2SO_4, scan rate 2

mV/s (Miller et al., 1997).

2.2.3. Carbon Nanotubes (CNTs)

Carbon nanotubes and carbon nanofibres attracted much attention due to

their tubular structure of high aspect ratio, their mechanical strength,

chemical and thermal stability and low specific resistance. Both

single-walled nanotubes (SWNTs)(An et al., 2002, An et al., 2001) and

multi-walled nanotubes (MWNTs)(Honda et al., 2007) have been approached

as electrode materials for supercapacitor. SWNTs can be visualised as

wrapping one-atom-thick layer of graphite into a seamless cylinder

(Mintmire et al., 1992). In its applications as EDLC electrode materials,

however, SWNT is known to suffer from pore swelling, electrode expansion

and partial debundling during charge / discharge, especially over wider

potential window with large ions (Ruch et al., 2009). MWNTs are graphite

honeycomb lattice rolled into a cylinder with concentric walls, which

are quite efficient for the accumulation of charges, as they possess

accessible mesopores formed by entanglement and by the central canal

(Taberna et al., 2003). Yet, electrodes fabricated with these materials

alone did not yield exceptional result. Typical specific capacitance of

CNTs varies from 15 to 80 F g^{-1} (Pandolfo and Hollenkamp, 2006, Chen et

al., 2002), generally inferior to the specifications of activated carbons, which is attributed to their lower surface area and conductivity.

Thus, different approaches have been taken to improve the electrochemical performance of CNTs as electrode material. It has been reported that the surface area of CNTs can be substantially enhanced through KOH treatment, and hence the capacitance (Jiang et al., 2002) (Frackowiak et al., 2002). Also, it was found out that by aligning the CNTs into the vertical direction of the current collector (Emmenegger et al., 2000), enhanced capacitive performance can be achieved even at an extremely high current discharge current density of 200 A g^{-1} (Honda et al., 2007). In addition, using special treatments, e.g. chemical, photoactive, to introduce surface functional groups onto CNTs have been claimed to be effective in enhancing capacitive behavior (Chen et al., 2002). Although these treatments have brought noticeable improvements, they are likely to cause physical damages to the structures of the CNT and impair their stability (Pandolfo and Hollenkamp, 2006, Jiang et al., 2002).

A more effective approach is to modify the CNTs with pseudocapacitive redox materials, including transition metal oxides and conducting polymers, to form composites. This approach will integrate the large pseudocapacitance from the redox-capacitive materials with the strength of CNTs and produce composites with advanced electrochemical properties (Hughes et al., 2002, Malinauskas, 2001) (Jin et al., 2007) (Fan et al., 2006, Sivakkumar et al., 2007) (Raymundo-Pinero et al., 2005). As shown in Fig.2.6, the addition of redox active polyaniline (PAni) leads to an exceeding increase of the capacitance for the aligned CNTs electrode (Gao et al., 2000).
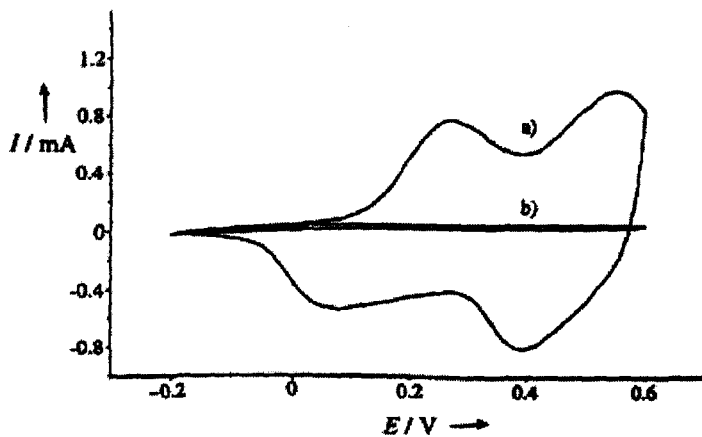
Fig. 2.6.CV of (a) PAni modified aligned CNTs; (b) bare alighed CNTs;

in 1 M H_2SO_4, scan rate 50 mV/s (Gao et al., 2000).

2.3. Oxidation Treatments and Functional Groups

It was found out that some oxidation treatments could introduce surface

functional groups, e.g. Carboxylic: R—C(=O)—OH, Hydroxylic: R—O—H , Lactonic:
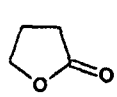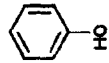
, Carbonyl A—C(=O)—B , Phenolic: , that can improve the

hydrophilicity of the carbon material and motivate redox processes

between the carbon material and the electrolyte, thus promote the

pseudocapacitance of the carbon material and enhance the overall

capacitive performance (Andreas and Conway, 2006). Some effective

treatments include: electrochemical polarization (Momma et al., 1996),

alkaline treatment (Jiang et al., 2002, Bleda-Martínez et al., 2006),

oxygen treatment (Hsieh and Teng, 2002), UV-ozone treatment (Najafi et

al., 2006), acid treatment with oxidizing acids (Du et al., 2005, Shaffer

et al., 1998, Esumim et al., 1996), oxidizing surfactants, etc. However,

some researchers have found out that both the stability and conductivity

of the activated high surface area carbon materials decrease with the

increase of surface area (Pandolfo et al., 1997) (Pandolfo and Hollenkamp,

2006). Besides, it was pointed out that carbons with a high concentration

of acidic surface functionalities are prone to exhibit high rates of

self-discharge (Pandolfo and Hollenkamp, 2006). Thus the treatment method

should be carefully chosen to reach a balance between the gain of functional groups and the loss of stability.

Particularly, intensive researches have been carried out to study the effect of these treatments on one carbon material: carbon nanotube. Due to its unique tubular structure with high aspect ratio, it is one of the most promising carbon materials that could ensure the mechanic strength, chemical and thermal stability and low specific resistivity. All of these are desirable properties for an eligible electrode material. After extensive researches in the treatments of the CNT, many researchers have reached an agreement that boiling CNTs in concentrated nitric and sulphuric acid of 1:3 ratio of was one of the most effective methods to modify CNT surface and induce functional groups (Li et al., 2004, Porro et al., 2007, Peng et al., 2007a, Ovejero et al., 2006, Kong et al., 2004).

2.4. Summary on Carbon Materials

Carbon, in its various forms, is a type of relatively low-cost electrode material with highly stable electrochemical performance for most electrolyte systems. However, the specific capacitance is largely limited by the surface area, pore size distribution and pore accessibility. Besides, due to the low compacted density and high surface-area, considerable amount of binder often required when building electrodes, which essentially reduces the electrical conductivities and volumetric capacitance of the electrode (Pandolfo and Hollenkamp, 2006). On the other hand, introducing some redox pseudocapacitive materials, e.g. RuO_x, can be an effective way to boost the capacitance.

3. Manganese Oxides (MnO_x)

3.1. Mechanism of Energy Storage in MnO_x

Within a certain potential range, MnO_x can exhibit, in good approximation,

rectangular cyclic voltammetry, as demonstrated in Fig. 2.7. This means the extent of charge acceptance (Δq) of MnO_x changes linearly, or almost linearly, with the change of potential (ΔE) (Conway, 1999). From Eq. 2.3, the capacitance is derived to be:

$$C = \frac{\Delta q}{\Delta E} = \frac{dq/dt}{dE/dt} = I/v \qquad \text{Eq. 2.6.}$$

where i is the current and v the potential scan rate. Note that the polarity of the current is determined by the direction of the potential scan. Nevertheless, MnO_x are highly resistive in nature, as seen in Fig.2.7 (e). Adding materials with higher electronic conductivity, e.g. carbons can ameliorate the situation (Fig. 2.7 e).
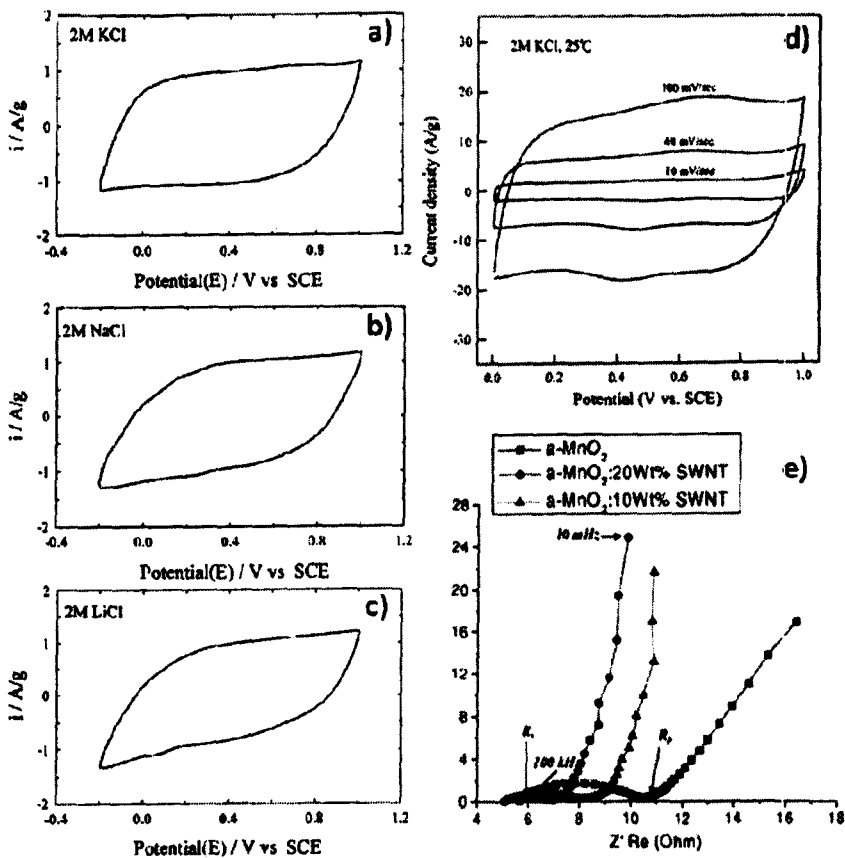
Fig. 2.7. Electrochemical characterisations of MnO_x a), b), and c) MnO_2 in different electrolyte (Lee and Goodenough, 1999); d) effect of scan rate of voltammetry behaviour (Chang and Tsai, 2003); e) EIS of MnO_2 with additional CNTs (Subramanian et al., 2006).

The pseudocapacitance of hydrous manganese oxides is attributed to the redox transitions of interfacial oxycation species in various oxidation states (Hu and Tsou, 2002). These redox transitions of hydrous manganese oxides include the transitions between Mn(III)/Mn(II), Mn(IV)/Mn(III) and Mn(VI)/Mn(IV) within the potential window of water decomposition (Hu and Tsou, 2002, Messaoudi et al., 2001). As depicted in Fig.2.8 (Pourbaix, 1966), the thermodynamic equilibriums of various manganese oxides are dependent on the potential and the pH of the system.
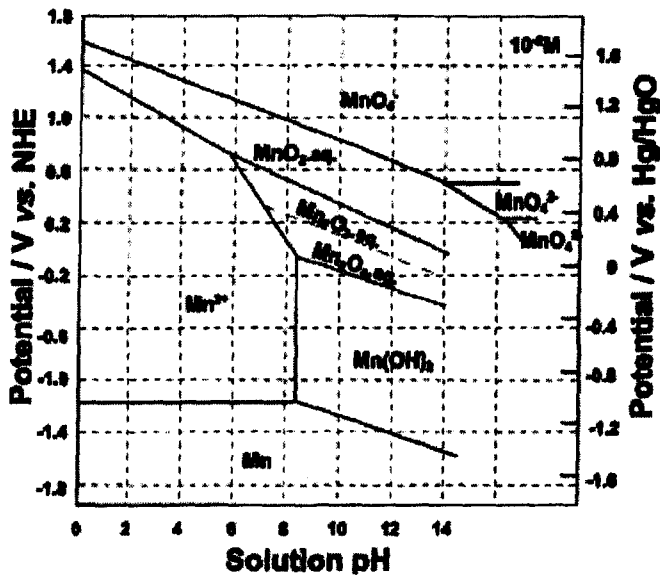
Fig. 2.8. Potential pH diagram of manganese in aqueous medium at 25 °C

(Messaoudi et al., 2001).

The charge storage mechanism of manganese oxides is depicted to be similar to ruthenium oxides (Hu and Tsou, 2002, Toupin et al., 2002b). Two generally accepted hypotheses for charge storage mechanisms of manganese oxides in supercapacitors were proposed by Goodenough's group (Lee and Goodenough, 1999) and Chapman's group (Pang et al., 2000). Goodenough suggested that the charge storage mechanism is due to surface adsorption of electrolyte cations (C^+) on MnO_2, as shown in Eq. 2.7 (Lee and Goodenough, 1999), represented in (Toupin et al., 2004):

$$((MnO_2)_{surface} + M^+ + e^- \rightleftharpoons (MnO_2^- \ M^+)_{surface} \qquad \text{Eq. 2.7.}$$
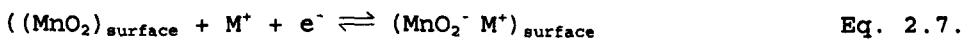
$$\text{where } M^+ = Na^+, \ K^+, \ Li^+$$

While Chapman et al. attributed it to the proton intercalation (Pang et al., 2000):

Positive electrode $MnOOH \rightleftharpoons H_{1-\delta}MnO_2 + \delta H^+ + \delta e$ Eq. 2.8(1).

Negative electrode $MnO_2 + \delta H^+ + \delta e \rightleftharpoons H_\delta MnO_2$ Eq. 2.8(2).
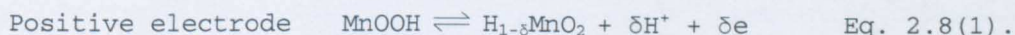
$$(0 < \delta < 0.5)$$

Recently, Simon and Gogotsi (Simon and Gogotsi, 2008) illustrated these successive multiple surface redox reactions into Fig.2.9, schematically demonstrated the charge storage mechanism of MnO_x, which leads to pseudocapacitance. In addition, the oxidants and reductants in this reaction have similar bond length, similar molecular structure, as well as extensively delocalised electrons. Thermodynamically, these conditions lead to small activation energy for the reactions and make the processes highly reversible (Fisher, 1996).
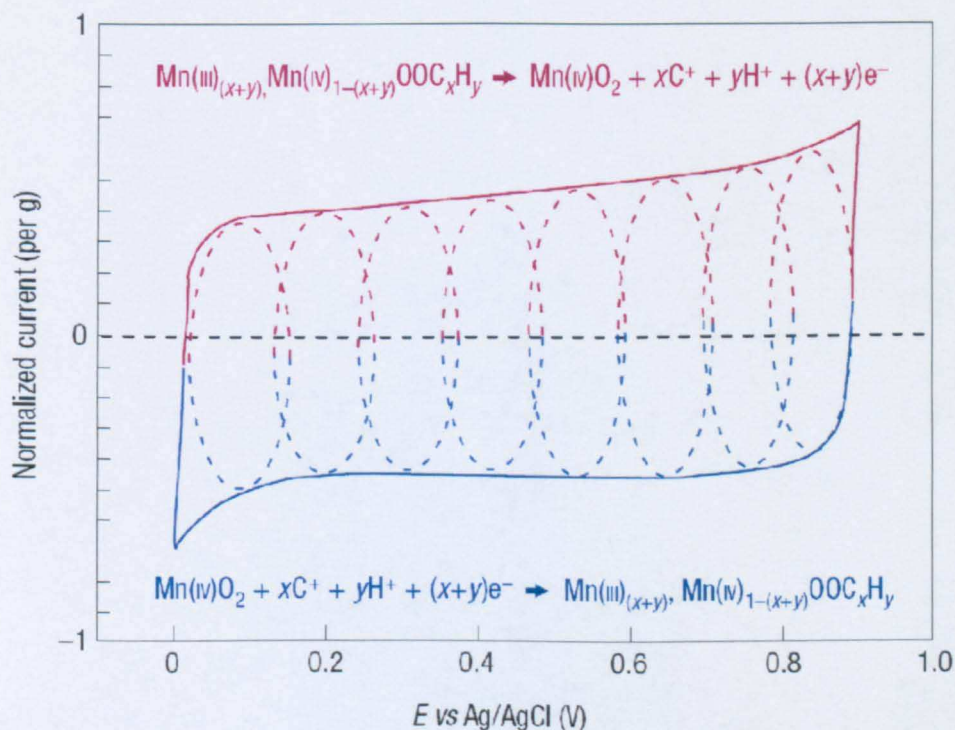
Fig. 2.9. Schematic CV of a MnO_x electrode cell in 0.1 M K_2SO_4 (Simon and Gogotsi, 2008).

It is to be noted that MnO_x has been widely used as an electrode material in both batteries and supercapacitors. The electrode reactions remain

the same or similar in both devices, as described by Eq. 2.4 and Eq. 2.5.

However, in supercapacitors, the loading of MnO_x on each electrode is

usually less than a few tens of mg per cm^2 in mass or a few tens of μm

in thickness. The consequence is that, in comparison with batteries,

supercapacitors have a smaller charge storage capacity, but a greater

overall charge transfer rate to enable high power performance.

3.2. Synthesis of Manganese Oxides

3.2.1. Chemical Synthesis

Common chemical approaches to obtain MnO_x include reducing permanganate

to manganese (II) ion in solution with low pH (Narita and Okabe, 1980)

by reducing agents, e.g. CH_3CH_2OH in acetonitrile (Li and Zhitomirsky,

2008, Im and Manthiram, 2002); and oxidizing Mn(II) into MnO_2 by oxidizing

agents, e.g. BrO^{-3} (Unuma et al., 2003) and $S_2O_8^{2-}$ (Mindt, 1971). By altering

the pH of the starting solution, various products including Mn_3O_4, β-MnOOH,

and γ-MnOOH can also be obtained (Unuma et al., 2003).

Another effective approach to synthesise α-MnO_2 is using Mn^{2+} to reduce

MnO^{4-}, e.g. adding $MnSO_4$ into $KMnO_4$ solution (Mulvaney et al., 1990, Pang

et al., 2000, Toupin et al., 2002b) or mixing $KMnO_4$ and manganese(II)

acetate solutions in water (Lee and Goodenough, 1999) (Lee et al., 2001)

(Kim and Popov, 2003). Such reactions are generalised in Eq.2.9 (Mulvaney

et al., 1990, Lee and Goodenough, 1999):

$$2\ MnO_4^- + 3Mn^{2+} + 2H_2O \rightleftharpoons 5MnO_2 + 4H^+ \qquad\qquad Eq.2.9.$$
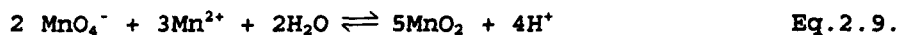
It is worth mentioning that MnO_4^- can be spontaneously reduced by carbon

and form a uniform coating of MnO_x onto the surface of a graphite electrode

through one-step reaction in acidic solution (Wu et al., 2004a), as shown

in Eq.2.10. This inspiring discovery proposes a simple route in

synthesising composites of MnO_x and vast range of carbons, including

carbon nanotubes (Jin et al., 2007, Ma et al., 2007a), activated carbon

materials (Ma et al., 2006), exfoliated graphite plates (Wan et al., 2007),

etc.

$$4KMnO_4+3C+2H_2SO_4 \rightleftharpoons 4MnO_2+3CO_2+2K_2SO_4+2H_2O \qquad Eq.2.10.$$
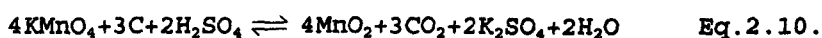
3.2.2. Electrochemical Synthesis

A prominent advantage of synthesising MnO_x through electrochemical

deposition is that the product will be in the form of a homogeneous thin

film on a conducting substrate, i.e. graphite, stainless steel, titanium

foil, etc., without using any type of binder. This can largely improve

the situation of a resistive electrode caused by the aggregation of

manganese oxide powders. The reaction of electrochemical deposition is

represented in Eq. 2.11 (Wu, 2005):

$$Mn^{2+} + 2H_2O \rightleftharpoons MnO_2 + 4H^+ +2e^- \qquad Eq.2.11.$$
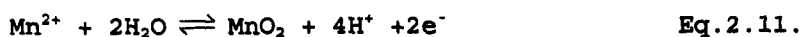
It is claimed that the electrodeposition process is not mass transport

limited, rather, the pH condition plays a more influential part (Clarke

et al., 2006). Because in more concentrated acid electrolytes Mn(III)

is lost to the bulk electrolyte through convection, and little manganese

dioxide can be formed from chemical disproportionation (Clarke et al.,

2006).

Successful electrochemical depositions have been carried out with various

precursors, including manganese acetate (Wu, 2005, Wu et al., 2004b, Chang

and Tsai, 2003), manganese sulphate (Chen et al., 2004, Broughton and

Brett, 2005, Zhou et al., 2006, Rajendra Prasad and Miura, 2004, Clarke

et al., 2006), manganese chloride (Chen et al., 2004), manganese nitrate

(Chen et al., 2004) etc. Manganese acetate is claimed to be a superior

precursor among all (Chen et al., 2004) due to its high deposition rate

at much lower potentials (Chen et al., 2004) and the existence of acetates

offered a more controllable reduction in the deposition potential

(Broughton and Brett, 2005). However, the capacitive performance is

independent of precursors as the mean oxidation state of Mn is not

significantly affected by changing the anions of manganese precursors

(Chen et al., 2004). Different electrodepositing conditions,

galvanostatic, potentiostatic and potentiodynamic conditions, were

compared (Rajendra Prasad and Miura, 2004) and the potentiodynamic

deposition was claimed to be able to produce superior MnO_2 with optimum

capacitive behaviour.

The deposition condition and deposition potential have been proved to

have profound influence on the oxidation state of manganese (Chang and

Tsai, 2003), the nanostructures (Wu, 2005), BET surface area (Wu and

Chiang, 2004). All these variables make strong impacts on the

electrochemical performance. On average, the specific capacitance of the

manganese oxides synthesised from electrochemical deposition is slightly

above 200 F g^{-1} when the thickness of the film is of several tens of

nanometre (Wu and Chiang, 2004). However, this figure may drop drastically

to about 50 F g^{-1} when the thickness increases (Broughton and Brett, 2005).

Another interesting finding is that electrochemical oxidation can be an

effective method to convert non-capacitive manganese metallic compound

(Broughton and Brett, 2004) and crystalline oxides Mn_3O_4 (Hu et al., 2008,

Nam and Kim, 2006, Chen et al., 2007, Dai et al., 2007) into capacitive

manganese oxides in aqueous solutions. The transformed manganese oxide

was confirmed to be layered structure birnessite (Dai et al., 2007). High

capacitance of 600~700 F g^{-1} was reported from 20 nm thin film with a low

current density of 160 μA cm^{-2} (Broughton and Brett, 2004); and a high

scan rate of 500 mV s^{-1} was also achieved, resulting in a capacitance of

170 F g^{-1} (Hu et al., 2008). An obvious advantage of this discovery is

that it separates the coating process from the activation process; thus

convenient techniques like sputtering (Broughton and Brett, 2004) and

electrostatic spray (Nam and Kim, 2006) can be employed to produce

homogeneous thin film at large quantity with low cost. However, for thin

films synthesised in this manner the thickness, corresponding to the

electrolyte accessibility, remained a limiting factor for the capacitance

and the maximum achievable capacitance reported was 50 mF cm^{-2} (Broughton

and Brett, 2004).

3.2.3. Sol-gel route

The sol-gel route is based on hydrolysis and condensation of manganese

ions; it was developed with the aim of producing colloidal sols contain

nano-size particles which can be deposited as very thin porous films on

a substrate via dipping or spinning procedures (Stadniychuk et al., 1996).

Results from various research groups have proved that homogeneous and

highly porous manganese oxide powders with particle size of submicron

meters can be synthesised through this route.

Often, Mn^{7+} is reduced into amorphous manganese dioxide by fumaric acid

(Xu et al., 1998, Stadniychuk et al., 1996) in a sol-gel route. The

particular reaction is presented in Eq.2.12 (Brousse et al., 2006) (Long

et al., 2000, Bach et al., 1990, Franger et al., 2002):

$$3C_4H_4O_4 + 10KMnO_4 \rightleftharpoons 10MnO_2 + 3K_2C_2O_4 + 4H_2O + 4KOH + 6CO_2 \qquad Eq.2.12.$$
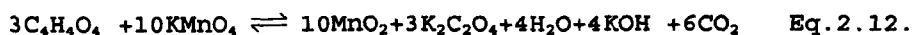
It is also reported that a stable colloidal MnO$_x$, with a high concentration

of MnO$_x$, can be prepared by reduction of tetraalkylammonium (methyl, ethyl,

propyl, and butyl) permanganate salts in aqueous solutions with 2-butanol

and ethanol (Brock et al., 1999). This sol-gel-derived tetrapropyammonium

MnO$_x$ thin film on nickel substrates exhibited good electrochemical

behaviour (Chin et al., 2002).

Drying the MnO_x gel at room temperature can produce a densified xerogel

of manganese oxides (Reddy and Reddy, 2003, Long et al., 2003). However,

xerogel has exhibited less satisfying capacitive behaviour compared with

porous hydrous manganese oxide film and underwent severe capacity loss

of 50 % after eight charge-discharge cycles (Long et al., 2003).

3.3. Determinants on the Electrochemical Performance of MnO_x

3.3.1. Crystalline Structure

In nature, manganese oxides have a number of polymorphs with many types

of tunnel and layered structures (Feng et al., 1998). The XRD patterns

of several commonly occurring MnO_x are presented in Fig.2.10 Crystalline

structure has profound impact on the electrochemical performance of the

manganese oxides (Brousse et al., 2006). Early researchers showed more

interests in amorphous MnO_2 and nanocrystalline compounds as electrode

materials (Lee and Goodenough, 1999, Hu and Tsou, 2002, Chang et al.,

2004b, Subramanian et al., 2005), with the assumption that the porous

morphology can enhance the ion accessibility and cation diffusion.

However, it is pointed out that these poorly crystallized MnO_2 contains

intergrowth of different tunnel structures, leading to more difficult

cations diffusion and resulting in higher resistance (Brousse et al.,

2006). Therefore, the maximum capacitance of this type of materials is

limited by the upper limit of BET surface area it can achieve.
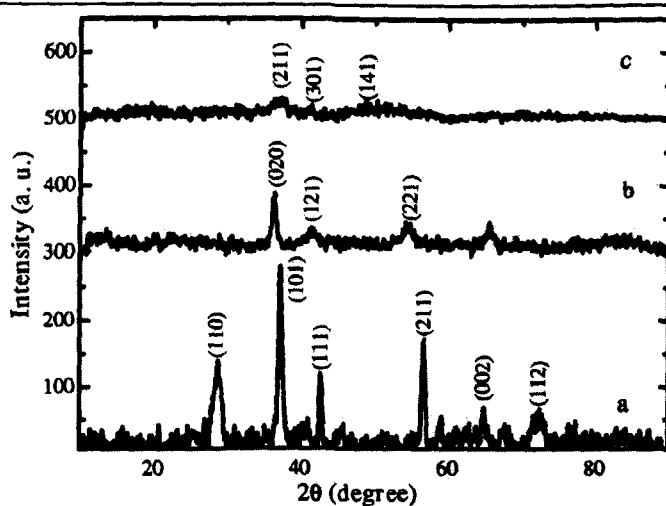
Fig. 2.10. XRD patterns of (a) β-MnO₂; (b) γ-MnO₂; (c) porous α-MnO₂ (Luo and Xia, 2007).

Recently, several attempts have been made to explore the potential of using crystallized MnO_2 materials (Brousse et al., 2006, Luo and Xia, 2007, Athouel et al., 2008). Various types of MnO_2, including α-MnO_2, β-MnO_2, γ-MnO_2, δ-MnO_2, with 1D and 3D tunnel structures, and birnessite ξ-$MnO2$ with layer structure have been tested for possible applications as the cathode material (Feng et al., 1998, Brousse et al., 2006). It was reported that for manganese oxides with various crystalline structures, the birnessite materials doped with potassium with 2D structure is at advantage as the presence of K^+ ions inside the 2D tunnels allows for the participation of a larger fraction of the MnO_2 to the charge storage process. On the other hand, specific capacitance of materials with 1D tunnel structures are generally low, e.g. γ-MnO_2 of 30 F/g and β-MnO_2 merely 5 F/g, because of its slow cation-diffusion which limited the charge storage processes to the surface (Brousse et al., 2006).

Further studies on crystallized Mg-doped sodium birnessite-type manganese dioxide (Athouel et al., 2008) revealed that the presence of magnesium as a dopant does not change the monoclinic structure of a classic birnessite, but contributes to the charge-transfer process upon charge

and discharge cycling as well as the Na^+ cations in Na_2SO_4 electrolyte. A stabilization of the MnO_2 structure upon oxidation occurs after about ten cycles and a progressive crystallinity loss of the material was observed upon potential cycling between the oxidized and reduced states (Athouel et al., 2008).

This theory of tunnel structure is also proved by an increased capacitance of more than 20 times the value of the origin spinel Mn_3O_4 can be achieved by transforming distorted spinel Mn_3O_4 to layered structure birnessite through CV in Na_2SO_4 (Dai et al., 2007), following the successful examples of electrochemical activation (Nam and Kim, 2006, Dai et al., 2007, Chen et al., 2007).

A more fundamental reason behind these crystal structure and the capacitance change is that the structure change also leads to significant change in conductivity (Taguchi et al., 2006), which eventually influences the pseudocapacitive behaviour. Due to the Jahn-Teller distortion of the $MnIIIO_6$ octahedral, the conductivity of manganese oxides involving trivalent Mn(III) is rather low as compared to that of MnO_2 or amorphous manganese (oxyhydro) oxides involving Mn(IV) (Taguchi et al., 2006). When transforming thermodynamically stable γ-Mn_2O_3 into α-Mn_2O_3 and Mn_3O_4, by mechanical grinding, the capacitance of manganese oxides decreased linearly with a decrease in the crystallinity of γ-MnO_2 due to the formation of $MnIIIO_6$ octahedral (Taguchi et al., 2006).

Therefore, it can be concluded that although the major attentions are still focused on the study of amorphous manganese oxides, crystalline manganese oxides with appropriate tunnel structures represent a group of rising candidates for the application as electrode materials in supercapacitors.

3.3.2. BET Surface area and Pore Structures

In general, larger surface area indicates higher accessibility of the active materials, leading to a better capacitive behaviour. Several research projects focusing on synthesising MnO_2 with larger effective surface area have yielded encouraging results (Devaraj and Munichandraiah, 2005a, Lee et al., 2001, Devaraj and Munichandraiah, 2007a). Efforts have been made to enhance the surface area and porosity of manganese oxide film by adding surfactant, e.g. sodium lauryl sulfate (SLS) (Devaraj and Munichandraiah, 2005a) and Triton X-100 (Devaraj and Munichandraiah, 2007a), during the electrodeposition. Enhanced surface area of 76.4 m^2 g^{-1} and 84.46 m^2 g^{-1} were reported with the addition of these two surfactants respectively, corresponding to 20 % and 60 % of improvement in specific capacitance. On the other hand, a fade of 40 % in capacitance has been reported due to a 50 % decrease of surface area from the aging of the co-precipitated MnO_2 (Brousse et al., 2006).

However, it was suggested that for amorphous MnO_2, the capacitance reaches a maximum at a surface area of 200 m^2/g, further increase of the surface area does not provide additional charge storage (Brousse et al., 2006). Moreover, it was declared that specific capacitance depends on the pore size distribution rather than BET surface area (Reddy and Reddy, 2003). Since the functions of pore size and pore structure on the double-layer capacitive processes have been well studied (Conway, 1999, Song et al., 1999, Fuertes et al., 2004), it may be worthwhile to extend the research into the process of pseudocapacitance.

Mathematical models considering the effect of the pore size distribution for the impedance of porous materials have been developed (Song et al., 1999, Jang et al., 2003), based on the transmission line model (de Levie, 1963, De Levie, 1965). Various research findings have complemented the

understanding. It was observed that for the two types of manganese oxides,

in the forms of xerogel and ambigel, with similar surface area of 63 m^2g^{-1}

and 72 m^2 g^{-1} respectively, xerogel only exhibited 56 % of the capacitance

of ambigel. Because the majority pore diameters of xerogel are <20 nm,

while ambigel are mesopores with diameter of 20-100 nm (Reddy and Reddy,

2003). A similar conclusion that a higher percentage of large pores can

ensure the delivery of higher power at higher charge/discharge rate was

also drawn from the manganese oxide film synthesised by potentiostatic

deposition (Wu and Chiang, 2004). Moreover, three types of porous MnO_2:

ordered mesoporous β-MnO_2 with [1×1] channels, disordered mesoporous

γ-MnO_2 with [1×2] and [1×1] channels and disordered porous α-MnO_2 with

[1×1] and [2×2] were synthesised to study the relationship between

electrochemical properties and pore structures of manganese oxide (Luo

and Xia, 2007). It was declared that the capacitance profiles of the three

types of 1D tunnel structure MnO_2 are clearly dependent upon the pore

structure despite of their crystalline structures; mesoporous,

especially ordered mesoporous MnO_2 has superior capacitive behaviour,

rate capability and high frequency performance in 1M Na_2SO_4 solution due

to its lower pore resistance and its better accessibility of ions to the

electrochemically active surface (Luo and Xia, 2007).

Thus, it is to conclude that surface area as well as the pore structures

are determinants for the accessibility of the MnO_x to the electrolyte,

which limiting the depth and rate of ions transfer within the bulk

materials. Engineering MnO_x with desirable structure of organised

mesopores and macropores may enhance the overall capacitive performance.

3.3.3. Thickness and Loading of the Manganese Oxides

Thickness is a key limiting factor for the capacitive performance of

manganese oxide materials; significant decrease of specific capacitance with the increase of electrode thickness have been reported with most of the research groups whether the material was synthesised by electrodeposition, sol-gel route or chemical deposition.

Often, exceedingly low loading of the manganese oxides was applied on to the electrode to ensure a 'high specific capacitance', on the order of tens of micrograms cm^{-2} (Nam and Kim, 2006, Wei et al., 2007, Devaraj and Munichandraiah, 2005a, Devaraj and Munichandraiah, 2007a) or with a thickness of tens of nanometres (Wu and Chiang, 2004). In such cases, e.g. at the loading of 0.03 mg/cm^2 even an extreme high specific capacitance of 1330 F/g would only provide a capacitance of 0.039 F/cm^2 (Devaraj and Munichandraiah, 2005a), which is of little use for real world application with high power and energy demand.

Even at low loading rates, the decreases of specific capacitance are discernable. A 55 % decrease of its initial specific capacitance of 330 F/g was reported when increase the loading from 18 to 116 $\mu g/cm^2$ for the thin layer of manganese oxides obtained from electrostatic spray deposition (Nam and Kim, 2006); similar observations were made with MnO_2 obtained from chemical deposition (Wei et al., 2007) and electrodeposition (Broughton and Brett, 2005).

Essentially, this limiting effect of the thickness of the MnO_2 loading is the combined results of the low electrical conductivity of manganese oxides, the obstruction from the longer path for diffusion of protons (Chen et al., 2004, Hu and Tsou, 2002) and other ions (Toupin et al., 2002b). It was also suggested that only a limited fraction of the MnO_2 composite is electrochemically active (Toupin et al., 2002a) (Toupin et al., 2004) (Brousse et al., 2006) (Athouel et al., 2008). In another

approach, $K_{0.02}MnO_2H_{0.33} \bullet 0.53H_2O$ was fabricated into films of different thickness (<5 µm ~100 µm) (Wu et al., 2004a). No change of the manganese oxidation state was detected for the inner layer of the thicker film electrode, a finding totally different from the case of thin film electrode. Besides, the specific capacitance obtained so far are still far from the theoretical value of more than 1000 F/gm (Devaraj and Munichandraiah, 2005b) (Raymundo-Pinero et al., 2005), which implies the existence of a vast amount of material that has not been utilised.

However, amelioration has been proved effective in improving the situation. For example, introducing CNTs into the MnO_x during synthesis can form a 3-D porous and conducting network of CNTs to assist the electron and ion transfer within the MnO_x. A electrode capacitance of 5 F cm^{-2} at high loading of 35 mg cm^{-2} was achieved in this manner (Jin et al., 2007). Various attempts to overcome the limitations of the thickness have been made and many of which have achieved encouraging results.

3.3.4. Annealing Temperature

A number of studies have been carried out about the effects of annealing temperature and annealing time on the electrochemical activity of MnO_x. Essentially, annealing treatment results in three transformations in the manganese oxides: loss of water content, decrease in surface area and changes in structure. The effects of annealing on these aspects will be discussed in detail.

Water content in MnO_2 is known to affect the electrochemical reactivity and thermodynamic stability of various MnO_2 phases as it causes a variation in crystal lattice and a consequent variation in electrical conductivity and electrode potential.(Pang et al., 2000) Heat treatment at a

temperature up to 200 °C is believed to remove both physically and chemically adsorbed water molecules (Toupin et al., 2002a). The loss of water molecules means a reduced weight, which may lead to a small increase of specific capacitance (Toupin et al., 2002a), however, it also leads to a decrease in surface area (Devaraj and Munichandraiah, 2007b) (Toupin et al., 2002a), which can vitally hinder the electrochemical activity. Furthermore, chemically bound water is believed to be essential for the transportation of active ionic species. Consequently, the loss of water content through heat treatment will lead to the loss of pseudocapacitance (Rajendra Prasad and Miura, 2004) (McKeown et al., 1999) (Reddy and Reddy, 2004). It was suggested that similar to the case of ruthenium oxides (McKeown et al., 1999), the increase of water content leads to increase of ionic transport while the decrease of electronic transport at the same time (Rajendra Prasad and Miura, 2004). Thus, heat treatment up to a certain level can possibly enhance the overall pseudo-capacitive behaviour (Pang et al., 2000) (Chin et al., 2002), although most researchers observed monotonic decrease of specific capacitance upon heat treatment even at temperatures below 200 °C (Toupin et al., 2002a) (Devaraj and Munichandraiah, 2007b) (Chang et al., 2004a) (Djurfors et al., 2003) (Nakayama et al., 2004).

Significant structure changes, together with a drastic decrease of surface area, will occur at an annealing temperature above 300 °C, as demonstrated in Fig. 2.11 (Toupin et al., 2002a). As described in Section 3.4.1, certain crystalline structures of MnO_x are less favourable for the charge-storage mechanism; transition into one of these crystalline structures will definitely diminish the pseudo-capacitance of the electrode material. The transformation from amorphous and hydrous MnO_x to Mn_3O_4 and Mn_2O_3 with crystalline structures were observed upon the increase of annealing temperature up to 600 °C (Toupin et al., 2002a)

(Chang et al., 2004a) (Chang and Tsai, 2005). Condensation, rearrangement,

reconstruction, and growth of the deposited MnO_x as a function of

temperature were recognised by atomic force microscopy during

annealing. (Chang et al., 2004a) It was concluded that heat-treatment at

temperatures higher than 200 °C will promote the formation of crystalline

Mn_3O_4 and Mn_2O_3 and consequently result in the loss of pseudo-capacitive

properties of the oxides (Toupin et al., 2002a) (Chang et al., 2004a)

(Chang and Tsai, 2005).
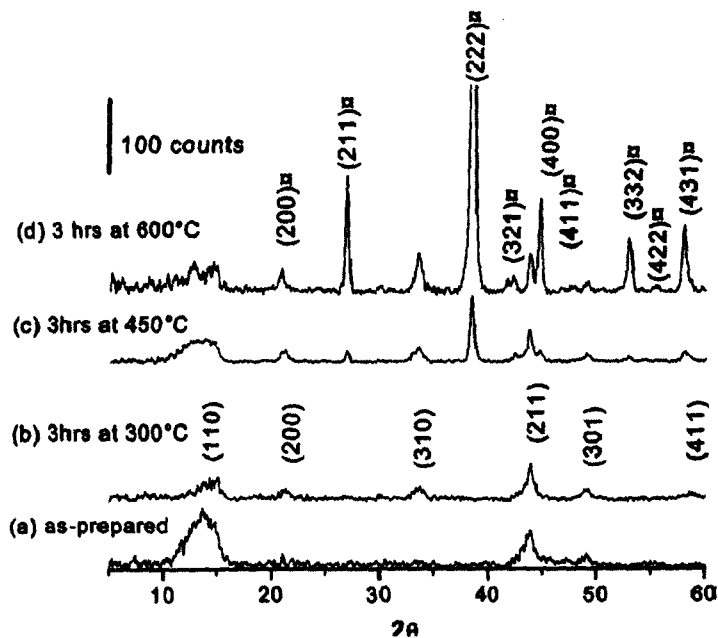
Fig. 2.11. The crystalline structure transition of α-MnO_2 upon annealing

treatment (a) as-prepared (b) 3 h at 300 °C, (c) 3 h at 450 °C, and (d)

3 hr at 600 °C (Toupin et al., 2002a).

The corresponding decrease in BET surface area upon the transition from

α-MnO_2 to Mn_2O_3 through annealing from 70 °C to 800 °C was also reported

(Devaraj and Munichandraiah, 2007b). Deterioration of α-MnO_2 with

tetragonal unit cell structure was observed with the increase of annealing

temperature, especially at temperatures higher than 300 °C. A continuous

decrease in BET surface area, from initially 190 m^2 g^{-1} to 145 m^2 g^{-1} at

300 °C and finally 8 m^2 g^{-1} for the Mn_2O_3 annealed at 600 °C and above

(Devaraj and Munichandraiah, 2007b), was attributed to agglomeration of particles on annealing. The corresponding degradation in capacitive performance was observed, with a loss of 13 % of its specific capacitance upon annealing at 200 °C, due to the loss of water content; and a further drastic 63 % loss at the annealing temperature above 400 °C, due to the transition from α-MnO$_2$ to Mn$_2$O$_3$ (Devaraj and Munichandraiah, 2007b).

In order to gain a clear understanding of the phase and phase evolution involved in MnO$_x$ materials during the thermal treatment, an in-depth microstructural characterisation of manganese oxide materials formed from the physical vapour deposition process was conducted (Djurfors et al., 2003). The cubic forms of Mn and MnO with a porous zigzag structure were formed from e-beam evaporation and deposition. Upon annealing at 300 °C, Mn is progressively oxidised to MnO, followed by further oxidation of MnO to Mn$_3$O$_4$. The zigzag structure near the surface was thus destroyed and replaced with a columnar oxide layer of cubic MnO and tetragonal Mn$_3$O$_4$. This capping effect ultimately reduces the usable surface area and is thought to account for the reduction in capacitance seen on annealing (Djurfors et al., 2003). Further researches confirmed that the thermally annealed sample did not contain hydrated manganese (Mn-O-H), but only anhydrous compounds (Mn-O-Mn) and free water (H-O-H), which is believed to be the reason of its poor pseudo-capacitive performance (Djurfors et al., 2005).

3.3.5. Electrolyte

The choice of electrolyte also has significant impacts on the performance of the manganese oxides electrodes. The pH condition is an important determinant of operating potential window; and different existing ions determine the rate of intercalation and the situation of corrosion. Thus, desirable electrode performance can be obtained by choosing the

electrolyte carefully.

pH Condition

As depicted in Fig. 2.8 (pH - potential performance), electrochemical reversibility and the charge storage mechanism of hydrous manganese oxides largely depend on the pH of the electrolyte (Hu and Tsou, 2002). The reactions of Mn(IV) to Mn(II) and Mn(IV) to Mn(VII) should be avoided during charging and discharging the capacitor, as Mn(II) and Mn(VII) are soluble in the electrolytic solution. These irreversible reactions will lead to the partial dissolution of the electrode and a subsequent decrease of capacitance and cycling reversibility (Raymundo-Pinero et al., 2005, Messaoudi et al., 2001, Chang et al., 2007). The transformations of Mn(IV) to Mn(II) and Mn(IV) into Mn(VII) occur at different potentials under different pH conditions. For example, it was reported that transformation of Mn(IV) to Mn(II) occurs at potentials of 0.47 and 0.05 V (vs. NHE) for pH 6.4 and 10, respectively; and equilibrium potentials for the transformation of Mn(IV) into Mn(VII) are 1.19 and 0.98 V (vs. NHE) for pH 6.4 and 10, respectively (Raymundo-Pinero et al., 2005). Thus, by optimizing the pH, the maximum operation potential window can be achieved.

On the other hand, it was suggested that pH condition affects the water decomposition and gas evolution, which also limits the maximum operating potential window (Hong et al., 2002). Gas evolution reactions are related to H_2O decomposition, H+ reduction, and OH- oxidation (Eq.2.13), the presence of excessive H^+ ions induces H_2 gas evolution at -0.2 V which limits the operating voltage window to about 1.2 V; while the presence of excessive OH- ions results in O_2 gas evolution at 0.7 V by their oxidation process, limiting the operating voltage window to 1.8 V. A operating voltage window of 2V was achieved with the 1M KCl electrolyte in which the electrode reactions for H_2O decomposition were observed at potentials

of 1.1 V (anode) and -0.9 V (cathode) versus Ag/AgCl reference electrode

(Hong et al., 2002). The negative shift of the cathode reaction potential

was likely responsible for the increased cell voltage (2.0 V) as the result

of a high overpotential for the hydrogen evolution reactions, i.e.

reactions Eq.2.13 (3) and Eq.2.13 (4) below, on the carbon material use

in the cathode.

$$2H_2O \rightleftharpoons O_2 \text{ (g)} + 4H^+ + 4e^- \qquad \text{Eq. 2.13 (1).}$$

$$4OH^- \rightleftharpoons O_2 \text{ (g)} + 2H_2O + 4e^- \qquad \text{Eq. 2.13 (2).}$$

$$2H^+ + 2e^- \rightleftharpoons H_2 \text{ (g)} \qquad \text{Eq. 2.13 (3).}$$

$$2H_2O + 2e^- \rightleftharpoons H_2 \text{ (g)} + 2OH^- \qquad \text{Eq. 2.13 (4).}$$
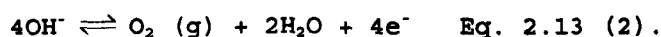
Ion- size and Intercalation

It was reported that electrolyte with equal transference numbers for the

cation and anion can promote capacitive behaviour and anions with smaller

hydration sphere and smaller particle size leads to faster diffusion and

higher chemisorptions rate (Jeong and Manthiram, 2002). Experiments

comparing the electrochemical performance of the MnO_2 material in several

neutral aqueous electrolytes including NaCl, KCl and LiCl with the same

concentration of 2M have been conducted (Lee and Goodenough, 1999, Jeong

and Manthiram, 2002). It was claimed that although Li^+ is smaller than

Na^+ and K^+, it has a larger hydration sphere, which makes it disadvantaged.

This theory is supported by the results from other research groups (Reddy

and Reddy, 2003) (Wu et al., 2004a).

However, a more recent study on the electrochemical behaviour of the MnO_2

electrode in 1 mol dm^{-3} KOH and 1 mol dm^{-3} LiOH (Yuan and Zhang, 2006)

declared that the reaction mechanism of MnO_2 electrode in LiOH appears

to be Li^+ ion insertion/extraction in the MnO_2 solid, followed the battery

reaction of $MnO_2 + xLi^+ + xe^- \rightleftharpoons Li_xMnO_2$. This finding may elicit further

thoughts upon the mechanism of the charge-storage within MnO_x.

Corrosion and Non-aqueous Electrolytes

Another major concern in selecting electrolyte is the issue of corrosion. Although chloride solutions normally have higher ionic conductivity which is desirable in diminishing the iR drop, they are likely to cause corrosion on stainless steel current collector (Athouel et al., 2008). Thus, platinum or titanium current collectors are normally applied in chloride electrolytes. On the other hand, sulfate-based salts, although with lower ionic conductivity and lower solubility, showed long-term cycling stability with stainless steel current collector (Athouel et al., 2008). This trade-off between ionic conductivity and corrosion-resistance is thus up to the individual researchers to decide.

Alternatively, using an organic solvent provides a solution for the corrosion issue. The electrochemical performance of electrochemically deposited Mn_3O_4 in degassed acetonitrile solution containing 0.1 mol dm^{-3} $TBAClO_4$ (TBA = tetrabutylammonium) and 0.2 mol dm^{-3} H_2O was studied. (Jiang and Kucernak, 2002) A 2 V potential window was achieved; the presence of water in the organic solvent facilitates the capacitive behaviour, yet limits the potential window. However, the higher resistance of the organic solvent impedes the capacitive performance of the electrodes. The specific capacitance calculated from organic solutions is only about 60 % of that from aqueous solutions (Jiang and Kucernak, 2002). Furthermore, a gel electrolyte of aqueous solution of KCl in potassium poly(acrylate) (PAAK) polymer with ionic conductivity in the order of 10^{-1} S cm^{-1} was proposed to be used in the $MnO_2 \cdot nH_2O$ supercapacitor (Lee and Wu, 2008). It was reported that the polymer component did not impose a negative effect on leakage current and the supercapacitor with the gel electrolyte in fact delivered substantially higher specific capacitances than those in the liquid electrolyte with the same salt (KCl) composition (1 mol dm^{-3}). This improvement was attributed to the hydrophobic nature

of the polymeric component in the gel, which enhanced the compatibility between the electrode matrix and the electrolyte and essentially increased the wettability. On the other hand, the swelling process of the polymer molecules within the electrode interior can open closed pores which increased the electrolyte accessibility (Lee and Wu, 2008).

3.4. Summary on Manganese Oxides

Manganese oxides, as a type of environmentally friendly material with various oxidation states, are well established electrode materials for both batteries and supercapacitors. Recent researches have explored the synthesis, determinants and favourable operating conditions for pseudocapacitive performance, as well as the mechanisms of the Faradaic process of this material. Despite of their relatively low conductivity, it is genuinely believed that MnO_x is a type of promising and competitive electrode material for applications in supercapacitors.

4. Conducting Polymers

4.1. Conductivity and Doping of Conducting Polymers

Polymers are generally insulating in nature. However, the conductivities of electronically conducting polymers (ECPs) can undergo an increase of 10 orders of magnitude or even more by oxidative doping (Fan and Maier, 2006). Compared with inorganic semiconductors, ECPs can be doped to a much higher level, i.e. one charge per three monomer units (Warren, 2005). Due to the high mobility of the electronic charges in the doped form of polymers, the excess electronic charge ends up in a highly delocalised state (Rudge et al., 1994a).

This exceptional conductivity change with the doping status of ECPs is illustrated in Fig.2.12. Upon the oxidation of ECPs, new energy states are produced between Valence Band and Conduction Band, creating lower

energy gaps (Fig. 2.12). Intrinsically, electrical conductivity depends on the electron mobility. Thus, lower bandgap will improve the electron mobility and result in enhanced electrical conductivity (Rasmussen and Pomerantz, 2007).
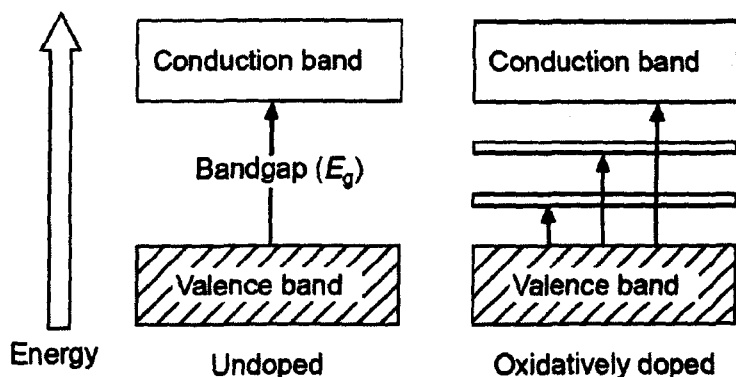
Fig. 2.12. Schematic Diagram of Bandgap (Eg) and Doping ECPs (Rasmussen and Pomerantz, 2007).

ECPs can be reversibly switched between their redox states. Interestingly, the redox sites of ECPs are not clearly defined and charges incorporated during redox switching are partially delocalised (Audebert and Miomandre, 2007). This made it possible for ECPs to create energy levels within the band gap (as shown in Fig.2.12), which stabilises charge incorporation within the macromolecular (Audebert and Miomandre, 2007)

It is generally agreed that the mechanism of conductivity in ECPs is based on the motion of charged defects within the conjugated framework (Rudge et al., 1994a). ECPs are extensively conjugated. Their chemical bondings lead to one unpaired electron per carbon atom, in which the carbon orbits are in the sp^2pz configuration and the orbital of successive carbon atoms along the backbone are overlapped, leads to electron delocalisation along the backbone of the polymer (Rudge et al., 1994a). This electronic delocalisation provides the highway for charge mobility along the backbone of the polymer chain (Feast, 1986). The charge carriers, either

positive p-type or negative n-type, are the products of oxidizing or reducing the polymer respectively (Rudge et al., 1994a).

It is worth mentioning that conducting polymers are only electroactive within certain potential ranges. Overoxidation is generally undesirable as it leads to the polymer chemical degradation as well as significantly reduction of conductivities (Audebert and Miomandre, 2007). This phenomenon is generally attributed to the localisation of charge carriers through H-bonding at high doping level (Zotti et al., 2003). However, the relationship between conductivity and doping level is rather complicated. It depends on the inherent charge carrier mobility of each individual conducting polymer (Audebert and Miomandre, 2007) as well as other external factors, e.g. the pH values of the aqueous electrolyte, which also influence the overoxidation (Li and Qian, 2000).

For conducting polymers, p-doping refers to the partial oxidation of the π backbone, i.e. abstracting electrons from the polymer backbone through external circuit and incorporating anions from electrolyte into the polymer film to maintain the electroneutrality (Rudge et al., 1994b). N-doping refers to the reverse mechanism of introducing electrons into polymer backbone from the external circuit and cations entering the polymer from the electrolyte (Rudge et al., 1994a). The majority of ECPs, including PAni and PPy, are p-doped type in aqueous electrolyte (Rudge et al., 1994a). However, ECPs that are capable of both p-doping and n-doping, e.g. poly-3-(4-fluorophenyl)-thiophene (PFPT), are possible through engineering.

Movements of the ions, i.e. cations and anions, are essential to maintain the electroneutrality during the doping process. For p-doped polymers, the electrochemical neutralisation processes can be anion-dominant

(anions are expelled from polymer film), cation-dominant (cation diffuse into the polymer film) or a combination of both (Irvin et al., 2007). The dominant process is determined by the size and the mobility of anions and cations. As shown in Fig.2.13 b, when anions are small and have high mobility, the neutralisation process is anion dominant; and when anions are large and immobile, the cations are incorporated into the polymer chain to maintain the charge neutrality (Fig. 2.13 c) (Smela, 2003). Therefore, solvent plays an important part in the redox processes of ECPs. The two major concerns for solvent include: ionic motion induced by the charge of the polymer chains; and the hydrophobic/ hydrophilic balance of the polymer matrix (Audebert and Miomandre, 2007).
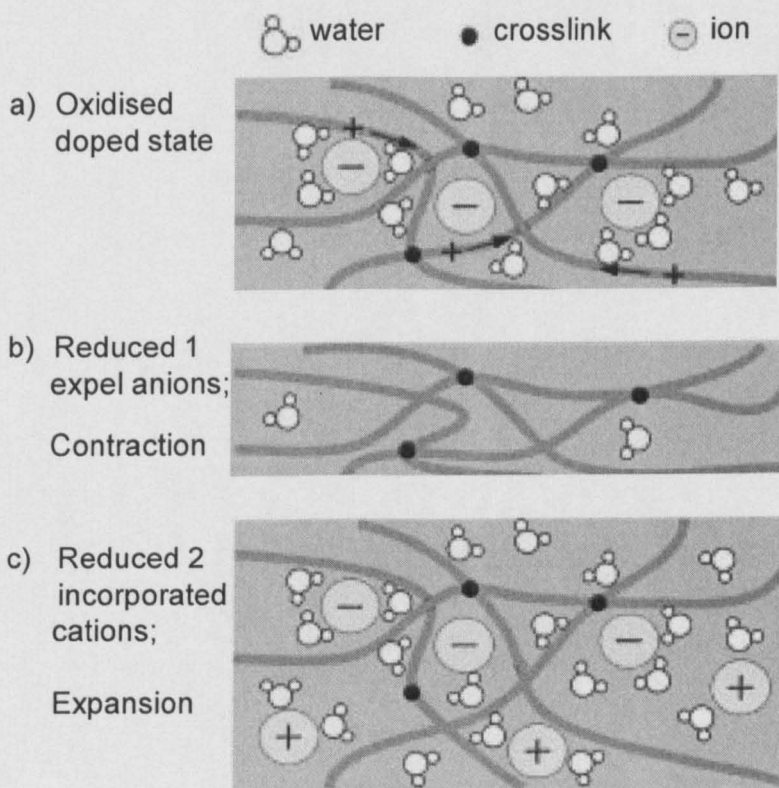
Fig. 2.13. Schematic diagram of redox processes of EPCs and volume change (Smela, 2003).

One of the major drawbacks of ECPs as electrode materials is their poor mechanical stability due to the structure and volume changes during redox processes. There are three main causes for the volume and structure

changes are (Cascales and Otero, 2004): the change of length of carbon-carbon bonds on the polymer backbone, interaction between the charged sites inside the polymer in its oxidized state and mass transport (Smela, 2003). As illustrated in Fig. 2.13, the polymer simply expands when ions and/or solvent enter and contracts when they exit (Smela, 2003). Study on PPy in aqueous system with chloride ions once identified an anisotropic swelling of 13 % upon oxidation and reduction (Cascales and Otero, 2004). Although the volume change of ECPs is highly desirable in some applications, e.g. artificial muscles and actuators, it decreases the mechanical stability of the polymers and impairs the cyclability in the applications as an electrode material.

4.2. Energy Storage Mechanism of Conducting Polymers

As a type of electrode material for supercapacitors, conducting polymers have the following advantages: low cost (compared with noble metal oxides), high doping-dedoping rate during charge-discharge process, high charge densities compared to high surface carbon, easy synthesis through chemical and electrochemical processing (Rudge et al., 1994a).

The electrochemical processes at the conducting polymers applied at the electrodes of supercapacitors are electrochemical redox reactions associated with sequential Lewis acid- or Lewis base-producing steps so that the neutral polymer molecules are converted to multiply charged structures through electrochemical Lewis-type reactions involving electron withdrawal or electron donation (An et al., 2002). The origin of pseudocapacitance at the surface of conducting polymer is illustrated in Fig. 2.12 (Peng et al., 2007b). When charged, the conducting polymer loses electrons and becomes polycations, causing the anions in the electrolyte (Cl- in this case) to intercalate into the conducting polymer

in order to maintain electro-neutrality (Peng et al., 2007b). The repeated

intercalation and depletion of ions during charging and discharging bring

high pseudocapacitance to the conducting polymers compare to the

double-layer capacitance of carbon materials. For different types of ECPs,

viz. PAni and PPy, their energy storage mechanisms will be explained in

the following two sub-sections.
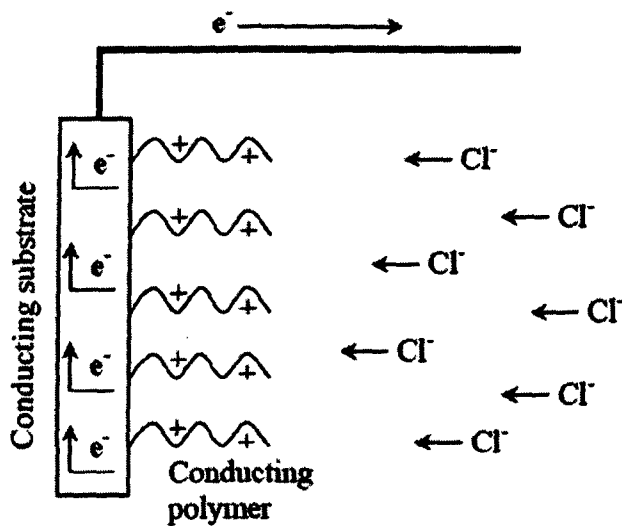
Fig. 2.14. The arising of pseudocapacitance in a conducting polymer (Peng
et al., 2007b).

4.2.1. Polyaniline

Electrical conductivity of polyaniline is in the range of 10^{-8} to 400 S

cm^{-1} and this figure will increase as better processing methods are

developed reducing structural defects (Hardaker and Gregory, 1999). The

conductivity of polyaniline depends on two variables: the degree of

oxidation of the PAni and the degree of protonation of the material (Huang

et al., 1986). Due to the presence of the chemically flexible -NH⁻ group,

polyaniline shows some interesting physicochemical properties such as

protonation and deprotonation.

Polyaniline is well known for its unique property that its electrical

properties can be reversibly controlled both by charge-transfer doping

and by protonation (Adhikari, 2004). Also, PAni can be easily synthesised

by protonic acid doping and the products are with good stability. In

general, the oxidation level of a polyaniline can be described by the

following molecular formula:

Leucoemeraldine

Protoemeraldine

Emeraldine

Nigraniline

Pernigraniline
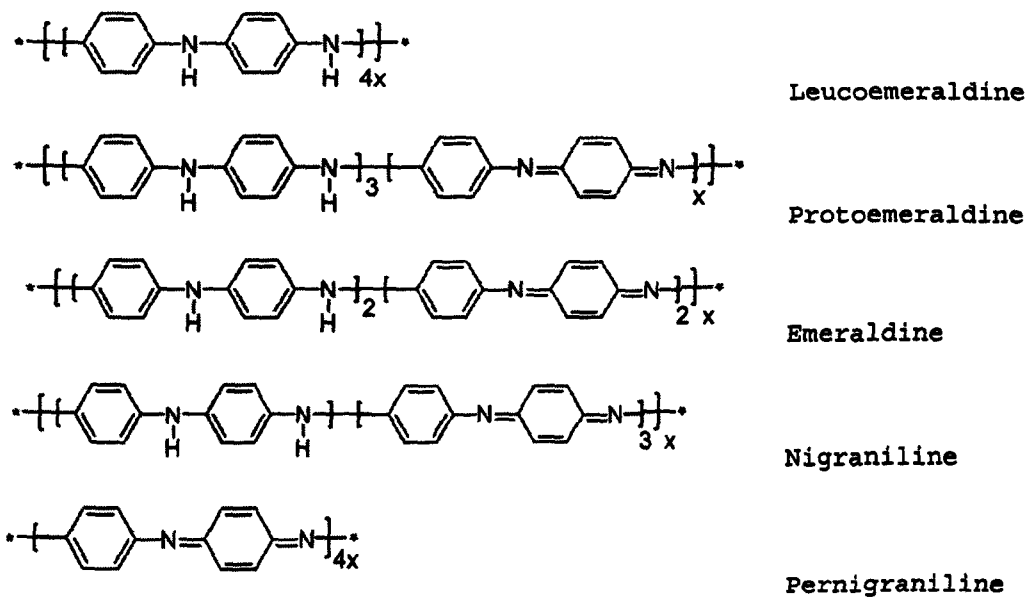
Among these oxidation forms, the half oxidized polyaniline (emeraldine)

is regarded as most conductive (Hardaker and Gregory, 1999, Huang et al.,

1986), due to the extensive π conjugation in the polymer chain (Huang

et al., 1986). During the oxidation, polyaniline is gradually oxidised

from its fully reduced form of leucoemeraldine (pale yellow), to the half

oxidized form of emeraldine (blue), and the fully oxidized pernigraniline

(violet), as depicted in Fig.2.15 (Huang et al., 1986, Ayad et al., 2004).
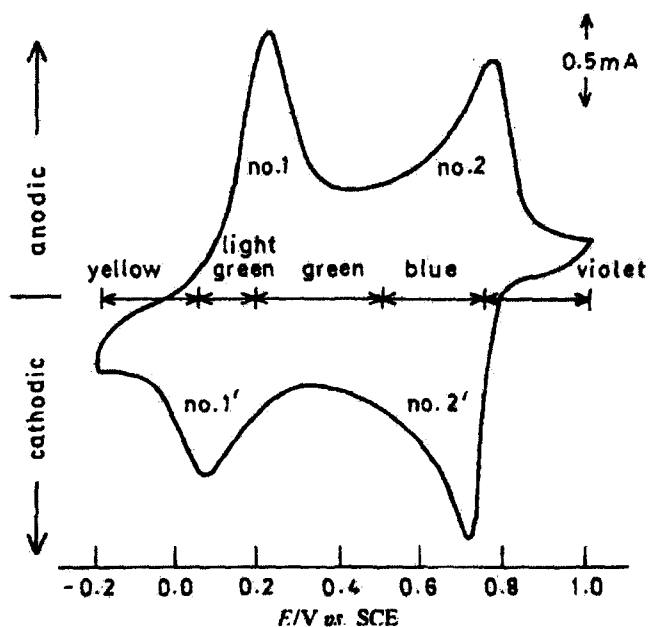
Fig. 2.15. Schematic CV of PAni in potential of peaks during its oxidation and reduction process with approximate colour changes (Huang et al., 1986).

Although these are the identified oxidation states of polyaniline, the actual oxidation is a continuum ranging from the completely reduced form (leucoemeraldine) to the completely oxidised form (pernigraniline) (Huang et al., 1986). Through this continuous electron flow, the differential charge (Δq) changes proportionally to the differential potential (Δv). Hence, pseudocapacitance ($C = \Delta q / \Delta v$) builds up.

Various methods have been used to study the oxidation and reduction processes of PAni, e.g. electrochemical quartz microbalance, radiotracers, electrochemical tunneling microscopy (Ybarra et al., 2000). MacDiarmid suggests that the doping process for PAni occurs by proton addition to the polymer rather than by the oxidation of polymer π system (Huang et al., 1986). Thus, the conductivity of PAni depends not only on the degree of oxidation of PAni, but also the degree of protonation (Huang et al., 1986). For the reaction of PAni:

$$AH_n \rightleftharpoons A + nH^+ + ne^-$$ Eq.2.14.

The Nernst equation for this reaction is (Huang et al., 1986):

$$E_{red} = E^0_{red} + \frac{RT}{nF} \ln \frac{[A][H^+]^n}{[AH_n]}$$ Eq. 2.15 (1).

$$E_{red} = E^0_{red} + \frac{RT}{nF} \ln \frac{[A]}{[AH_n]} + \frac{RT}{nF} \ln[H^+]^n$$ Eq. 2.15 (2).

Clearly, this reaction is pH dependent. Further studies have pointed out that the oxidation of PAni is completed by proton expulsion at low pH values, followed by anion insertion (Orata and Buttry, 1987, Ybarra et al., 2000).
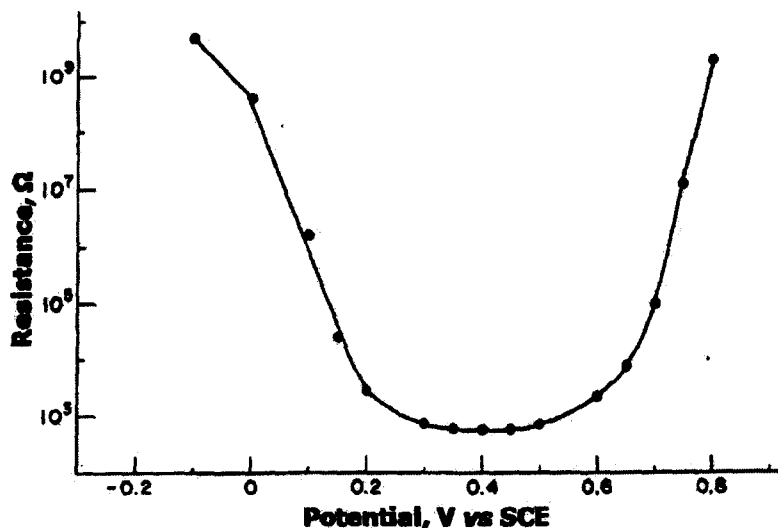
Fig. 2.16. Resistance of PAni as a function of electrochemical potential (Paul et al., 1985).

It is concluded that without sufficient acidity (when pH > 4), no significant protonation can occur and PAni is essentially electrochemically inactive (Huang et al., 1986) (Hardaker and Gregory, 1999) (Ybarra et al., 2000). Thus, as an electrode material, PAni should only be used in acidic electrolyte.

4.2.2. Polypyrrole

Due to its stability in the oxidized state, high conductivity, and its long term stability of its conductivity, polypyrrole is one of the wildly studied conducting polymers (Hughes et al., 2002, Fan and Maier, 2006, An et al., 2002, Adhikari, 2004, Chen et al., 2000).

The oxidation states of PPy are shown in the Fig. 2.17 (Cho et al., 2007).

The conductivity of polypyrrole changes dramatically through the oxidation processes. Some researchers attribute the change in conductivity to the change in Energy gap (Cho et al., 2007). In neutral status (Fig. 2.17 a), the band gap for PPy is 3.16 eV (Fig. 2.18 a), too wide for electrons transfer from Valence Band to Conducting Band (Cho et al., 2007). Upon oxidation, a local deformation to quinoid structure happens (Fig. 2.17 b); the unpaired spin and the positive charge are referred to as a polaron. With further oxidation, PPy loses another electron and forms a bipolaron (Fig. 2.17 c), a structure that is energetically favoured over the formation of two polarons (Cho et al., 2007). The electronic energy states of bipolaron lie further away from the band edges (Fig. 2.18 c) With further oxidation, the energy state of bipolarons overlaps, (Fig. 2.18 d) forming a narrow intermediate band structures (Cho et al., 2007).
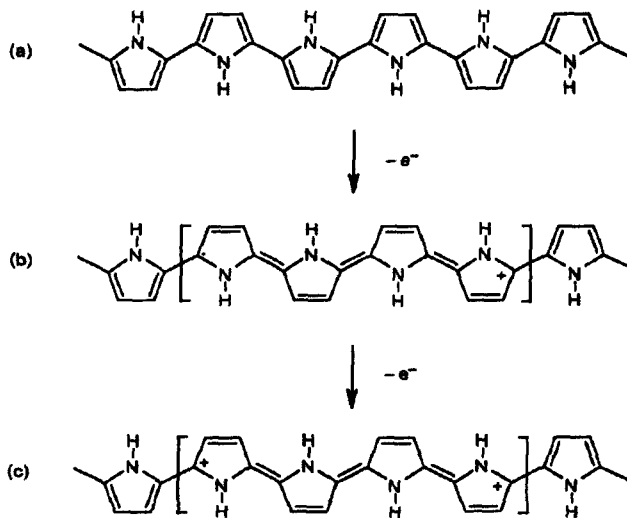
Fig. 2.17. Electronic structures of (a) neutral PPy (b) polaron in partially doped PPy and (c) bipolaron in fully doped PPy (Cho et al., 2007)
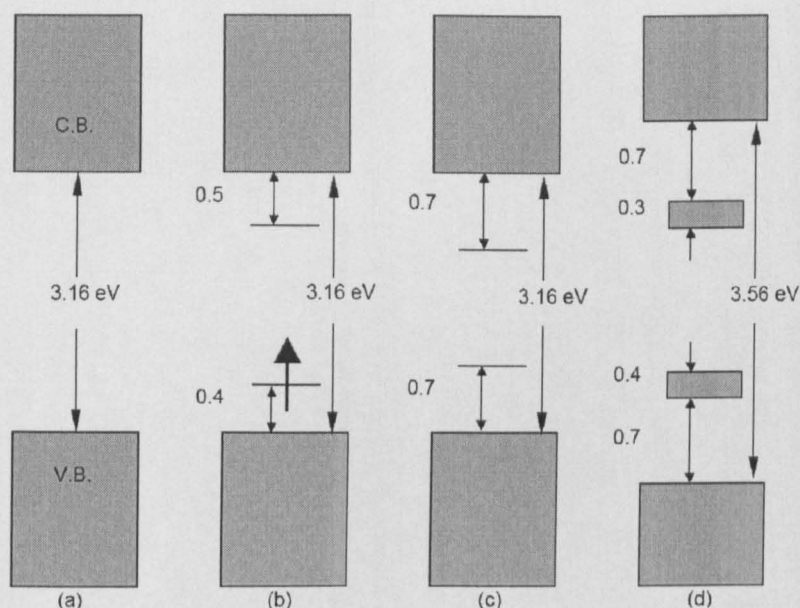
Fig. 2.18. Schematic diagrams of electronic energy of (a) neutral PPy, (b) polaron, (c) bipolaron, and (d) fully doped PPy (Cho et al., 2007).

When applied as the electrode material, the charge-discharge process of PPy could be described as following: during charging process, a positive charge is introduced on the PPy chains by p-doping, resulting from a Lewis ionisation process which involves oxidation with electron transfer. The discharge process involves a reduction process with release of hydroxyl ions. This ionisation process will also invoke a quasi-linear, one-dimensional cylindrical double layer between the electrode and the counterions of the electrolyte (An et al., 2002). Therefore, the pseudocapacitance by faradaic redox process in polypyrrole, together with the stimulated double layer capacitance made up the total specific capacitance.

It is to be noted that the conductivity of polypyrrole reaches a threshold at the potential of -0.1 V, as demonstrated in Fig. 2. 19 (Feldman et al., 1985). Therefore, for its applications as an electrode material, the potentials negative to – 0.1 V should be avoided.
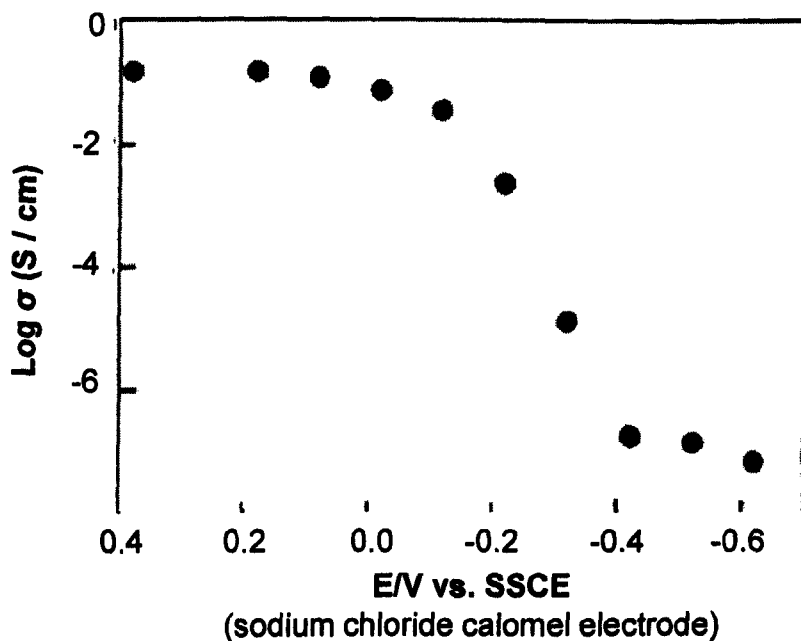
Fig. 2.19. Conductivity of PPy Vs potential change in 0.1 M Et₄NClO₄/CH₃CN

(Feldman et al., 1985).

4.3. Synthesis

Some simple intrinsically conductive polymers, such as polyaniline, polypyrrole, polythiophene have drawn great attention (Kötz and Carlen, 2000, Feast, 1986, Salaneck et al., 1996, An et al., 2002, Rudge et al., 1994a, Wu et al., 2005b, Hughes et al., 2002, Wu et al., 2004a), as they could be synthesized by various methods such as chemical, electrochemical, vapour phase etc.

4.3.1. Chemical Synthesis

Aniline monomer could be chemically oxidized into polymer in aqueous solution by a variety of oxidants, including $(NH_4)S_2O_8$, $K_2Cr_2O_7$, KIO_3, $FeCl_3$, $KMnO_4$, $KBrO_3$, $KClO_3$. The principal function of the oxidant is to withdraw a proton from an aniline molecule, without forming a strong co-ordination bond either with the substrate / intermediate or with the final product (Cao et al., 1989). However, smaller quantity of oxidant is used to avoid oxidative degradation of the polymer formed (Adhikari, 2004).

Many researches have been conducted to reveal the polymerization process of the aniline monomer. The polymerization of aniline was found to be a highly exothermic reaction; in acidic media, the conductive emeraldine is rapidly formed in one step (Fu and Elsenbaumer, 1994, Cao et al., 1989, Ayad et al., 2004). Fu and Elsenbaumer (Fu and Elsenbaumer, 1994) found out that the larger initial aniline concentration leads to less induction time; overoxidation with excessive oxidant cause the formation of higher oxidation states of polyaniline, the hydrolysis of polymer chain and chlorine substitution.

Cao et al (Cao et al., 1989) studied the chemical polymerization of aniline as a function of a wide variety of synthesis parameters: pH, relative concentration of reactants, polymerization temperature, time with a number of oxidizing agents and different protonic acids. They claimed that the reaction yield was not sensitive to most variables, while the molecular weight and the electrical conductivity of the polymerized polyaniline could be remarkably affected. Also, they reported that the long-time stirring of as-polymerized polyaniline with concentrated HCl leads to significant degradation of polyaniline. Also, the studies (Armes and Miller, 1988, Ayad et al., 2004) of the effect of the oxidant/monomer initial mole ratio found out that the conductivity, yield, elemental composition and the degree of oxidation of the resulting polyaniline are essentially independent of this ratio when its value is below 1.15.

Similarly, it is very easy to oxidise pyrrole monomer with a variety of oxidising agents due to its low oxidation potential. Oxidative transition metal ions from the metallic salts such as: $FeCl_3$, $Fe(NO_3)_3$, $Fe(SO_4)_3$, $K_3Fe(CN)_6$, $CuCl_2$ are common oxidising agents for the synthesis of highly conducting PPy (Nalawa et al., 1985) cited in (Adhikari, 2004). The scheme

is given in Eq.2.16 below.

$$n \underset{\underset{H}{N}}{\langle} \Big/ + 2n\ FeCl_3 \longrightarrow \left[\underset{\underset{H}{N}}{\left(\langle\Big/\right)} Cl_{/3}\right]_n + 2n\ FeCl_2 + n\ HCl$$
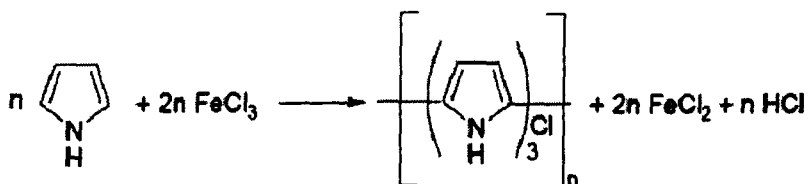
Eq. 2.16. Reaction scheme of PPy chemical synthesis (Adhikari, 2004).

This reaction is proposed to be initiated by the cationic radical $C_4H_5\cdot+$, which coordinates with the other pyrrole units ((Hsing et al., 1983) cited in (Adhikari, 2004)). The transition metal ion acts as the electron acceptor, probably forms a donor acceptor complex with pyrrole at the chain initiation step as well as the polymer intermediate at the final re-aromatisation step.

4.3.2. Electrochemical Synthesis

Electrochemical synthesis offered an alternative route to synthesis conducting polymers. This method has some advantages over chemical synthesis as it provides a precise control of potential and state of charge of the resulting polymers (Nova´k et al., 1997). Common practices in electrochemical synthesis include: cyclic voltammetry scanning between the oxidation potential of the monomer and the reduction potential of the polymer; applying a potential step against the time (potentiostatically); and by applying a current step (galvanostatically) in the solutions of monomer (Audebert and Miomandre, 2007), (Wu et al., 2005a). Electrochemical synthesis produces EPCs of uniform thin films attached to the working electrodes, with controllable thickness by varying the cycling and deposition time (Huang et al., 1986).

Oxidation of Monomer:

| Oxidation, generates **cation radical** | → | **Coupling** of cation radicals | → | **Deprotonation** of coupled cation radical | → | Formation of **Dimer** |

Oxidation of Dimer:

| Oxidation of **Dimer**, forms **longer chains** |

| Polymerisation continues |
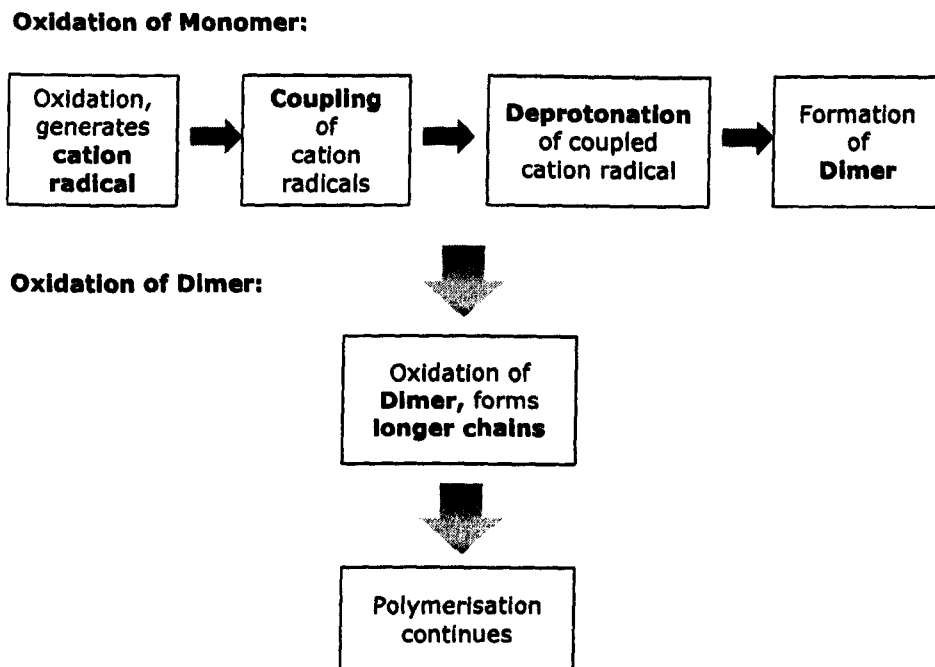
Fig. 2.20. Schematic diagram of mechanism of the polymerisation.

The mechanism of electrochemical polymerisation was generalised by Audebert and Miomandre as presented in Fig.2.20 (Audebert and Miomandre, 2007). The initial oxidation step generates cation radical, followed by the coupling and deprotonation of the cation radical and the formation of dimer. Compared with monomer, dimer is easier to oxidise. The oxidation of dimer produces longer species and precipitation of the polymer occurs at the electrode/electrolyte interface eventually (Audebert and Miomandre, 2007).

A research conducted by MacDiarmid's group confirmed that the synthesis methods, viz. chemical or electrochemical, do not have fundamental influences on the electrochemical behaviour of PAni. As shown in Fig.2.21, the CVs are almost identical to each other.
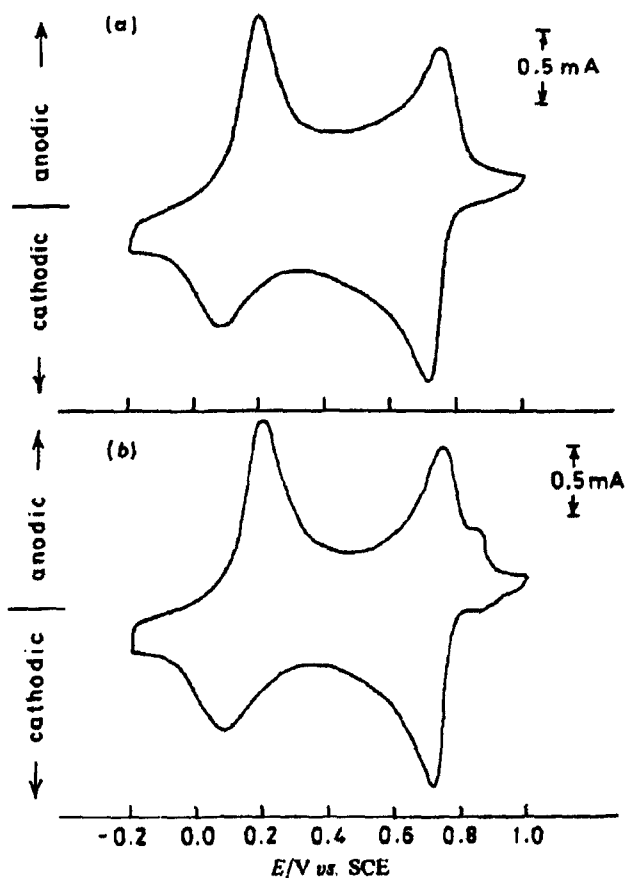
Fig. 2.21. Comparison of CV of (a) chemically synthesised PAni (emeraldine); and (b) electrochemically synthesised PAni emeraldine. Scanrate, 50 mV S^{-1}, in 1.0 mol dm^{-3} aqueous HCl (Huang et al., 1986).

4.4. Electrochemical Performance and Limitations

Both polyaniline and polypyrrole show typical pseudocapacitive behaviour during electrochemical characterisation. The capacitive behaviour is exemplified by the rectangular-shaped CV, as presented in Fig. 2.22. This capacitive current response is attributed to a series of continuously reversible redox reactions on the ECPs electrodes.

As mentioned earlier in 4.1, the mechanical stability is the major drawback of conducting polymers. The repeated intercalation and depletion of ions during charging and discharging causes series damage to the

mechanical stability. It has been reported that for PAni and PPy, a general

loss of 20 % of the initial capacitive value is expected during the first

300 cycles (Park and Park, 2002). Although some researchers have reported

a maintained constant capacity for up to 20,000 cycles after the initial

loss (Belanger et al., 2000), it is desirable if this initial loss could

be minimised or avoided at all.
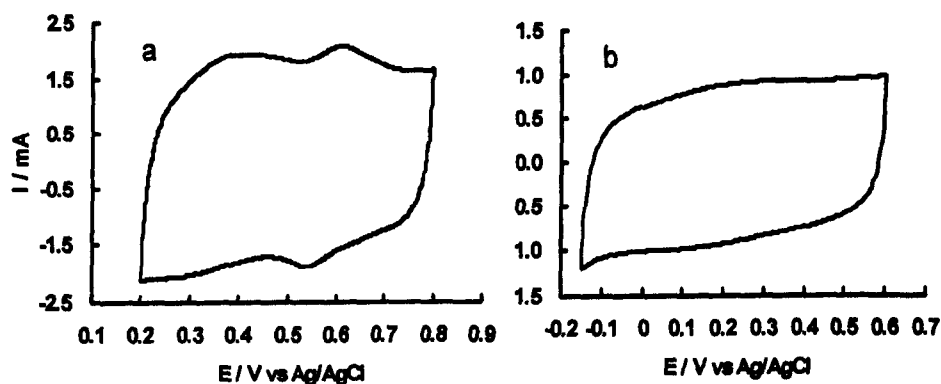
Fig. 2.22. Electrochemical performance of a) PAni in 1 M H_2SO_4; and b) PPy

in 1 M KCl during cyclic voltammetry characterisations (scan rate 20 mV

s^{-1}).

Strong evidences have proved that by depositing EPCs onto some carbon

materials with strong mechanical strength, much enhanced cycling

stability can be achieved (Peng, 2007, Peng et al., 2008). Therefore,

composites of conducting polymers and carbon materials would be a good

choice to utilise the intrinsic pseudocapacitive properties of ECPs

without the deficiency of poor cycling stability.

4.5. Summaries on EPCs

Electrically conducting polymers, with their inherent ability to be doped

and de-doped through ion-intercalation, can be an excellent electrode

material for the supercapacitors. EPCs are capable of fast Faradaic

reactions to attain high pseudocapacitance within suitable potential

range. Moreover, EPCs can be easily synthesised through various methods,

many of which are suitable for industrial scale-up production. Their poor

cycling stability, a major drawback of EPCs, can be offset by combining

EPCs with carbon materials to form a composite with high redox

pseudocapacitance and strengthened mechanical stability.

5. Electrochemical Capacitors

Although extensive studies have been conducted in the synthesis and

characterisations of electrode materials, few attentions are extended

to the characterisation of cell performance. This is partly because the

low loading of the electrode material, which favours the three-electrode

cell characterisation and yields excellent capacitance profile, cannot

give equally satisfying energy and power profile in cell characterisation.

Nonetheless, some general approaches have been established in

constructing and characterising two-electrode cells, which will be

explained in this section.

5.1. Symmetric Cell

Traditionally, electrochemical capacitors have a symmetric structure,

i.e. the negative and positive electrode of a cell has identical weight

and composition, especially for those made of carbon materials with high

surface areas. The total cell capacitance is determined by the electrode

with a smaller value of the capacitance (Eq.2.16). Therefore, the maximum

cell capacitance is to be achieved when the two electrodes have identical

capacitance.

$$\frac{1}{C_{cell}} = \frac{1}{C_{positive}} + \frac{1}{C_{negative}} \qquad \text{Eq. 2.16.}$$

In addition, energy density and power density, which can be derived from

Eq. 2.17 and Eq.2.18, respectively, are the two widely used

characterisations for supercapacitors for their practical applications.

It is worth pointing out that energy and power densities are both related

with the cell voltage and can only be meaningful for a cell or a stack

of multiple cells. They should not be used to describe individual

electrode materials.

$$E = \frac{1}{2} C_m V_{max}^2 \qquad \text{Eq. 2.17.}$$

$$P = I V_{max} \qquad \text{Eq. 2.18.}$$

where C_m is the mass specific capacitance; V_{max} is the maximum operating

voltage during charge-discharge.

Symmetrical two-electrode cells with a-$MnO_2 \cdot nH_2O$/CNT composite

(Raymundo-Pinero et al., 2005), MnO_2 (Cottineau et al., 2006), ternary

composite of CNT/PPy/MnO_2 (Sivakkumar et al., 2007), and ECPs/CNT

composites (Frackowiak et al., 2006) as the electrode materials were

fabricated respectively. In a cell configuration like this, the limited

operating voltage window is a major drawback (Sivakkumar et al., 2007,

Raymundo-Pinero et al., 2005), since a small operating voltage window

limits the energy and power performance directly (Eq.2.17 and Eq.2.18).

Moreover, the electrochemical stability is a fundamental issue for

symmetric cells. For instance, the negative electrode of the symmetric

MnO_x/CNTs cell was reported to operate in the range of an irreversible

Mn(IV) to Mn(II) reaction, which results in the dissolution of the

electrode, and consequently, poor cycling stability (Sivakkumar et al.,

2007). For symmetric cells with EPCs electrodes, conducting polymers are

at the risk of being converting to their insulating phases at negative

potentials. This process, unfortunately, is irreversible. Hence, the

achievable operating voltage restricted.

5.2. Asymmetric Cells

Due to the disadvantages of the symmetric cells, hybrid cells employing

asymmetric electrodes with different operating voltage windows were

proposed (Hong et al., 2002). A prominent advantage of the hybrid cell

system is the enlarged operating voltage window, which noticeably

enhances the energy and power performance (Eq. 2.17 and Eq. 2.18). In

aqueous systems, this is of particular interest as it may allow the capacitor to be operated at a voltage window wider than the water decomposition voltage of 1.2 V, if electrode materials with high overpotentials for hydrogen or oxygen evolutions are carefully selected (Ng et al., 2008). One particular issue with hybrid supercapacitors is nonlinear charge-discharge (Burke, 2000), nevertheless promising results from various research groups indicated that this can be avoided by appropriate cell fabrication.

Carbon materials, with their well-known advantages of high overpotential for hydrogen evolution, are of particular interests. Besides, many carbon materials possess high double-layer capacitance, with good electrical conductivity and mechanical stability. Therefore, they become a favourable choice in constructing asymmetric supercapacitors.

Hybrid supercapacitors with MnO_x as the cathode and carbon materials such as activated carbon (Cottineau et al., 2006, Hong et al., 2002, Brousse et al., 2004) and multiwalled CNTs (Wang et al., 2005) as the anode have been fabricated. These hybrid systems exhibited superior capacitive behaviour in comparison with the symmetrical MnO_x systems. Operating voltage windows at or larger than 2 V (Fig. 2.23) were realised in most cases (Cottineau et al., 2006, Hong et al., 2002, Brousse et al., 2004, Khomenko et al., 2006a). Although it was pointed out that by narrowing the operating voltage window to 1.5 V, a better cycling stability can be achieved (Brousse et al., 2004), since the reduction of Mn(IV) to soluble Mn(II) species, and hydrogen and/or oxygen evolution occurred when the hybrid cell was cycled over an operating voltage window of 2.2 V (Brousse et al., 2004). However, a 24 % decrease of the initial energy density was still observed with this hybrid cell after 23000 cycles tested between 0 and 1.5 V in 0.65 mol dm^{-3} K_2SO_4 (Brousse et al., 2004) which

was believed to be caused by the ions being trapped in the MnO_2 electrode,

blocking the active sites, rather than the dissolution of Mn(IV) (Brousse

et al., 2004).
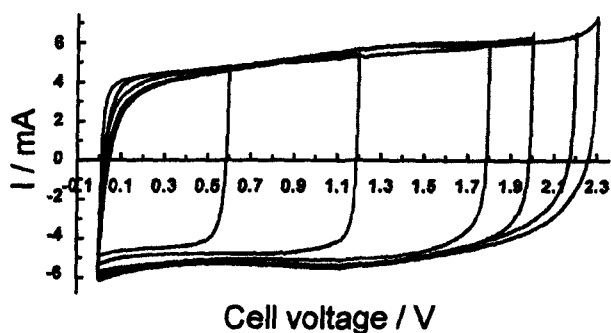
Fig. 2.23. Performance of asymmetric cell: MnO_x Vs activated carbon

electrode in 2 mol dm^{-3} KNO_3 electrolyte, scan rate 10 mV s^{-1} (Khomenko

et al., 2006a).

On the other hand, asymmetric supercapacitors have been constructed with

different pseudocapacitive materials to exploit the redox reactions on

both positive and negative electrodes. Typically, the two chosen

electrode materials have different potential windows for redox reactions.

By coupling these two materials, a much enlarged cell voltage can be

realised. In this approach, MnO_x has been coupled with Fe_3O_4 (Brousse and

Belanger, 2003), $LiMn_2O_4$ (Ma et al., 2007b), and SnO_2 (Ng et al., 2008)

respectively, to form the asymmetric cells. The Fe_3O_4/MnO_2 cell exhibited

an operating voltage window of 1.8 V in the aqueous solution (Brousse

and Belanger, 2003), although the cell performance was later described

to be inferior to the MnO_2/carbon cell (Cottineau et al., 2006). In

addition, asymmetric cells with ECPs and metal oxides as electrodes have

also been built. Conducting polymers, including PAni, PPy and PEDOT have

been respectively fabricated into asymmetric supercapacitors with MnO_x

(Khomenko et al., 2006b). Naturally, the MnO_x /conducting polymer cells

exhibit higher capacitance, but narrower operating voltage windows

comparing to the MnO_x/carbon hybrid cell. Still, considerably wider cell

voltage of 1.2 V, 1.4 V and 1.8 V have been achieved with α-MnO_2/PAni,

α-MnO_2/PPy and α-MnO_2/PEDOT asymmetric cells respectively (Khomenko et

al., 2006b).

5.3. Hybrid Cells

Hybrid cells are constructed with one battery electrode, e.g. Li-ion

battery (Pasquier et al., 2004, Christensen et al., 2006, Naoi et al.,

2005, Zheng, 2003), lead-acid cell (Lam and Louey, 2006), et cetera, and

one supercapacitor electrode. The battery electrode with a potential near

either low or high end of the potential window is selected, to optimise

the energy density of this hybrid system (Zheng, 2003). These hybrid

energy storage devices utilise both the intercalation and redox process

or lectric-double-layer capacitance. This design has claimed to enhance

the power density and life cycle compared to the original battery (Lam

and Louey, 2006), while improve the energy profile for the supercapacitor.

However, due to the nature of energy storage mechanism, this type of

devices is considered as a battery system rather than supercapacitor

system in this study and therefore will not be discussed further.

6. Summary

An overall review of the origin of capacitance, including double-layer

capacitance and pseudocapacitance, suggests that superiority of

pseudocapacitance, which is not limited by surface area. Typical

electrode materials with pseudocapacitive behaviour, viz. conducting

polymer and metal oxides, as well as their energy storage mechanisms,

have been introduced. The synthesis methods and the electrochemical

performances, including advantages and limitations, of these electrode

materials in aqueous electrolytes have been described. Some determining

parameters for good capacitive behaviours have been identified. It is

then concluded that by engineering these electrode materials, viz. ECPs
and metal oxides, with carbon materials with appropriate mechanical
strength and nano-structures will significantly enhance the
pseudocapacitive behaviour. Further reviews in the cell configuration
confirmed that these composites can be constructed into symmetric and
asymmetric supercapacitors. It is also revealed that asymmetric cell
structure, with carbon materials as negative electrode, could extend the
cell voltage with the high hydrogen overpotential of carbon materials.

1. General Strategy

In essential, the aim of this research project is to develop advanced electrode materials for supercapacitors with satisfying performance and at low cost. The synthesis procedures of the electrode materials should be simple, effective and easy to control. It should also be adaptable for industrial mass production for future application. An eligible candidate for the electrode material should meet all the requirements: high level of homogeneity in the morphology, excellent capacitive behaviour, reliable electrochemical performance, physical and electrochemical stability during cycling, as well as that it should be inexpensive and environmental friendly.
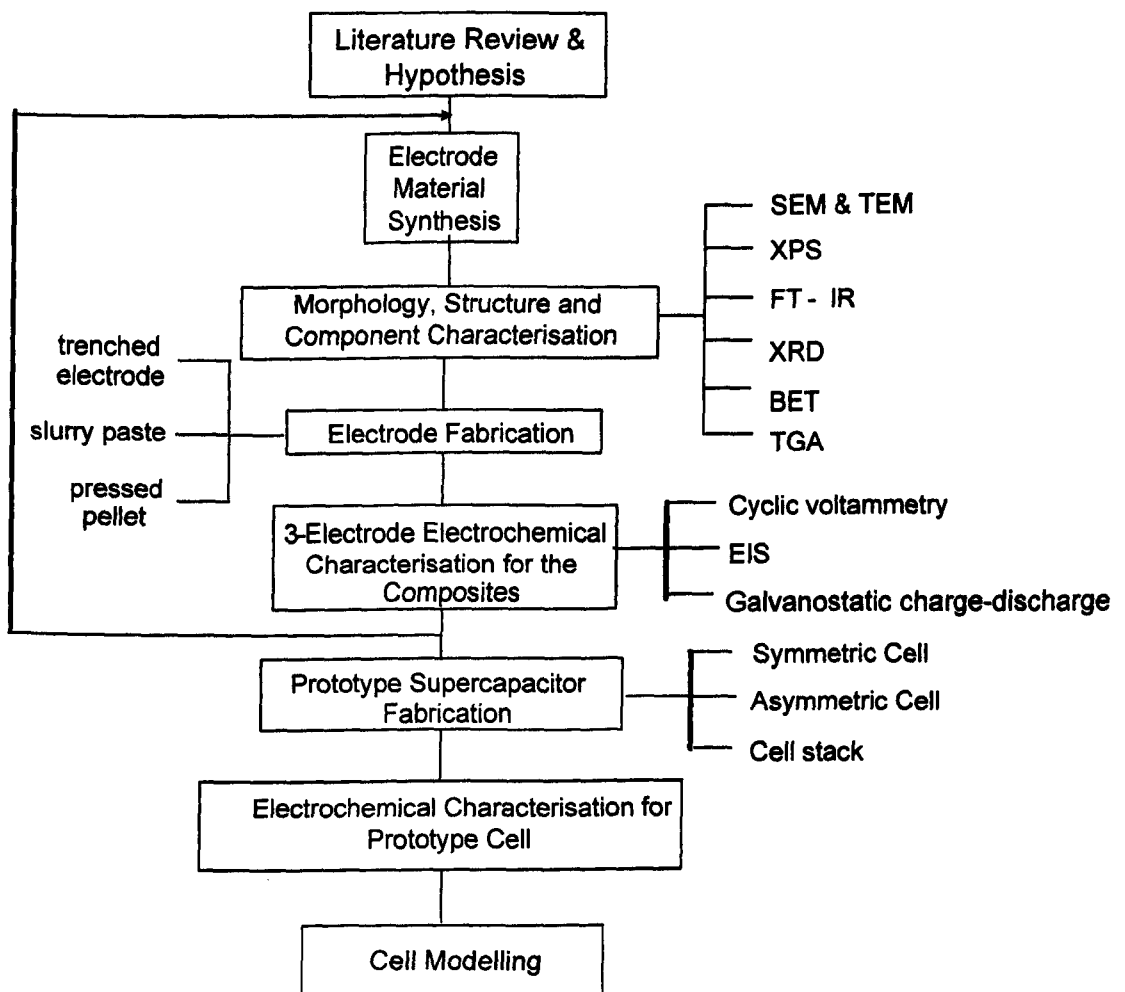
Fig. 3.1. Schematic diagram of methodology.

The general strategy of this work is presented in Fig.3.1. After the composites are synthesised, general characterisations and three-electrode electrochemical characterisations will be carried out. Prototype supercapacitors will be constructed with composites shown promising behaviours in a variety of tests. After the tests on the prototype cells, a general model with equivalent circuits will be proposed to represent the electrochemical system within the prototype cells.

2. Chemicals and Equipments

Chemical	Formula	Supplier	Description
Aniline	$C_6H_5NH_2$	Aldrich	99.5+%
Pyrrole	C_4H_4NH	Aldrich	98%
Potassium Chloride	KCl	Sigma	>99.0%
Nitric Acid	HNO_3	Fisher	70%
Sulphuric Acid	H_2SO_4	Pharmacos	98%
Multi-walled Carbon Nanotubes	C	NTP	purity 90-95%
Polytetrafluorethylene	$(-CF2CF2-)n$	Aldrich	60wt% in water
Potassium Hydroxide	KOH	Acros Organic	ACS Reagent
Ammonium Sulfate	$(NH4)_2SO4$	SpeciFied	99+%
Hydrochloric acid	HCl	Fisher	37%
Potassium Sulfate	K_2SO_4	Fisher	>99%
potassium permanganate	$KMnO_4$	Fluka	≥ 99.0%
Activated Carbon (M1300)	C	Cabot	fluffy pigment black bulk density: 320 g/L
aligned carbon nanotubes	C	NTP	purity >95%

Table 3.1. List of chemicals used in this thesis.

Equipment	Model	Manufacturer
TEM [1]	JEM-2000FX	JEOL
TEM [2]	JEM-2011	JEOL
Autolab	PGSTAT30	Eco Chemie
Balance	Sartorius Supermicro Type s4	GmbH Göttingen
ChI	CHI440	CH Instruments Inc.
XRD	Hiltonbrooks X-powder Diffraction DG3	Hiltonbrooks Ltd
TGA	Pyris 1	Perkin Elmer
Sonication	U 500H	Ultrawave Ltd
SEM	FEI-QUANTA 600	FEI Company
BET	ASAP 2000	Micromeritics
XPS	AXIS Ultra DLD	Kratos
electronic pipette	EDP3	Rainin
power assisted hydraulic press	Atlas Power T8	Specac
FT-IR	360 FTIR	Nicolet Avatar

Table 3.2. List of equipment used in this thesis.

3. General Characterisation of the Materials

3.1. Electron Microscopy

Electron microscopy is a general term for a group of microscopy technologies, including scanning electron microscopy (SEM), transmission electron microscopy (TEM), scanning transmission electron microscopy (STEM), etc. These technologies utilise electron, instead of light photon, to imaging the specimens. Since the resolution of the microscopy is determined by Abbe's Equation (Hayat, 1973):

$$d = \frac{0.612 \times \lambda}{n \sin\alpha}$$
Eq. 3.1.

in which: d is the resolution, λ is the wavelength of imaging radiation, $n \sin\alpha$ is the numeric aperture.

For an electron with charge of -e traversing a region with potential change of V_0, it has the energy of (Spence, 2003):

$$eV_0 = \frac{p^2}{2m} = \frac{h^2}{2m\lambda^2}$$ Eq. 3.2.

where h is Planck's constant and p is the electron momentum and:

p = mv = h/λ   (de Broglie equation)   Eq. 3.3.

Therefore, the wavelength of this electron is (Spence, 2003):

$$\lambda = \frac{h}{\sqrt{2me\,V_0}}$$ Eq. 3.4.

As suggested by Eq.3.4, shorter wavelength, leading to higher resolution, can be achieved by increasing the electron's velocity and potential change. Typically, resolution of SEM falls in the range of 1 - 20 nm (Reed, 2005), and high resolution TEM has the limit of 0.2 nm (Spence, 2003). These figures, compared with the theoretical limit of 200 nm for light microscope, are much more advantaged in imaging.

Fig.3.2 provides a schematic comparison of light microscopy (LM), TEM and SEM. It can be concluded that the structures of these three devices are fairly similar, particularly for TEM and LM. Some technique details of SEM and TEM will be introduced in the following two subsections.
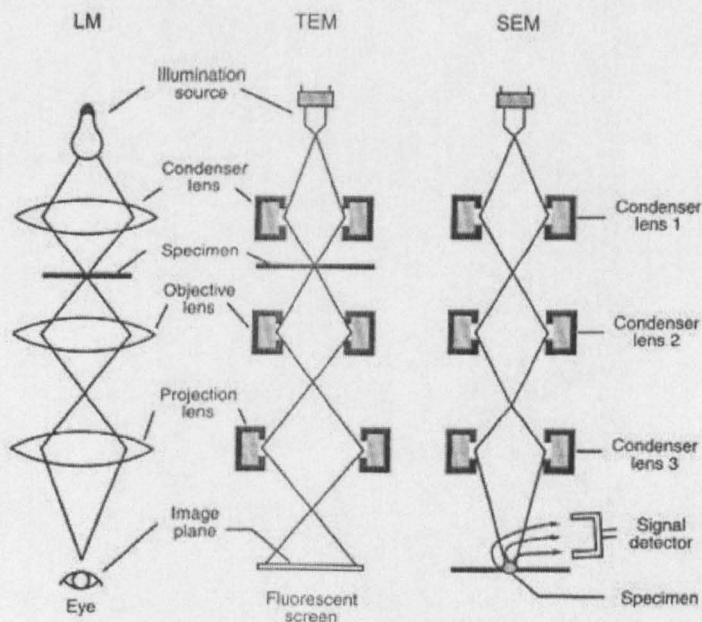
Fig. 3.1. A schematic comparison of light microscopy, transmission electron microscopy and scanning electron microscopy (Iowa, 2008b).

3.1.1. Scanning Electron Microscopy (SEM)

By scanning the sample with a high-energy beam of electrons in a raster
scan pattern, high resolution images of the surface topography of the
sample can be produced. Moreover, compositional contrast (mean atomic
number) of the sample can be obtained by choosing the appropriate
detection mode (Reed, 2005).

Typical setup of a SEM is presented in Fig.3.3. As shown, electrons are
thermionically emitted from a cathode and are accelerated towards an anode.
Tungsten or lanthanum hexaboride (LaB6) are common material for cathode,
due to their higher melting point and lower vapour pressure, thereby
allowing it to be heated for electron emission. The electron beam is then
focused into a beam with a very fine focal spot sized 1 nm to 5 nm. The
beam passes through pairs of scanning coils in the objective lens, which
deflect the beam in a raster fashion over the sample surface (Dawn and
Goodhew, 1990).
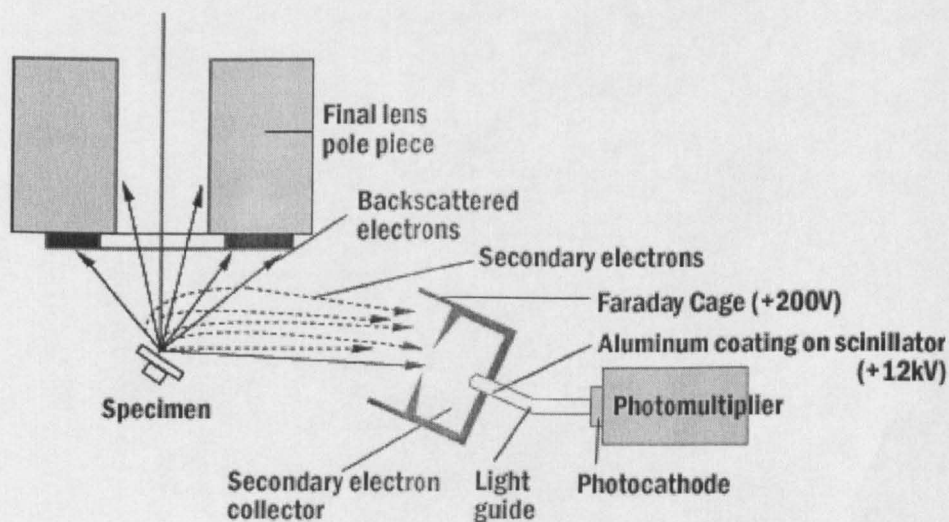
Fig. 3.2. A schematic diagram of a scanning electron microscope (Iowa,
2008a).

As the primary electrons strike the surface of the specimen, they interact
in either an elastic or inelastic way with atoms of the specimen. In an

elastic scattering event, the path of the primary electron can be changed up to 180° with a minimal velocity loss, this electron will then be termed as 'back scattered' electron (as shown in Fig.3.3). Backscattered electrons are often employed to exam the atomic homogeneity and to produce depth profile, because the number of backscattered electrons emitted from a specimen under a certain beam current increases with an increasing atomic number (Reed, 2005). In an inelastic scattering event, the primary electron undergoes a change in direction as well as transferring energy to the specimen. One type of the signals collected through inelastic scattering is secondary electron (as seen in Fig.3.3). The energy range for secondary electrons is 0-50 eV (Iowa, 2008a). Secondary electrons have relatively weaker energy, compared with backscattered electrons, therefore the depth of the specimen within which the electron can escape is limited. Hence, secondary-electron emission is more commonly employed to study the surface morphology of the sample.

In this work, SEM is employed to study the surface morphology of the carbon nanotubes and nano-composites. Therefore, all the images obtained with SEM in this study are from secondary electron emissions.

3.1.2. Transmission Electron Microscopy (TEM)

Transmission electron microscopy is widely used in material science to study the morphology and the crystal diffraction of the samples. In TEM, a beam of electrons is focused onto a specimen causing an enlarged image of the sample with a mechanism very similar to light microscopy (as illustrated in Fig.3.2). Electrons used in TEM techniques have both wave properties and particle properties desired to generate a beam of electromagnetic radiation (Spence, 2003).

Electrons are usually generated in an electron microscope by thermionic emission from a filament, usually tungsten, in the same manner as a light bulb, or by field emission. The electrons are then accelerated by an electric potential (measured in volts) and focused by electrostatic and electromagnetic lenses onto the sample (Spence, 2003). The transmitted beam contains information about electron density, phase and periodicity. All of the information is to be used to form an image.

One of the few drawbacks of TEM is that it requires the specimens to be thin enough for the beam to penetrate. Moreover, the specimen should be able to withstand the high vacuum present inside the instrument. Therefore, applications of TEM in some fields, e.g. medical and biological, are quite restricted.

In this work, TEM is applied to inspect the ECPs and MnO_x coating on the outer surface of carbon nanotubes, to confirm the individual homogeneity of the nanocomposites.

3.2. Brunauer-Emmett-Teller (BET) Surface Adsorption

BET theory is a well-known rule for the physical adsorption of gas molecules on a solid surface, named after its developers: Brunauer, Emmett, and Teller (Brunauer et al., 1938). With several hypotheses, BET theory extended the existing Langmuir theory to multilayer adsorption and thus provided the basis for the measurements of specific surface area.

The BET theory presumes that: (a) gas molecules physically adsorb on a solid in layers infinitely; (b) there is no interaction between each adsorption layer; and (c) the Langmuir theory can be applied to each layer (Brunauer et al., 1938). The resulting the BET equation:

$$\frac{P}{v[P_0-P]} = \frac{1}{v_m c} + \frac{c-1}{v_m c}\left(\frac{P}{P_0}\right) \qquad \text{Eq. 3.5.}$$

Where P and P_0 are the equilibrium and the saturation pressure of adsorbates at the temperature of adsorption, v is the adsorbed gas quantity (for example, in volume units), and v_m is the monolayer adsorbed gas quantity. c is the BET constant, expressed by:

$$c = \exp\left(\frac{E_1 - E_L}{RT}\right)$$ Eq. 3.6.

E_1 is the heat of adsorption for the first layer, and E_L is that for the second and higher layers and is equal to the heat of liquefaction.

The shape of gas adsorption isotherms is widely used to reveal the structural surface information of the sample. Six types of isotherm are identified, as presented in Fig. 3.4.
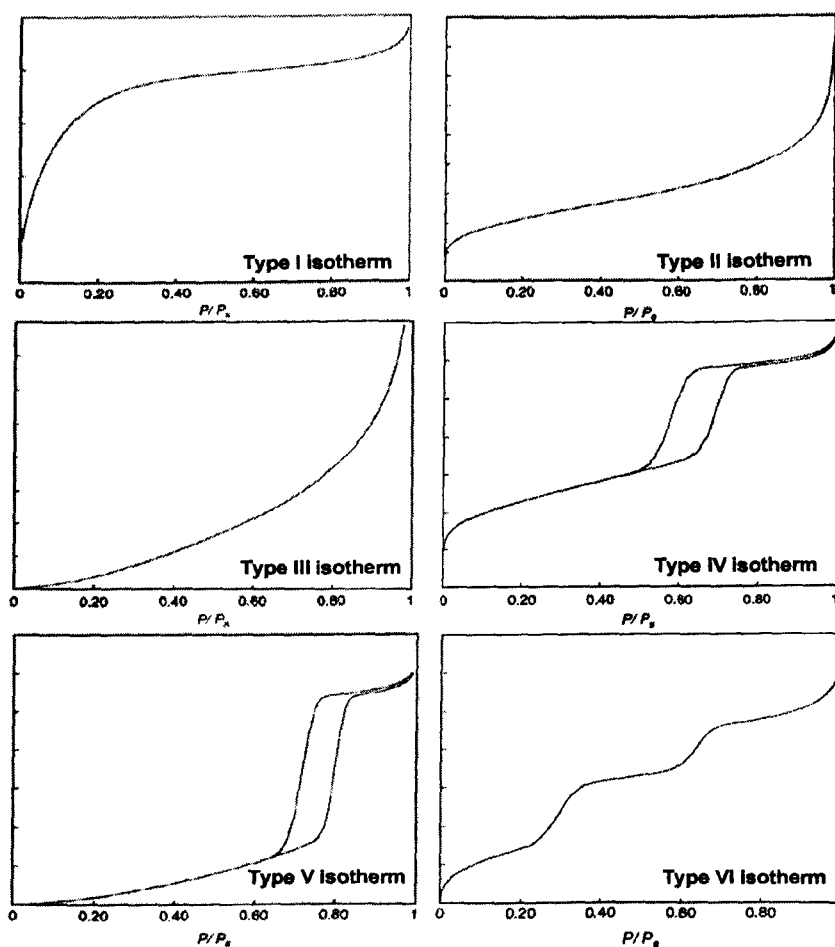
Fig. 3.3. Adsorption Isotherm Types (Condon, 2006).

Each type of adsorption isotherm indicates the specific surface property

of the material. Type I is characteristic of either a chemisorptions

isotherm or physisorption on a material with micropores; Type II is

typical for non-porous or macroporous materials with high energy of

adsorption; Type III indicates that the material is non-porous or

macroporous, and has low energy of adsorption. Type IV is for mesoporous

materials with high energy of adsorption, the hysteresis attributes to

the mesoporosity; Type V is for mesoporous materials with low energy

adsorption; and Type VI is for more complicated adsorptions with possible

processes including: a solid forming a structure layer, multiple pore

sizes, different energies of adsorption, and sharp steps on the adsorbate

surface (Condon, 2006).
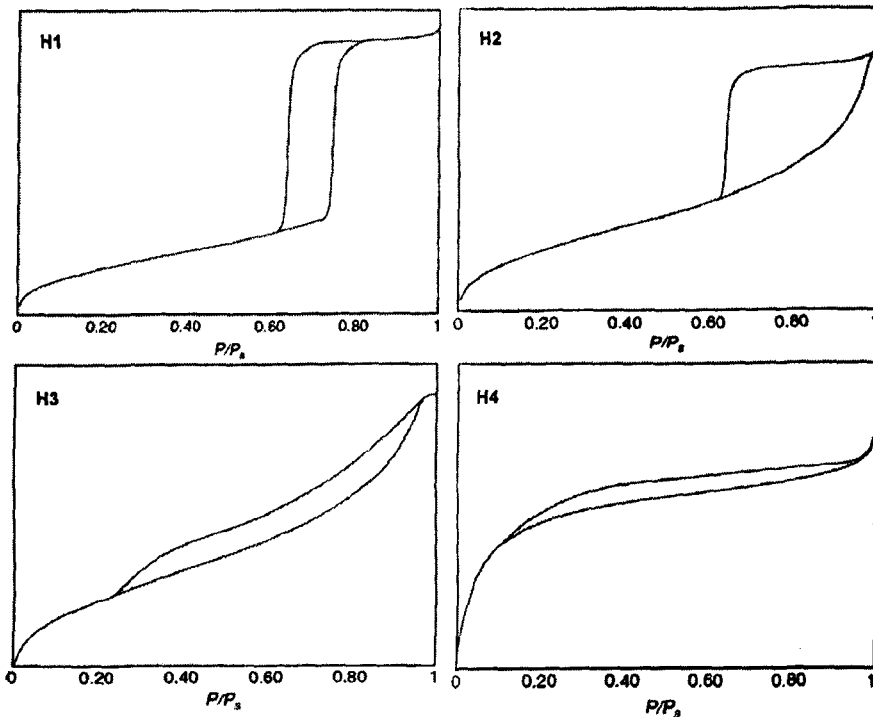
Fig. 3.4. Schematic representations of Hysteresis loops (Condon, 2006).

In surface adsorption, hysteresis is used to describe the phenomenon of

the desorption isotherm being different from the adsorption isotherm,

viz. the amount of adsorbate is greater for desorption (Condon, 2006).

Conventionally, four types of hysteresis loops are identified (Fig. 3.5).

Hysteresis loops reveal more details of pore structures of the materials:

H1 type hysteresis loop suggests that the material has regular even pores without interconnecting channels; H2 type of loop indicates that the pores with narrow and wide sections and the materials have possible interconnecting channels; H3 type is for type II isotherm with slit-like pores; and H4 is for slit-like pore for type I adsorbent - adsorbate pair (Condon, 2006). However, these interpretations of hysteresis loops are very general and some comprehensive models are still under construction (Condon, 2006). Thus, cautions should be take while applying interpreting the pore structures.

In this thesis, nitrogen adsorption-desorption isotherms of samples were measured with ASAP 2000 (Micromeritics) at a temperature of 77K to obtain the specific surface area and the pore size of the pristine CNT, acid treated CNT, polymer/CNT composites and MnOx/CNT composites.

3.3. Thermogravimetric Analysis (TGA)

TGA is an analytical technique commonly applied to investigate the thermal stability of materials and the fraction of volatile components by monitoring the change in mass under heating conditions. The analysis can be carried out in reactive, oxidizing or inert atmosphere (Bottom, 2008). Mass changes occur upon reacting with the atmosphere or losing materials when heating at specific temperatures (Bottom, 2008). By plotting the mass change against the temperature and or time, substantial information can be extracted, e.g. the volatile constituents, thermal decomposition temperature, oxidation of metals, organic and inorganic components, etc (Bottom, 2008). Further derivation of the TGA curve with respect to temperature or time could obtain a more sophisticated differential thermogravimetric (DTG) curve which manifests the mass change against temperature change (Bottom, 2008).

In this work, TGA is mainly employed to study the thermal stability of the materials and to determine the content of manganese oxide in the MnO_x/CNT composites.

3.4. X-ray Diffraction Studies

X-rays are electromagnetic waves of 1 or 2 Ångströms in wavelength. Like other waves, diffraction will occur when X-rays encounter obstacles with the distance spacing of the same magnitude. By interpreting the diffraction of X-ray through the crystals, crystallographic information can be revealed as the diffraction will happen at signature angles depending on the crystal orientation and structure (Cullity and Stock, 2001). Particularly, powder X-ray diffraction is a powerful analytical technique to characterize crystallographic structure, grain size and other crystalline properties of solid samples.

According to Bragg's law: $n\lambda = 2d \sin\theta$ Eq.3.7.

where d is the distance between two parallel planes, λ is the wavelength of the x-ray and θ the scattering angle (as shown in Fig. 3.6). Intense peaks of reflected radiation can only be produced for certain specific wavelength.

plane normal
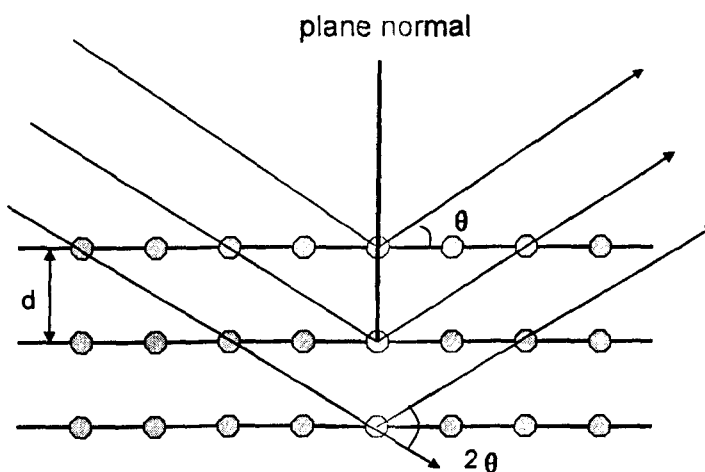
Fig. 3.5. Diffraction of X-ray by a crystal (Cullity and Stock, 2001).

By bombarding a metal target with high energy electrons, *ca* 10-100 keV,

emission of core electrons will be triggered; an electron from the outer

shell then fills the vacant hole in the inner shell and emits an x-ray

photon (Blackman, 2005). The X-ray will then hit the sample and its

diffracted beam will be recorded by photographic film or image storage

plates (Cullity and Stock, 2001). Different substances have different

characteristic diffraction patterns, particularly the scattering angle

θ. By comparing the diffraction data with the existing database, the

containing elements can be identified.

In this work, XRD technique is applied to characterise the crystalline

properties of manganese oxides and MnO_x/CNTs composites synthesised.

3.5. Infra Red Spectroscopy

Infrared spectroscopy is the study of the composition to finding out a

compound's structure and composition based on the percentage

transmittance of IR radiation through a sample. Different stretches and

bends in the molecular bonds in the sample absorb infra red light at

different frequencies. Therefore, the existence of certain structures

can be identified by comparing the experimentally obtained absorption

peaks to the standard adsorption peaks library. Moreover, the deviation

in the absorption peak frequencies could be used as a good indication

for the alteration of the structures in the sample.

The advantage of infrared spectroscopy lies in the fact that it can be

applied to analyze any sample in any state (Stuart, 2004). The theory

of infrared spectroscopy is developed based on the fact that molecules

have specific frequencies at which they rotate or vibrate corresponding

to discrete energy levels.
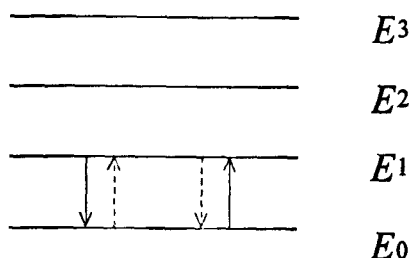
Fig. 3.6.Illustration of quantized discrete energy levels (Stuart, 2004).

As shown in Fig. 3.7 each atom or molecule in a system must exist in one or other of these discrete energy levels. In a large assembly of molecules, there will be a distribution of all atoms or molecules among these various energy levels. Whenever a molecule interacts with radiation, a quantum of energy is either emitted or absorbed. The energy of the quantum of radiation must fit the energy gap exactly and shall obey Bohr equation:

$$\Delta E = h\nu \qquad\qquad Eq. \ 3.8.$$

Thus, the frequency of emission or absorption of radiation can be obtained:

$$\nu = \Delta E \ / \ h \qquad\qquad Eq. \ 3.9.$$

In practice, by passing a beam of infrared light through the sample, IR spectra can be plotted through the examination of the transmitted light revealing how much energy was absorbed at each wavelength.

On interpreting the spectrum, different stretches and bends in different molecular bonds appeared at different frequencies; and peaks appear at fingerprint group frequencies can be assigned to particular parts of a molecule (Stuart, 2004).

Fourier transform infrared (FTIR) spectroscopy is a common measurement technique for collecting infrared spectra. Instead of recording the amount of energy absorbed when the frequency of the infra-red light is varied (monochromator), the IR light is guided through an interferometer. After passing the sample the measured signal is the interferogram.

Performing a mathematical Fourier transform on this signal results in

a spectrum identical to that from conventional (dispersive) infrared

spectroscopy (Griffiths and De Haseth, 2007).

In this study, selected samples are analysed in their powder form in KBr

pellets. The shift, appearance and disappearance of the absorption peaks

of the samples are discussed to reveal the effect of the chemical

treatments and deposition synthesis.

3.6. X-Ray Photoelectron Spectroscopy

X-ray photoelectron spectroscopy (XPS) is a quantitative spectroscopic

technique that measures the composition and electronic state of the

surface region (1-10 nm) of a sample by using a soft x-ray (200-2000eV)

to irradiate the surface. Relaxation energy of the ionised atoms can

dissipate either as an x-ray photon (Fig.3.8 b), filling the core vacancy

with an electron from an outer shell, or it can be given to a second electron,

an Auger electron (Fig.3.8 a) (Bexell, 2003).
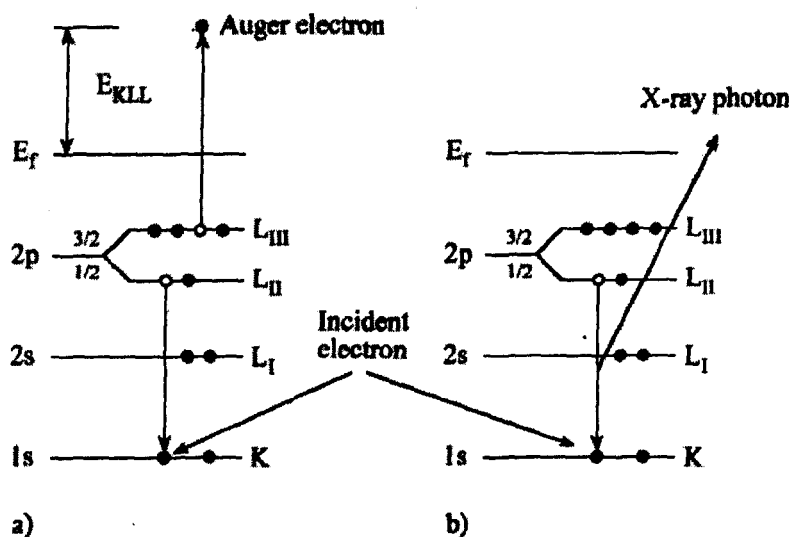
Fig. 3.7. Schematic diagram of X-ray fluorescence emission (Bexell, 2003).

XPS is developed based on the fundamental work of Rutherford started in

1914:

████████████   Eq. 3.10.

Where: E_k is the kinetic energy of the β-rays (photoelectrons); hv is

the incident photon energy ($E = hv$); and E_B is the electron binding energy.

Thus, E_B can be determined by a set of known hv and E_k. The two most commonly

used X-rays are: Mg Kα (hv=1253.6 eV) and Al Kα (hv=1486.6 eV). The output

is a plot of electrons detected (count per second) vs. binding Energy.

Because each element has a unique atomic number and its corresponding

atomic orbital, it can produce a set of characteristic XPS peaks at

characteristic binding energy values. Thus, different elements can be

identified. Moreover, the binding energy of a photoelectron is sensitive

to the chemical surrounding of the atom; it is possible to distinguish

the individual chemical states of the element (Briggs and Riviere, 1990).

With the aim of extracting the maximum amount of information from XPS

data, many analysis methods have been developed through decades of studies.

Some common operations include: smoothing, background subtraction,

satellite subtraction. The differentiation of spectral data will remove

the background contribution and often enhance the presence of overlapping

peaks. (Sherwood, 1990)

Although this interpretation process is straightforward with the aid of

data library based on vast amount of studies have been done previously,

difficulties arise in the elements with variable valences. In such cases

additional features such as intensity ratios and the magnitude of the

multiplet splitting can help in assignment (Wagner, 1994).

In this work, XPS is applied to characterise the composition of MnO_x/CNT

composites, particularly, to detect the valence of manganese and the

existance hydroxide form of the manganese oxides.

4. Electrochemical Characterization

4.1. Cyclic Voltammetry (CV)

Like many other voltammetries, cyclic voltammetry studies current response at a potential simulation due to the change of concentration profiles in complex chemical reactions (Scholz and Bond, 2005). As one of the most widely practiced electrochemical methods for initial electrochemical studies of electrochemical systems, CV is proven to be very powerful in the study of redox properties of chemicals and interfacial structures (Christense and Hamnett, 1994).

The standard cell configuration consists of three electrodes immersed in the electrolyte: the working electrode (WE), counter electrode (CE), and reference electrode (RE). The potential at the WE is monitored and controlled precisely with respect to RE follows a linearly ramping potential vs. time, as shown in Fig. 3.9 (a).
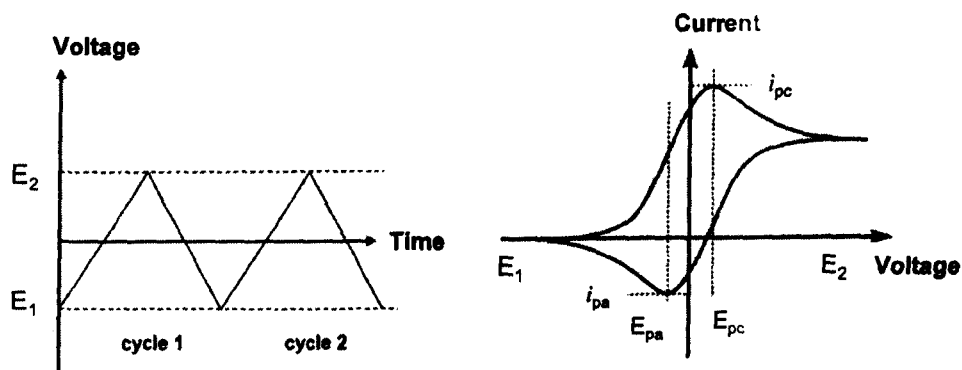
Fig. 3.8. (a) Cyclic Potential Waveform; (b) Resulting i-E cyclic voltammogram (Brett and Brett, 1993).

While the current flowing between the WE and CE is measured and the resulting I/V trace is then plotted out as current (i) vs. potential (E) as shown in Fig 3.9 (b).

The potential is given at any time by (Nicholson and Shain, 1964):

$$0 < t/\lambda \leq 1 \qquad E = E_1 - v\, t \qquad Eq.3.11.a$$

$$1 < t/\lambda \leq 2 \qquad E = E_1 - 2v\,\lambda + vt \qquad Eq.3.11.b$$

where E_i is the initial potential; t is the time; λ is the set sweep

switching time (or at the switching potential, E_λ); and v is the scan

rate.

It was pointed out that the selection of E_1 and E_2 significantly affects

the results. (Compton and Banks, 2007). For an oxidation reaction, e.g.

$A + ne^- = B$, no current flows at relatively positive potential, since

the potential is insufficient to drive the reaction happens. On the other

hand, if the potential scan range $|E_2 - E_1|$ is not large enough, the current

peak (i_{pa}) of the reverse scan will become a function of E_2, leading to

a false representing of the reaction mechanism (Compton and Banks, 2007).

Also, proper concerns should be given to the electrolyte systems while

selecting the E_2 and E_1, as oxidation and reduction of electrolyte is highly

undesirable (Speiser, 2002).
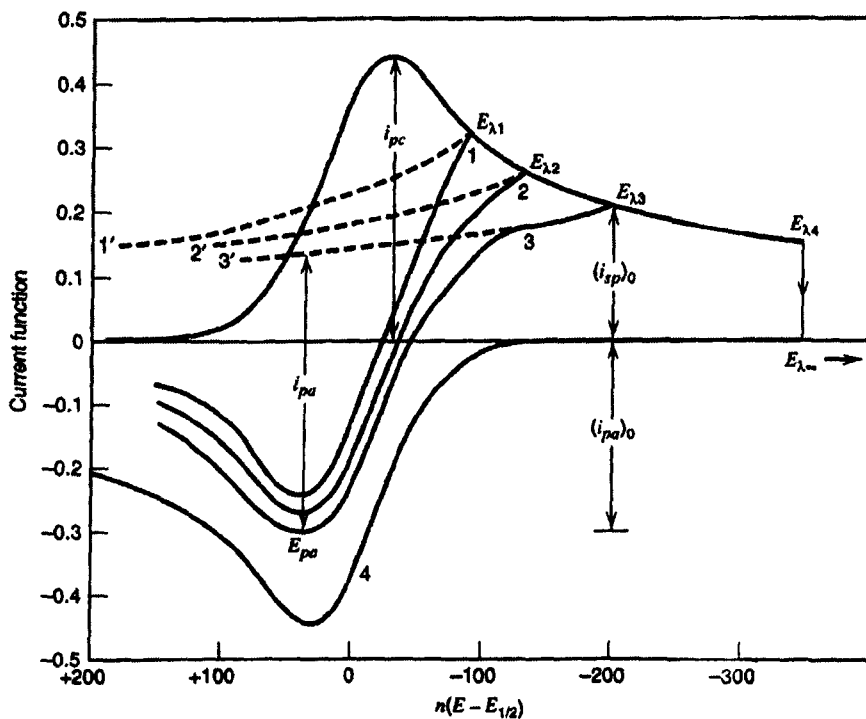
Fig. 3.9. Cyclic voltammograms of the same reaction with different

reversing point E2: (1) E1/2 - 90/n; (2) E1/2 - 130/n; (3) E1/2 - 200/n

mV; (4) for potential held at $E\lambda_4$ until the cathodic current decays to

zero (Bard and Faulkner, 2001).

As shown in Fig.3.10,, i_{pc} and i_{pa} are the cathodic and anodic peak current

of the redox reaction. The current peak of the reverse scan (i_{pa} in this

case), is determined by the extrapolation of the forward scan current

(Fig. 3.10). Theoretically, the ratio of cathodic and anodic peak current

is used to determine the stability of the homogeneous coupled chemistry.

For the situation where:

$$\frac{i_{p,c}}{i_{p,a}} = 1$$ Eq. 3.12.

the resulting species is stable; otherwise then less unity (Compton and

Banks, 2007). However, the non-linear extrapolation required to determine

the current peak in the reverse scan can be very ambiguous at sometimes

(Compton and Banks, 2007).

The second matter to concern regarding conducting a cyclic voltammetry

test is the scan rate v. Scan rate plays a substantial part in

differentiating a reversible process from an irreversible electrode

process. Reversible electrode process is for electrode with rapid

kinetics, where the current – potential relation can be presented in a

Nernst Form (Bard and Faulkner, 2001):

$$E = E_0 + \frac{RT}{nF} \ln \frac{[Ox]_{(o,t)}}{[Red]_{(o,t)}}$$ Eq. 3.13.

In reversible electrode processes, the kinetic parameters k^0 and a are

not involved. In the cases whose electrode kinetics are very sluggish

(k^0 is very small), the anodic and cathodic cannot be simultaneously

significant, and the electrode processes become irreversible. (Bard and

Faulkner, 2001) Compton pointed out that the differentiation of

reversible and irreversible process, in essential, is the competition

between the electrode kinetics and mass transport. (Compton and Banks,

2007) According to Fick's first law:

$$J = -D \frac{\partial \Phi}{\partial x}$$ Eq. 3.14.

where J is the diffusion flux, which measures the amount of substance
that will flow through a small area during a small time interval; D is
the diffusion coefficient; Φ is the concentration (mol m^{-3}); and x is the
position. Thus, for a fixed concentration drop, great flux occurs over
thinner diffusion layer. In another word, the thickness of diffusion layer
controls the rate of mass transport to the electrode (Compton and Banks,
2007). On the other hand, scan rate decides the time it takes to scan
from E_1 to E_2; the longer the time, the thicker the diffusion layer would
be (Compton and Banks, 2007).

Therefore, when fast scan rates are applied:

$\quad\quad\quad\quad$ m_T (mass transport) $>> k^0$ (electrode kinetics)

the process is irreversible.(Compton and Banks, 2007) A parameter, Λ,
was introduced to quantify the reversible and irreversible limits
(Compton and Banks, 2007):

$$\Lambda = \frac{k^0}{\left(\frac{FDv}{RT}\right)^{1/2}} \quad\quad\quad\quad \text{Eq. 3.15.}$$

For reversible processes: $\quad$ $\Lambda \geq 15$, $\Lambda \geq 0.3 \ v^{1/2}$ cm s^{-1} $\quad$ Eq. 3.16.

Irreversible processes: $\quad$ $\Lambda \leq 10\text{-}3$, $k^0 \leq 2 \times 10^{-5} \ v^{1/2}$ $\quad$ Eq. 3.17.

And the ones fall in between these limits are quasi-reversible processes
(Compton and Banks, 2007).

It is clear that the scan rate v determines the value of Λ, and determines
whether the processes are reversible or irreversible.

For reversible reactions: $\quad$ $i_{peak} = -0.446nFA \ [C]_{bulk}\sqrt{\frac{nFvD}{RT}}$ $\quad\quad$ Eq. 3.18.

where n is the number of electrons transferred, F is the Faraday constant
(96485.3399 C mol-1), A is the electrode area, [C] bulk is the
concentration (mol cm^{-3}), D is the diffusion coefficient, v is the scan
rate, R is the gas constant (8.314472 J K^{-1} mol $^{-1}$) and T is the temperature
(K). Thus, for reversible processes, the peak current $i_{peak} \propto v^{1/2}$.

It is worth mentioning that for electrode materials, the reversibility

is of significant importance as the materials will undergo thousands of

charge-discharge cycles in application and irreversible electrode

processes lead to deterioration of the materials and impair the cell

performance.

As the applied potential is reversed, it will reach a potential that will

reoxidise the product formed in the first reduction reaction, and produce

a current of reverse polarity from the forward scan. This oxidation peak

will usually have a similar shape to the reduction peak. As a result,

information about the redox potential and electrochemical reaction rates

of the compounds is obtained.

In systems with capacitive behaviour, the capacitance can be calculated

from: $C = \frac{\Delta q}{\Delta E} = \frac{dq/dt}{dE/dt} = \frac{I}{v}$ Eq. 3.19.

        where v is scan rate, and I is the peak current.

Cyclic voltammetry has diagnostic strength, because it is easy to

interpret the qualitative and semi-quantitative behaviour of a system.

However, it is not an ideal method for quantitative evaluation of system

properties that must be derived from peak heights (e.g. concentration

of an electroactive species, rate constant of a coupled homogeneous

reaction) (Bard and Faulkner, 2001).

In this thesis, CV technique is first used to qualitatively investigate

the potential window and electrochemical processes of the system. AgCl/Ag

reference electrode is used in all the three-electrode tests. Further

quantitative analyses are carried out with CV technique to estimate the

capacitance of the system. Finally, CV is employed to examine the

stability of the systems within the potential window by cyclic tests.

4.2. Electrochemical Impedance Spectroscopy (EIS)

4.2.1. Introduction

Electrochemical impedance spectroscopy is a powerful non-invasive technique for investigating electrochemical systems and processes with its speciality of interrogating relaxation phenomena with time constants ranging over several orders of magnitude (Karause, 2003). This method is based on perturbation of the electrochemical cell with an alternating signal of small magnitude thus the measurements are made at the equilibrium state of the system (Karause, 2003). In an electrochemical process, if the time constants of the different processes are well separated, the individual processes, e.g. ohmic resistance, charge transfer resistance, can be identified by alternating-current and voltage over a wide frequency range (Ho et al., 1980).
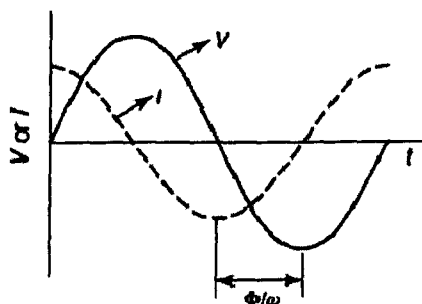
Fig. 3.10. Sinusoidal voltage perturbation and current response (Karause, 2003).

For a sinusoidal voltage perturbation:

$$V(t) = V_0 \sin\omega t \qquad\qquad \text{Eq. 3.20.}$$

$$I(t) = I_0 \sin(\omega t + \Phi) \qquad \text{Eq. 3.21.}$$

$$Z = V(t) / I(t) \qquad\qquad \text{Eq. 3.22.}$$

where V_0 is the voltage amplitude, I_0 is the current amplitude, $\omega = 2\pi f$ and Φ is the phase angle.

With these simple relations between impedance (Z), V(t) and I(t) and the well-known properties of common electronic components, e,g. capacitor, resistor, inductor, etc., analysing the EIS data can provide an insight

into the electrochemical system of the sample (Pletcher et al., 2001).

4.2.2. Data Presentation

Data obtained from impedance tests can be presented in different formats

to emphasise particular electrochemical behaviours of interests.

Impedance, admittance and capacitance can be specifically represented

respectively.

Impedance

Data presented in Impedance formats provide a clear view of the

electrochemical behaviours at low frequencies. Thus, impedance

presentations are commonly employed for systems that are influenced by

mass transfer and reaction kinetics (Orazem and Tribollet, 2008).

Complex-plane is the most common format in presenting impedance in which

Z_{im} vs Z_{re} are displayed for different values of ω (as shown in Fig. 3.12)

Different elements, e.g. double-layer capacitance, Faradaic resistance,

series resistance, pseudocapacitance, etc. can be clearly presented in

such plots (Conway, 2005). The shape of the locus of points can give clear

indications of the possible mechanisms or governing phenomena of the

electrochemical processes (Bard and Faulkner, 2001). The major

disadvantage of Nyquist plot is that the frequency dependence is not shown

explicitly, although this shortage can be mitigated by labelling some

characteristic frequencies (Orazem and Tribollet, 2008).
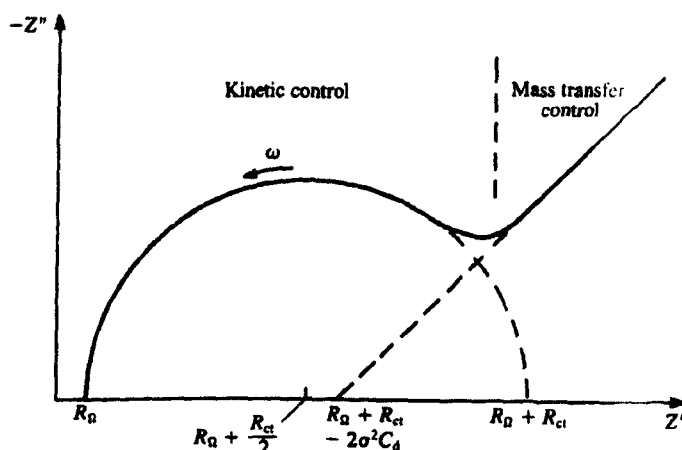
Fig. 3.11. Nyquist plot of impedance in the complex plane of a simple

electrochemical system: O + ne⁻ = R (Brett and Brett, 1993).

Bode plot, where magnitude, log|Z|, and phase angle, Φ, are both plotted

against log ω, on the other hand gives a clear indication of the frequency

dependence (as shown in Fig. 3.13). Phase angle, Φ, is sensitive to system

parameters: $\Phi = tan^{-1}(\frac{z''}{z'})$ Eq. 3.23.

The transition between the asymptotic values in Bode plots marks the

frequency regions where ohmic and capacitive reactions have comparable

values (Pletcher et al., 2001). Bode representation is often used in

systems that have several time constants (Pletcher et al., 2001), thus

are useful in circuits analysis (Bard and Faulkner, 2001, Orazem and

Tribollet, 2008). One of the drawbacks of Bode plots is that the ohmic

electrolyte resistance may influence the estimation of characteristic

frequencies of phase angle plot and inaccuracies arise in such occasions

(Orazem and Tribollet, 2008).

For ideal capacitive behaviour, phase-angle approaches -90° when ω

approaches zero. Deviations from such behaviour indicate the existence

of Constant phase element, CPE (Conway, 2005).
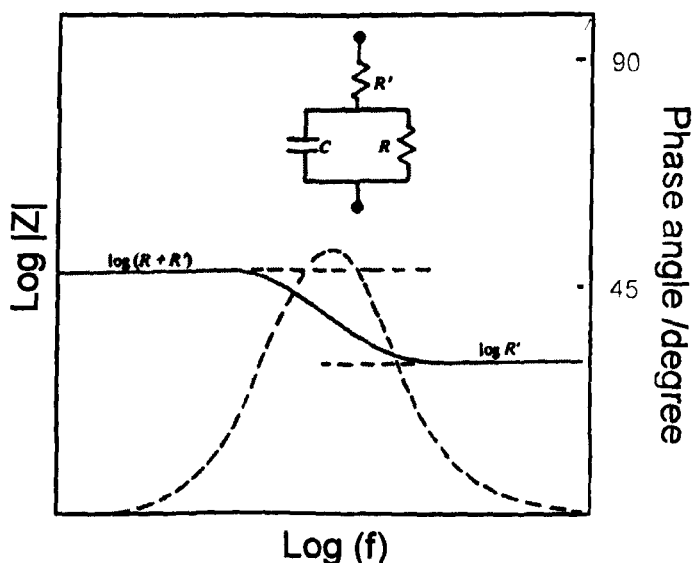
Fig. 3.12. Bode plot for a series-parallel circuit (Pletcher et al.,

2001).

Admittance

Admittance, Y, is the inverse of impedance. Admittance representation

emphasises on the behaviours at high frequencies (Orazem and Tribollet,

2008), and is especially useful in analysing parallel circuits as the

overall admittance of parallel elements is the sum of individual

admittance (Bard and Faulkner, 2001).

Admittance representation is suitable for systems in which **electrolyte**

resistance can be ignored, e.g. solid-state systems. However, **Admittance**

presentation is not heavily used in this thesis due to the **fact that this**

method is inadequate in identifying Faradaic processes in **parallel to**

capacitance (Orazem and Tribollet, 2008). It is mainly **employed to**

identify the knee frequency of the electrode processes.
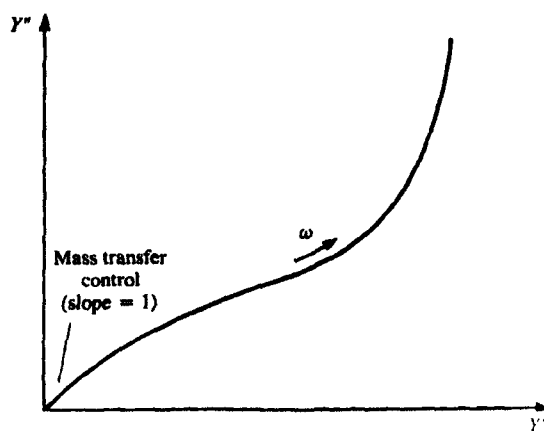
Fig. 3.13. Admittance in Complex format (Brett and Brett, 1993).

Complex Capacitance and Effective Capacitance

For systems in which capacitance is the main feature of interests, the

format of complex capacitance is often employed in data presenting.

Several formats, including C' *vs* C'', C' *vs* f, C'' *vs* f can be applied

to study the frequency dependence of the capacitance. Particularly, the

effective capacitance for an electrochemical system can be obtained from

(Orazem and Tribollet, 2008):

$$C_{eff} = -\frac{1}{\omega Z''}$$ Eq. 3.24.

Effective capacitance, C_{eff}, provides a means to quantifying the electrode

| electrolyte capacitance of a system (Orazem and Tribollet, 2008). At

high frequencies, C_{eff} provides accurate values for the double-layer

capacitance of the system (Orazem and Tribollet, 2008); while at low

frequencies C_{eff} is the total capacitance of the system (Conway, 1999).

In characterising systems with capacitive behaviour, it is suggested that

the frequency range can be divided into three regions: high-frequency

region, medium frequency region and low frequency capacitive region

(Sugimoto et al., 2005). The high-frequency and medium frequency is

divided by the knee frequency. The low-frequency region is characterised

by a slope of -1 in Bode plot; ideal capacitive behaviour can be observed

at the frequency f_0 at which phase-angle $\Phi = -45°$, and the reciprocal

of f_0 is defined as characteristic response time, T_0. Obviously, smaller

T_0 corresponding to faster response and thus better pulse power

performance (Lufrano et al., 2003).

4.2.3. Equivalent Circuit and Modelling

The most attractive aspect of impedance spectroscopy is that it allows

researchers to investigate the direct connection between the behaviour

of a real system and the idealised model circuits consisting of discrete

electrical components (Raistrict et al., 2005). By modelling an

electrochemical system, the individual processes can be distinguished.

Also, interpretation and prediction of the behaviour of the

electrochemical system can also be made, which is of significant

importance in designing and improving the systems.

Equivalent circuit, consisting of resistors and capacitors that pass current with the same amplitude and phase angle as the real system does, is one of the most commonly used methods in modelling (Bard and Faulkner, 2001). Equivalent circuit model is of particular interest in impedance spectroscopy as the frequency response behaviour of linear electrical circuits is extensively studied and well understood (Raistrict et al., 2005).

However, there are some limitations regarding the equivalent circuits and this method should be handled with caution (Raistrict et al., 2005). First of all, the equivalent circuits are not unique: several different circuits can have exactly the same impedance behaviour under investigation (Bard and Faulkner, 2001, Brett and Brett, 1993). Secondly, the effects of geometry on the current distribution are still to be thoroughly studied. Thirdly, some electrochemical properties treated as frequency independent, e.g. conductivity, interface capacitance, are actually frequency dependent. Thus, equivalent circuit should only be used once a comprehensive understanding of the electrode processes has been established (Raistrict et al., 2005).

In this thesis, EIS measurements are conducted in the frequency range of 0.01 Hz - 10000 Hz with an AC signal of 5 mV. EIS is applied to give an insight into the mechanism of the electrode processes and to confirm the capacitance of the system calculated from CV results. In addition, impedance models of electrode processes are built with equivalent circuits to gain a deeper understanding of the electrochemical processes that could be beneficial in improving the cell performance.

4.3. Chronopotentiometry

Different from CV, Chronopotentiometry records the potential response

of a controlled current excitation. Controlled current citations commonly

applied are shown in Fig. 3.15. Chronopotentiometric techniques are also

called gavanostatic techniques, as a small constant current is applied

to study the potential as a function of time (Bard and Faulkner, 2001).
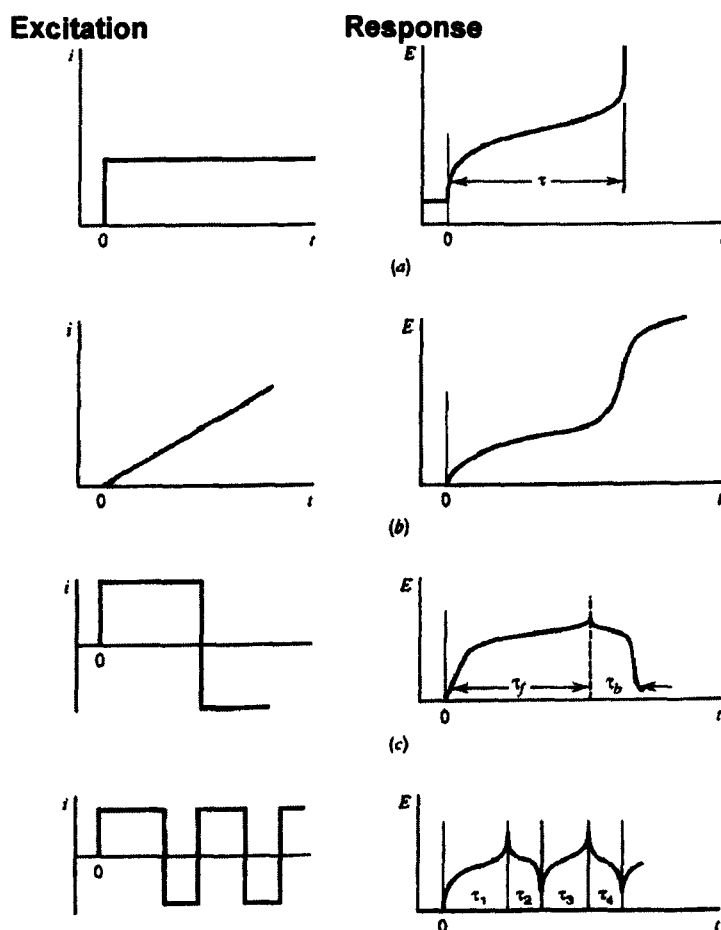
Fig. 3.14.Schematic presentation of different types of chronopotentiometry techniques: (a) Constant-current chronopotentiometry; (b) Chronopotentiometry with linearly increasing current; (c) Current reversal chronopotentiometry; (d) Cyclic chronopotentiometry (Bard and Faulkner, 2001).

Bard points out that a fundamental disadvantage of Chronopotentiometry

is that it is difficult to correct the amplified double-layer charging

effects occur throughout the experiment. Besides, the E-t transient

curves are usually less well-defined than the i-E curves obtained from

potential sweep (Bard and Faulkner, 2001).

Constant current chronopotentiometry, i.e. galvanostatic

charge-discharge, is commonly applied to investigate the charge

capacitance and stability of power sources, e.g. batteries, fuel cells

and electrochemical capacitors. In the application of electrochemical

capacitors, the capacitance can be calculated by:

$$C = \frac{\Delta Q}{\Delta E} = \frac{it}{\Delta E}$$ Eq. 3.25.

Where i is the constant current applied, t is the charge or discharge

time and ΔE is the cut-off potential setting during the examination. It's

worth mentioning that an ohmic drop, also known as iR_s drop, is commonly

observed in such experiments due to the resistance within the solution,

electrode and connection interface (Bard and Faulkner, 2001). In the work

of developing energy storage devices, the existence of iR drop complicates

the potential profiles and should be eliminated if possible (Brett and

Brett, 1993).

In this thesis, constant current chronopotentiometry is applied to

examine the performance of prototype cells and cell stacks and to

determine the equivalent series resistance of the cells.

1. Acid Treatment of Carbon Nanotube

2 g of multi-walled CNTs (20~50 nm in diameter, Shenzhen Nanotech Port Co., Ltd.) were boiled in 40 ml mixture of concentrated nitric acid (78 %) and sulphuric acid (98 %) with the volume ratio of 1:3 for 15 minutes. After this acid treatment, the CNTs were vacuum filtered via filtering crucible of porosity 4. Then, the filtrate was washed with distilled water for several times until the pH reaches 7 before being placed in the oven at the temperature of 60 °C for 48 hrs. The dried sample was then ground to fine powder in a pestle mortar. All the CNTs used in the synthesis were acid treated, unless otherwise specified.

2. Electrically Conducting Polymer/CNTs Composites

The schematic view of synthesis of conducting polymer/CNTs composites is presented in Fig. 4.1. The details of the synthesis for two different types of ECP/CNTs composites are presented in the following two subsections.
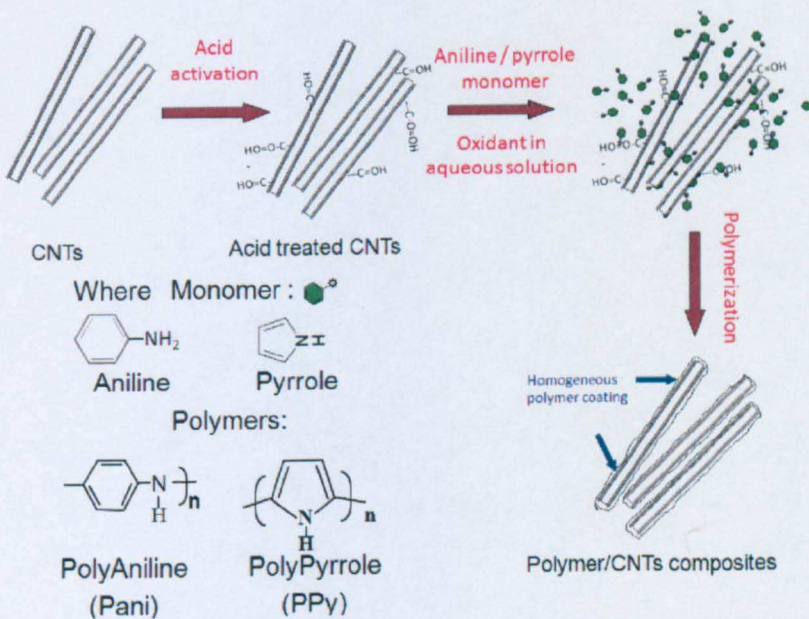
Fig. 4. 1. Schematic illustration of synthesising ECP/CNTs composites.

2.1. Polyaniline/CNTs Composites

0.4 ml aniline (Fluka) was added into 30 ml 1 M HCl aqueous solution; adding appropriate amount of CNTs to produce composites with 100 wt%, 90 wt%, 80 wt% and 70 wt% of polyaniline respectively. The suspension was placed under sonication for 1 hr to ensure a proper dispersion the CNTs and aniline in the aqueous solution. 0.4 g potassium dichromate was dissolved in 20 ml 1 M HCl as oxidant, and then being added to the aniline and MWNT dispersion drop by drop at an interval of 10 minutes. This was followed by further 60 min sonication to ensure proper dispersion during polymerization. The nanocomposites materials would then vacuum filtered via filtering crucible of porosity 4. The filtrate was washed with distilled water. The precipitate was dried at a temperature of 60 °C for 24 hours. Later the sample was ground to fine powder and weighed.

2.2. Polypyrrole/CNTs Composites

0.5 ml pyrrole (Aldrich) was added into 30 ml 1 M HCl aqueous solution; adding appropriate amount of CNTs to produce composites with 100 wt%, 90 wt%, 80 wt% and 70 wt% of polyaniline respectively. The suspension was placed under sonication for 1 hr to ensure a proper dispersion the CNTs and aniline in the aqueous solution. 1.2 g ferric chloride (Sigma) was dissolved in 20 ml 1 M HCl, and was added to the aniline and CNTs dispersion drop by drop at a interval of 10 minutes. Further 60 min sonication to ensure proper dispersion during polymerization; The nanocomposites materials would then vacuum filtered via filtering crucible of porosity 4. The filtrate was washed with distilled water. The precipitate was dried at a temperature of 60 °C for 24 hours. The sample was weighed, ground to fine powder.

3. Manganese Oxides/CNTs

3.1. In Acid Condition

1 g of acid treated CNTs was added to 0.01 M $KMnO_4$ (Fisher, company) at 70°C (100 mL, 200 mL, 400 mL for the composites with 15 wt%, 30 wt%, 60 wt% manganese oxides content respectively). 1 M HCl was added to adjust the pH of the solution to 3.1. The solution was placed under heating (70 °C) and magnetic stirring (450 rpm) for 2 hr, until the rosy colour of the solution disappear. Then, switch off the heater and keep the solution under constant magnetic stirring at the speed of 450 rpm (Stuart, S160) for 40 hrs. The MnO_x/CNTs composites were vacuum-filtered via filtering crucible of porosity 4 and the filtrate was washed with distilled water for several times until the pH reaches 7 before being placed in the oven at the temperature of 60 °C for 48 hrs. The dried sample was then ground to fine powder in a pestle mortar before use.

The synthesis of composite with higher manganese oxide content (60wt %) takes longer to complete. The reaction was estimated to complete in 15 days. Although the addition of HCl speeds up the synthesis process, it leads to crystallised MnO_x in the composites. These crystallised structures might cause inferior electrochemical performance in their application as electrode material for supercapacitors.

3.2. In Neutral Condition

MnO_x/CNTs composites were synthesized in the same method as described in 3.1, apart from the fact that no HCl was added during synthesis. As observed, for the composites with same manganese oxide content (e.g. 60wt %) the reaction takes longer to complete in neutral condition. However, the products are more homogenous (as confirmed by TEM results in Chapter 5). Therefore, the MnO_x/CNTs composites tested as electrode material for supercapacitors in this work are all synthesised in neutral condition.

1. Scanning Electron Microscopy (SEM)

SEM is employed to provide an overview of the surface morphology of the samples. All the samples are examined with SEM to study the results of chemical treatments and processes.

1.1. Effects of Acid Treatment
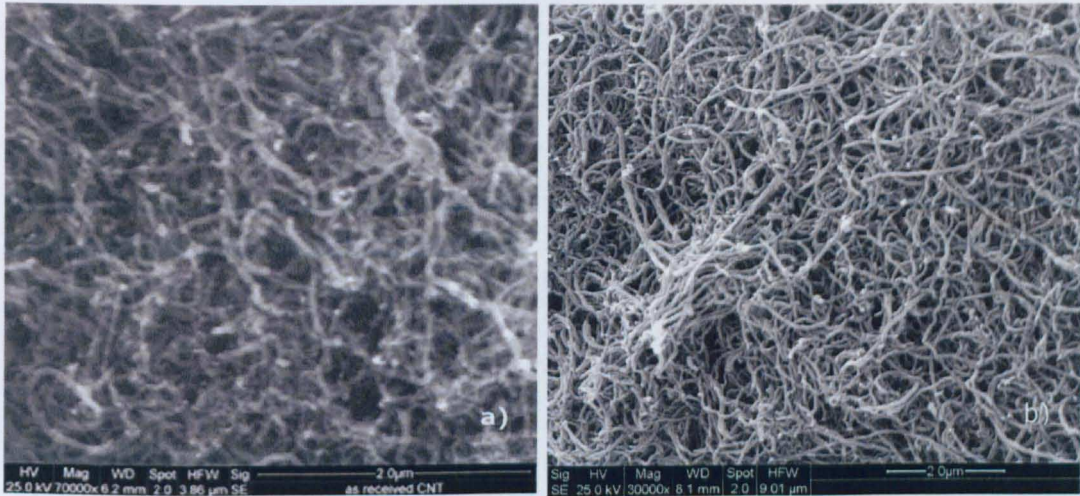
Fig. 5. 1. SEM images of: a) as received CNTs; b) acid treated CNTs.

By comparing the morphology of as received CNTs and acid treated CNTs, it is concluded that the acid treatment does not substantially alter the morphology of the carbon nanotubes (Fig.5.1). Some minor alterations can still be noticed. For instance, the acid treatment seems to be able to remove some CNTs with odd diameters, producing CNTs with more uniform sizes (Fig. 5.1 b). Also, CNTs appear to be slightly shorter in length and more compacted after treatment, these alterations are attributed to the washing and drying process as the evaporation of the water can form local alignments of CNTs. A compact 3-D network of tangled CNTs is clearly presented in Fig.5.1 b. In the research for electrode materials, this 3-D network is of significant importance as it creates micro- and nano-channels facilitating electron and ion transfer, hence essentially promotes Faradaic process and results in improved electrode performance.

1.2. The Role of CNTs in Composites

The surface morphology of PANI/CNTs and PPy/CNTs nanocomposites, in comparison to pure PAni and pure PPy, are shown in Fig.5.2. Pure polyaniline and pure polypyrrole synthesized show typical granular and irregular morphology. The granule size of the pure polymer lumps varies randomly, leading to heterogeneity in many physical and electrochemical aspects, e.g. conductivity and porosity.

(a)   (b)

(c)   (d)
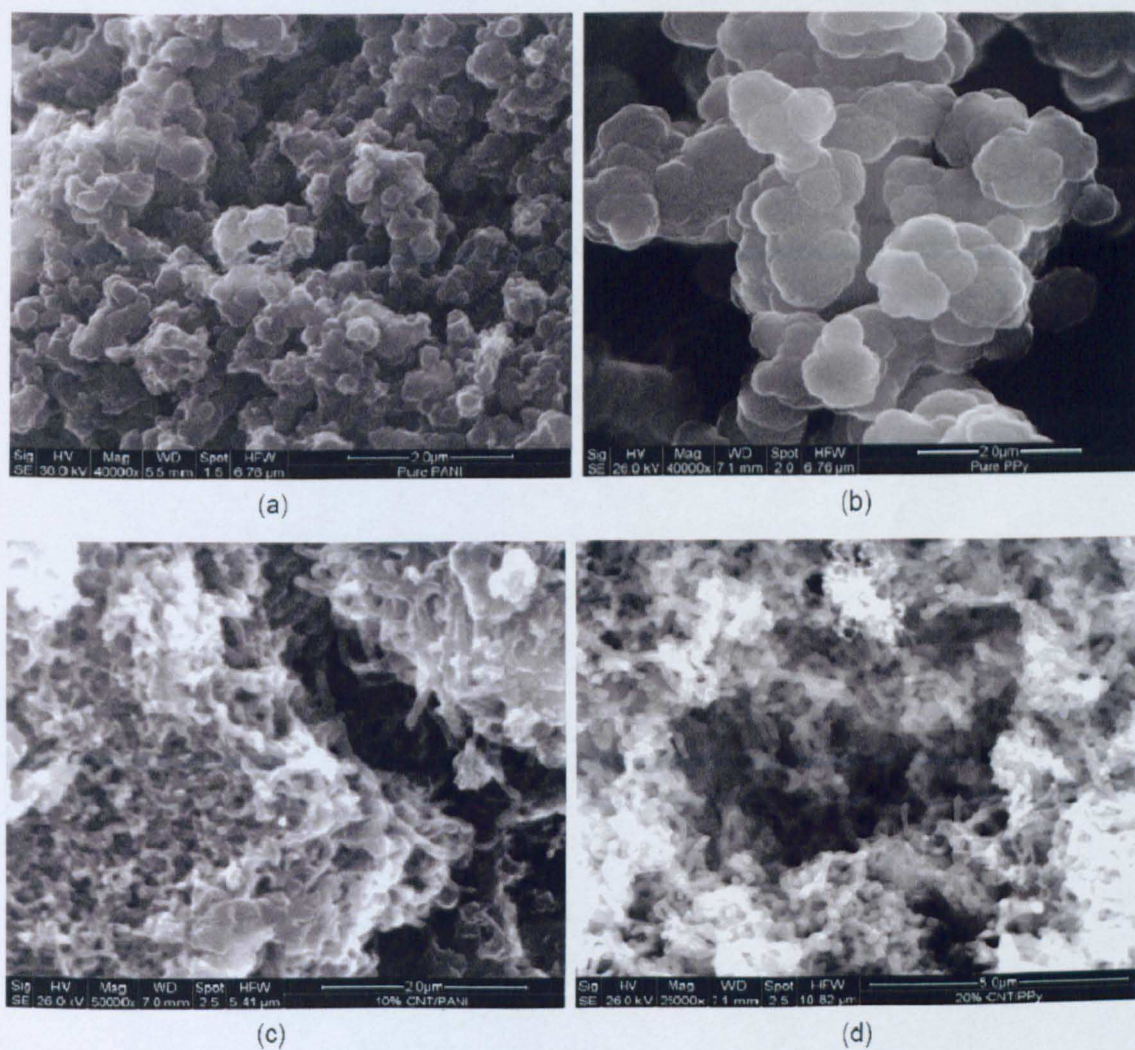
Fig. 5. 2. Scanning Electron Microscopy of (a): Pure Polyaniline; (b) Pure PolyPyrrole; (c) PANI/CNTs composite with 10 wt% of CNTs; (d) PPy/CNTs composite with 20 wt% of CNTs.

On the contrary, PAni/CNTs and PPy/CNTs composites show fibril structures with a coralloid network (Fig. 5.2 c and d). This coralloid network is formed by homogeneous polymer deposition on to CNTs 3-D network during the polymerisation. Some polymer agglomerates could be spotted, particularly in the case of PAni (Fig.5.2 c). This is due to the fact that polyaniline tends to deposit on itself rather than on CNTs after the initial period of polymerisation.

Similar to the cases with conducting polymers, manganese oxides form a homogenous coating outside the CNTs 3-D network during the reduction, as shown in Fig. 5.3. The MnO_x/CNTs composite is uniform and consistent in general, with very few lumps of manganese oxides agglomerates in sight.
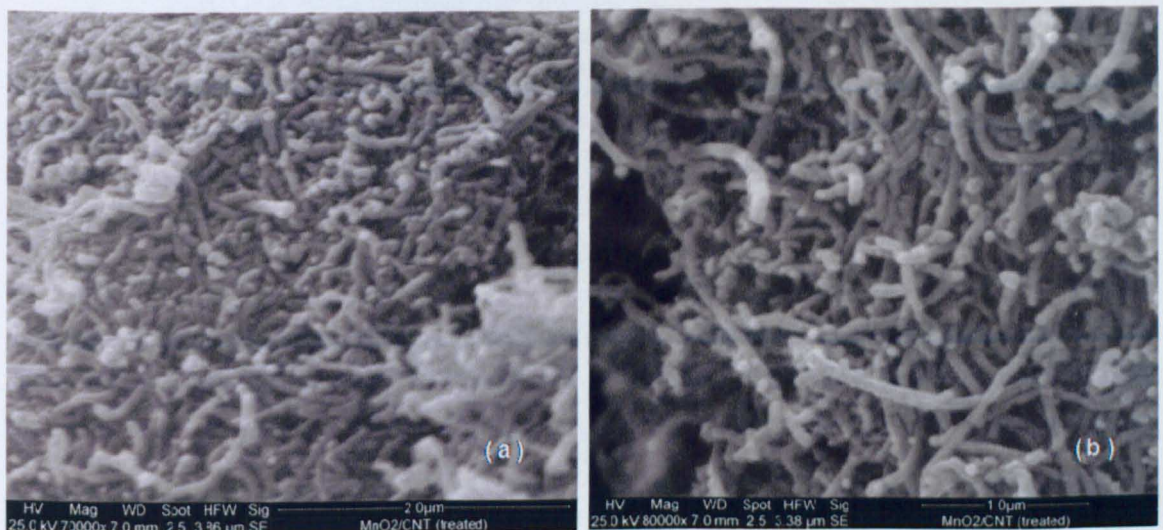
Fig. 5. 3. SEM images of 30 wt% MnO_x/CNTs: a) magnification 70K; b) magnification 80 K.

2. Transmission Electron Microscopy

High resolution transmission electron microscopy (HR-TEM) is used to study the structure of sample materials in detail.

2.1. Coating of Conducting Polymers

Fig. 5.4 shows the morphology of polypyrrole and its composites with different CNTs contents. The structure of multi-walled carbon nanotube is clearly presented in Fig. 5.4 b: multi-layers of carbon sheets with a total thickness of 10nm wrapped to form a hollow tube with a diameter of 6 nm.

The TEM images confirm that the polypyrrole forms a homogeneous coating outside the carbon nanotubes (Fig. 5.4 a) during the polymerisation, well in agreement with the SEM results. The arrows in Fig. 5.4 indicate the presence of CNTs in the nanocomposites. It is to be noted that the thickness of the polymer coating can be controlled by several parameters during the polymerisation, particularly the ratio of CNTs and monomer, and the synthesis condition (polymerisation time, temperature, pH, oxidants, etc.). From Fig. 5.4 b, a 7 nm polypyrrole coating is estimated for this 80 wt% PPy/CNTs composites. Also, a coating of 50 nm is observed with 90 wt% PPy/CNTs composite and longer polymerisation time (Fig. 5.4 c). Pure polypyrrole forms irregular lumps after polymerisation (Fig. 5.4 d). This result confirms with the observation with SEM in Fig. 5.2.
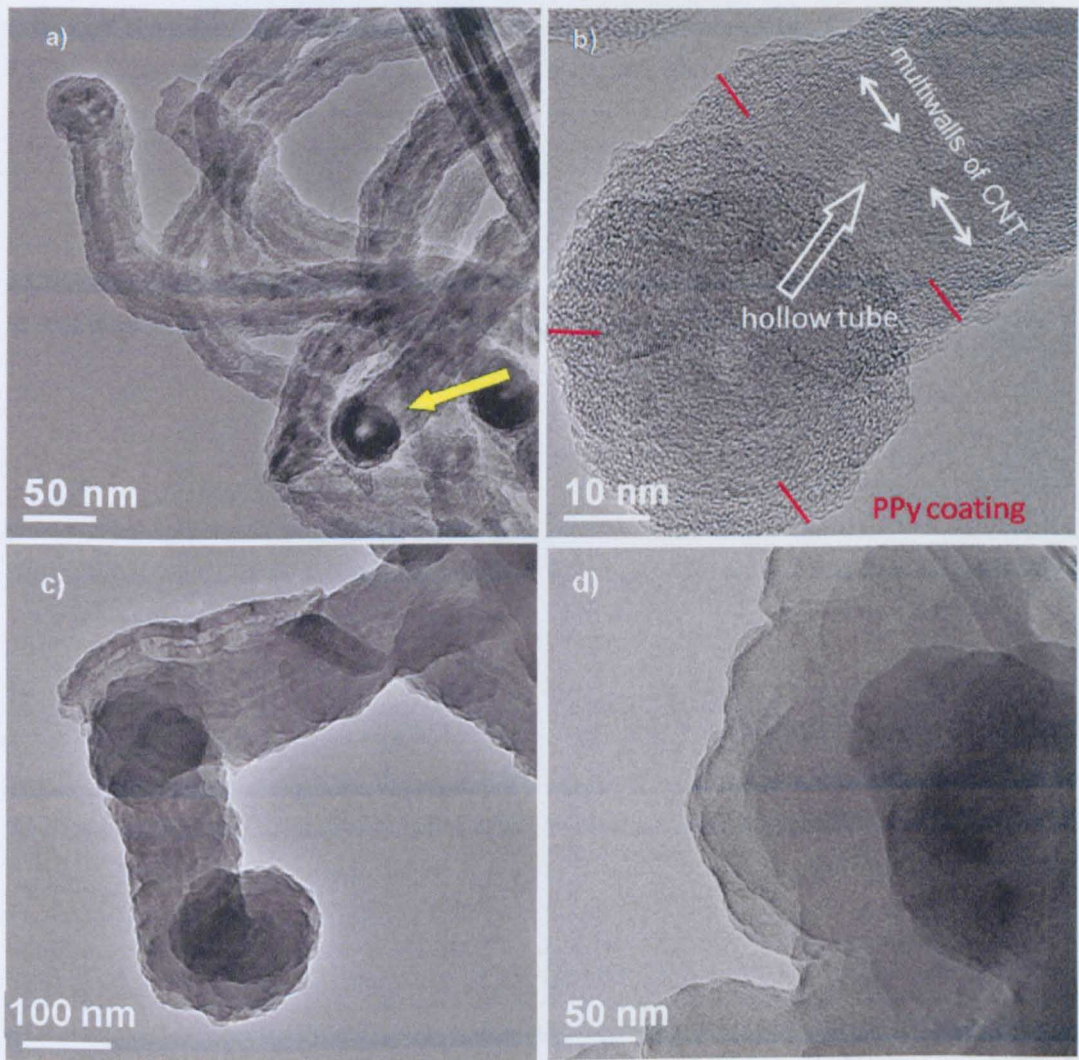
Fig. 5. 4. TEM of pure PPy and PPy/CNTs composites: a) and b) 80 wt% PPy/CNTs with an enlarged view of an end point; c) 90 wt% PPy/CNTs; d) pure PPy.

TEM morphology of PAni/CNTs composites is presented in Fig. 5.5. The thickness of polyaniline coating can be identified in a similar manner. A polyaniline coating of 3 nm is observed in 70 wt% PAni/CNTs composites (Fig. 5.5 a) while in 80 wt% PAni/CNTs composites thicker polymer deposition is recorded. As polyaniline prefers to deposit on itself rather than on CNTs, inhomogeneity, to some extent, could happen at any point in the polymerisation (as revealed in the asymmetric thickness of coating in Fig. 5.5 b)
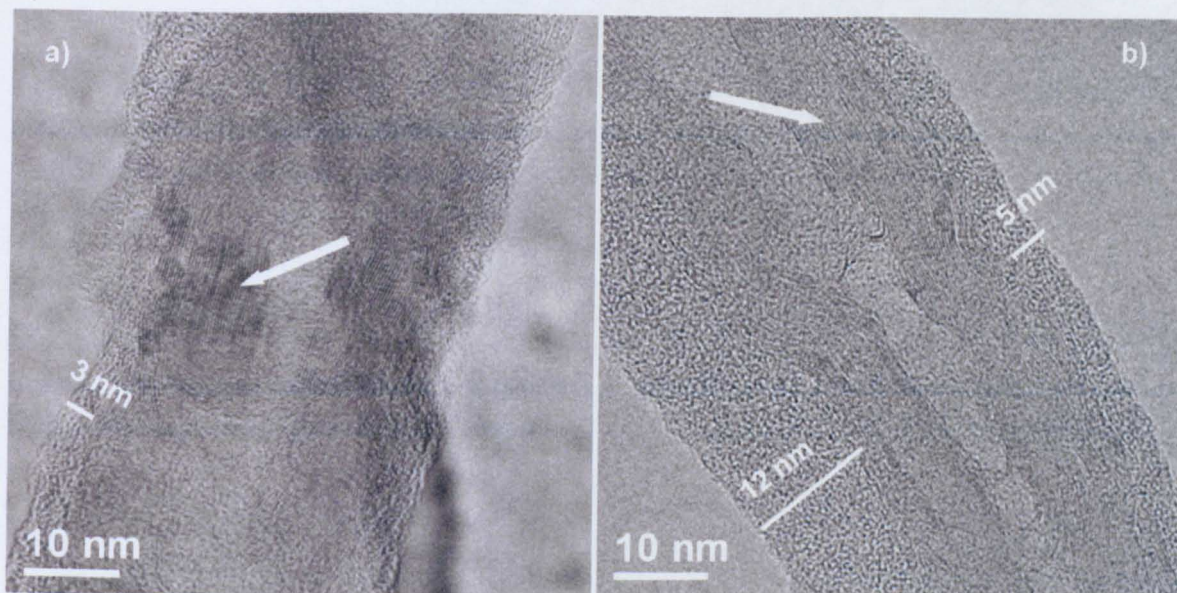
Fig. 5. 5. TEM images of PAni/CNTs composites: a) 70 wt% PAni/CNTs composite;
b) 80 wt% PAni/CNTs composite. (The arrows indicate the fringe spacing of CNTs.)

Nevertheless, TEM images of the composites have confirmed the homogeneity
of the polymer coatings on the carbon nanotubes at individual level.

2.2. The Crystallinity of MnO_x Deposits

The TEM images of MnO_x/CNTs composites with various manganese oxides
contents are presented in Fig. 5.6. At lower concentration, MnO_x is
amorphous or nanocrystalline. It forms a thin and homogeneous layer of
coating outside carbon nanotubes (Fig. 5.6 a and b). Evidently, the
thickness of MnO_x coating increases with the increase of MnO_x content in
the composites. The red arrows in Fig. 5.6 c indicate that fractures and
bend sites on carbon nanotubes. It is observed that these sites are more
likely to cause lump deposition. Interestingly, some crystalline
structures have been detected with the composite with higher manganese
oxides content (Fig. 5.6 d).

As described in Chapter 4, it takes significantly longer time to complete
the redox-deposition processes (30 days) for this composite. The

existence of this crystalline structure suggests that the manganese oxides formed are no longer amorphous. More details of the crystalline are presented in Fig. 5.7. As illustrated, the yellow arrows indicate clear crystal lattice of MnO_x formed during deposition. The white arrow indicates the fringes of multiwall of carbon nanotube. The fringe spacing for this MWNT is about 0.33 nm and the basal spacing of MnO_x nanocrystalline is about 0.63 nm.
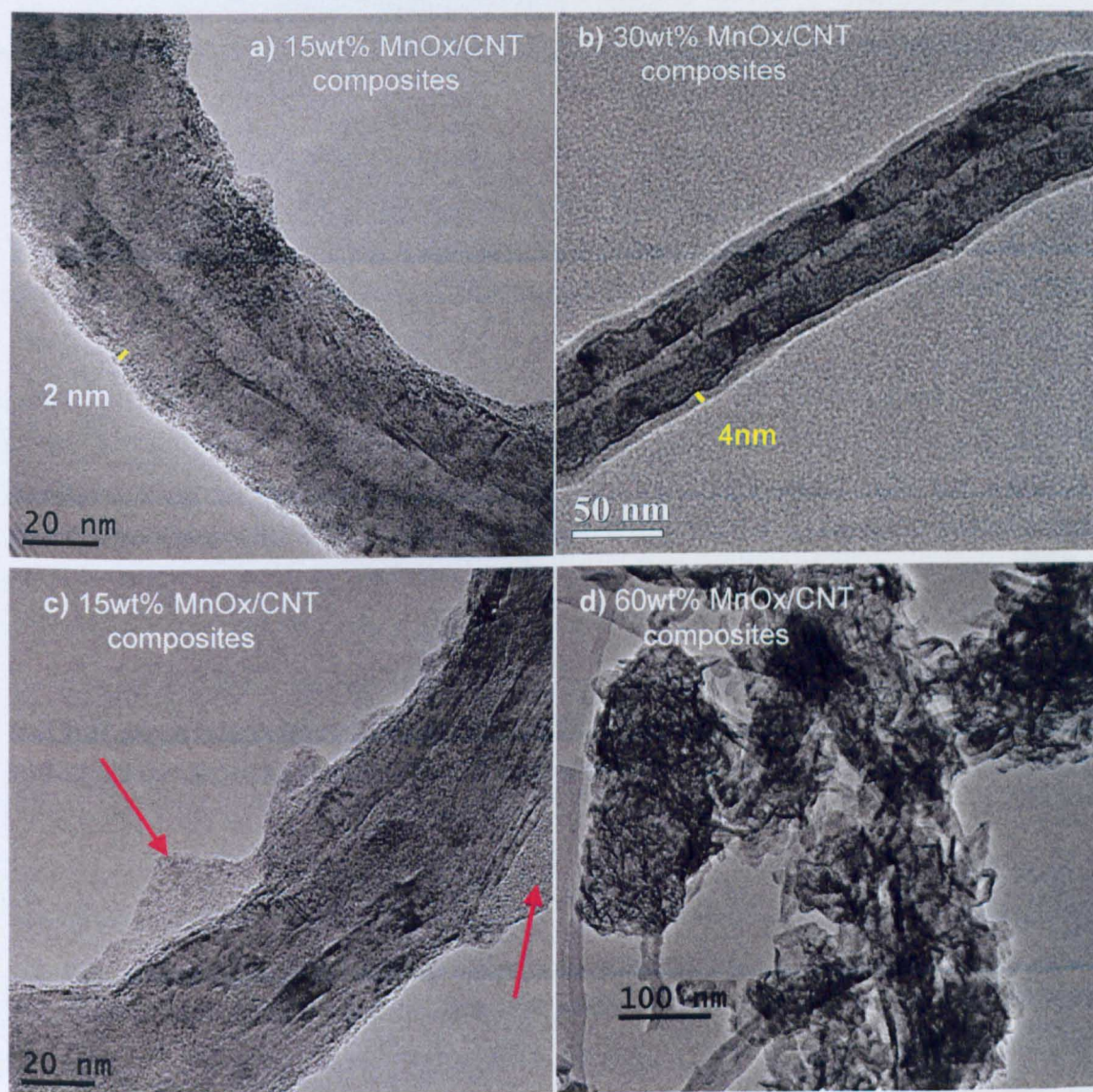
Fig. 5. 6. TEM images of MnO_x/CNTs composites: a) 15 wt% MnO_x /CNTs; b) 30 wt% MnO_x/CNTs; c) 15 wt% MnO_x/CNTs with lump MnO_x deposition; d) 60 wt% MnO_x/CNTs with crystalline structures.
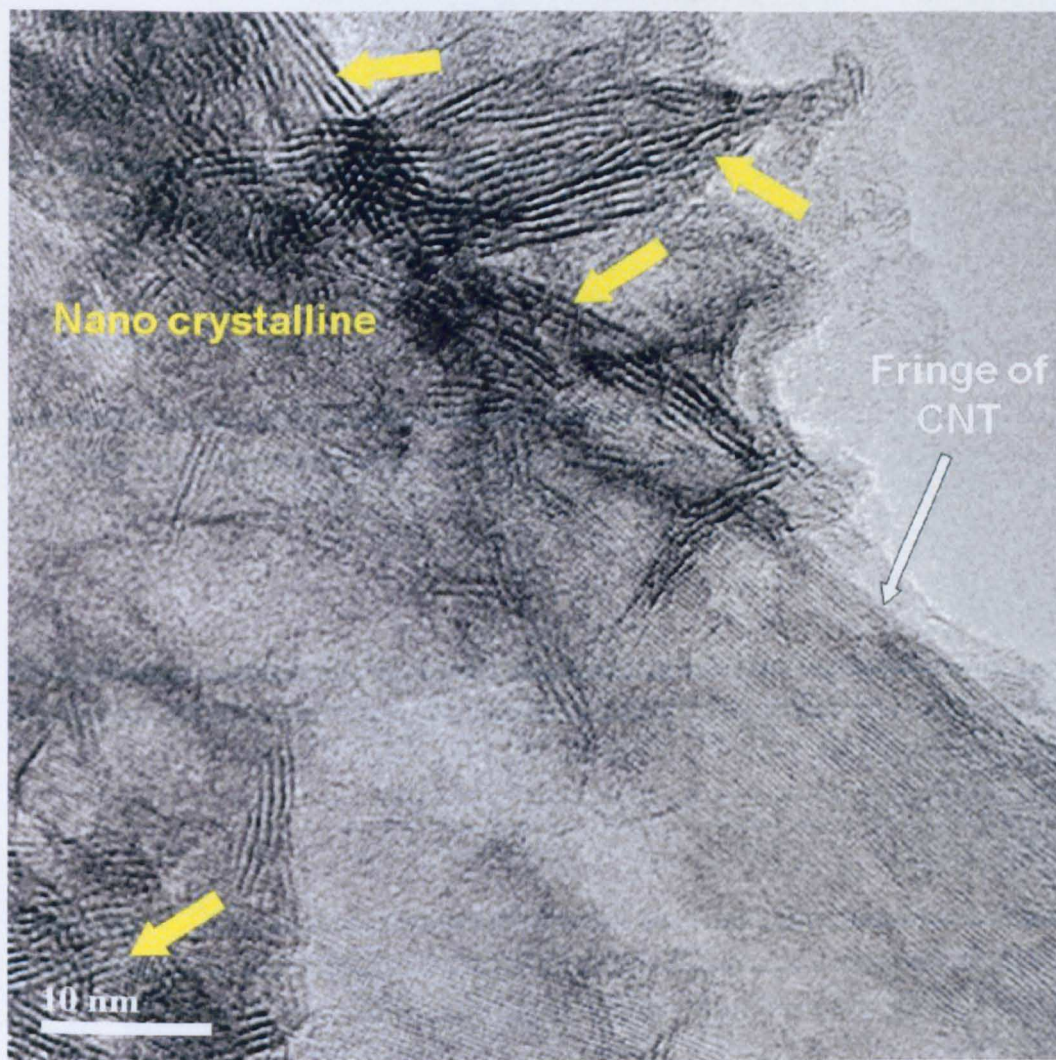
Fig. 5. 7. HR-TEM image of 80 wt% MnO$_x$/CNTs with details of crystal lattice.

For the application as an electrode material in supercapacitors, existing literatures are in favour of amorphous manganese oxides. It is generally believed that a porous morphology can enhance the ion accessibility and cation diffusion. Although attempts have been made recently to explore crystallised manganese oxides as alternative electrode materials, very few successful results have been reported. Thus, only amorphous MnO$_x$/CNTs composites are studied in this thesis as electrode materials for supercapacitors.

3. Porosity and Surface Area

BET nitrogen adsorption is applied to investigate the surface area, pore volume and the pore structure of the samples. Surface area and porosity play important part in determining the capacitive behaviour. Particularly, surface area and porosity are the prime determinants for double layer capacitance. Therefore, the porosity profile of the sample can provide an insight into the origin of the capacitance and help to select the most suitable electrode material.

The BET adsorption isotherms of carbon nanotubes, conducting polymer/CNTs composites and MnO_x/CNTs composites are presented in Fig. 5.8, Fig. 5.9 and Fig. 5.10 respectively.

First of all, it is to be noted that all the absorption isotherms (Fig. 5.8 – 5.10) are Type II isotherm, in which the monolayer coverage completes in the middle section of isotherm and a linear section begins suggesting the start of multilayer adsorption (Sing et al., 1985). Unlike Type I and Type III isotherm, the accurate surface area can be obtained with materials that yield type II and Type IV adsorption isotherm (Sing et al., 1985). Type II isotherm represents unrestricted monolayer - multilayer adsorption(Sing et al., 1985). Two adsorption energy levels can be clearly identified; the first adsorbed proportion requires higher energy value while to increase the number of molecules lower energy value would be sufficient (Khalfaoui et al., 2003). Type II isotherm normally indicates that the adsorbent is neither mesoporous nor microporous. The adsorbent is likely to be either non-porous or macroporous.

The nitrogen adsorption curves of different types of CNTs used in this thesis are presented in Fig. 5.8 and their surface area is listed in Table 5.1. The CNTs after acid treatment shows identical adsorption isotherm

with the as received CNTs. However, a 19.8 % increase in surface area
has been recorded after the acid treatment. As acid treatment is expected
to etch the carbon nanotubes and cause a rougher surface. For carbon
materials, larger surface area is usually desirable since this would
normally lead to enhanced double layer capacitance and other beneficial
properties. On the other hand, aligned carbon nanotubes (ALCNTs) have
much lower surface area, only 61.2 % of the untreated CNTs. Possibly due
to the facts that: ALCNTs are much longer (5-15 µm), compared with CNTs
of 1-2 µm; and ALCNTs are narrower, with a diameter of 10-20nm, compared
with CNTs of 20-40nm diameter.
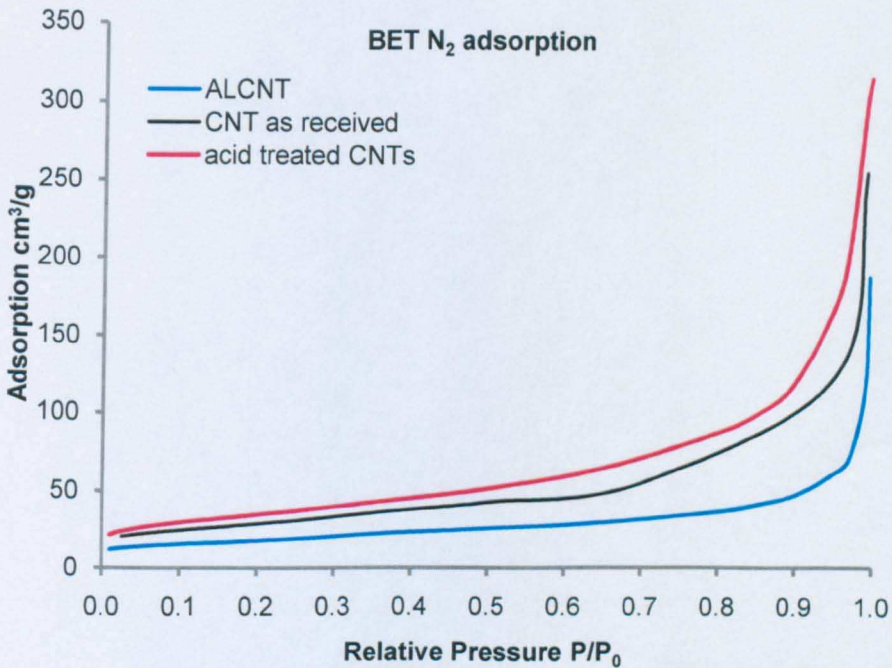
Fig. 5. 8. BET of CNTs with different treatments.

Sample	BET surface area (m^2/g)
As received CNTs	102.1415
Acid treated CNTs	122.4133
Aligned CNTs	62.4902

Table 5. 1. Surface area of CNTs with different treatments.

BET adsorption isotherms of the conducting polymer/CNTs composites are
presented in Fig. 5.9 and the figures of surface area are listed in Table

5.2. Polypyrrole/CNTs and polyaniline/CNTs composites show similar adsorption curve and comparable surface area. Their surface area are much smaller, less than half of the value, compared with CNTs. Since it requires significant value of surface area (2000 - 4000 m^2/g) to create appreciable double-layer capacitance (Frackowiak and Beguin, 2001), it may then be safe to conclude that the capacitance originates from these composites should be attributed to pseudocapacitive processes of the conducting polymers.
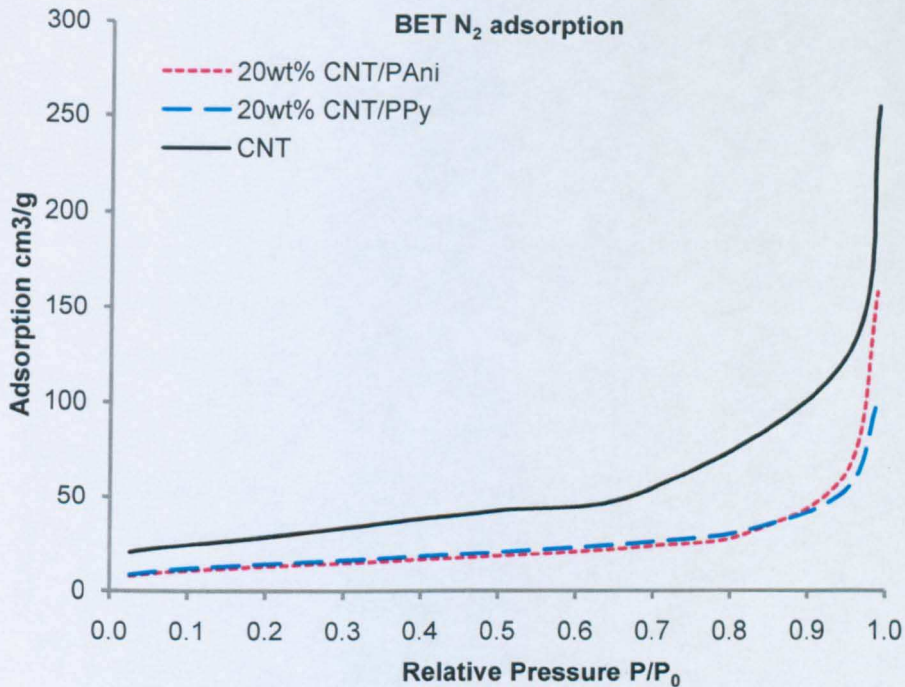
Fig. 5. 9. BET of Conducting polymer/CNTs composites.

Sample	BET surface area (m^2/g)
CNTs	102.1415
PAni/CNTs 20 wt%	45.1587
PPy/CNTs 20 wt%	50.5329

Table 5. 2. Surface area of conducting polymer/CNTs composites.

Fig. 5.10 presents the adsorption and desorption curves of MnO_x/CNTs composites with various MnO_x content. The desorption hysteresis loops of these composites are clearly H3 type, which confirm the Type II adsorption isotherm of these materials with slit-like pores. Similar adsorption isotherms and hysteresis loops are recorded with a range of

MnO_x/CNTs composites and acid treated CNTs, except for the composite with 80 wt% MnO_x content. The surface area and mesopore volume of these composites are presented in Table 5.3, in comparison with CNTs. Evidently, the surface area of the composites decreases with the increase of the MnO_x content in the composite. Again, most of the composites show significantly smaller surface area than acid treated CNTs and a surface area as low as 7.4131 m^2/g is recorded with the composite with 80 wt% MnO_x content. This indicates that the capacitive behavior of the composites originate from pseudocapacitive processes rather than the double-layer capacitance.
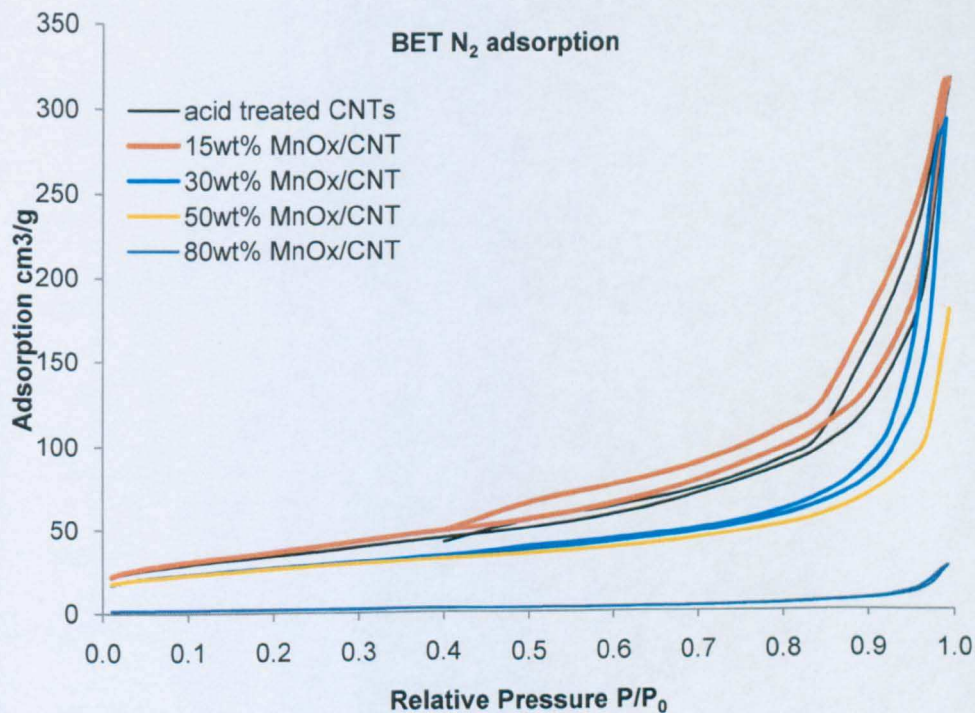
Fig. 5. 10. BET of MnO_x/CNTs composites with different MnO_x content.

In addition, considerable decrease in pore volume is noticed with the increase of MnO_x content in the composites. A decrease in pore volume of 33.5 % is recorded when the MnO_x content increases from 15 wt% to 30 wt%; and a decrease of 95.5 % is recorded when the MnO_x content reaches

80 wt% in the composite. A possible explanation is that with the proceeding of reduction, reduced MnO_x deposit into the pore structure of carbon nanotubes. The pore size distribution of the MnO_x/CNTs composites is presented in Fig 5.11. The majority of the pores within the MnO_x/CNTs composites have a diameter of about 50 nm (Fig. 5.11).

Sample	BET surface area m^2/g	Pore volume * cm^3/g
Acid treated CNTs	122.4133	0.313707
15 wt% MnO_x/CNTs	134.1925	0.346159
30 wt% MnO_x/CNTs	96.5401	0.22987
50 wt% MnO_x/CNTs	73.9651	0.0515069
80 wt% MnO_x/CNTs	7.4131	0.015703
Aligned CNTs	62.4902	0.06859

Table 5. 3. BET adsorption surface area and pore volume of MnO_x/CNTs

*accumulative desorption pore volume of mesopores with diameter between 2- 50 nm.
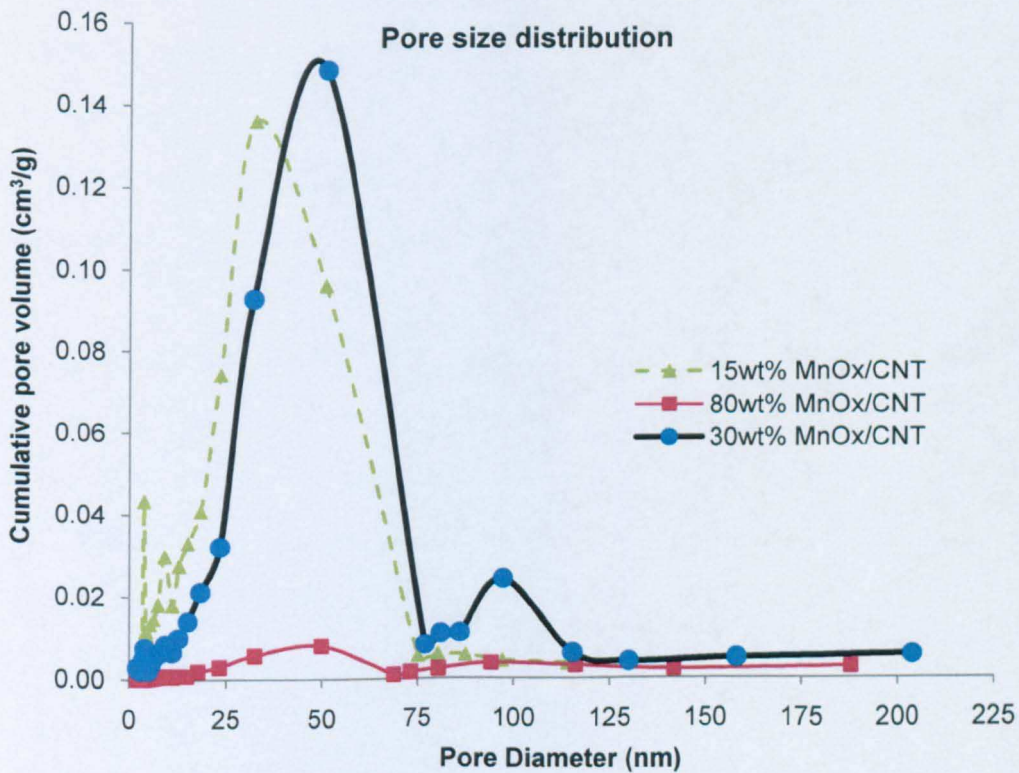
Fig. 5. 11. Pore size distribution of MnO_x/CNTs composites with different MnO_x content.

4. Thermal Stability

In this work, thermogravimetric analysis (TGA) was used to investigate

the thermal stability of the samples and to verify the metal oxide content

in the MnO_x/CNTs composites.

Fig. 5.12 compares the thermal stability of CNTs with different acid

treatments. As could be observed from the mass-time (temperature) curves,

the acid treatments obviously accelerate the onset of degradation.

Untreated CNTs start to loss weight in air at the temperature of 580 °C,

which is attributed to the oxidation of graphene walls; its weight remains

stable at 800 °C with a residue of 2 wt%. The acid-treated CNTs exhibit

a broad slope over the range of 200-500 °C, as the degradation of acid

functionalized CNTs may involve complex degradation mechanisms due to

the existence the amorphous carbon and the oxy groups in the surface,

which thereby make the degradation slope broader (Shanmugharaj et al.,

2007). However, the drastic degradation did not start until the

temperature reach about 580 °C. A residue of 2.5 wt% of the initial sample

weight is recorded after 30 min under 800 °C. This could be the impurity,

possibly metal catalyst residue, in the untreated CNTs sample.

It is interesting to observe multiple degradation steps in the degradation

curve of the over-oxidised CNTs. The over-oxidised CNTs were treated with

the same sulphuric acid and nitric acid mixture for a prolonged period

of 60min under boiling temperature. A rapid degradation started at 480 °C

with the over-oxidised CNTs in air, 100 °C lower than the degradation

temperature of as received CNTs. Therefore, it is concluded that although

the thermal stability can be damaged by overoxidation, the acid treatment

applied in this work did not impair the thermal stability of CNTs.
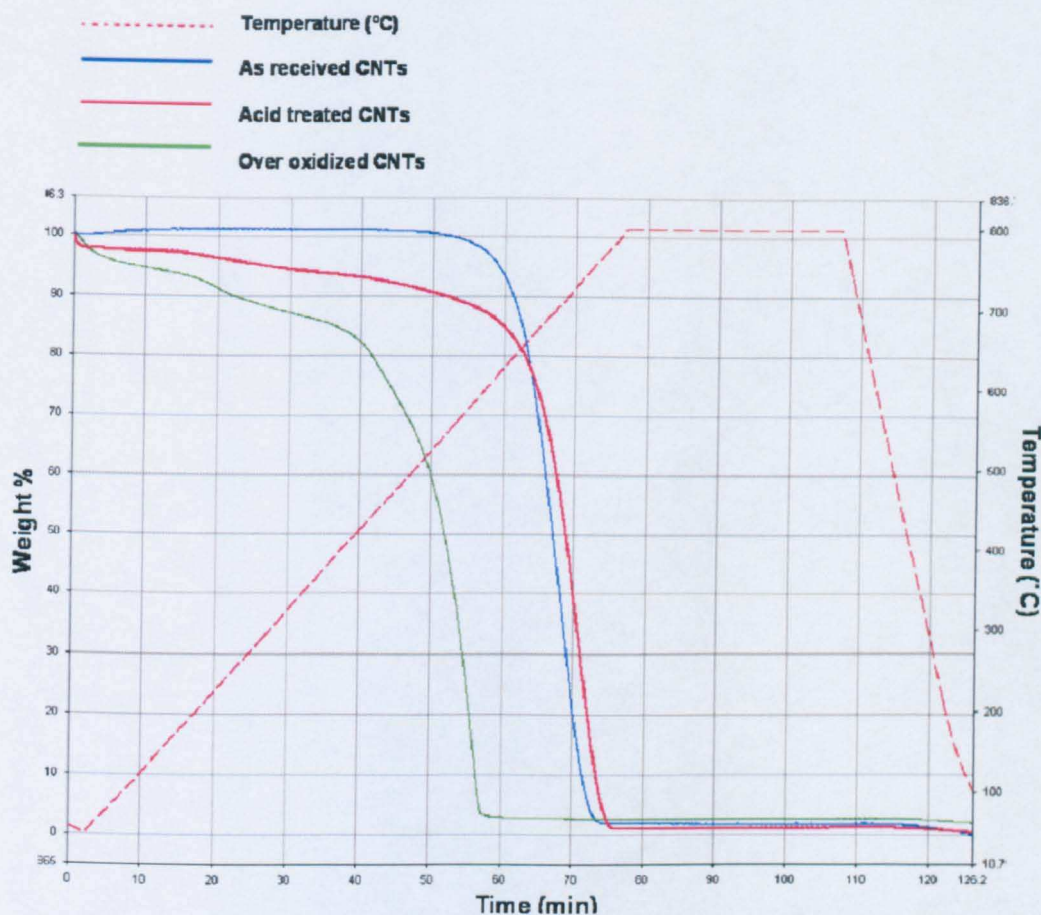
Fig. 5. 12. Thermal stability of CNTs in air with different acid
treatments.

The TGA of 30 wt% MnOx/CNTs composite is presented in Fig. 5.13. About
6 % of the weight loss occurred below 150 °C, mainly due to the release
of interlayer water in MnOx/CNTs composite accumulated from physisorption.
This could be an indication that the MnOx is hydrous in nature. An
additional weight loss of 5 % between 250 and 330 °C might correspond
to the loss of oxygen atoms from the octahedral layer framework in relation
to the partial reduction of Mn(IV) to Mn(II) (Gaillot et al., 2005, Ma
et al., 2007). The continuous weight loss between 400 °C and 550 °C are
attributed to the loss of carbon nanotube in the composites. The 32 wt%
residue after TGA at 800 °C confirms that there is 30 wt% MnOx content
in the MnOx/CNTs composite.
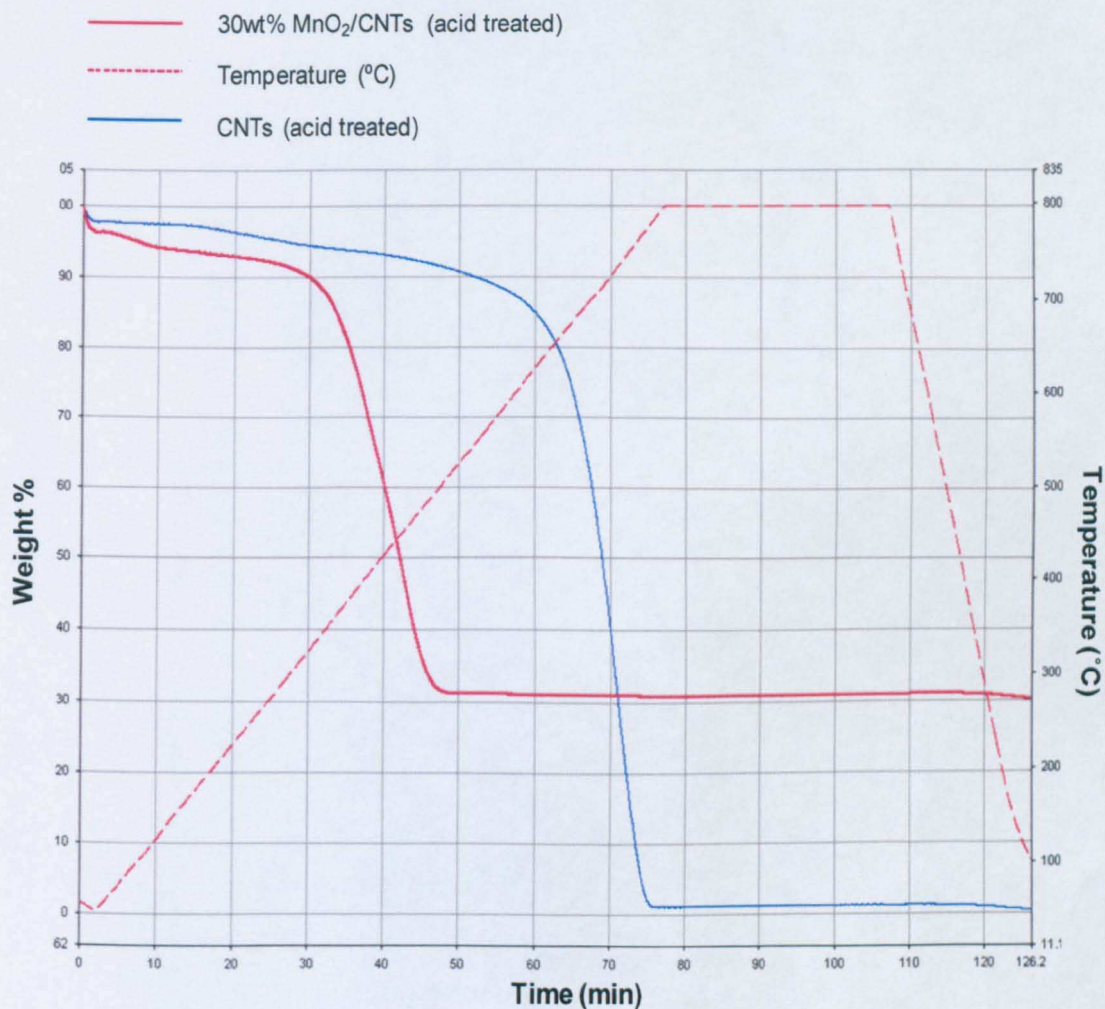
Fig. 5. 13. TGA of MnOx/CNTs with comparison to CNTs.

5. Crystallinity

The crystallinity of CNTs and MnOx/CNTs composites are examined with X-ray Diffraction (XRD). In general, carbon nanotubes have a multiple orientation as compared to the X-ray incident beam. Diameters and chiralities distribution can be observed as well as various numbers of layers. As shown in Figure 5.14, the graphite like peak at 26.2° presents as the main features of the XRD pattern of CNTs. Acid treatment does not introduce new crystallinity structure. However, over oxidised CNTs exhibit a more amorphous structure with less distinct characteristic peaks. As the degree of crystalline and the size and arrangement of crystallites have profound effects upon the physical strength and

113

conductivity, to reach the ideal status by controlling the acid treatment applied is very important for the future experiments.
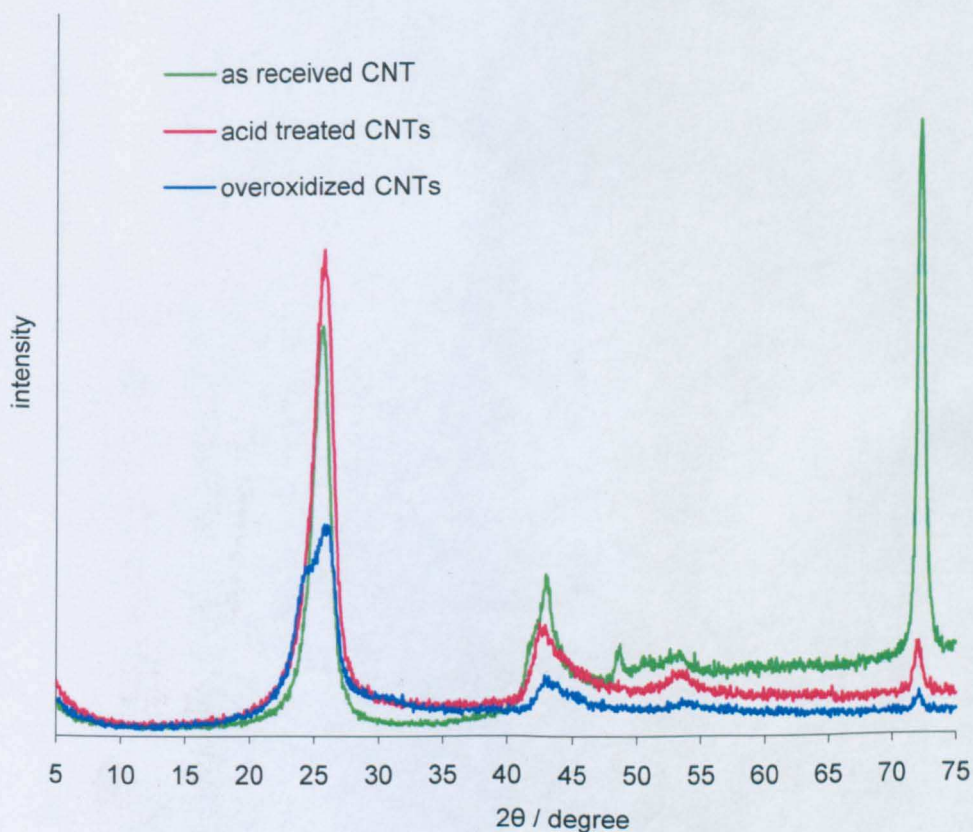
Fig. 5. 14. XRD of CNTs with different acid treatments.

Compared with acid treated carbon nanotube, MnO_x/CNTs composite seems to be more amorphous (Fig.5.15 a). The characteristic peaks for carbon materials at 26° and 42° are still discernible in the composites, though with much lower intensity. The broad peaks at 13°, 37° and 65° (Fig. 5.15 b) imply that the manganese oxide in the composites is birnessite-type MnO_2 including an amorphous phase (Ma et al., 2007, Huang et al., 2007). Fig. 5.16 compares the XRD pattern of MnO_x/CNTs composites with different MnO_x content. The composites are amorphous or nano-crystalline in general. Three characteristic peaks for birnessite-type MnO_2 at 13°, 37° and 65° 2θ are perceptible for both composites with 20 wt% and 80 wt% MnO_x. The composite with the higher

MnO_x content shows a lower intensity of characteristic carbon peak at 26°.
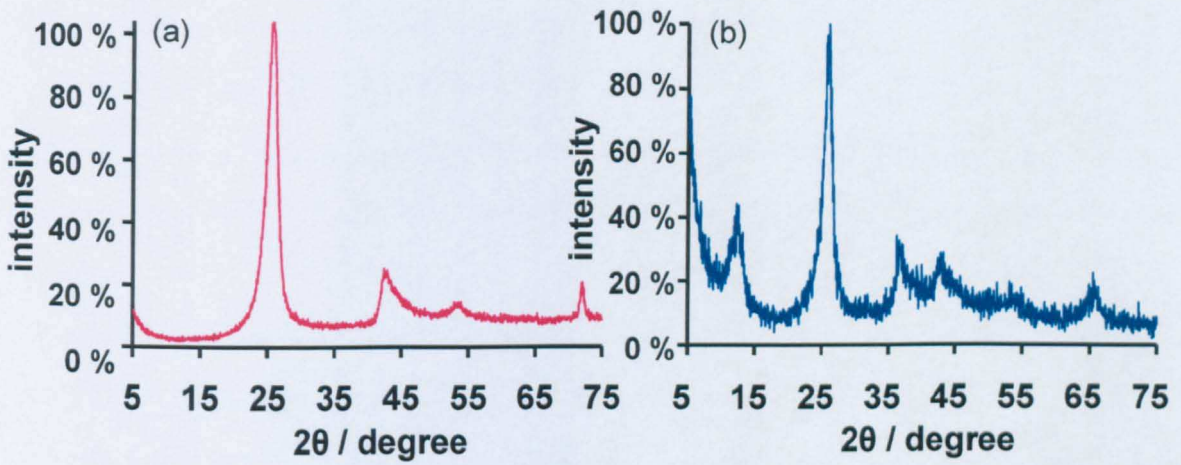
Fig. 5. 15. XRD of 30 wt% MnO_x/CNTs composite (b), in comparison with

CNTs (a).
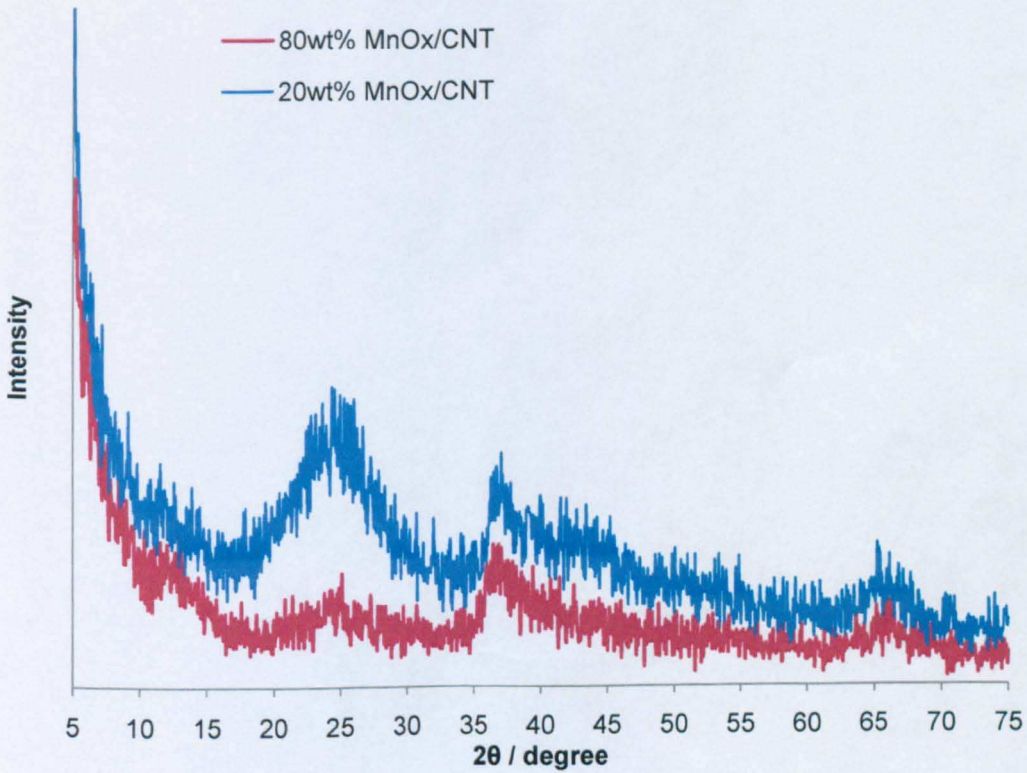
Fig. 5. 16. XRD of MnO_x/CNTs with different MnO_x content.

6. Infrared Spectroscopy

The infrared spectra of as received and acid treated carbon nanotubes are presented in Fig. 5.17. Compared to as received CNTs, more bands can be observed with acid treated CNTs, due to the formation of surface functional groups created by acid oxidation. The band at 1710 cm^{-1} is referred to >C=O in carboxylic anhydrides (Shanmugam and Gedanken, 2006); the broad band around 1210 (Shanmugam and Gedanken, 2006) and 1170 cm^{-1} (Peng, 2007) is the indication of C-O stretching in phenols, carboxyl and carboxylic anhydrides (Shanmugam and Gedanken, 2006); and the 1576 cm^{-1} band is assigned to aromatic ring stretching (Ros et al., 2002). The broad band at 3400 cm^{-1} is attributed to the O-H stretching of water molecules trapped in between the multi-walls of the CNTs, possibly introduced by the washing and drying process after the acid treatment.
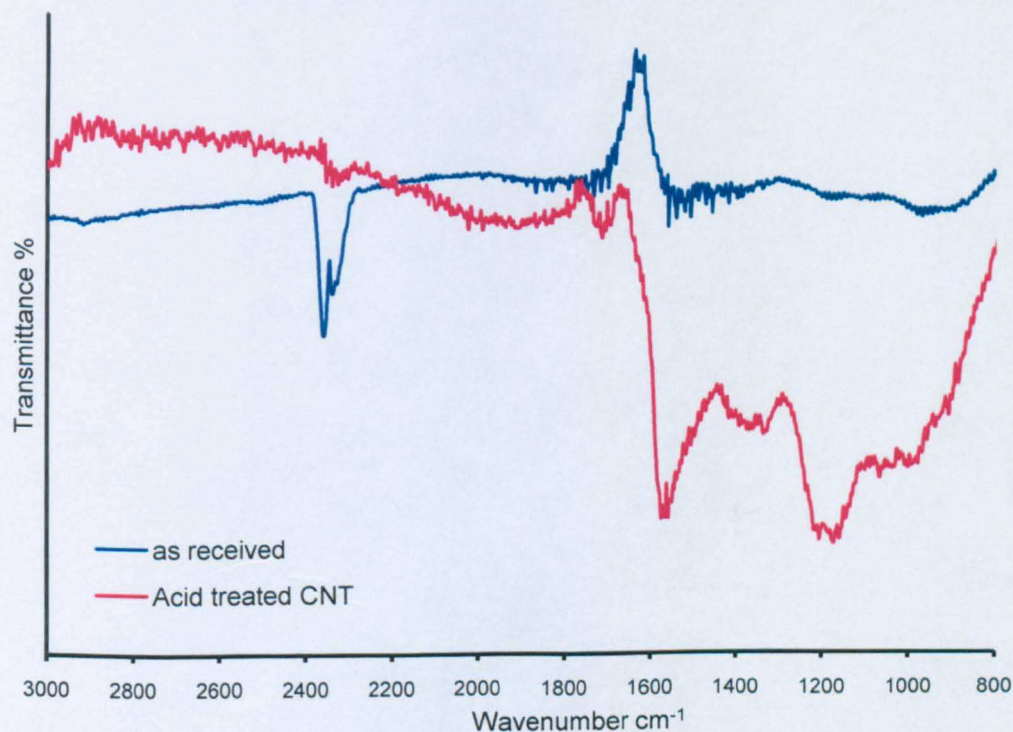
Fig. 5. 17. FTIR spectra of as received and acid treated CNTs.

As shown in Fig. 5.18, pure polyaniline and PAni/CNTs composite have similar FTIR spectra with almost identical peak position and similar intensity. This signifies that carbon nanotubes serve as the backbone

to provide mechanical support in polymerisation of PAni/CNTs composites, without interfering with the chemical bonding of polyaniline. All the samples show absorption peak at 1560 cm^{-1} (line A) indicates the quinoid N=Q=N stretching (Q: quinoid ring) (Adhikari, 2004, Wu et al., 2004). This is usually taken as an indication of the presence of emeraldine state of PAni (Trchov et al., 2005). The sharp peak at 1297 cm^{-1} (line B) is assigned to C-N stretching. Together with a broad peak at 1123 cm^{-1}, characteristic for C=N, it suggests the presence of leucoemeraldine state of PAni.

It is to be noted that there is a slight shift among the polyaniline samples with different polymer content, from 1295.7 cm^{-1} to 1297.9 cm^{-1}. Also, the peak around 1142 cm^{-1} (line C) shifts to lower wavenumbers gradually, from 1142 cm^{-1} for 70 wt% PAni/CNTs to 1130 cm^{-1} for 90 wt% PAni/CNTs. This wavenumber is assigned to a vibration mode of the –NH·$^{+}$– structure (Konyushenko et al., 2006). Some researchers (Lefrant et al., 2003) believe this band is associated with charge transfer between PAni and CNTs, thus it is well in agreement with the higher specific capacitance of the PAni/CNTs nanocomposites with higher polymer content. On the other hand, the shift to lower wavenumbers indicates the delocalisation of the electrons to a more stable status (Wu et al., 2004).
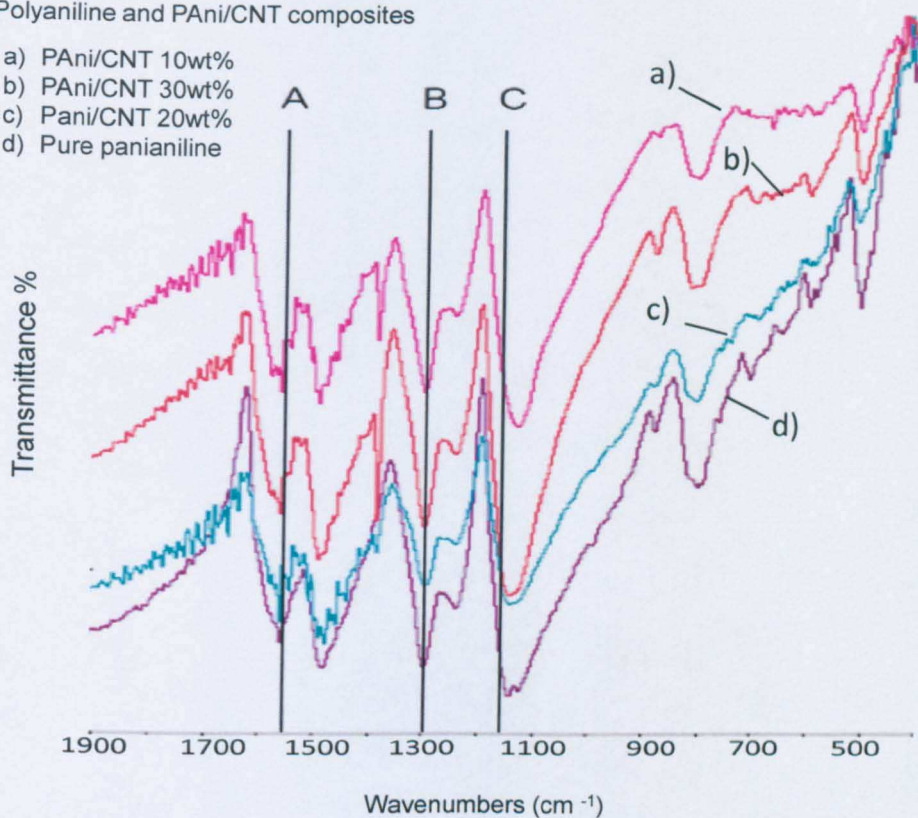
Fig. 5. 18. FTIR spectra of Polyaniline and PAni/CNTs composites.

FTIR spectra of polypyrrole and PPy/CNTs composites are presented in Fig. 5.19. Similarly, the infrared spectra of PPy/CNTs composites resemble that of pure PPy, indicating that the addition of carbon nanotubes does not change the chemical bonding of polypyrrole. C-C stretching and C=C stretching can be identified at wavenumber 1526-1529 cm^{-1}; and the characteristic C-N stretching of the polypyrrole occur at the wave number 1445 cm^{-1} (Tian and Zerbi, 1990). For polypyrrole, the band at 1560 cm^{-1} indicates the antisystemmetric ring stretching, its intensity decreases with the increase of the symmetric ring stretching at 1480 cm^{-1} (Tian and Zerbi, 1990, Cho et al., 2001). Thus, the level of delocalisation is inversely proportional to the intensity ratio between the two bands at 1560 and 1480 cm^{-1} (Cho et al., 2001). Therefore, it suggests that lower level of delocalisation occurs with the increase of CNTs content in the

composites. Similar conclusion can be drawn from a shift of 3-15 towards

more positive wavenumbers after the introduction of carbon nanotubes at

1036.38 cm^{-1}, signifying the C=C stretching, and at 1171.82 cm^{-1},

associated with C-H stretching of benzene ring.
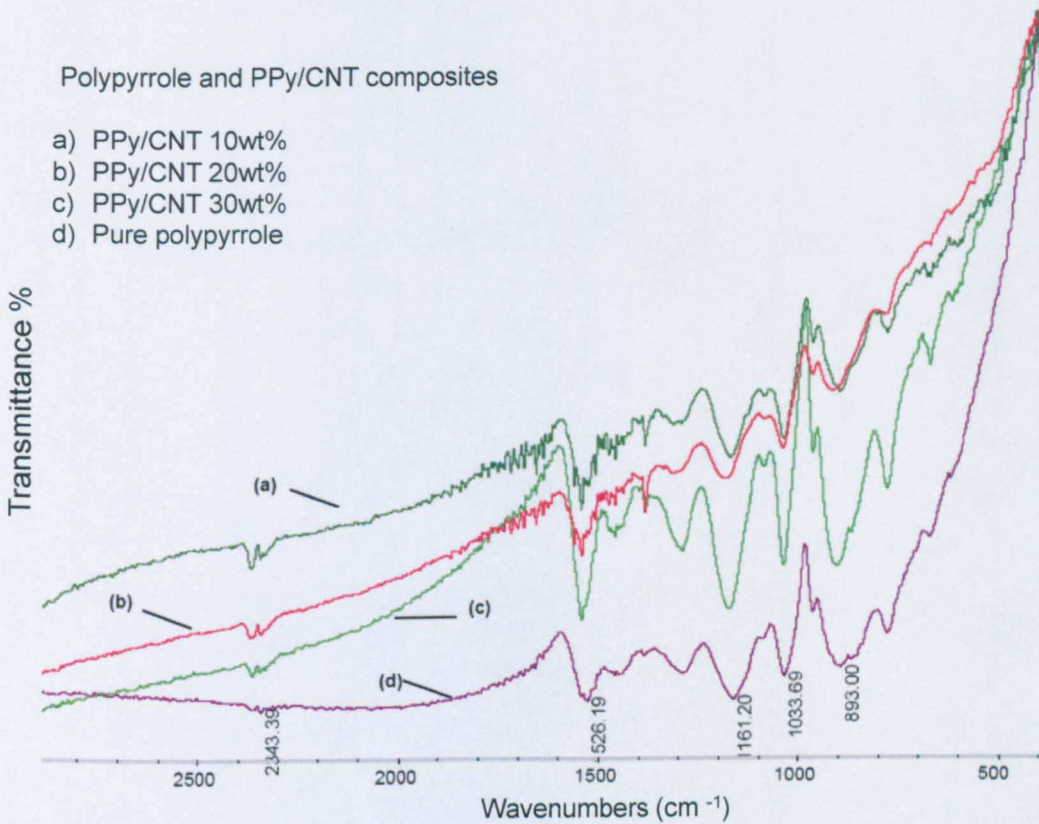
Fig. 5. 19. FTIR spectra of Polypyrrole and PPy/CNTs composites.

Fig. 5.20 presents the FTIR spectra of MnO$_x$/CNTs composites with different

MnO$_x$ content. The two composites, 15 wt% MnO$_x$/CNTs and 30 wt% MnO$_x$/CNTs

have identical peak position with slightly different peak intensity. The

bands at 514 and 482 cm^{-1}, corresponding to Mn-O stretching vibration,

are characteristic bands for birnessite MnO$_x$ (Potter and Rossman, 1979).

However, only one band can be observed from their FTIR spectra: 476 cm^{-1}

for 15 wt% MnO$_x$/CNTs and 440 cm^{-1} for 30 wt% MnO$_x$/CNTs. These phenomena

of overlap and shift towards low wavenumber can be explained by the

increase of Mn-O band strength through the protonation of manganese oxides

(Yang et al., 2004). It was suggested that the positions of the major

bands in 1400 cm^{-1} – 200 cm^{-1} region indicating that the MnO_x material has

a layer structure (Potter and Rossman, 1979).
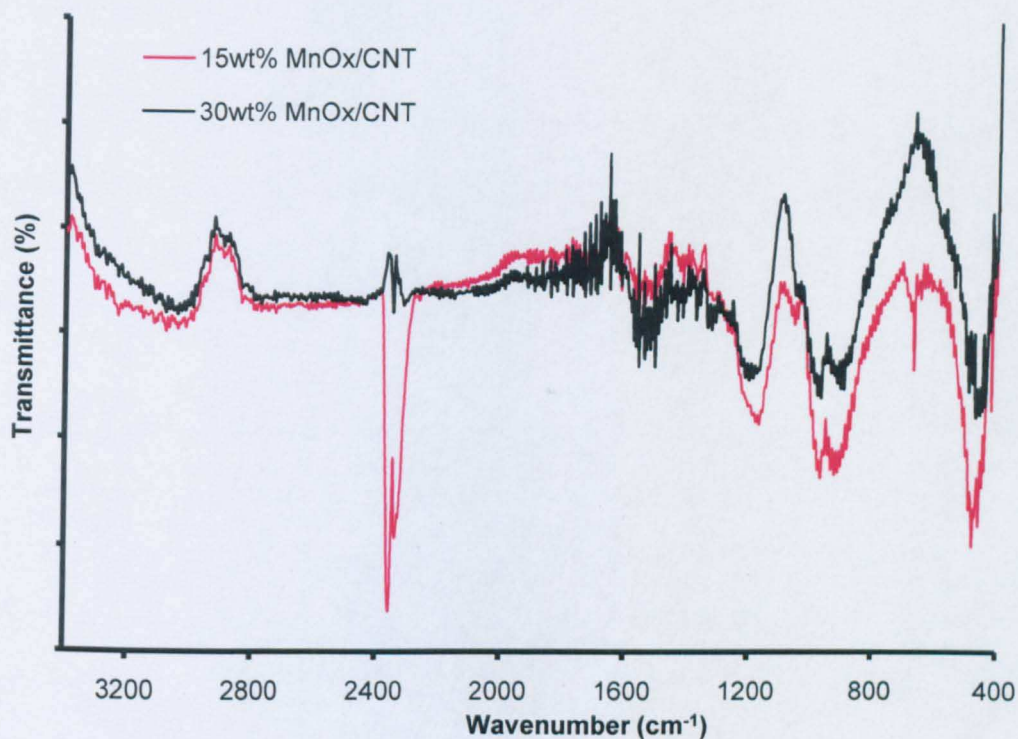
Fig. 5. 20. FTIR spectra of MnO_x/CNTs composites.

MnO_x composites are not investigated with FTIR in this study, as the

characteristic bands of Mn-O actually appear in the near infrared region

(Ozaki et al., 2007). Bands in this region strongly overlap with each

other, due to their origins in overtones and combinations of fundamental.

Moreover, near infrared bands are weaker and generally broad in general

(Ozaki et al., 2007). Therefore, the composition analysis of MnO_x is to

be conducted with other technique, e.g. XPS.

7. Composition of MnO_x/CNTs Composites

X-ray Photoelectron Spectroscopy (XPS) was applied to characterise the

composition of MnO_x/CNTs composites. As shown in Fig. 5.21, Mn 2P, O 1s,

C 1s are the dominant peaks for the composites, incidating the composition.

The XPS spectra of MnO_x/CNTs composites with different MnO_x content show

identical peak positions with varied intensities (Count per second). The atomic ratio of the elements and the empirical fomula of the composites are presented in Table 5.4. Sodium and potassium can be identified in both of the two composites, possibly due to the cation intercalation during the redox reaction of manganese oxides. As a matter of fact, the presence of intercalated potassium and sodium ions in birnessite-type manganese dioxide are believed to participate and contributes to the charge storage processes in some electrolytes (Athouel et al., 2008) (Brousse et al., 2006).

On the other hand, considering the Mn to O ratio in 30 wt% MnO_x/CNTs composite (1:3.5) and 60 wt% MnO_x/CNTs (1:2.2), it is deduced that the majority of manganese eventually exists as MnO_2 in the composite over the reduction process. Some manganese presents as Mn(VII) in the product and this is particularly the case for MnO_x synthesised in a limited reaction time (72 hr).
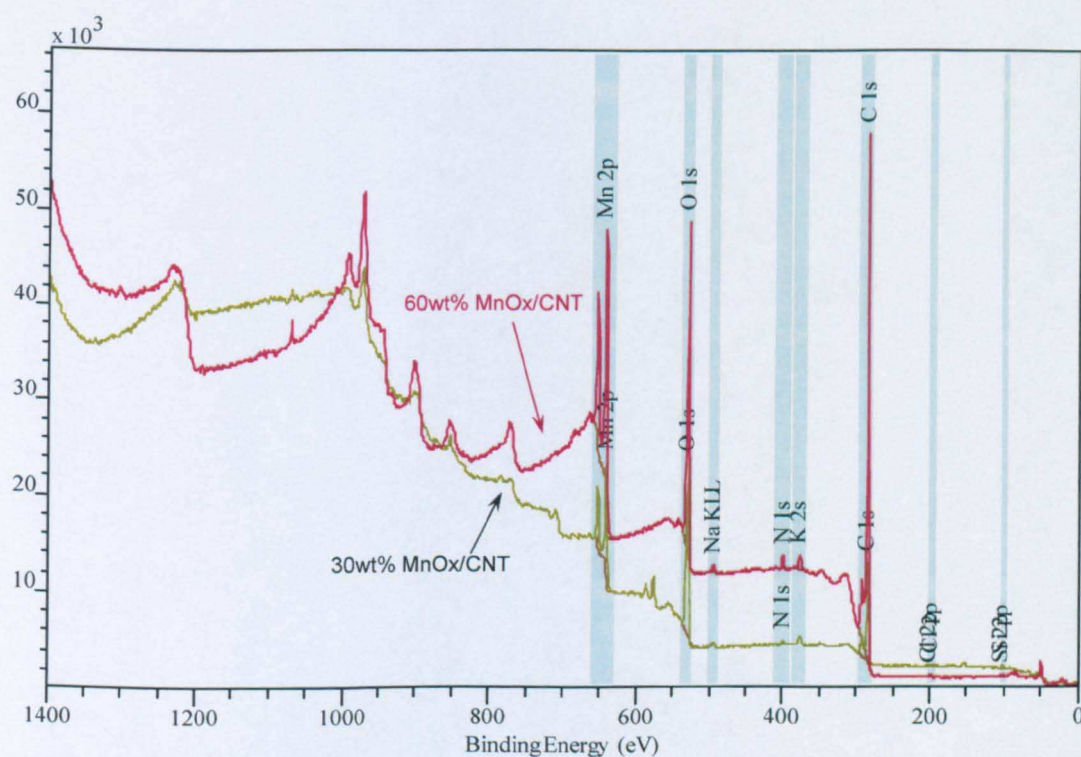
Fig. 5. 21. XPS wide scan of 30 wt% MnO_x/CNTs and 60 wt% MnO_x/CNTs

Atomic %	O 1s	N 1s	C 1s	Mn 2p	K 2s	Na KLL
30 wt% MnO$_x$/CNTs	9.4951	0.8259	83.9036	2.6885	2.9732	0.1138
Empirical formula	Na$_{0.03}$ K Mn$_{0.9}$ O$_{3.2}$ $\cdot$ C					
60 wt% MnO$_x$/ALCNTs	12.5428	0.9583	78.8636	5.7284	1.6530	0.2538
Empirical formula	Na$_{0.58}$ K Mn$_{3.47}$ O $_{7.58}$ $\cdot$ C					

Table 5. 4. Atomic ratio of MnO$_x$/CNTs composites by XPS.

To gain more insight into the composition and valence of the element in the composites, deconvolution of characteristic peaks is a common practice.

Mn 2P$_{3/2}$ is such a characteristic peak and its deconvolution peaks are commonly used in differentiating manganese compounds of different valences (Chigane and Ishikawa, 2000, Hu and Tsou, 2002). In addition, it is suggested that the O 1s spectrum can be used as supporting materials in analysing the Mn bonds in the composites (Masaya and Masami, 2000).

The XPS spectra and the devolutions of Mn 2P$_{3/2}$ and O 1s regions of 30 wt% MnO$_x$/CNTs and 60 wt% MnO$_x$/CNTs are presented in Fig. 5.22 and Fig. 5.23. The positions and the concentrations of the deconvoluted peaks are listed in Table 5.5. Table 5.6 provide reference of binding energy of Mn 2P$_{3/2}$ (Foord et al., 1984) in various Mn bonds.
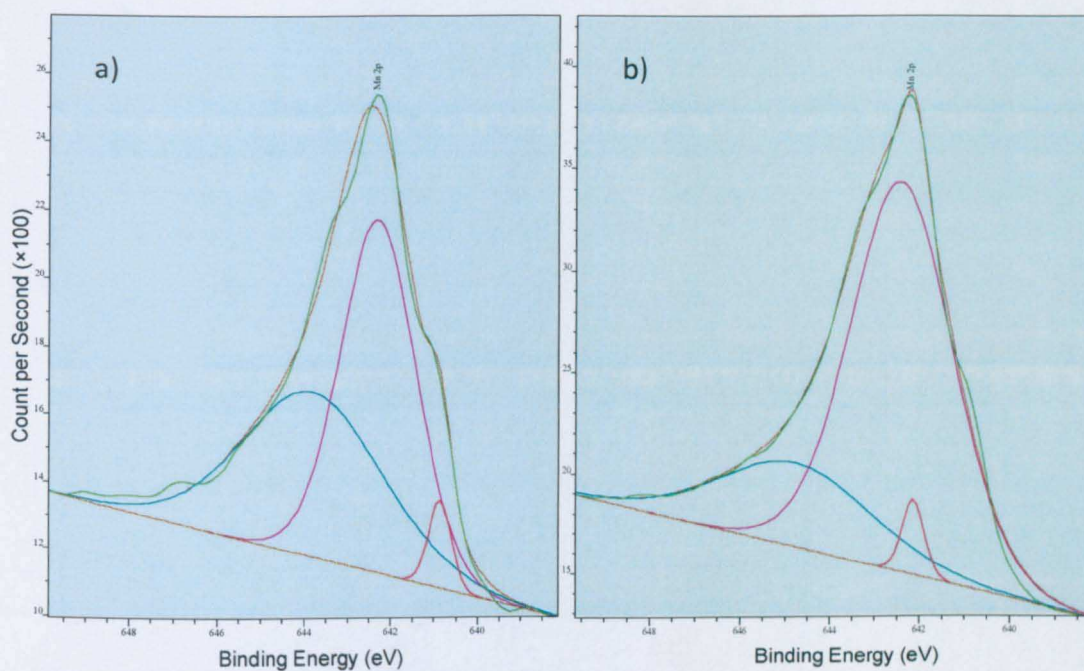
Fig. 5. 22. XPS spectra of Mn 2P3/2 region a) 30 wt% MnO_x/CNTs composite;

b) 60 wt% MnO_x/CNTs composite.
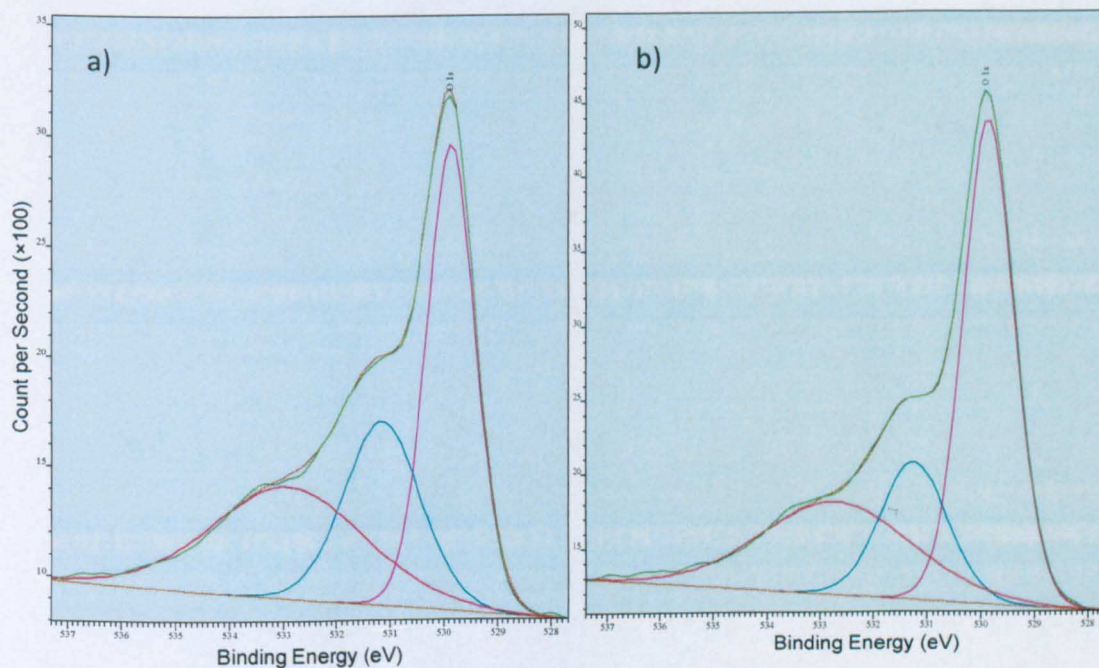
Fig. 5. 23. XPS spectra of O 1s region of a) 30 wt% MnO_x/CNTs composite;

b) 60 wt% MnO_x/CNTs composite.

Sample	Mn $2P_{3/2}$ (eV)			O 1s (eV)		
	Peak 1	Peak 2	Peak 3	Peak 1	Peak 2	Peak 3
30 wt% MnO_x/CNTs	643.8	642.3	640.8	532.9	531.1	529.8
Concentration %	44.80%	51.35%	3.85%	31.90%	26.20%	41.87%
60 wt% MnO_x/CNTs	644.7	642.4	642.1	532.7	531.2	529.8
Concentration %	23.81%	73.10%	3.06%	29.30%	19.00%	51.70%

Table 5. 5. Deconvolution of XPS spectrum Mn 2P3/2 and O 1s of 30 wt%

MnO_x/CNTs and 60 wt% MnO_x/CNTs.

Chemical Bond	Binding energy Mn $2P_{3/2}$
Mn	638.7 eV
MnO	640.9 eV
Mn_2O_3	641.8 eV
MnO_2	642.5 eV
$KMnO_4$	643.3 eV

Table 5. 6. Binding energy of Mn 2P3/2 in various Mn bonds (Foord et al.,

1984).

Upon examining the binding energy peak positions of Mn $2P_{3/2}$ with reference

to Table 5.6, it is noted that a positive shift in its binding energy

of Mn $2P_{3/2}$ is expected with the increase of oxidation state of manganese.

In Table 5.5, peak 1 of Mn $2P_{3/2}$ refers to $MnO4^-$ bond and peak 2 at 642.4

eV indicates the MnO_2 bond. Therefore, it is revealed that 51.4 % and

73.1 % of the manganese in the composites exist as MnO_2 in 30 wt% and

60 wt% MnO_x/CNTs respectively. Together with the atomic ratio data in

Table 5.4, the MnO_2 content in 30 wt% and 60 wt% MnO_x/CMT composites is

1:3. This is explained by the fact that a considerable amount (44.8 %)

of manganese in 30 wt% MnO_x/CNTs composite is not fully reduced and still

exists as $MnO4^-$. This finding is in agreement with the result from previous

atomic ratio analysis. In addition, results presented in Table 5.5 suggest

that a small amount of manganese (3.85 %) exists as MnO in 30 wt% MnO_x/CNTs

composite.

On the other hand, O 1s spectrum, in view of manganese oxides, can be

deconvoluted into constituents corresponding to different oxygen chemical bonds (Masaya and Masami, 2000):

	Chemical Bond	Binding energy
O 1s	H-O-H (water molecule)	531.8 - 532.8 eV
	Mn-O-H (hydroxide)	530.5 - 531.5 eV
	Mn-O-Mn (oxide)	529.3 - 530.0 ev

Therefore, 30 wt% and 60 wt% MnO_x/CNTs composites have similar water content: 3.02 % and 3.67 %, indicated by the H-O-H bond (Peak 1 for O 1s in Table 5.5) and the O 1s atomic ratio (Table 5.4). Peak 2 of O 1s in Table 5.5 indicates the Mn-O-H hydroxide bond and Peak 3 refers to Mn-O-Mn oxide bond. It confirms that the oxide and hydroxide forms of manganese co-exist in the composite, with the atomic ratio of 1:1.6 for 30 wt% MnO_x/CNTs and 1:2.7 for 60 wt% MnO_x/CNTs.

8. Summary

General characterisations of the composites and carbon materials, including morphology, BET surface area, composition analysis and crystallinity are performed in this Chapter. SEM and TEM results show homogeneous deposition of conducting polymers and manganese oxides on the carbon nanotube backbone. Coralloid 3-D structures of the composites have been observed, which would be beneficial to the electron and ion transfer as an electrode material. Further results from FT-IR confirm that CNTs only provide mechanical support in the composites, without forming chemical bonding. FT-IR results also reveal that both polyaniline and polypyrrole exist in various oxidation states in the composites. BET adsorption isotherms confirmed that the capacitance from the composites is pseudocapacitive in nature. Also, the majority of the pores within

the MnO_x/CNTs composites have a diameter of about 50 nm. Therefore the composite is between mesoporous and macroporous. TGA results verify the thermal stability of the materials of interests in this study and confirm the manganese content in MnO_x/CNTs composites. Moreover, the MnO_x/CNTs composites have been proved to be amorphous in nature with XRD. Finally, XPS results reveal that manganese exists in both oxide and hydroxide forms in the composites. Also, higher MnO_2 content has been discovered with the composite synthesised with longer reduction time, suggesting that the reduction of Mn from MnO_4^- to MnO_2 is a slow and time-consuming process.

PAGE
NUMBERING
AS
ORIGINAL

1. Introduction

The composites were fabricated into electrodes and tested in a standard one compartment three-electrode cell first. Ag/AgCl was used as reference electrode. A graphite rod with a diameter of 5 mm was used as counter electrode. Working electrodes are fabricated with synthesized composites with the following three different methods: trenched loading, sol-casting and rolling. Several different types of neutral aqueous solutions were used as electrolyte, including: 0.1 M K_2SO_4, 0.1 M $(NH_4)_2SO_4$, 0.1 M KCl. 0.5 M HCl and 0.5 M H_2SO_4 were used for polyaniline tests.

Two-electrode prototypes were then fabricated with the composites yielded encouraging results during the three-electrode cell test. The electrodes for the prototypes were mainly fabricated by pressing the nanocomposites powder into pellets.

All the electrochemical characterisations were conducted at room temperature.

2. Trenched Electrode

A graphite rod with a diameter of 5 mm was coated with epoxy resin before being trenched with a sharp knife across its uncoated cross-section (as shown in Fig. 6.1. a). Composites were loaded onto the graphite rod individually by gently pressing the rod against the composites powder. A loaded graphite rod is shown in Fig. 6.1.b.

Trenched graphite rod has been proved to be a good sample holder and current collector for the electrochemical characterisation without introducing unwanted oxidizing or reducing processes. No additional

chemical was added, so the electrochemical processes are purely originated from the sample. Besides, due to the fact that the total amount of loading onto the electrode is small, other effect such as active material diffusion, electrolyte accessibility, etc. can be effectively restrained. Thus, the electrochemical properties of the samples can be clearly represented. However, some of the samples loaded fell off the graphite rod when being immersed into electrolyte. This shortcoming limits the application of this method in quantitative study as the exact amount of the sample loaded can not be determined.

In this study, electrodes fabricated in this method are used for primary characterisations including: potential window, capacitive behaviour, and resistance of the samples.

a) before loading   b) after loading
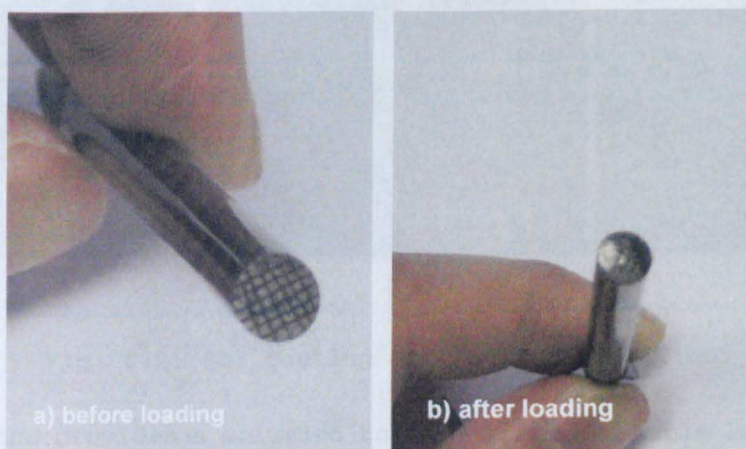
Fig. 6.1. Fabrication of trenched electrode.

3. Sol-Casting

Sol casting method was applied to fabricate large electrode with diameter of 30 mm. The sample powders were made into sol first and then uniformly spread over the graphite disk, thus the amount of sample loaded is controllable. The detailed method is given below.

An engineered graphite disk with an effective area of 7.07 cm^2 (dia

= 30 mm) was coated with epoxy resin on the side (Fig. 6.2.a). Mix a certain amount of sample powder with 10 wt% PTFE binders and certain amount of distilled water; the mixture will undergo 20 min sonication to form a homogeneous sol. An electronic pipette with the accuracy of 0.5 uL was used to take the favourable amount of the sol and spread the sol over the graphite disk (Fig. 6.2.b). After drying in the oven at 60°C for 2 hr, a uniformly coated electrode can be obtained (Fig. 6.2.c).

Fig. 6.2. Sol casting electrode fabrication.

This method provides a solution to determine the sample loading, not only the total amount (mg) but also the density of loading (mg/cm^2) can be controlled. However, PTFE binder added is hydrophobic in nature, which increased the resistance of the electrode mixture in the aqueous electrolyte and slightly impaired its performance. In this work, this method of fabrication is mainly applied to investigate the specific capacitance of carbon material, i.e. activated carbon M1300.

4. Membrane from Rolling-Process

Composite powder was well mixed with 10 wt% of PTFE binder (60 wt% PTFE

in water) and 7 wt% acetenyl black. The mixture was then rolled repetitively to form uniform membranes (Fig. 6.3.a) and dried in oven at 60 °C. The desirable shape and size of the membrane will then be cut with a sharp knife. The sample piece can be weighted and easily attached to current collector. The obvious defect of this method is that the rolling process can not ensure a uniform thickness of the membrane; besides, a homogeneous distribution of the components within the membrane is also difficult to achieve. On the other hand, some porous materials, e.g. polypyrrole, needs substantial amount of binder to form a membrane with satisfactory mechanical strength. Excessive PTFE added increases the hydrophobicity and resistance of the electrode membrane drastically. Thus, this rolling method was applied sparely in this research.
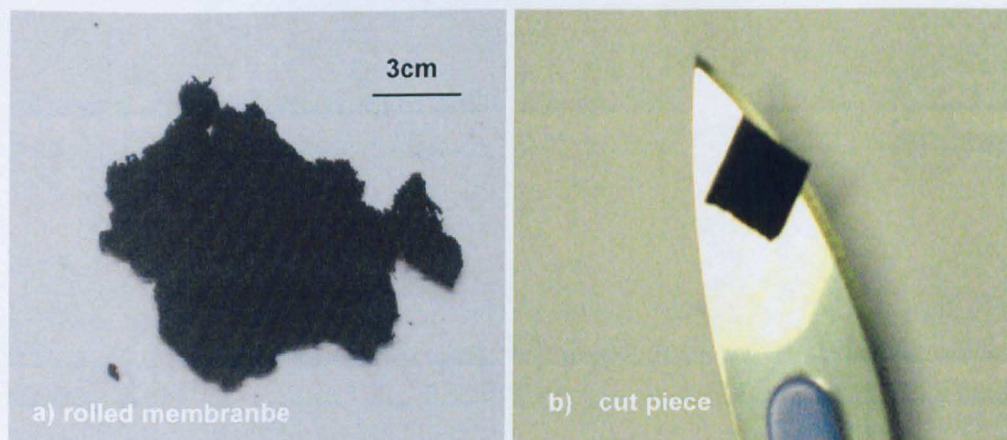
Fig. 6.3. Electrode membrane from rolling process.

5. Pressed Pellet

A certain amount of nanocomposites were pressed in a hydraulic press at 1 Ton (7.39×10^4 kPa) into 1.327 cm^2 (dia = 13 mm) pellet without adding any binder. Carbon materials can be added as conducting additive to enhance the conductivity of the electrode pellet. In this work aligned carbon nanotubes (ALCNTs) was used. ALCNTs were thoroughly mixed with sample powder in a pestle mortar before pressing. Large

loading of sample up to 50 mg per electrode can be achieved, depending on the density of the composites. Two electrode pellets, together with a separator and two current collectors, will then be assembled into a prototype supercapacitor cell. Different prototype cells, e.g. symmetrical, asymmetrical and cell stacks can be easily constructed by changing the electrode pellets. Mild aqueous solutions were used as electrolyte. Fig. 6.4 shows the pressed electrodes forming a two-electrode prototype cell.
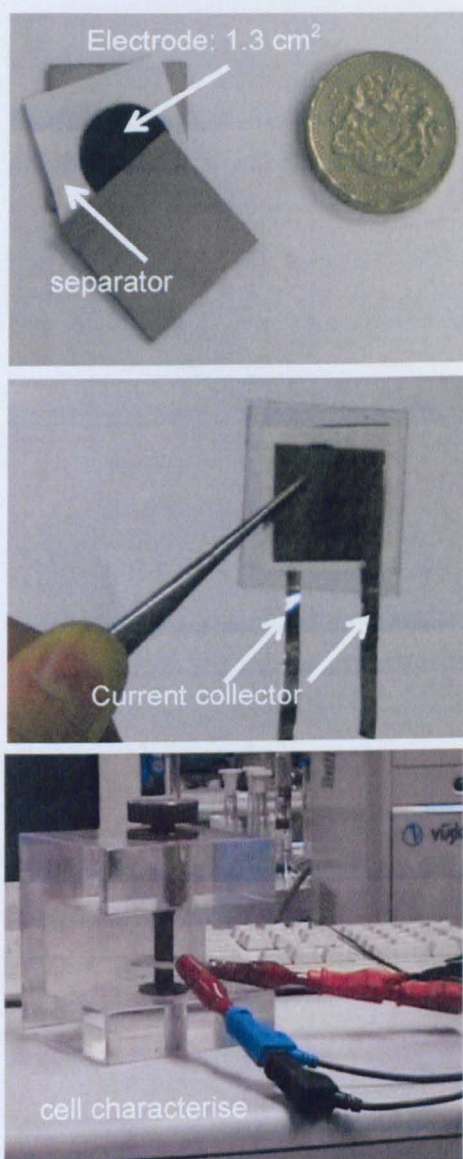
Fig. 6.4. Pellet Electrodes for Cell Test.

1. Introduction

In this chapter, the electrochemical properties of the synthesised composites were thoroughly investigated in the three-electrode testing system with Ag/AgCl as the reference electrode. The redox processes on the electrodes, from which the pseudocapacitance originates, were examined by cyclic voltammetry (CV) to identify the suitable operational potential window, reversibility and the limiting scan rate. Electrochemical impedance spectroscopy (EIS) was applied to further study the capacitive behaviour of the composites, their frequency and potential dependences and the susceptivity towards electrolyte concentration. Different presentations, including impedance complex plane, Bode plot, Admittance and effective capacitance, were employed to emphasise the different aspects of the capacitive behaviour. Finally, the cycling stabilities of the composites were characterised by continuously scanning the composites for several thousands of cycles with CV, highlighting the improvement from the addition of carbon nanotubes.

It is to be noted that all the investigations in this chapter were performed on the trenched carbon rod electrode with loaded composites (as described in Chapter 6). The results only give qualitative or semi-quantitative characterisations of the composites. However, these results provide valuable information of the electrochemical properties of the composites and the electrolyte systems, which are essential in prototype cell construction and investigation.

2. Background Characterisations

The electrochemical properties of the background, e.g. unloaded carbon rod, were first characterised. The background characterisation provides an overview of the electrode | electrolyte system before active composites

were introduced. As seen in Fig. 7.1, the CV of the unloaded carbon rod

and that with activated carbon has no discernable redox peaks, indicating

that no redox reactions took place during the potential scanning.

Semi-rectangular CVs with small currents were recorded, arising from

double-layer capacitance at the electrode | electrolyte interface.
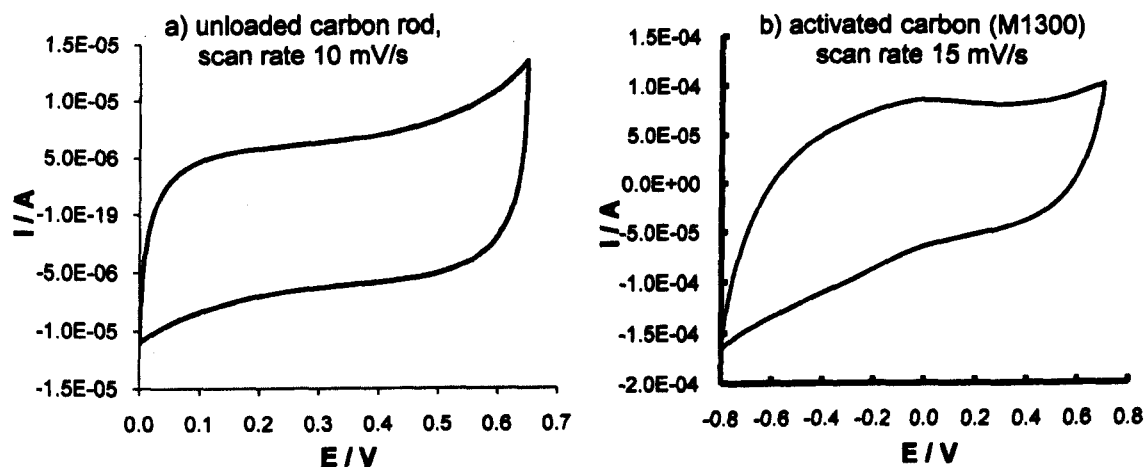
Fig. 7.1. CV background characterisation of: a) unloaded carbon rod and

b) activated carbon on carbon rod in 1 M KCl aqueous electrolyte.

The CV characterisation of CNTs is presented in Fig. 7.2. Interestingly,

the CNTs show a pair of distinct redox peaks after acid treatment, which

are originated from the surface functional groups created by acid

treatments. The presence of the surface functional groups were confirmed

with Infrared in Chapter 5. These surface functional groups enhance the

capacitance of carbon nanotubes by introducing pseudocapacitive

behaviour. Nevertheless the peaks experienced a notable shift and a

gradual wear out during the 400 cycle scans. However, this could be an

indication of the falling of CNTs from the trenched carbon electrode.
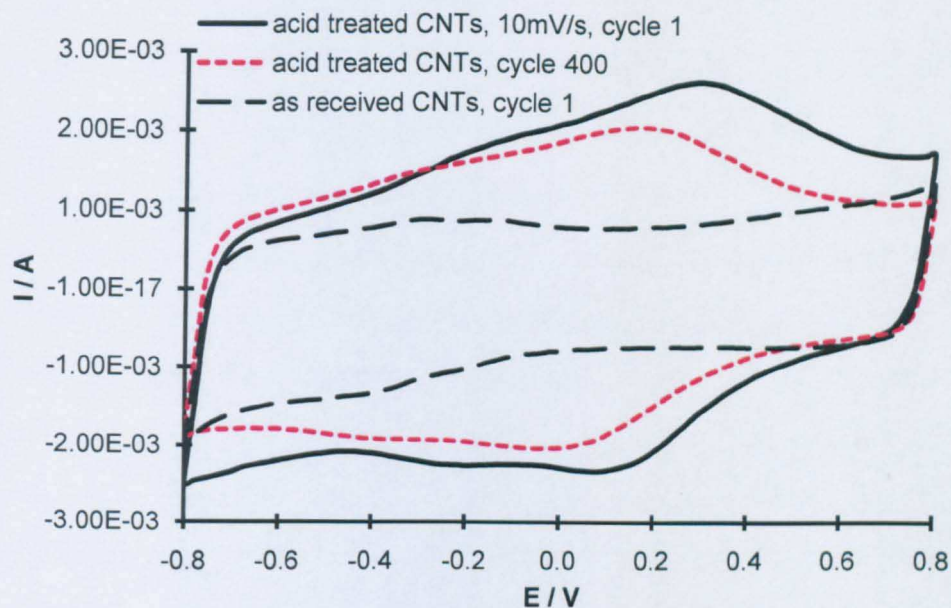
Fig. 7.2. CV of acid treated CNTs, in comparison with the as received CNTs, in 1 M KCl, scan rate 10 mV/s.

3. Redox Reactions and Characteristic Peaks

The CV of conducting polymer/CNTs and MnOx/CNTs composites are presented in Fig. 7.3 and Fig. 7.4 respectively. First of all, typical capacitive behaviour, exemplified by the quasi rectangular-shaped CV, is observed with all the composites examined. Early researchers associated this charging/discharging currents with interfacial double-layer, especially for the highly porous conducting polymers (Feldman et al., 1985) (Feldberg, 1984). However, this capacitive current response is later attributed to a series of continuously reversible redox reactions on the electrode.

The positions of the current peaks on potential axis are related to the formal potentials of the redox processes. Therefore, they are termed as characteristic peaks in this thesis. For polyaniline, cyclic voltammetry can reveal the ratio between amine and imine content: at the potential of 0.1 V (vs Ag/AgCl), imine concentration is low and PAni exists mainly as Leucoemeraldine; with the progress of voltage scanning, imine content

135

gradually increase to about 50 % at ~ 0.4 V and PAni is mainly in the

Emeraldine phase; finally, imine content reaches almost 100 % at ~0.7

V and PAni exists as Nigraniline (Mottaghitalab, 2006). Thus, for pure

PAni (Fig. 7.3 a), the oxidation peaks at 0.37 V and 0.64 V, and their

corresponding reduction peaks at 0.15 V and 0.54 V, indicating the switch

between these three status. With the addition of CNTs, the PAni/CNTs

composite exhibit almost identical CVs with slightly shifted peak

position (Fig. 7.3 b): the oxidising peaks shift towards a less positive

potential at 0.33 V and 0.58 V and the reduction peaks at 0.13 V and 0.52

V respectively. By introducing CNTs, the switching potential between

Leucoemeraldine, Emeraldine and Pernegraniline can be achieved at lower

potentials, due to the inter action of large π bonded surface of CNTs

with conjugated structure of PAni via π stacking (Mottaghitalab, 2006).

It is to be noted that these characteristic peaks gradually diminish with

the cycling (Fig. 7.3 a and b). This is caused by the irreversible processes

of completely reducing PAni to non-conducting Leucoemeraldine at

potential below 0.1 V (Huang et al., 1986).

The redox processes of polypyrrole involve the switch between its

conducting and insulating states. Polypyrrole is conducting in its

oxidised state and the switch from its insulating state can be achieved

by removing electrons from its delocalised π- system (Feldberg, 1984,

Chen, 1992, Peng, 2007). The characteristic peaks for polypyrrole and

its composite are not as obvious as those of polyaniline (Fig. 7.3 c).

One pair of small redox peaks can be clearly identified with anodic peak

at 0.59 V and cathodic peak at 0.57 V. The redox reactions behind this

pair of peaks are possibly due to the full oxidation of polypyrrole. The

emerging anodic peak at potential above 0.75 V is due to the evolution

of oxygen.
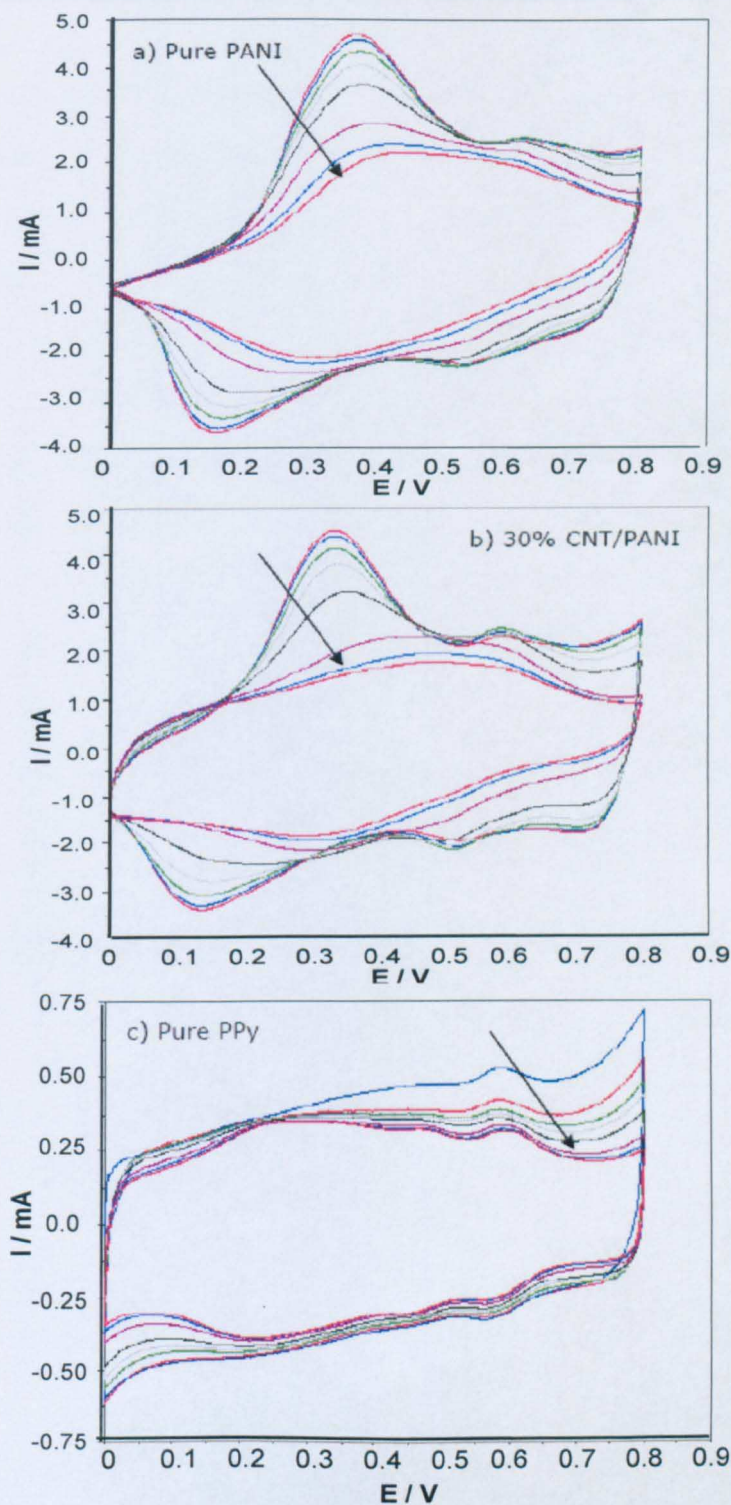
Fig. 7.3. Characteristic peaks of conducting polymers during CV scans in 1 M H2SO4: a) Pure PAni; b) PAni/CNTs composite; c) PPy. Cycle number: 10, 20, 50, 100, 200, 500, 800, 1000 scans. The arrow indicates the direction of the increase of scan-numbers (scan rate: 15m V/s).

Redox peaks in Fig. 7.4 indicate the redox transitions in manganese oxides and hydroxides between different valence states during the potential scan between -0.8 V – 0.9 V. According to Pourbaix's chart for manganese in neutral aqueous media, this redox system of Mn includes the transition between MnO_4^- and MnO_2 (0.9 V), MnO_2 and Mn_2O_3 (0.4 V), Mn_2O_3 and Mn_3O_4 (0.2 V), Mn_3O_4 and Mn^{2+} (-0.3 V) (Pourbaix, 1966). Thus, the anodic peak at 0.15 V demonstrates the oxidising of Mn_2O_3 to Mn_3O_4; the anodic peak at 0.35 V reveals the reduction of Mn_2O_3 to MnO_2 and the anodic peak at - 0.4 V suggests the formation of Mn(II). However, some of the redox processes are irreversible; which results in the gradual loss of active manganese oxides and decreased capacitance with further cycling scans (Fig. 7.4). Hence, it is necessary to limit the potential range of voltage scanning in order to achieve reasonable cycling stability, as to be discussed further in the following section of this Chapter.
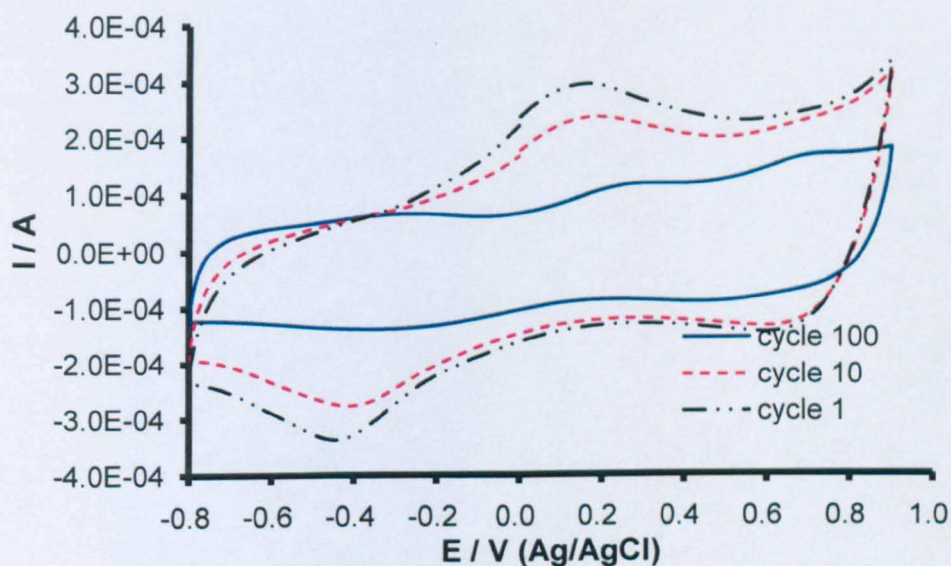
Fig.7.4. Characteristic peaks of MnO_x/CNTs composites in 0.1 M K_2SO_4 at 20 mV/s.

4. Operational Potential Window

Operational potential window is the potential range beyond which unwanted reactions occur. It is also commonly addressed as 'potential window'. For electrochemical capacitor, a wide potential window is desirable as

the potential window is closely related to the energy storage and power

output. The potential window of a particular system is defined by the

oxidation and reduction processes of the elements within the system,

including electrolyte, electrode materials, impurities and catalyst. In

the electrochemical systems using aqueous solution as electrolyte, the

decomposition of water is a major restriction to the potential window

due to hydrogen and/or oxygen gas evolution. Another important limiting

factor is the occurrence of irreversible reactions, leading to the

dissolution or deposition of the active materials. The potentials at which

unwanted reactions take place should be avoided. Therefore, the

operational potential window is restricted.

Although wider potential windows are generally desirable, stretching the

potential range often destroys the electrochemical activity and cycling

stability of the electrode materials. As shown in Fig. 7.5 (a), current

response to the potential change is rather small at potentials below 0.15

V. This indicates that the polymer is switched into a non-conducting

status and no longer suitable for the application as an electric energy

storage material. Also, the stability of polyaniline is seriously damaged

while cycling within a potential range of 0.0 V - 0.8 V. However, by

limiting the potential range to 0.15 V - 0.60 V a much improved stability

can be observed with the same electrode material in the same electrolyte

(Fig. 7.5 b).

Similar observations have been made with manganese oxides in K_2SO_4

electrolyte (Fig. 7.6). While cycling in a wide potential range of -0.8

V - 0.9 V, 60 % decrease in capacitance is observed in the first 1000

cycles due to the electrode material loss caused by irreversible reactions

(Fig.7.6 a). When limiting the potential range between 0.0 V and 0.85

V, a much improved stability has been obtained with 9000 cycles with
negligible decrease (Fig.7.6 b).
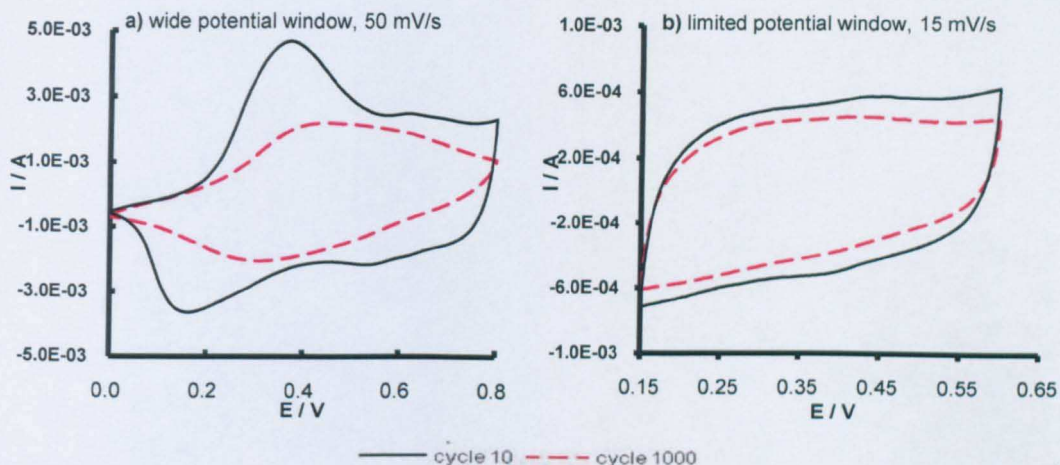
Fig.7.5. Cycling test of pure PAni in 1 M H_2SO_4 with different potential windows.
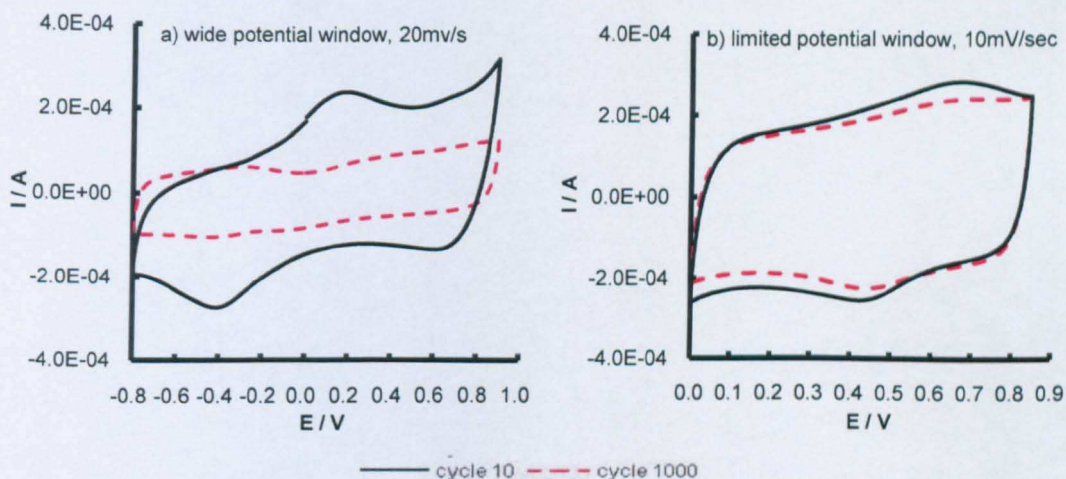
Fig. 7.6. Cycling test of 60 wt% MnO_x/CNTs in 0.1 M K_2SO_4 with different
potential window.

The maximum potential window for a particular electrode/electrolyte
system which ensures optimum cycling stability can be chosen by trial
and error. Table 7.1 lists the optimum potential window for the electrode
materials investigated in this thesis. It is worth mentioning that the
overpotential for H_2 or O_2 gas evolution can be changed by adjusting the
pH condition, electrolyte concentration and other parameters. Therefore,
the potential windows listed in Table 7.1 only provide references for
the investigations carried out in this thesis.

15 wt% MnOx/CNTs
30 wt% MnOx/CNTs
60 wt% MnOx/CNTs
PAni/CNTs 20 wt%
Pure PAni
PPy/CNTs 20 wt%
Pure PPy
acid treated CNTs
activated carbon M1300
aligned CNTs
blank carbon rod

-1.00 -0.90 -0.80 -0.70 -0.60 -0.50 -0.40 -0.30 -0.20 -0.10 0.00 0.10 0.20 0.30 0.40 0.50 0.60 0.70 0.80

Potential / V (Vs Ag /AgCl)
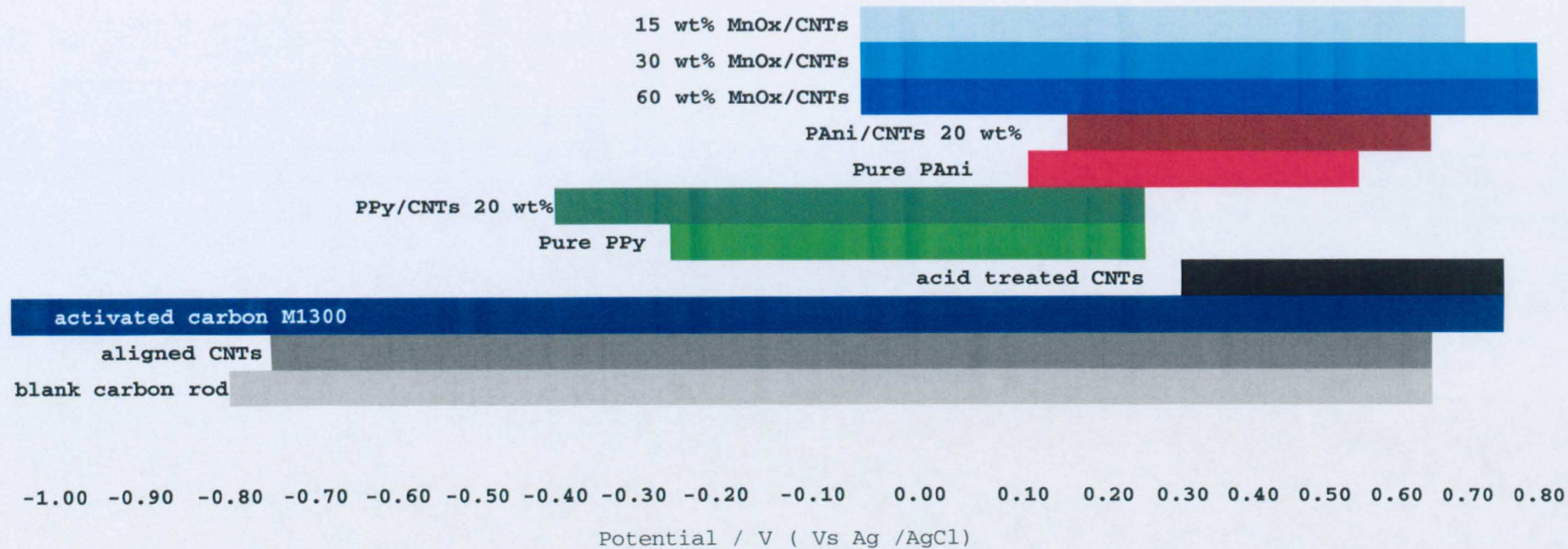
Table 7.1. Potential window of electrode materials determined by CV in 1.0 M KCl

(PAni and its composites are characterised in 1.0 M H_2SO_4)

5. Influences of Scan Rate

Scan rate is the potential sweep rate at which an electrical perturbation is applied to the system. In cyclic voltammetry, the potential is changed linearly with time. Therefore, the scan rate is expressed as voltage per second. The potential sweep rate is an important variable in cyclic voltammetry. In this study, the variation of scan rate affects the capacitive behaviour.

For an ideal capacitor with instant current response upon potential scan, the current increases linearly with the increase of scan rate:

$$C = \Delta Qdt/\Delta Udt = i/v \qquad \text{Eq. 7.1.}$$

In real applications, however, an upper limit for scan rate commonly exists. At scan rate above this upper limit, olive-shaped CV can be identified. This implies that it is difficult for redox reactions to proceed properly at this potential scan rate, due to mass transfer or electron transfer barrier, or both. As shown in Fig.7.7, Fig. 7.8 and Fig. 7.9, the upper limits for the scan rate are 100 mV/s for PAni/CNTs, 200 mV/s for PPy/CNTs and 300 mV/s for MnOx/CNTs composites. Composites exhibit proportional current response with the increase of scan rate until this upper limit. Thus, constant and rapid capacitive behaviour, independent of scan rate, have been observed below the upper limits. On the other hand, this upper limit of scan rate is susceptible of many factors, e.g. ion accessibility, bulk conductivity in the electrode. Therefore, this upper limit of scan rate should be case dependent.
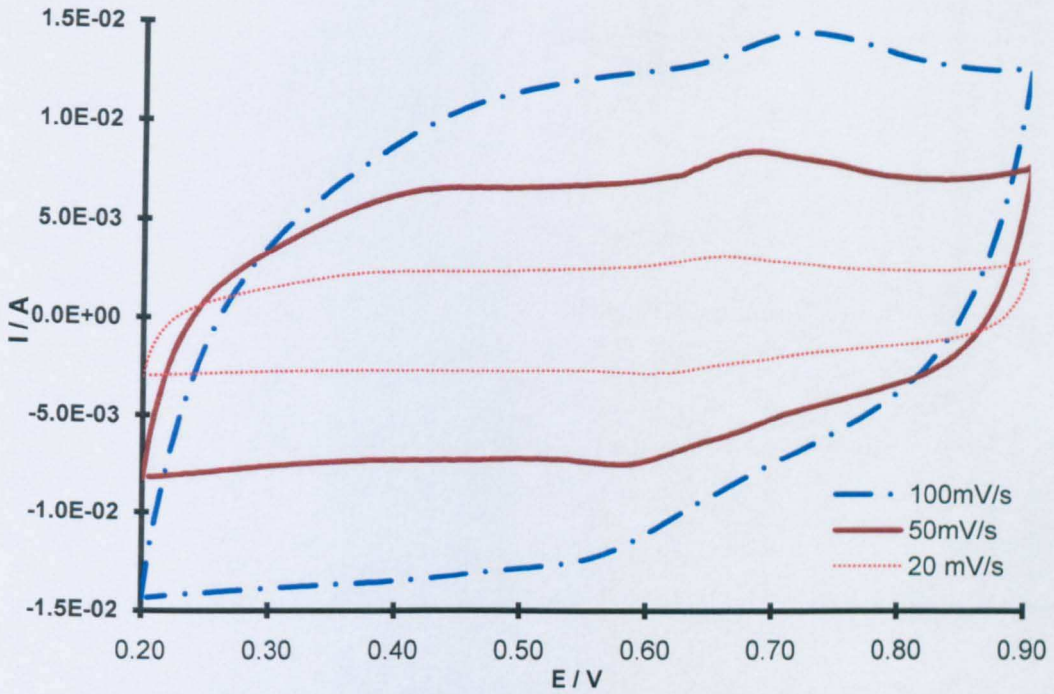
Fig. 7.7. The consequences of the increased of scan rate in CV: for 80 wt% PAni/CNTs in 1 M H_2SO_4.
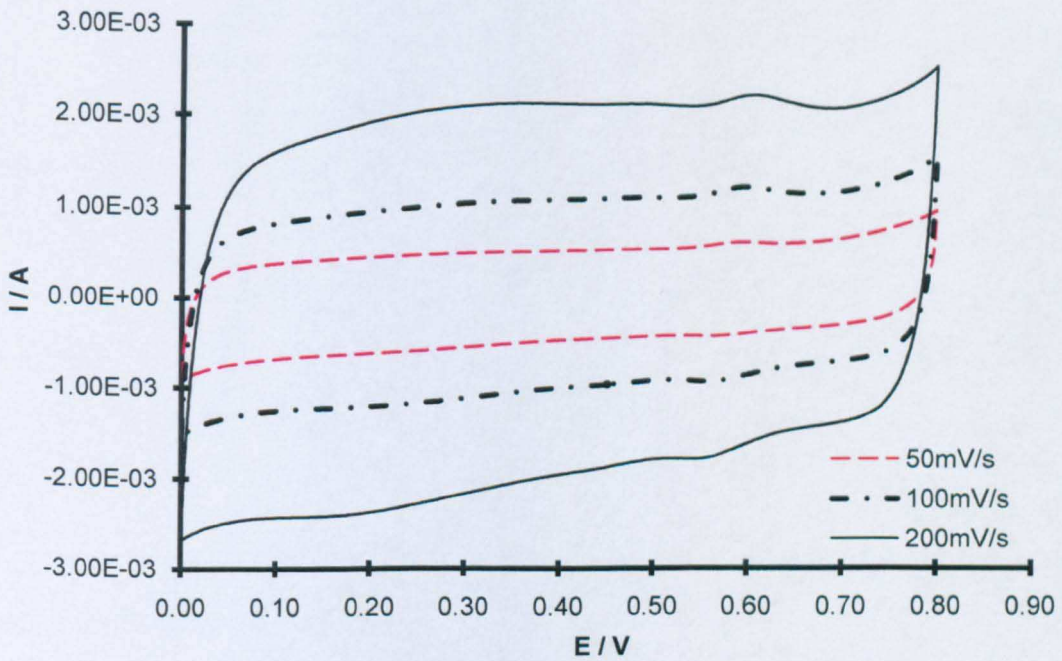
Fig. 7.8. The consequences of the increased of scan rate in CV of 80 wt% PPy/CNTs in 1 M KCl: 50 - 200 mV/s.
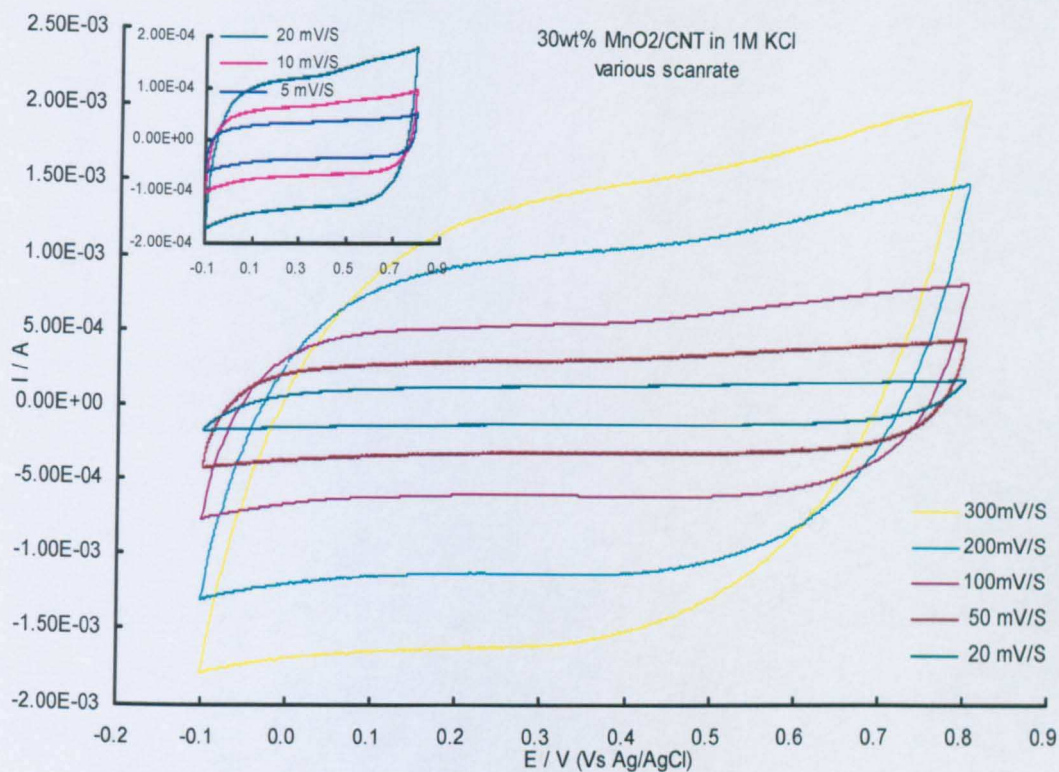
Fig. 7.9. The consequences of the increased of scan rate in CV for 30 wt% MnO_x/CNTs in 1 M KCl: 5 – 300 mV/s.

6. Electrochemical Impedance Spectroscopy Characterisation

The kinetics of the redox processes are further characterised by electrochemical impedance spectroscopy (EIS). The impedance, Z, of different processes has different frequency-dependencies. Therefore, by recording the impedance response between 0.01 Hz and 10000 Hz, it is possible to gain an insight of the kinetics of electrochemical processes of the system.

6.1. Capacitive Behaviour

Principally, the impedance of an ideal capacitor is expressed as:

$$Z_c = Z' - Z'' = R - \frac{1}{j\omega C} \quad \text{Eq. 7.5.}$$

With a zero real component (R=0), an ideal capacitive behaviour is therefore characterised by a straight line vertical to Z' axis in

impedance complex-plane and -Z'' approaches infinity when frequency ω
approaching zero.

The impedance responses of the three types of composites are presented
in complex-plane in Fig. 7.10, Fig. 7.11 and Fig. 7.12. Approximate
straight lines with slopes close to 90°, indicating capacitive behaviour,
can be observed at low frequencies for all the three composites. The
deviation from 90° slope can be observed, particularly with PPy/CNTs,
indicating the non-ideality of the electrode as a capacitor. This
non-ideality of pseudocapacitive behaviour originates from the
inhomogeneity of the electrode, the porosity and roughness, and the
intrinsic potential-dependent Faradaic reaction resistance (Conway,
2005).

Enlarged views of impedance complex-plane plots at high frequencies are
also presented in Fig. 7.10, Fig. 7.11 and Fig. 7.12. The impedance
behaviour at high frequencies give a clear examination on knee frequency
and ohmic resistance. Knee frequency indicates the transfer between
capacitive and diffusive behaviour. In other words, knee frequency
reveals the maximum frequency at which predominantly capacitive behaviour
can be maintained (Hughes et al., 2002). Therefore knee frequency is of
particular interesting in studying the capacitive behaviour of the
composites. More detailed discussion on knee frequency will be given in
section 7.

The uncompensated ohmic resistance is revealed by the intercept on the
Z' axis. Resistances of 4.5 Ω, 14.3 Ω and 19.1 Ω have been recorded with
the PAni/CNTs (Fig. 7.10), PPy/CNTs (Fig. 7.11), and MnO$_x$/CNTs (Fig. 7.12)
systems studied here. However, as will be discussed in Section 10, this
resistance is strongly dependent on the electrolyte concentration and

the resistances recorded here are only valid for the respective electrode

| electrolyte systems.

Usually, a charge-transfer controlled region, appearing as a semi-circle,

or part of a semi-circle, above the Z′ axis in the Complex plane at the

upper limit of the frequency range, can be identified. However, this

region cannot be distinguished with the composites studied here. The

absence of this charge-transfer controlled region in the Impedance

complex-plane plot indicates an inconsequentially small charge transfer

resistance, R_{ct}, and a desirable facile charge-transfer process at the

current collector | electrode material, and electrode material |

electrolyte interfaces.

The linear correlation of Z′ and -Z′′ with a slope close to 1 at high

frequency indicates the diffusion - controlled electrode processes,

dominated by mass transfer on the electrode (Fig. 7.10 b, Fig. 7.11 b

and Fig. 7.12 b). This is then taken over by capacitive behaviour at

frequencies below the knee frequency.
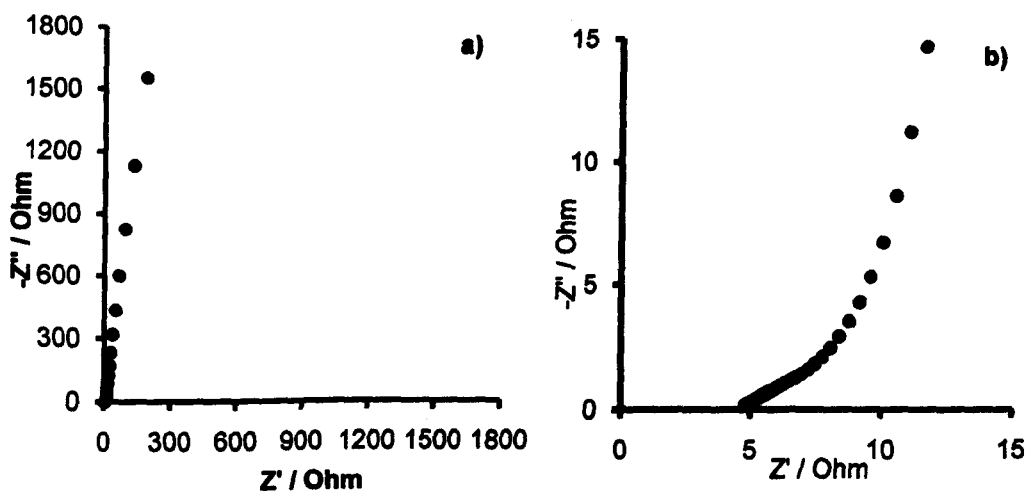
Fig. 7.10. Impedance complex-plane of 80 wt% PAni/CNTs in 1 M H_2SO_4 at

0.0 V with b) enlarged view at high frequencies.
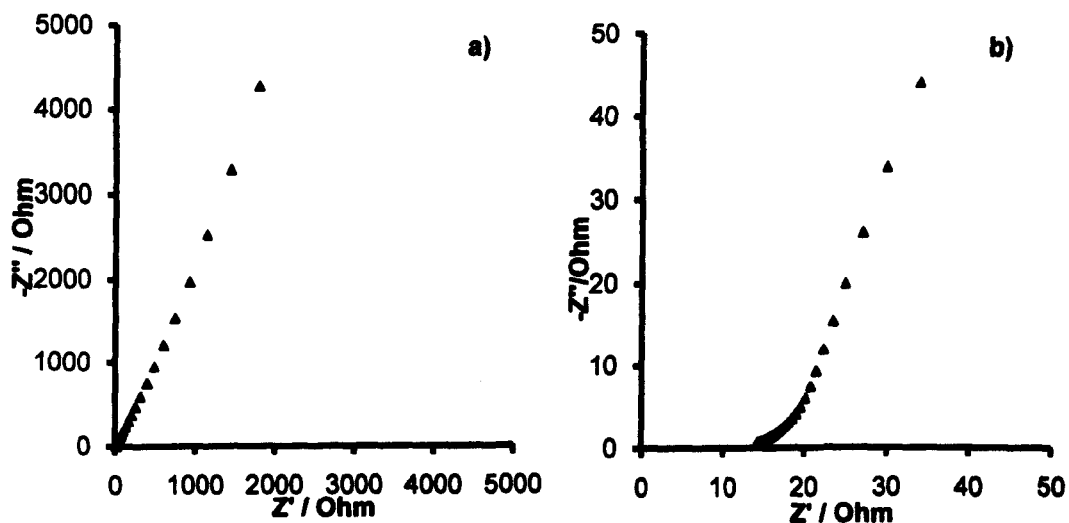
Fig. 7.11. Impedance complex-plane of 80 wt% PPy/CNTs in 0.8 M KCl at

0.0 V with b) enlarged view at high frequencies.
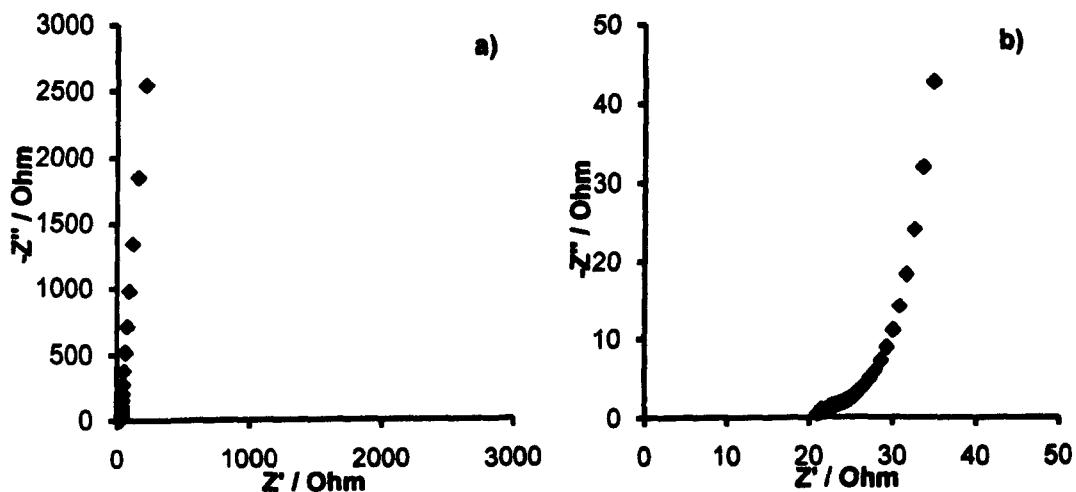
Fig. 7.12. Impedance complex-plane of 30 wt% MnOx/CNTs in 1.0 M KCl at

0.0 V with b) enlarged view at high frequencies.

6.2. The Potential Dependence of Capacitive Behaviour

The potential dependence of the impedance for the three composites is

presented in Fig. 7.13. Clearly, the composites only exhibit capacitive

behaviour in limited potential ranges. For PAni/CNTs, this potential

range is 0.2 V-0.6 V (Fig. 7.13 a); 0.0 V - 0.4 V for PPy/CNTs (Fig. 7.13

b); and 0.0 V – 0.8 V for MnOx/CNTs (Fig. 7.13 c). At potentials outside the potential range, significant deviations from vertical line can be observed. This suggests that other electrochemical processes, rather than capacitive behaviour, have become dominant and the electrode material is not suitable to work at these potentials. For example, at very negative potentials, PAni and PPy are at their non-conducting reduced form (Chen, 1992). The suitable potential ranges identified by EIS are in agreement to the potential window defined by CV in Section 4.

In addition, the enlarged view of impedance at high frequencies are also presented. Constant ohmic resistance, despite of the variation of potential, has been confirmed for all the three composites studied. Also, the absence of the charge-transfer controlled region, represented by a semi-circle or part of a semi-circle on Z' axis, verifies a negligible kinetic barrier to reaction at the applied potentials. Except the extreme potentials at which irreversible electrochemical processes, other than charge-storage processes, take place, e.g. PPy/CNTs at -0.4 V, MnO_x/CNTs at -0.2 V and 1.2 V.

a) PAni/CNT 20wt% in 1 M H_2SO_4

enlarged view

○ 0.8V
▲ 0.6V
● 0.4V
◆ 0.2V
✳ 0.0V
△ -0.2V

b) PPy/CNT 20wt% in 0.8 M KCl

enlarged view

■ 0.6V, 0.8M KCl
▲ 0.4V, 0.8M KCl
◇ 0.2V, 0.8M KCl
✳ 0.0V, 0.8M KCl
○ -0.2V, 0.8M KCl
◆ -0.4V, 0.8M KCl
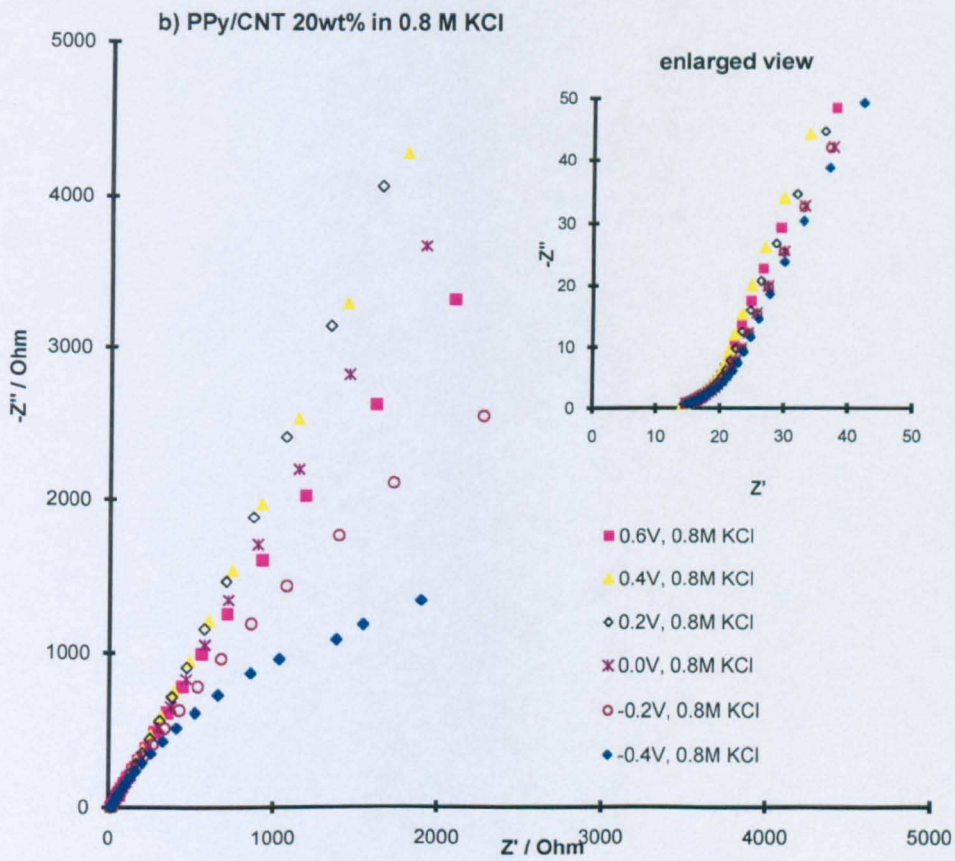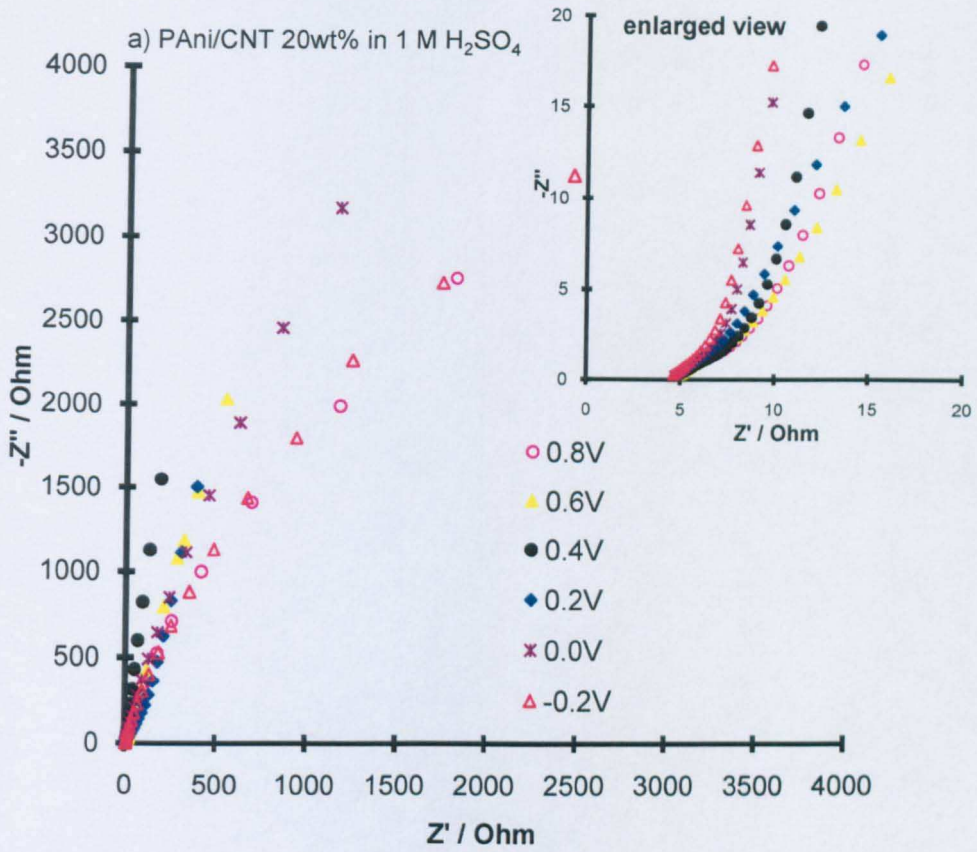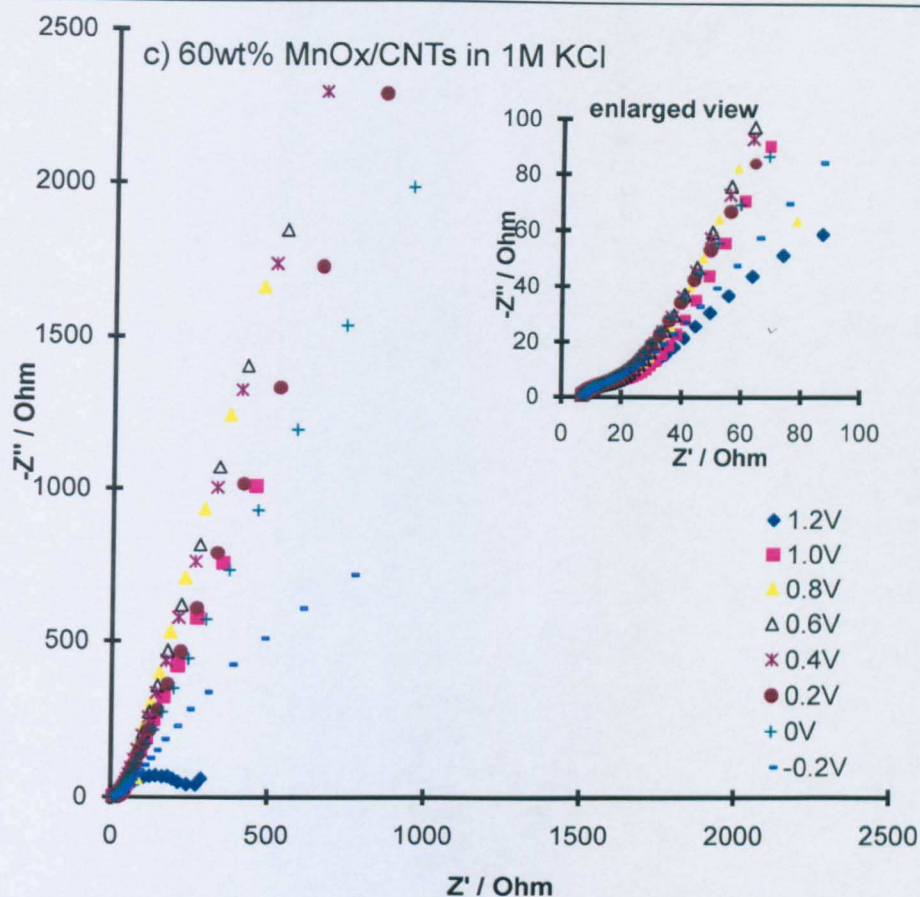
Fig. 7.13. Potential-dependence of impedance, presented in complex-plane with enlarged view at high frequencies at a range of potentials: a) 80 wt% PAni/CNTs; b) 80 wt% PPy/CNTs; and c) 60 wt% MnO$_x$/CNTs.

7. Knee Frequency

For systems with capacitive behaviour, the frequency range between zero and infinity can be divided into three regions: high-frequency region, medium frequency region and low frequency capacitive region (Sugimoto et al., 2005). The high-frequency and medium frequency regions are divided by the knee frequency. The knee frequency indicates the maximum frequency at which predominantly capacitive behaviour can be maintained (Hughes et al., 2002). In other words, the energy stored is not accessible at the frequency above the knee frequency (Niu et al., 1997). Therefore, a high knee frequency is genuinely desired.

Knee frequency can be more conveniently identified in the Admittance plot (Sugimoto et al., 2005). Admittance, Y, is the inverse of impedance. Therefore, the region with higher frequencies is emphasised in Admittance plot.

The Admittance plots, with manifested knee frequencies (as indicated by the arrows), of PAni/CNTs, PPy/CNTs and MnOx/CNTs are presented in Fig. 7.14. The admittances at different potentials are superimposed for each of these composites. It can be observed that the knee frequency varies with the variation of potential, particularly at extreme potentials, e.g. -0.2 V for MnOx/CNTs (Fig. 7.14 c). In addition, the potential dependence of knee frequency and the influence of electrolyte concentration are plotted in Fig. 7.15, Fig. 7.16, and Fig. 7.17 for PAni/CNTs, PPy/CNTs and MnO_x/CNTs composites respectively.

Evidently, electrolyte concentration plays an important role in determining the knee frequency. At a fixed potential, the knee frequency could be 100 times higher in more concentrated electrolytes than in the diluted ones (Fig. 7.15 b, Fig. 7.16 and Fig. 7.17 b). This is explained by the fact that higher electrolyte concentration enhances the electrolyte accessibility and assists diffusion processes; while these are the two key contributing factors in deciding knee frequency (Hughes et al., 2002). The potential dependence of knee frequency, on the other hand, is relatively insignificant. Sugimoto suggests that knee frequency reveals charge-transfer resistance in the electrode system (Sugimoto et al., 2005). However, with the results from this study, it is concluded that knee frequency is rather related to the combined processes of both mass-transfer and charge-transfer.
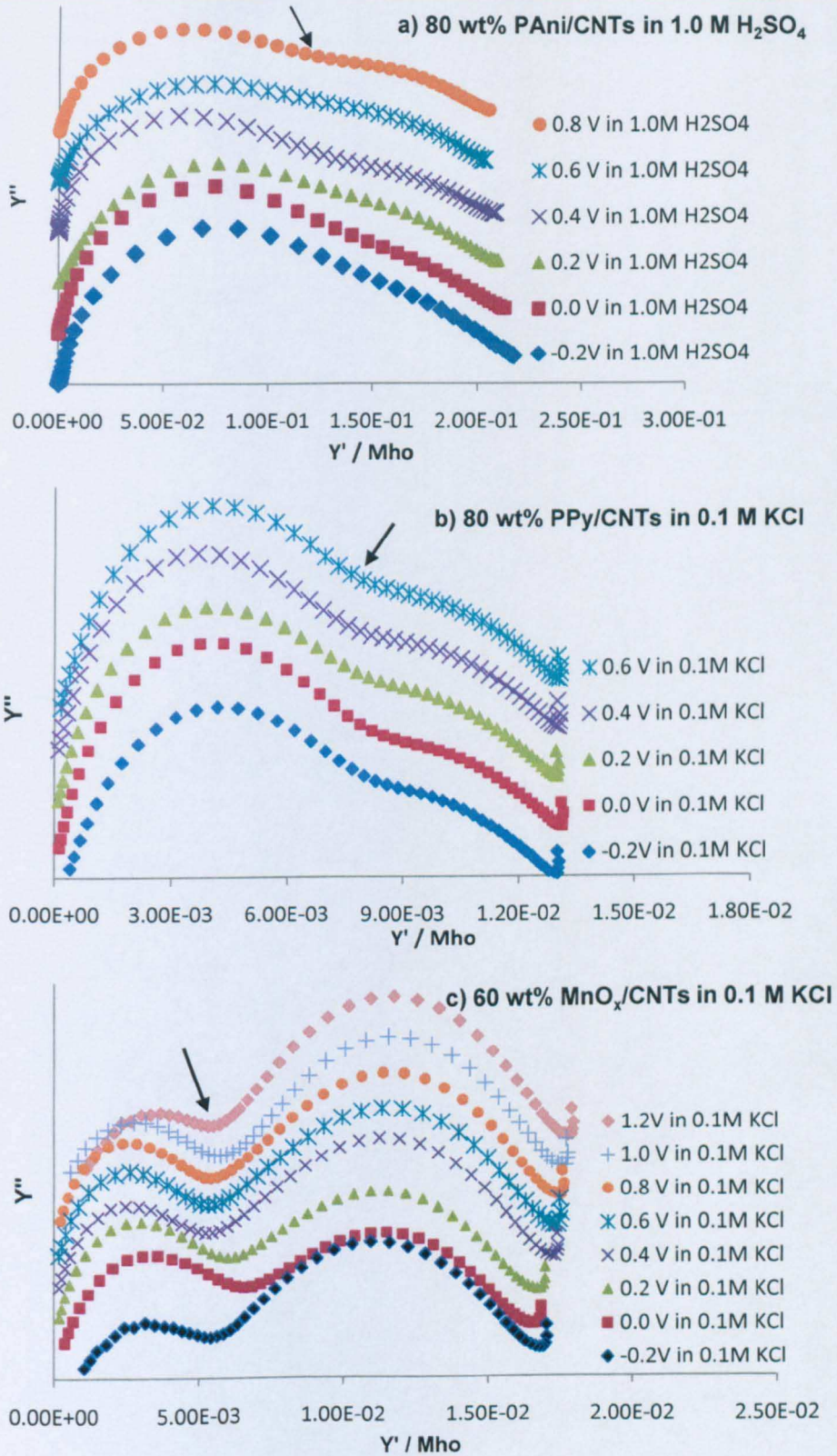
Fig. 7.14. Superimposed admittance of composites over a range of potentials: a) PAni/CNTs; b) PPy/CNTs; c) MnO$_x$/CNTs. (the arrows indicate the knee frequencies)
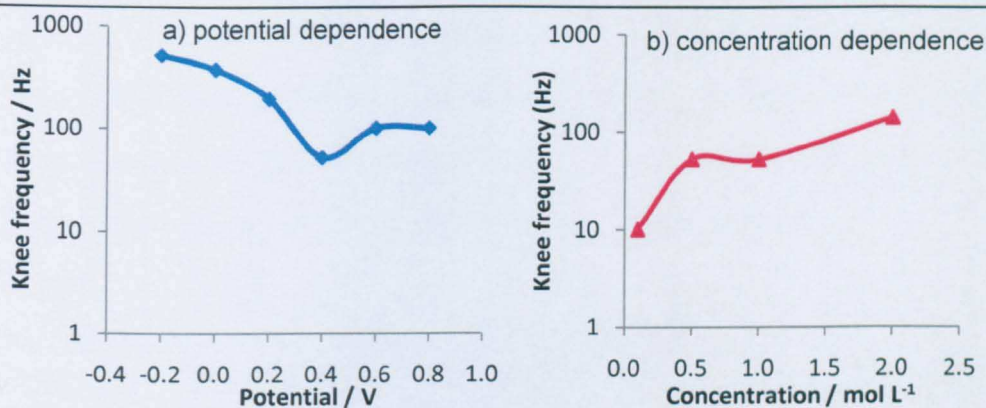
Fig. 7.15. Potential and concentration dependence of knee frequency of 80 wt% PAni/CNTs in H_2SO_4 electrolyte.
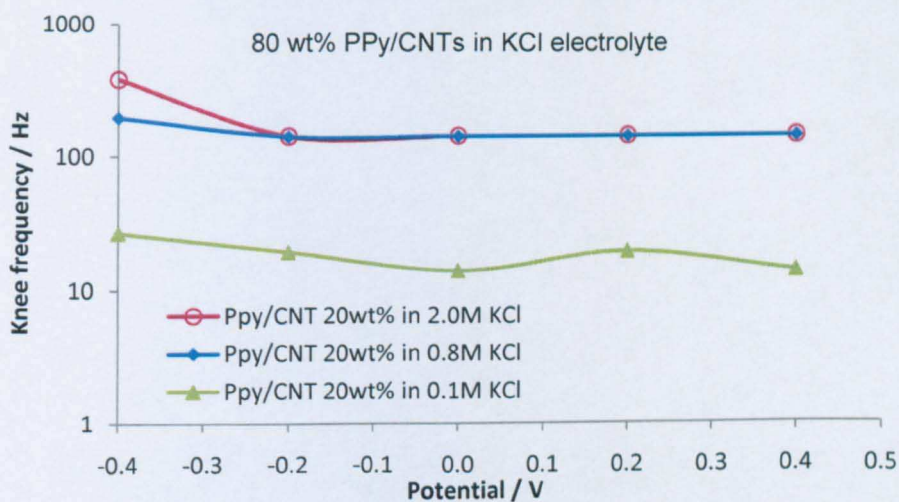
Fig.7.16. Potential dependence of knee frequency of 80 wt% PPy/CNTs in KCl.
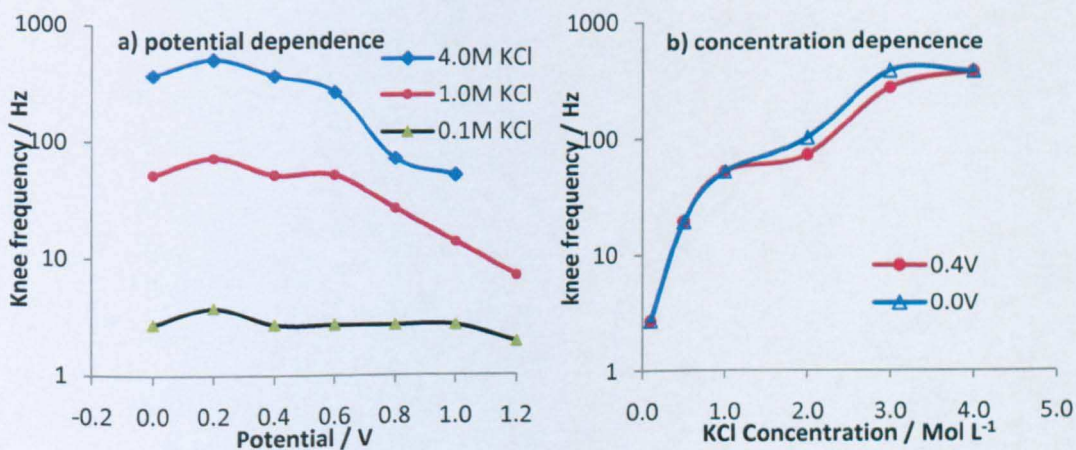
Fig. 7.17. The potential and concentration dependence of knee frequency demonstrated by 60 wt% MnO_x/CNTs in KCl.

Most of the commercial capacitors designed for high power applications have knee frequency <1 Hz (Niu et al., 1997). In this study, all the three composites studied show knee frequency significantly higher than 1 Hz, demonstrating superior charge-storage properties.

8. Frequency Dependence of Impedance data

Bode plot, in which the magnitude of impedance |Z| and phase angle Φ are plotted against frequency on logarithmic scale, is applied to reveal the frequency dependence of the electrochemical processes. Due to the fact that logarithmic scale is used in Bode Plot, the frequency dependence at high frequencies can be presented more clearly.

For an ideal capacitor, C:

$$Z_c' = 0; \qquad\qquad \text{Eq. 7.5.}$$

$$Z_c'' = \frac{1}{j\omega C}; \qquad\qquad \text{Eq. 7.6.}$$

$$|Z| = \sqrt{(Z')^2 + (-Z'')^2} = \frac{1}{\omega C} = \frac{1}{2\pi f C} \qquad \text{Eq. 7.7.}$$

Hence, in its |Z| vs frequency plot with logarithmic scale, a characteristic straight line with slop of -1 can be observed. On the other hand, for a pure resistance, |Z| is independent of frequency and |Z|=R.

The potential and frequency dependence of impedance magnitude |Z|, are shown in Fig. 7.18. Clearly, for both PAni/CNTs and PPy/CNTs, |Z| is almost independent of frequency in the high frequency region, indicating resistive behaviour; This is followed by a straight line with the slop of -1 after transition frequency, indicating capacitive behaviour at lower frequencies (Fig.7.18 a and b). Therefore, it is simplified that the conducting polymer/CNTs composites behaved like a resistor at high frequencies and a capacitor at lower frequencies. In the case of MnOx/CNTs, some complexities arise, since |Z| is a function of frequency even in the high frequency region.
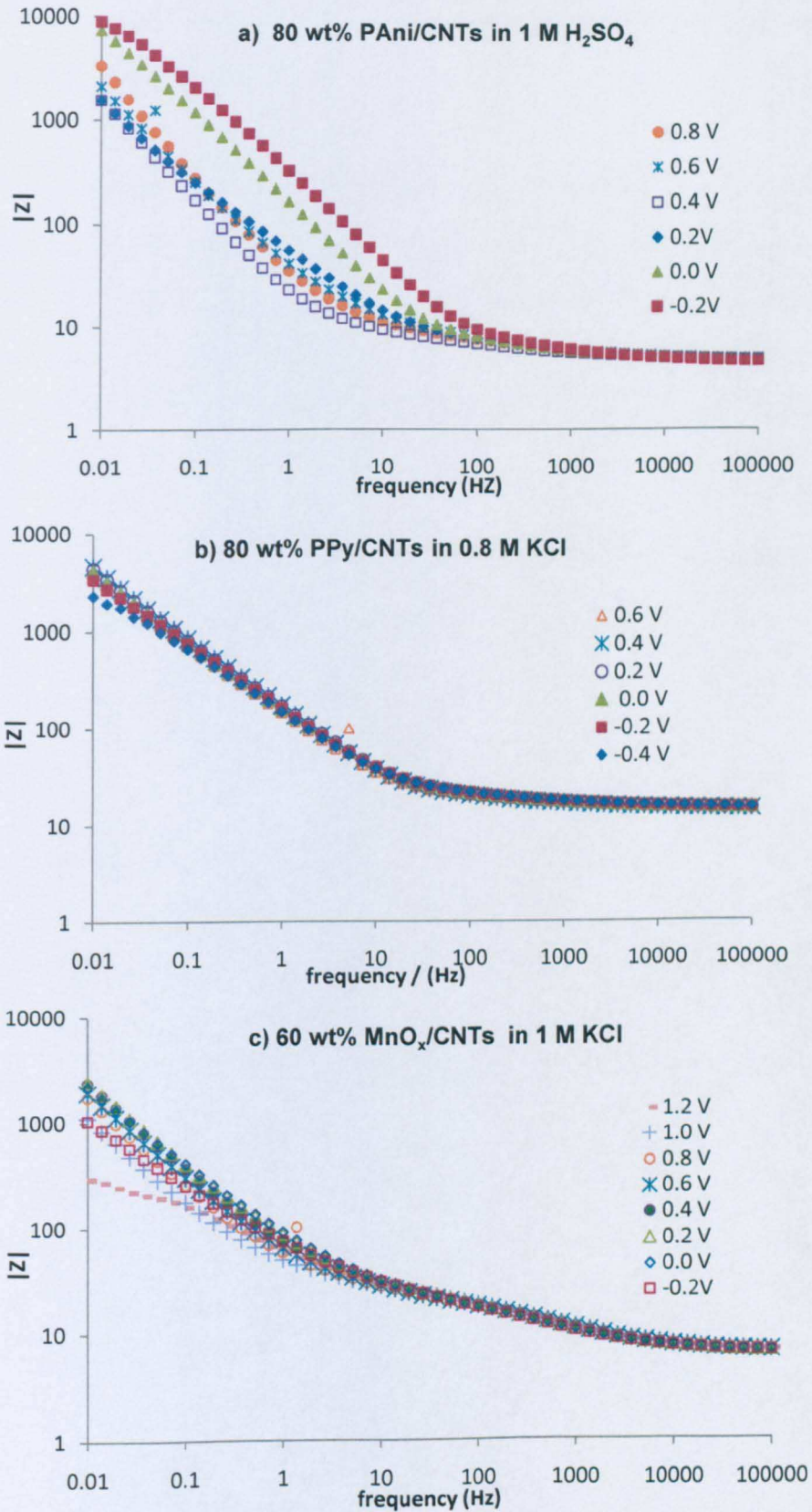
Fig. 7.18. Potential dependence of impedance magnitude |Z|: a) PAni/CNTs;

b) PPy/CNTs; c) MnO$_x$/CNTs.

Still, a characteristic slope of -1 in low frequency region can be observed with MnOx/CNTs (Fig. 7.18 c).

Certain deviations are noticed with the variation of potential. Particularly, at the potentials that are outside the suitable potential range for the electrode materials. Extremely positive or negative potentials are found to aggravate the deviation. Typical examples include 0.6 V and 0.8 V for PAni/CNTs (Fig. 7.18 a), 1.2 V, 1.0 V and -0.2 V for MnO_x/CNTs (Fig. 7.18c).

Fig. 7.19 shows the frequency and potential dependence of phase angle of the three composites. Theoretically, for pure capacitor:

$$I = C \frac{dV}{dt} = \omega C V_0 Sin(\omega t + \frac{\pi}{2}) \qquad \text{Eq. 7.8.}$$

A phase angle of $-\pi/2$ is expected. In reality, however, this is rarely the case. Due to inhomogeneity, porosity and other non-idealities of the electrode, dispersion of capacitance and resistance are usually observed. For pseudocapacitance, the processes of charge transfer will further complicate the situation. Generally, pseudocapacitive behaviour in the low frequency region has a phase angle in the range of -65° to -85°, approaching but can hardly ever reach -90°. The variation of the phase angle at different potentials indicates different electrochemical processes. Again, severe deviations can be observed at the potentials outside the potential window for each of these composites.
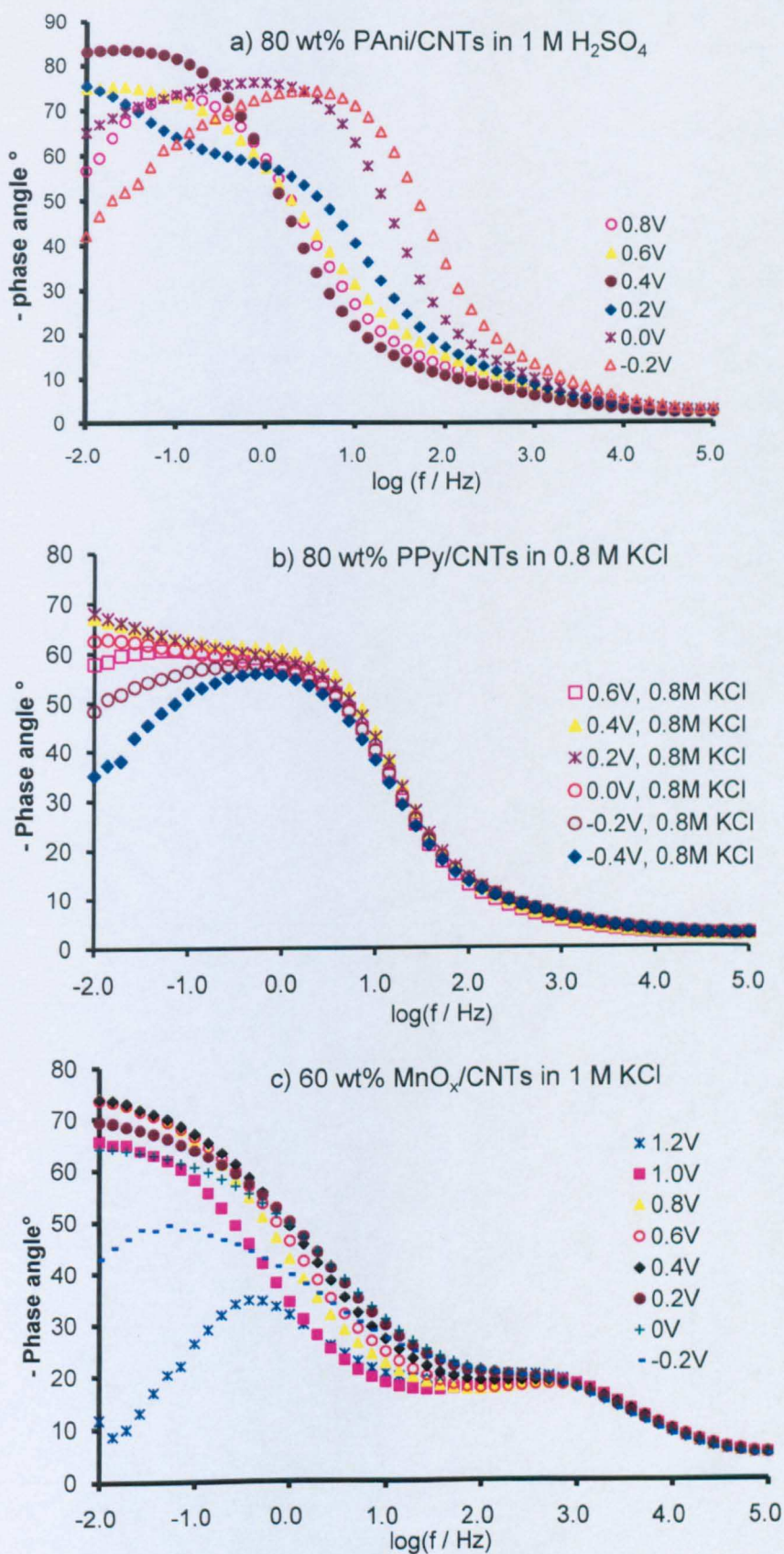
Fig. 7.19. Potential and frequency dependence of phase angle Φ: a) PAni/CNTs; b) PPy/CNTs; c) MnOx/CNTs.

Nevertheless, it is clear that capacitive behaviour will not be observed at phase-angle Φ below $-45°$, at which $|Z''| = |Z'|$ (Sugimoto et al., 2005) (Lufrano and Staiti, 2004). Thus, the frequency at which $\Phi = -45°$ is defined as capacitor response frequency, f_0. The reciprocal of f_0 is defined as characteristic response time, T_0 (Lufrano and Staiti, 2004, Sugimoto et al., 2005). Shorter response time, T_0, indicates a faster response mechanism and thus better pulse power performance (Lufrano and Staiti, 2004). Consequently, shorter response time is desired for power sources. The response time, T_0, for PAni/CNTs in 1 M H_2SO_4, PPy/CNTs in 0.8 M KCl and MnOx/CNTs in 1 M KCl at 0 V are: 0.037 sec, 0.139 sec and 0.56 sec correspondingly. These values of T_0 suggest promising energy-storage capability of the electrode materials. However, similar to knee frequency, T_0 is also strongly dependent on the concentration of electrolyte. Increase the electrolyte concentration can significantly reduce the T_0 to a more favourable value.

9. Effective Capacitance

Since capacitance is the main feature of interests in the electrochemical systems studied in this thesis, plots of effective capacitance are produced to reveal the capacitive behaviour of the systems. Effective capacitance, C_{eff}, provides a means to quantifying the electrode | electrolyte capacitance (Orazem and Tribollet, 2008). For a non-blocking electrochemical system:

$$C_{eff} = -\frac{1}{\omega Z''} = C + \frac{1}{\omega^2 R^2 C} \qquad \text{Eq. 7.9.}$$

The effective capacitances of the three types of composites with frequency variation are presented in Fig. 7.20.

One of the advantages of presenting C_{eff} as function of frequency is that the double layer capacitance can be evaluated at the high frequency limit

(Orazem and Tribollet, 2008). Because at high frequencies, Faradaic current is blocked and all current passes through the double layer capacitance (Orazem and Tribollet, 2008):

$$C_{eff} = \lim_{\omega \to \infty} -\frac{1}{\omega Z''} = C_{dl} \qquad \text{Eq. 7.10.}$$

Therefore, the double-layer capacitances are: 1.02×10^{-5} F, 2.19×10^{-6} F and 2.88×10^{-6} F for PAni/CNTs, PPy/CNTs and MnOx/CNTs systems respectively. Compared with the C_{eff}, obtained at low frequencies, the double layer capacitance makes up 0.05%, 0.307% and 0.034% of the total capacitance for the three systems: PAni/CNTs, PPy/CNTs and MnOx/CNTs correspondingly.

In the lower frequency region, C_{eff} approaches a constant when frequency approaching zero (Fig. 7.20). It is to be noted that the C_{eff} calculated here is the total capacitance from a number of processes, including the double layer charging at the outer Helmholtz plane, irreversible redox reactions, electrosorption of ions onto the electrode surface, and the pseudocapacitance of the material (Sugimoto et al., 2005) (Sugimoto et al., 2004). Consequently, the value of C_{eff} is close to, but not equal to, the actual value of pseudocapacitance in the system.

10. Influence of Electrolyte Concentration

As discussed in Section 7, the electrolyte concentration plays an important part in determining the knee frequency. In this section, the influences of electrolyte concentration upon the electrochemical systems will be further discussed.
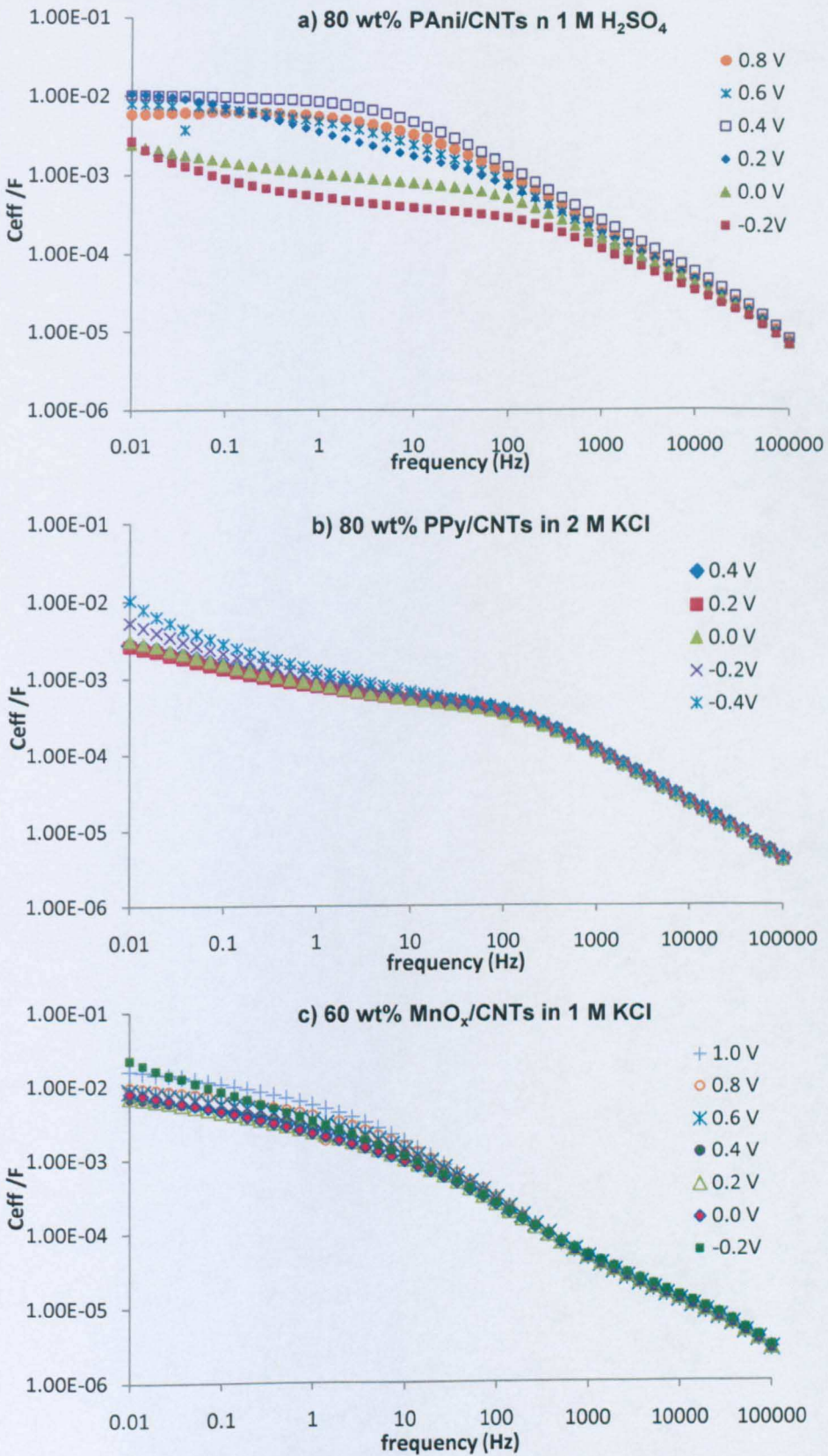
Fig. 7.20. Potential and frequency dependence of effective capacitance:

a) PAni/CNTs; b) PPy/CNTs; c) MnO$_x$/CNTs.

10.1. Ohmic Resistance

The impedance of composites: PAni/CNTs, PPy/CNTs and MnO$_x$/CNTs in electrolytes with various concentrations are presented in Fig. 21, Fig. 7.22 and Fig. 7.23 respectively. As described in Section 6.1, the intercept on Z′ axis is the uncompensated ohmic resistance within the system, which can be identified from the insets of the enlarged view at high frequency. In addition, the ohmic resistance of each system against the concentration variation is plotted in Fig.7.24.

As shown, in all cases ohmic resistance can be significantly higher at low electrolyte concentrations, i.e. 0.1 M. This ohmic resistance decreases upon the increase of electrolyte concentration, particularly between the concentrations of 0.1 M and 0.5 M (Fig.7.24). At concentrations higher than 1.0 M, however, the ohmic resistance gradually reaches a certain value (Fig.7.24).

This can be simply explained by the conductivity change of the electrolyte with the variation of concentration. For strong electrolytes, such as KCl and H$_2$SO$_4$, there is a linear dependence of conductivity on concentration when the electrolyte is diluted. Thus, for a certain electrode in electrolyte: $R \propto \rho \propto \kappa^{-1}$, where R is the ohmic resistance, ρ is the resistivity and κ is the conductivity of the electrolyte. At higher concentrations, however, the dependence of conductivity on concentration is no longer linear, due to the fact that the increased interionic interactions would hinder the ion mobility (Hamann and Vielstich, 1998).
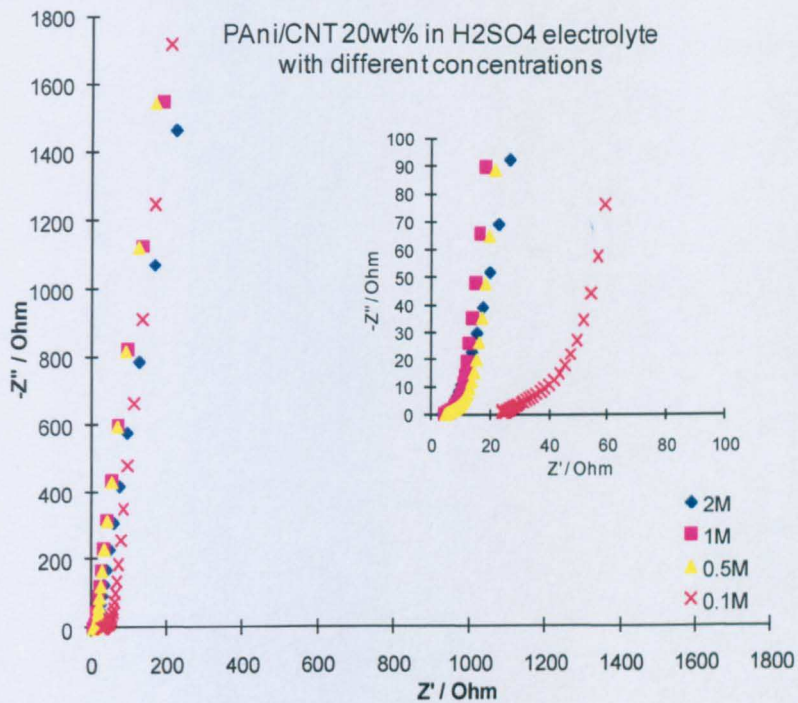
Fig. 7.21. Impedance complex-plane for PAni/CNTs in H_2SO_4 with different

concentrations: 0.1 M ~ 2.0 M.
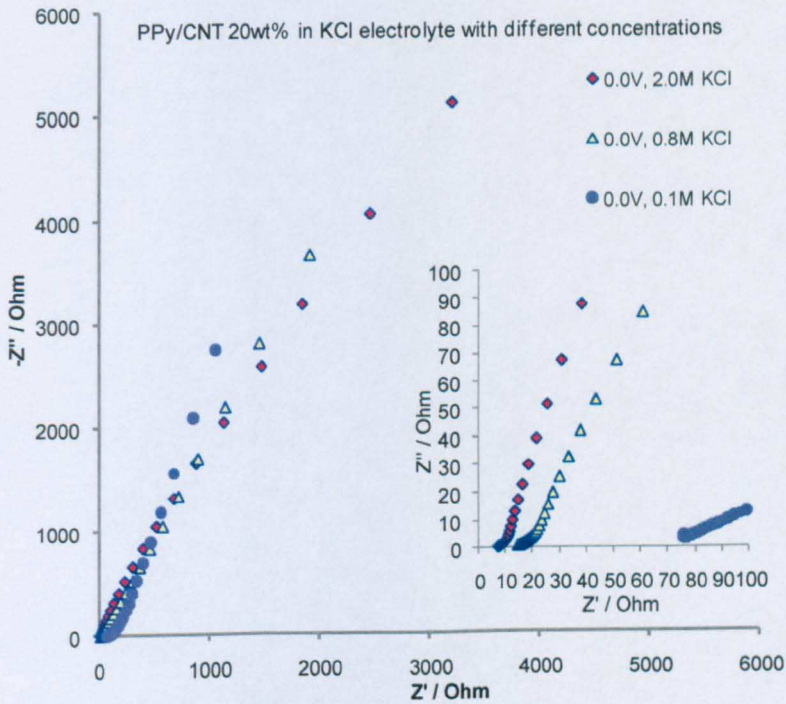
Fig. 7.22. Impedance complex-plane for PPy/CNTs in KCl with different

concentrations: 0.1 M ~ 2.0 M.
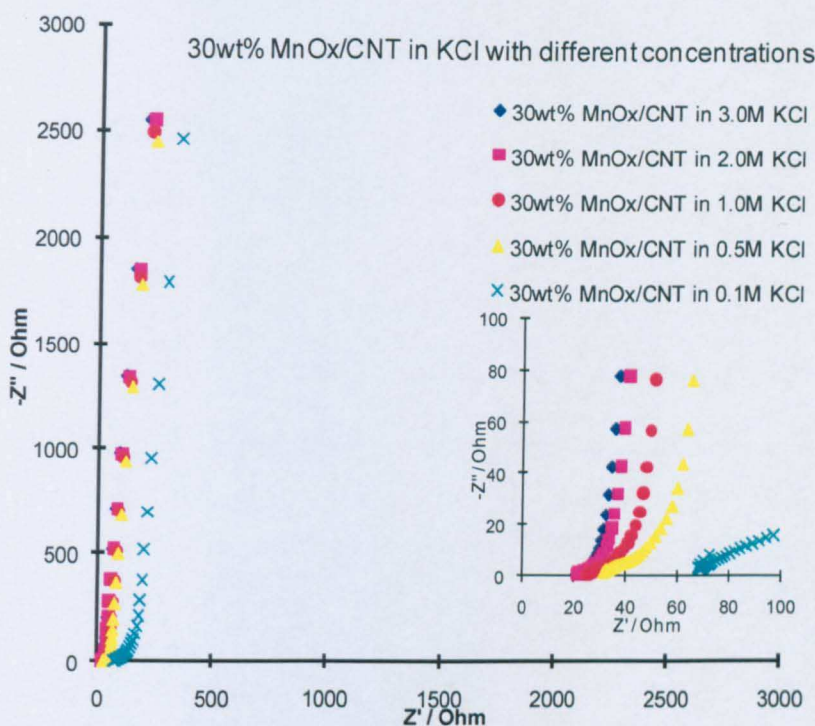
Fig. 7.23. Impedance complex-plane for MnO_x/CNTs in KCl with different
concentrations: 0.1 M ~ 3.0 M.
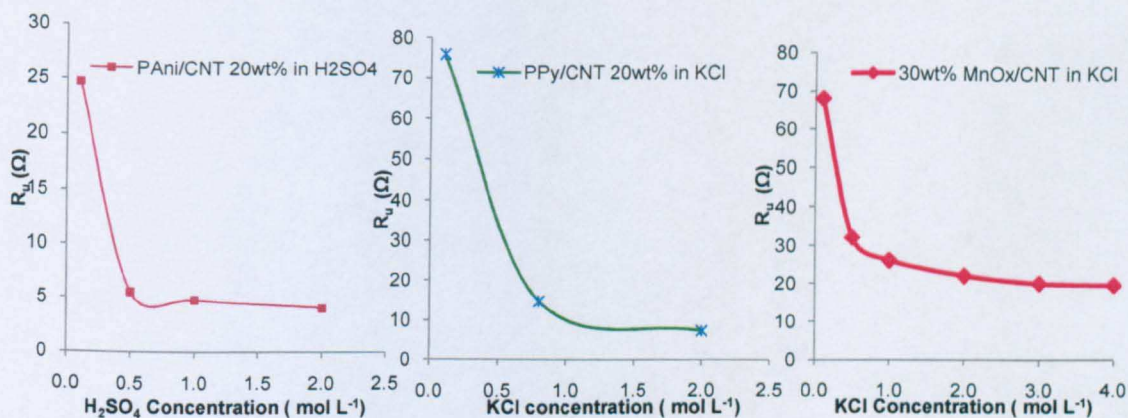
Fig. 7.24. Ohmic resistance *vs* electrolyte concentration of PAni/CNTs,
PPy/CNTs and MnO_x/CNTs.

Once the electrode materials are fabricated into prototype cells and cell
stacks, the ohmic resistances will add up. Large resistance is undesirable
as it causes significant iR drop and impairs power profile of the cell.
Therefore, electrolyte with a concentration higher than 1.0 M is preferred
for cell applications to limit the ohmic resistance.

10.2. Influences on Capacitive Behaviour

The variations of capacitive behaviour with the electrolyte concentrations for the three types of composites studied are presented in Bode Plots (Phase angle) and C_{eff} plots.

As presented in Fig. 7.25, Phase angle curves of the composites in electrolyte of low concentrations show some level of deviation from ideal capacitive behaviour (see Section 8 for discussion on phase angle). Nonetheless, similar phase angle value is achieved regardless the concentration of the electrolyte. Also the phase angle approaches 90° when frequency approaches zero. Except for the case where water is used (concentration approaching zero), the phase angle reaches a value of 30° in low frequency region with 30 wt% MnOx/CNTs (Fig. 7.25 c).

The influence of electrolyte concentration on effective capacitance is presented in Fig. 7.26. For all the three types of composites studied, similar frequency dependence of C_{eff} can be observed in electrolytes with concentration higher than 0.5 M. In addition, the value of C_{eff} when $\omega \rightarrow 0$ is independent of electrolyte concentration. This suggests that the total capacitance of an electrochemical system with a number of processes, is independent of the electrolyte concentration.

Furthermore, following the discussion of knee frequency's dependence on electrolyte concentration in Section 7, it is found out that response frequency, f_0, and response time, T_0, are also strongly dependent on the electrolyte concentration. For example, the variations of T_0 and knee frequency with the variation of electrolyte concentration of MnO_x/CNTs are presented in Table 7.2. Therefore, discussions on the knee frequencies and response time should be carried out in the context of specific electrolyte and its concentration.
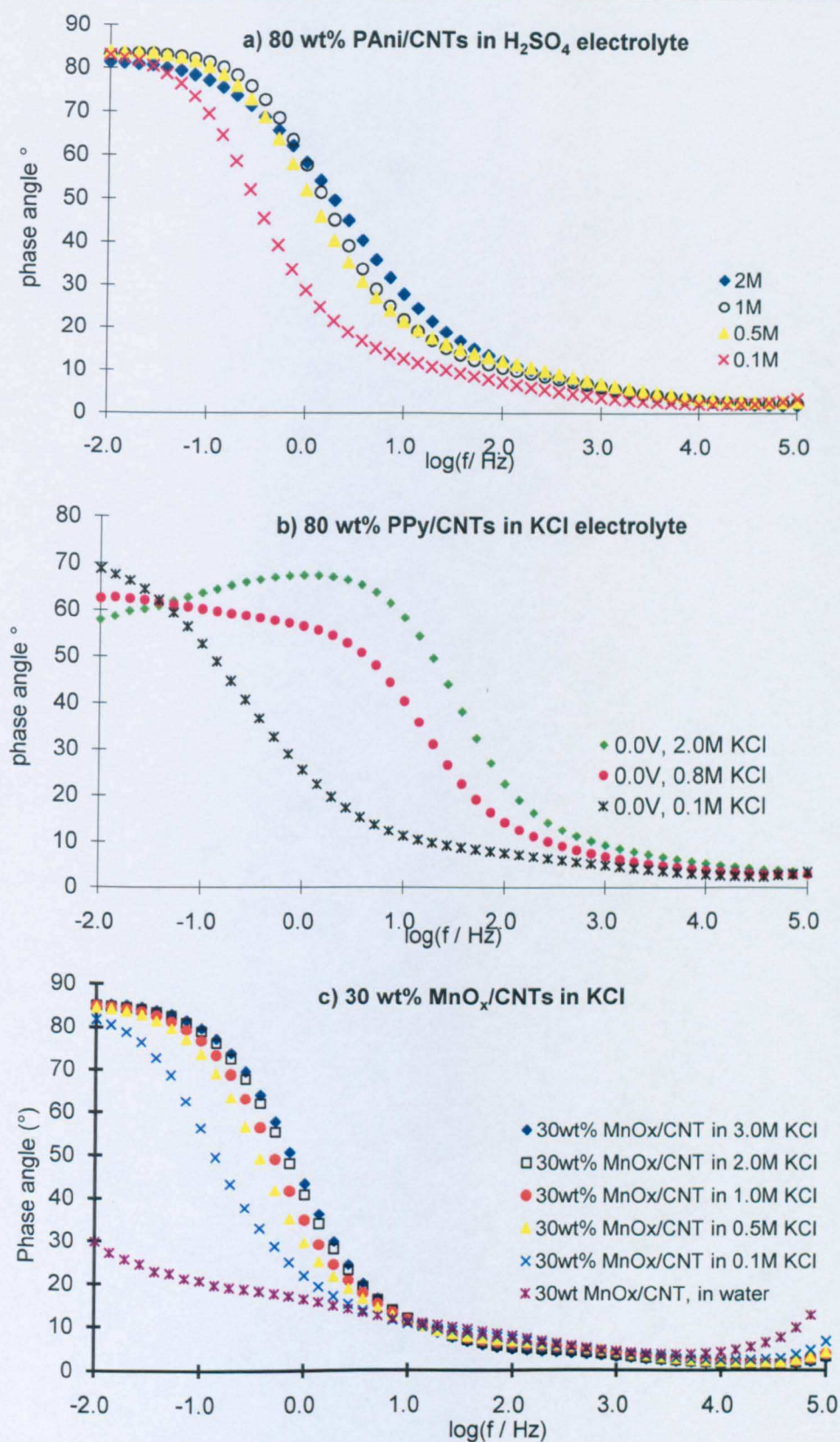
Fig. 7. 25. Variation of Phase angle in electrolyte of different concentrations:

a) PAni/CNTs in H_2SO_4; b) PPy/CNTs in KCl; and c) MnO_x/CNTs in KCl.
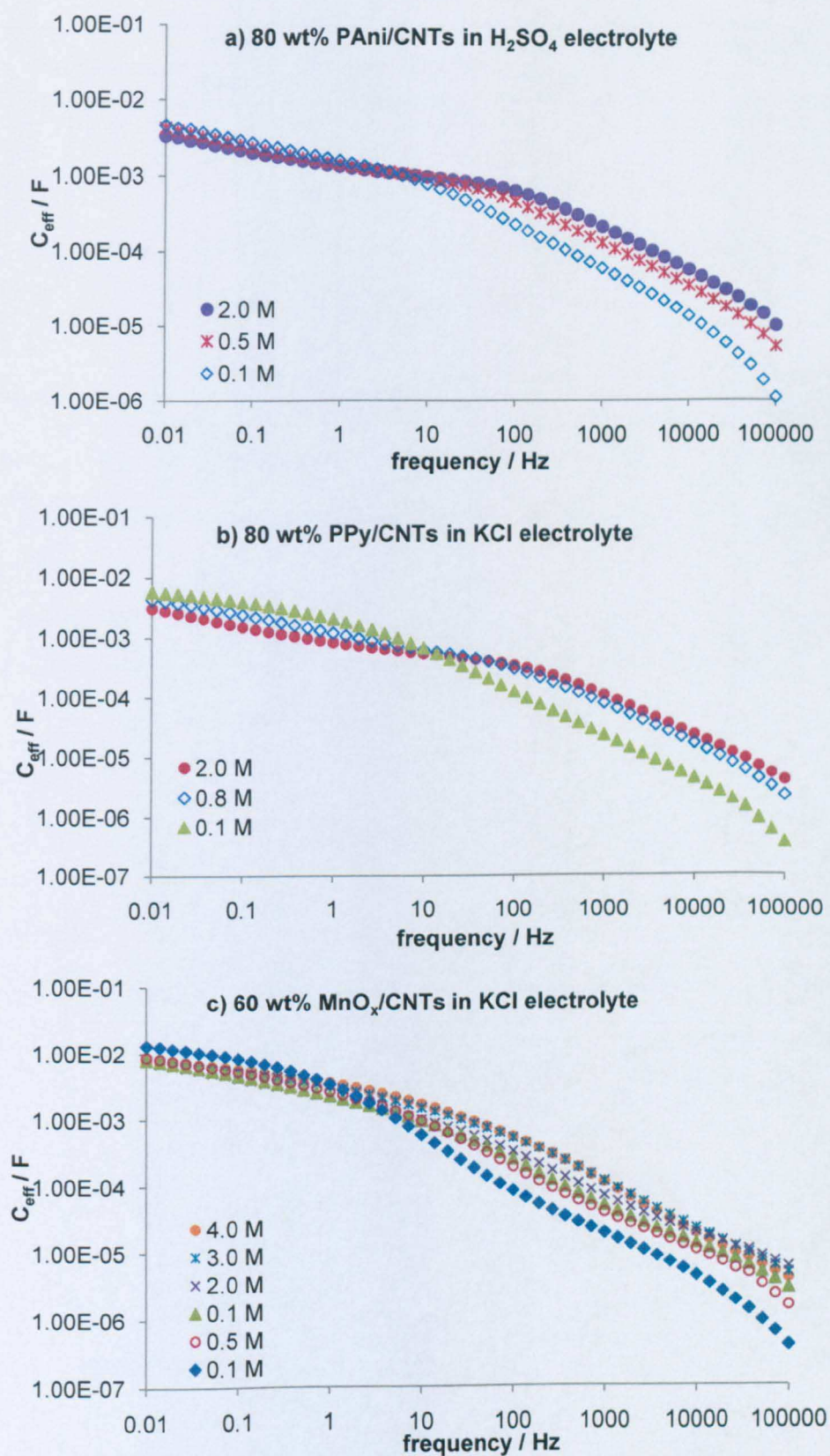
Fig.7.26. Effective capacitance in electrolytes of different concentrations: a) PAni/CNTs in H_2SO_4; b) PPy/CNTs in KCl; and c) MnO_x/CNTs in KCl.

Potential	Electrolyte concentration	f_0 (Hz)	T_0 (sec)	Knee frequency (Hz)
0.0 V	0.1 M	0.0518	19.31	2.683
	0.5M	0.518	1.93	19.31
	1.0 M	1.8	0.56	72
	2.0 M	5.18	0.19	100
0.4 V	0.1 M	0.086	11.63	1.931
	0.5M	0.518	1.93	19.31
	1.0 M	1.39	0.72	37.3
	2.0 M	3.73	0.27	100

Table 7.2. The response time and knee frequency and of 60 wt% MnO_x/CNTs in KCl electrolyte with various electrolyte concentrations.

11. Cycling Stability

Good cycling stability is essential for electrode materials for power source, as the equipment is likely to be charged and discharged for thousands of times during its life-time. Fig. 7.27 compares the cycling stability of pure PAni and PAni/CNTs composite. The decrease of CV currents when increasing the cycle number is plotted in Fig. 7.28. After the 1st 500 cycles, the PAni/CNTs composites reach a stable phase and its capacitance is maintained at a constant level to 4000 cycles. On the other side, the current response of pure PAni dwindles away during the cycling test, particularly, after 1000 cycles. It can be seen that the cycling stability of the conducting polymers can be substantially improved by the addition of CNTs in the composites. The oxidation and reduction of conducting polymers involve the injection and withdraw of ions to and from the polymer chain. The repetitive ion inserting and withdrawing lead to physical damages on the polymer chains inevitably. By introducing CNTs into the polymer during polymerisation, much enhanced stability can be achieved. CNTs, with their outstanding mechanical strength, act as a backbone to provide sufficient support.
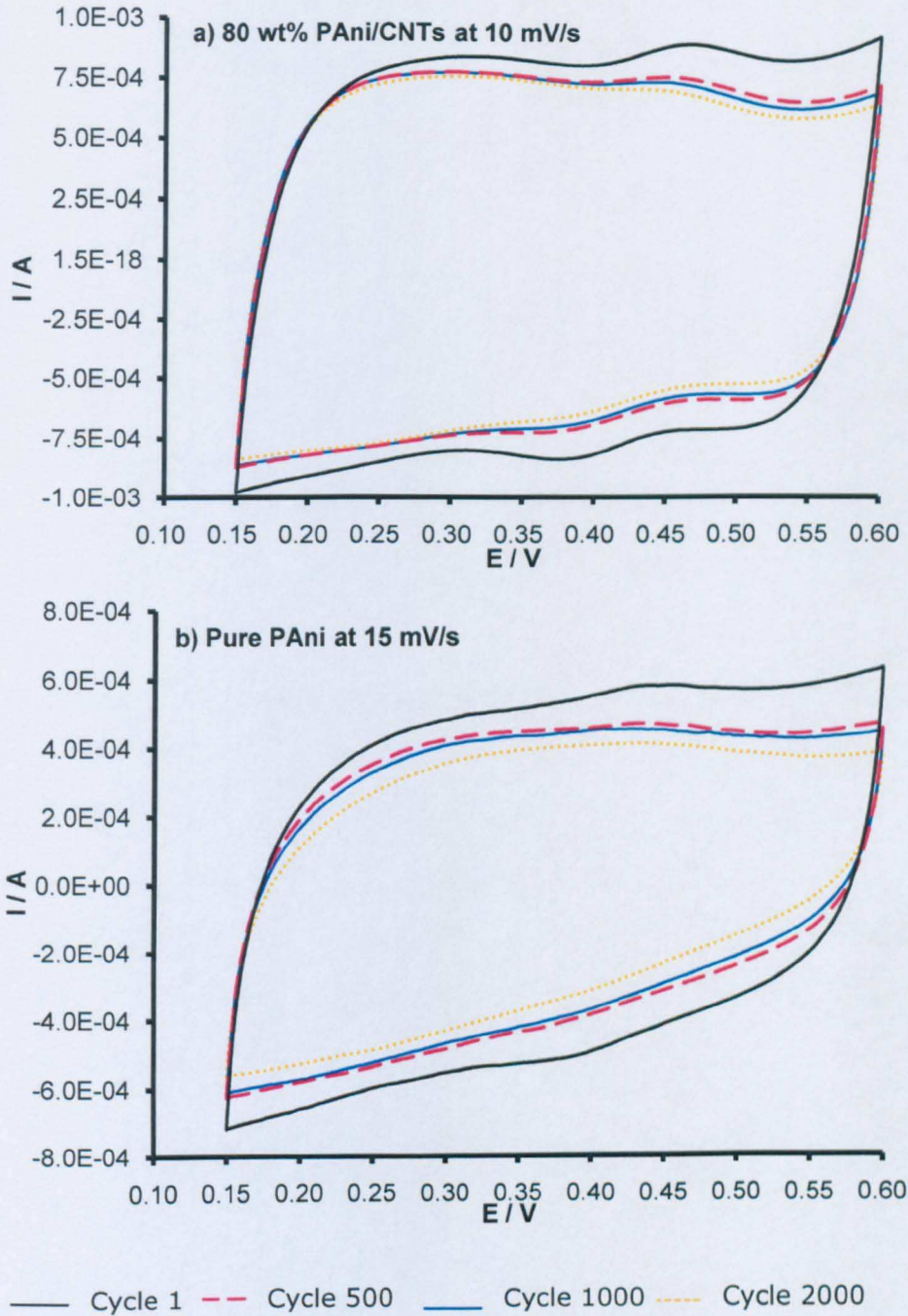
Fig. 7.27. Comparison of the stability of pure PAni and PAni/CNTs composite during 2000 cycling tests in 1 M H_2SO_4: a) 80 wt% PAni/CNTs composite; b) Pure PAni.
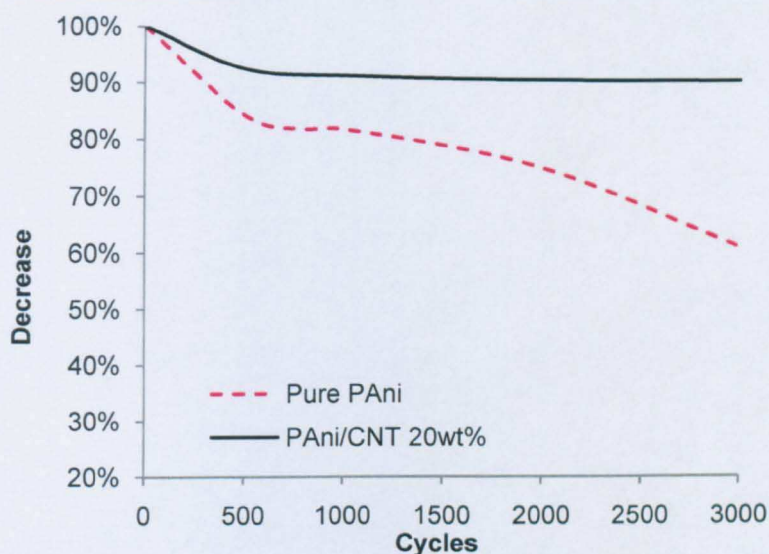
Fig. 7.28. Cycling stability of pure PAni and PAni/CNTs.

The stabilities of polypyrrole and PPy/CNTs composites are illustrated in Fig.7.29. With a potential window of 0.0 - 0.6 V in 1 M H_2SO_4, PPy is reasonably stable during the 1000 cycles of scans. As shown in Fig. 7.29 b) and c), the addition of CNTs levels the current response of PPy, resulting in a preferable capacitive behaviour. However, the CNTs content in the composites does not significantly alter the electrochemical properties or stability of polypyrrole.

The stability of MnOx/CNTs composites is presented in Fig. 7.30. Manganese oxides, like many other transition metal oxides, have good stability through repetitive cycling. As shown in Fig. 7.30, little decrease is observed with MnO_x/CNTs composite during 9000 cycles of scans between 0.0 V and 0.85 V in aqueous electrolyte.
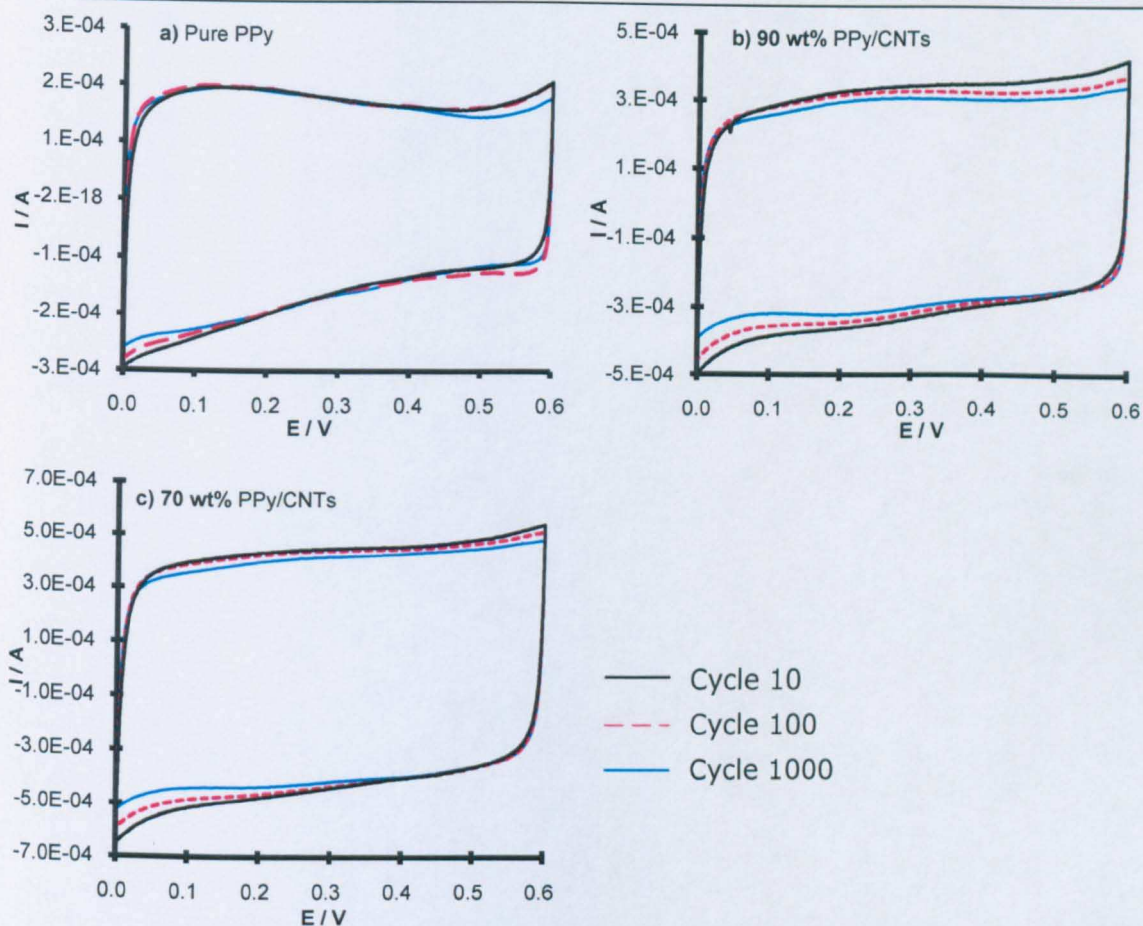
Fig. 7.29. Stability of PPy and PPy/CNTs composites by Cyclic Voltammetry tests, in 1 M H_2SO_4 at 50 mV/s.

To conclude, the electrode materials used in this thesis, i.e. PAni/CNTs, PPy/CNTs and MnOx/CNTs, show good stability through cycling in their optimum potential windows. The CNTs act as backbone in the composites with conducting polymer and significantly enhances the stability through cycling. Moreover, CNTs assist the electron and ion transfer within the electrode materials, thus level the current response and lead to a more desirable capacitive performance. On the other hand, increasing the content of CNTs in the composites does not substantially alter the electrochemical behaviour of the composites; to achieve the maximum specific capacitance from conducting polymer and manganese oxides with sufficient mechanical support from CNTs become the prime aim.
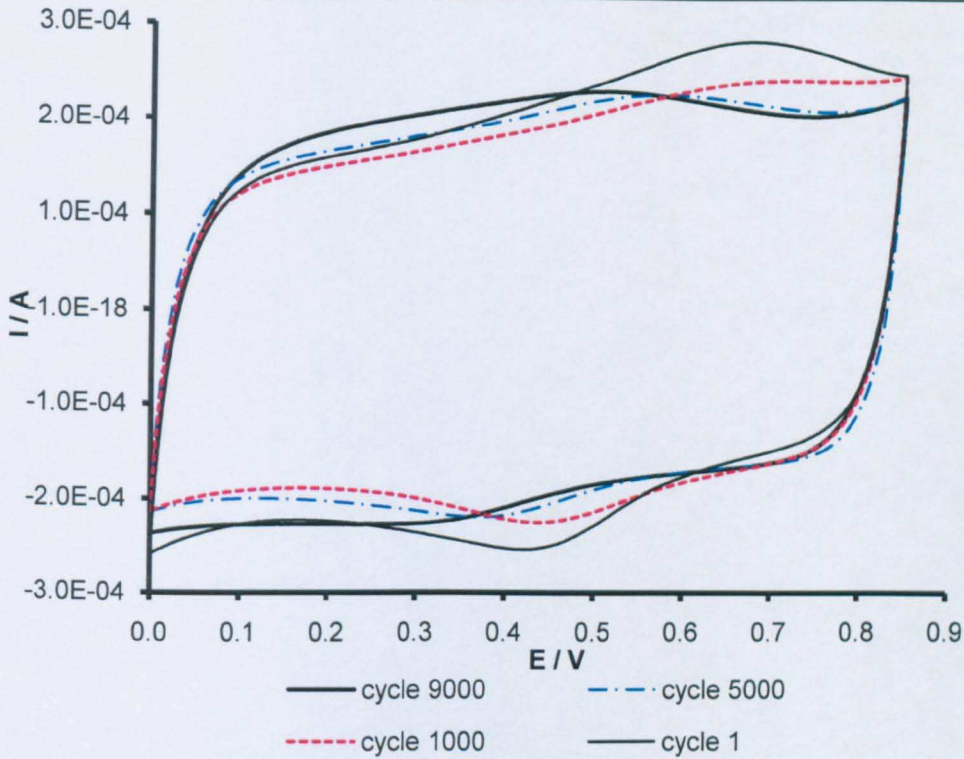
Fig. 7.30. 9000 cycles cycling test of 60 wt% MnO_x/CNTs in 0.1 M K_2SO_4 at 10 mV/s.

12. Summary

Promising capacitive behaviour of the synthesised composites have been proved by both cyclic voltammetry and electrochemical impedance spectroscopy. Appropriate operational potential window and scan rate have been identified for each of the composites to ensure desirable capacitive electrochemical behaviour with good reversibility. For each system, different kinetics with different characteristic time frames, including ohmic polarisation and concentration polarisation, have been revealed in impedance complex-plane plots. Some characteristic parameters for charge-storage applications, i.e. knee frequency, f_0, and T_0, have been found to be strongly dependent on the electrolyte concentration. In general, electrolyte with higher concentration provides higher ion-mobility and accessibility which facilitates both diffusion and charge-transfer processes. Finally, excellent cycling stability of the

composites has been demonstrated. It is found out that CNTs act as backbone in the composites with conducting polymer and they significantly enhance the stability through cycling. Moreover, CNTs assist the electron and ion transfer within the electrode materials, thus level the current response and lead to a more desirable capacitive performance.

To conclude, the electrochemical characterisations given in this chapter have confirmed the desirable capacitive behaviour of the composites. These composites will be fabricated into prototype cells for further tests in Chapter 8.

1. Introduction

Based on the promising results from qualitative characterisations carried out on the composites in Chapter 7, this Chapter studies the performances of the composites in prototype cells. Often, electrode materials show different electrochemical behaviours in cells (Frackowiak et al., 2006). Complication arises from many contributing factors, including: cell configuration, the performance of the counter electrode, the thickness of the loading, electrolyte, separator thickness and resistance, etc. Therefore, prototypes of two-electrode cells are built to conduct quantitative investigations on the performances of these electrode materials in working conditions. Furthermore, the performances of electrode materials in different cell configurations: symmetrical, asymmetrical and cell-stacks, are compared to optimise the operational conditions and achieve enhanced cell performance.

2. Construction of the Prototype Supercapacitors

2.1. Symmetrical Cell

Traditionally, electrochemical capacitors are structured symmetrically. This is based on a simple fact that the achievable cell capacitance is limited by the smaller value of the capacitance of each electrode (Eq. 8.1). Therefore, the maximum cell capacitance is to be achieved when the two electrodes have identical capacitance.

$$\frac{1}{C_{cell}} = \frac{1}{C_{positive}} + \frac{1}{C_{negative}} \qquad \text{Eq. 8.1.}$$

In addition, energy density (Eq.8.2) and power density (Eq.8.3) are two substantial characterisations for supercapacitors for their real world applications:

$$E = \frac{1}{2} C_m V_{max}^2 \qquad \text{Eq. 8.2.}$$

$$P = I V_{max} \qquad \text{Eq. 8.3.}$$

where C_m is the mass specific capacitance; V is the operating voltage

window.

Essential understandings of electrode performances can be obtained in this cell configuration. This is also the most commonly employed cell configuration for electric double-layer supercapacitors.
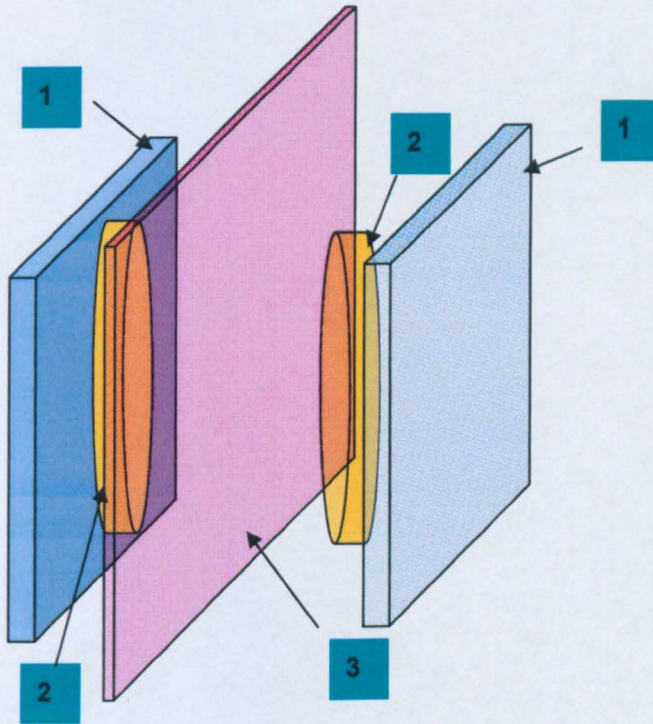
1. Current Collector;   2. Electrode pellet; 3. Separator with

electrolyte

Fig. 8.1. Schematic view of a sandwich-type supercapacitor.

2.2. Asymmetrical Cell

For pseudocapacitive electrochemical capacitors, the symmetrical cell configuration imposes a severe limitation on the cell voltage. Since each of the electrode material has positive and negative potential limits for reversible potential scans (see Chapter 7.4), the maximum achievable cell voltage is restricted to prevent overoxidation and overreduction of the electrode material. Hence, asymmetrical cell structure employing materials with different electrochemical properties for positive and negative electrodes has been proposed (Hong et al., 2002). A prominent

advantage of this asymmetrical cell system is the enlarged operating

voltage window, which noticeably increases the value of energy and power

performance (Eq. 8.2 and Eq. 8.3). In aqueous system, this is of particular

interest as it allows the electrochemical capacitor to operate at a

voltage window wider than the water decomposition voltage of 1.2 V. This

can be realised by choosing positive and negative electrode materials

with high overpotentials for hydrogen or oxygen gas evolutions (Ng et

al., 2008). One particular issue with asymmetrical supercapacitors is

nonlinear charge-discharge (Burke, 2000). Nevertheless encouraging

results from various research groups have indicated that this can be

avoided by appropriate cell fabrication.

2.3. Cell Stack with Bipolar Electrodes

Higher operational cell voltage can be achieved simply by stacking the

prototype cells together. As for cells in series, the total stack voltage

is the sum of the voltages of individual cells. Fig. 8.2 gives a schematic

view of the configuration of a cell stack. One of the advantages of this

stack structure is that it can effectively remove the connection

resistance between individual cells (Ng et al., 2009). Any internal

resistance will contribute to the iR drop of the cell stack and therefore

should be eliminated if possible. By employing this stack structure; cell

voltage can be easily adjusted to meet the demands from end users.

1. Current Collector;   2. Electrode pellet;
3. Separator with electrolyte; 4. Bipolar plate.
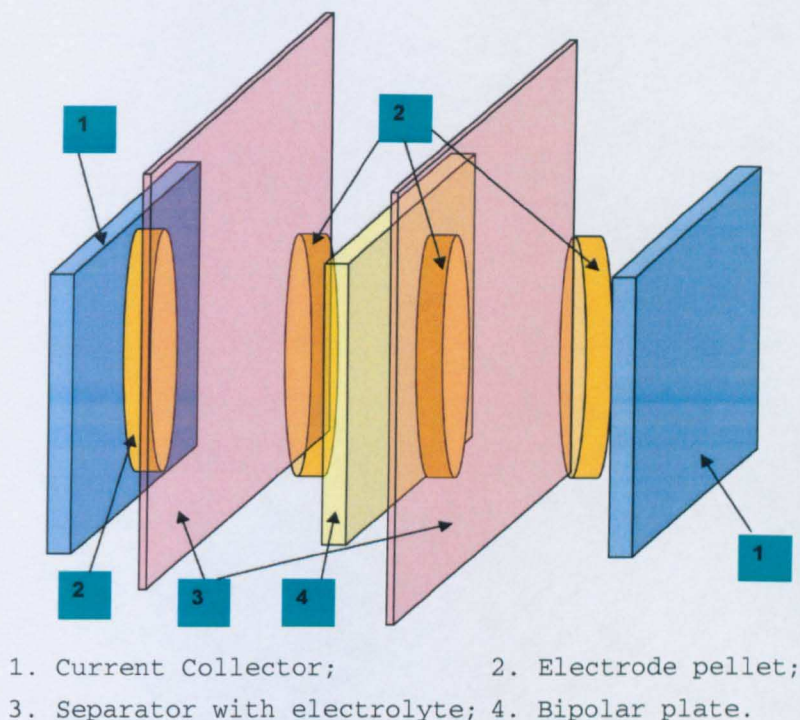
Fig. 8.2. Schematic view of a cell stack.

3. Cell with Carbon Materials as Electrodes

Due to the fact that all the electrodes fabricated contain carbon materials, either as conducting agent or in the composites, the electrochemical properties of the carbon materials, including aligned carbon nanotubes (ALCNTs), carbon nanotubes (CNTs), activated carbon (Mornarch 1300®), are characterised.

The electrochemical behaviour of these symmetrical prototype cells with carbon materials as electrodes were characterised with CV, as presented in Fig.8.3. The investigations were performed in 2.0 M KCl at scan rate of 10 mV per second.
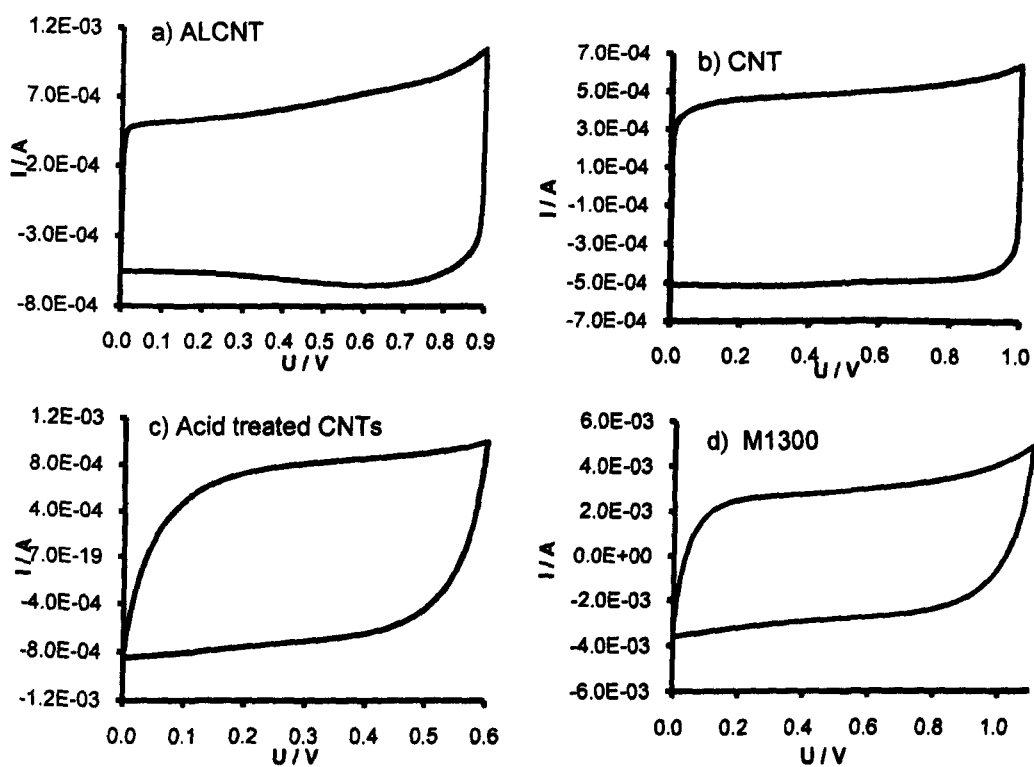
Fig. 8.3. Cells made of carbon materials characterised with CV: a) aligned carbon nanotubes; b) carbon nanotubes; c) acid treated carbon nanotubes; and d) Monarch 1300. (scan rate 10 mV/s in 2.0 M KCl).

Carbon Materials	Loading (mg per electrode)	Electrolyte	Cell capacitance (mF)	C_M (F/g)
ALCNTs	25	2 M KCl	63	5.04
CNTs	15	2 M KCl	68.4	9.12
Acid treated CNTs	6	2 M KCl	76	25.3
M1300	10	2 M KCl	285	57

Table 8.1. Cell capacitance of carbon materials.

The cell capacitance listed in Table 8.1 is calculated according to:

$$C = \frac{\Delta Q}{\Delta V} = \frac{\frac{\Delta Q}{\Delta t}}{\frac{\Delta V}{\Delta t}} = \frac{I}{\upsilon}$$ Eq. 8.4.

Where I is the current and υ is the scan rate.

Specific capacitance is calculated according to:

$$C_F = \frac{C_{electrode}(F)}{active \cdot mass(g)} = \frac{2 \times C_{cell}(F)}{active \cdot mass(g)} \qquad \text{Eq. 8.5.}$$

It is to be noted that the specific capacitance of carbon materials calculated here is notably smaller than the values reported in literature(Chen et al., 2000, Frackowiak and Beguin, 2001, Laforgue et al., 2001). For example, the mass specific capacitance reported for CNTs is normally between 30 - 60 F/g. This is likely to be caused by the compact surface structure formed while pressing the materials into electrode pellets. This compact surface structure reduces the ion and electron accessibility in the inner layers of the electrode and decreases amount of utilizable material.

4. Pseudocapacitive Symmetrical Cells

4.1. MnO$_x$/CNTs Cells

4.1.1. 15 wt% MnO$_x$/CNTs Symmetrical Cell

Symmetrical cells were fabricated with 15 wt% MnO$_x$/CNTs composite; each electrode contains 12.75 mg composite and 2.25 mg aligned CNTs as conducting carbon material (the detailed fabrication methods were described in Chapter 6). 2.0 M KCl aqueous solution is employed as electrolyte.

As presented in Fig. 8.4, the rectangular CV demonstrates that the prototype supercapacitor shows excellent capacitive behaviour. Furthermore, this superior capacitive behaviour is maintained at scan rate as high as 200 mV/s.
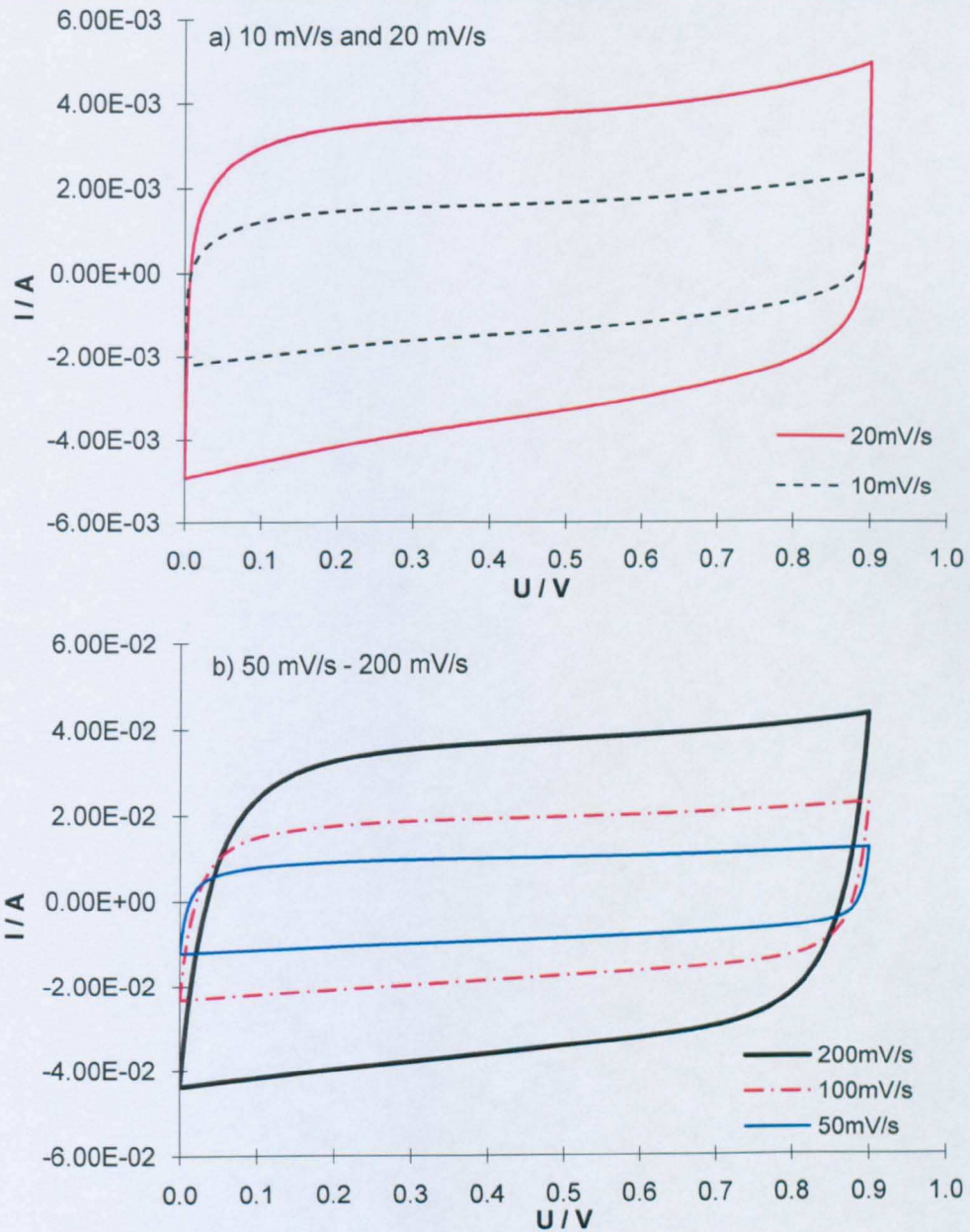
Fig. 8.4. Cyclic voltammetry characterisation of 15 wt% MnO$_x$/CNTs cell

in 2.0 M KCl at various scan rates: 10 mV/s – 200 mV/s.

The cell capacitance can thus be calculated from the CV with Eq. 8.4 and

the specific capacitance (F/g) is calculated with Eq. 8.5. The geometry

capacitance is obtained by:

$$C_{area} = \frac{C_{electrode}(F)}{electrode\ area(cm^2)} = \frac{2 \times C_{cell}(F)}{electrode\ area(cm^2)} \qquad \text{Eq. 8.6.}$$

The capacitance, specific capacitance and geometry capacitance

calculated from different scan rates are presented in Table 8.2. The cell

capacitance remains approximately constant within the scan rates between
10 - 200 mV/s, and the specific capacitance of 15 wt% MnO_x/CNTs in 2.0
M KCl is about 28 F/g on average.

Scan rate	Cell capacitance (mF)	Specific capacitance (F/g)	Geometry capacitance mF/cm^2
10 mV/s	153	23.9	229.3
20 mV/s	180	28.2	270.4
50 mV/s	190	29.8	285.9
100 mV/s	188	29.5	282.7
200 mV/s	181	28.4	272.5

Table 8.2. Specific capacitance of 15 wt% MnO_x/CNTs from cyclic
voltammetry.

The cell capacitance appears to experience a gradual increase of 24 %
with the increase of scan rate from 10 mV/s to 50 mV/s (Table 8.2). This
is due to the system error during the measurement: a fixed potential step
of 0.002 V was applied in all the measurements. For measurement taken
at low scan rate, e.g. 10 mV/s, this potential increment (0.002 V) between
two successive current measurements is too large to obtain an accurate
value of the current response. Therefore, the measurements taken at scan
rate below 50 mV/s do not represent the accurate current response, hence
the capacitance, of the system. It is also observed that the cell
capacitance underwent a small decrease of 4.7 % with the increase of scan
rate between scan rate of 50 mV/s and 200 mV/s (Table 8.2). This decrease,
however, is expected. Due to the existence of mass transfer and electron
transfer barriers, electrode material has an upper limit for scan rate
to exhibit capacitive behaviour. Above this upper limit, the current
response will no longer be proportional to the potential input. Upon
further increasing the scan rate, olive-shaped CV, indicating the
difficulties for redox reactions to proceed at this potential scan rate,

will be observed.

Impedance spectroscopy technique is also applied to characterise the cell

performance. As shown in Fig. 8.5, a semicircle associating the charge

transfer on electrolyte | electrode interface can be observed at high

frequencies limits (Fig. 8.5 b); it is followed by a transient diffusion

region at lower frequencies and finally approaches capacitive behaviour

is identified for this symmetrical cell. The cell capacitance can be

calculated according to Eq. 8.7:

$$C = \frac{1}{2\pi f \times (-Z'')}$$ Eq. 8.7.
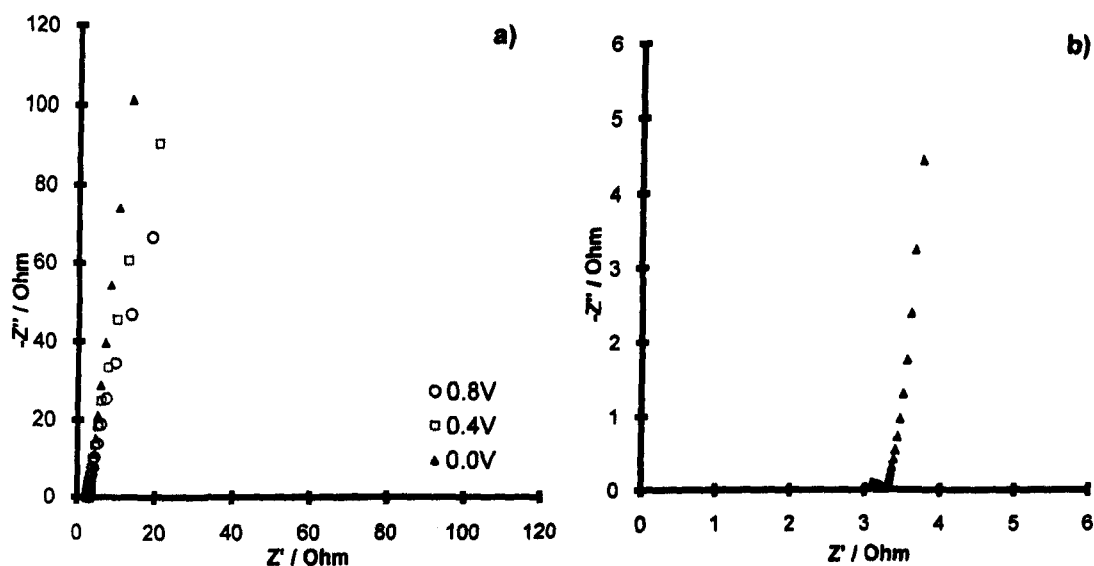
Fig. 8.5. AC Impedance of 15 wt% MnO$_x$/CNTs symmetrical cell in 2.0 M KCl
with enlarged view at high frequencies (b).

The cell capacitance calculated from Eq.8.7 is presented in Table 8.10,

in comparison with other MnO$_x$/CNTs based cells.

The charge transfer resistance, R$_{ct}$, can be calculated from the enlarged

complex-plane impedance plot. As discussed in Chapter 3, R$_{ct}$ = diameter

of the semi-circle on the Z' axis. A detailed discussion on R$_{ct}$ will be

given in 4.1.4.

Last   but   not   least,   Chronopotentiometry,   i.e.   gavanostatic

charge-discharge, is applied to confirm the charge and discharge capability of the cell. The charge-discharge of the cell between 0.0 - 0.8 V at different current densities is presented in Fig. 8.6. The cell capacitance can be calculated from:

$$C = \frac{dQ}{dE} = \frac{i}{dE/dt}$$
                                                   Eq. 8.8

The charge and discharge cell capacitances calculated from Galvanostatic charge-discharge test are presented in Table 8.3.
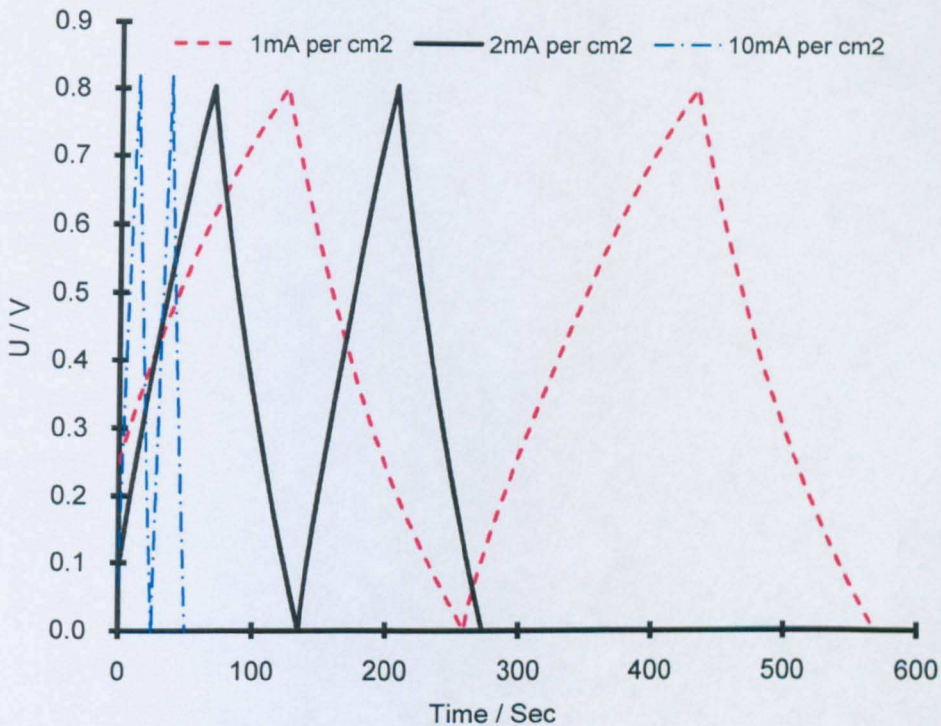
Fig. 8.6. Galvanostatic charge-discharge of the 15 wt% MnO_x/CNTs symmetrical cell.

Noticeably, charge capacitance of the cell is generally larger than the discharge capacitance, indicating a quicker response in charging than in discharging. This observation is in agreement with the CV results (Fig. 8.6), In which the quantity of charge (Q^+) is generally larger than the quantity of discharge (Q^-). This asymmetrical charge-discharge behaviour is an intrinsic property of the electrode material. Also, the difference between the two values decreases with the increase of charge-discharge current density (Table 8.4). In addition, both charging and discharging

capacitance decline at high charge / discharge current density.

Current density	charge time (s)	discharge time (s)	cell C charge (mF)	Cell C discharge (mF)	Specific C Charge (F/g)	Specific C discharge (F/g)	Coulombic efficiency
1mA per cm²	174.3	134.1	257.6	198.2	40.4	31.1	76.94 %
2mA per cm²	67.8	64.6	200.4	190.9	31.4	29.9	95.28 %
10mA per cm²	12.7	12	187.7	177.3	29.4	27.8	94.49 %
20mA per cm²	5.7	5.6	168.5	165.5	26.4	26.0	98.25 %

Table 8.3. Specific capacitance of 15 wt% MnO_x/CNTs from galvanostatic charge-discharge.

In the studies of supercapacitors, discharge capacitance, instead of charge capacitance, is generally taken as the index of the capacitive property. Because the primary concern of their application is to release the electrochemical energy stored while required. The cell capacitance obtained from discharge during galvanostatic tests has similar value with the capacitance calculated from cyclic voltammetry and impedance spectroscopy. The cell capacitance gradually decreases with the increase of charge / discharge current density, indicating that the capacitive behaviour of the prototype cell is rate-limited. This observation confirmed the results from CV characterisations.

For batteries and other energy storage cells, Coulombic efficiency, η, is defined to describe the charge efficiency of the cell. Coulombic efficiency η of a cell can be calculated according to:

$$\eta = \frac{Q_{discharge}}{Q_{charge}} = \frac{It_{discharge}}{It_{charge}} \times 100 \% \qquad \text{Eq. 8.9.}$$

where I is the current density, t_{charge} is the charging time, and $t_{discharge}$

is the discharging time obtained in the Galvanostatic charge-discharge tests.

The coulombic efficiencies of the 15 wt% MnO_x/CNTs symmetrical cell at different charge-discharge current densities are listed in Table 8.4. Good coulombic efficiency, close to 100 %, is obtained with the charge-discharge current density between 2 and 20 mA/cm^2. At 1 mA/cm^2, however, a coulombic efficiency of 76.94 % is recorded. This is in accordance with the deviation from the linear voltage-time relation at exceedingly low current density.

4.1.2. 30 wt% MnO_x/CNTs Symmetrical Cell

The performance of symmetrical cell with 30 wt% MnO_x/CNTs as the electrode material is characterised with CV, AC impedance and Gavanostatic charge-discharge techniques in the similar manner. The results are presented in the Figures and Tables below. More detailed discussion comparing the performance of cells made of different MnO_x/CNTs composites will be given in Section 4.1.4.

Excellent capacitive behaviour has been confirmed for the 30 wt% MnO_x/CNTs symmetrical cell with cyclic voltammetry technique between the scan rates of 5- 100 mV/s, as shown in Fig. 8.7. The cell capacitance, mass specific capacitance and geometry capacitance calculated from CV characterisation are summarised in Table 8.4. Similarly, the cell capacitance increase with the increase of scan rate up to 20 mV/s, due to the system error described in Subsection 4.1.1. Further increasing the scan rate incurs a decrease of the capacitance due to the rate-limit of the capacitive behaviour of the materials.
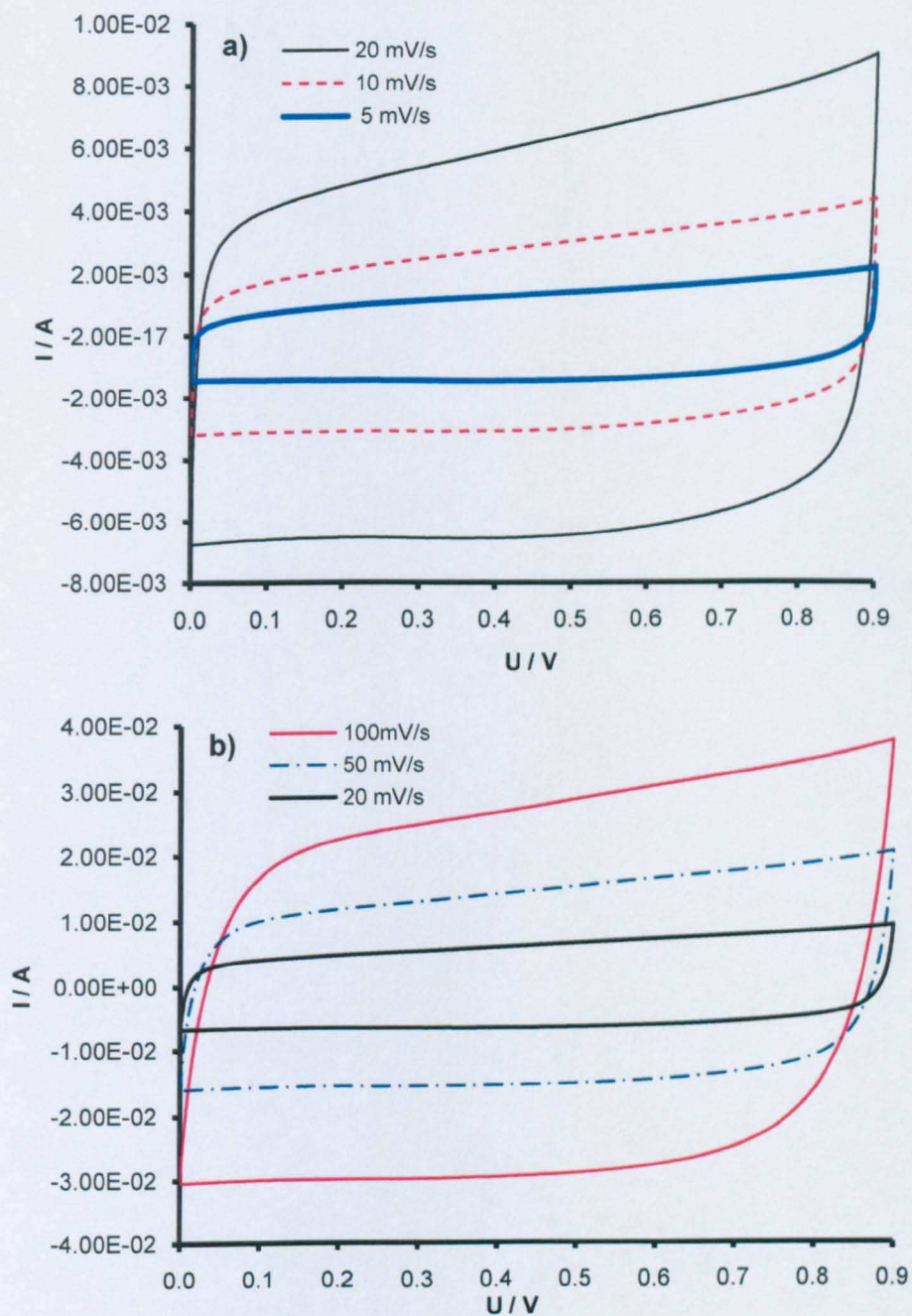
Fig. 8.7. Cyclic Voltammetry of 30 wt% MnO$_x$/CNTs cell in 2.0 M KCl at various scan rates: 5 mV/s – 100 mV/s.

Scanrate	Cell capacitance (mF)	Specific capacitance (F/g)	Geometry capacitance mF/cm^2
5 mV/s	279	43.8	419.5
10 mV/s	298	46.7	448.1
20 mV/s	317.5	49.8	477.4
50 mV/s	301	47.2	452.6
100 mV/s	286	44.9	430.1
200 mV/s	265.5	41.6	399.2

Table 8.4. Specific capacitance of 30 wt% MnO_x/CNTs from cyclic

voltammetry.
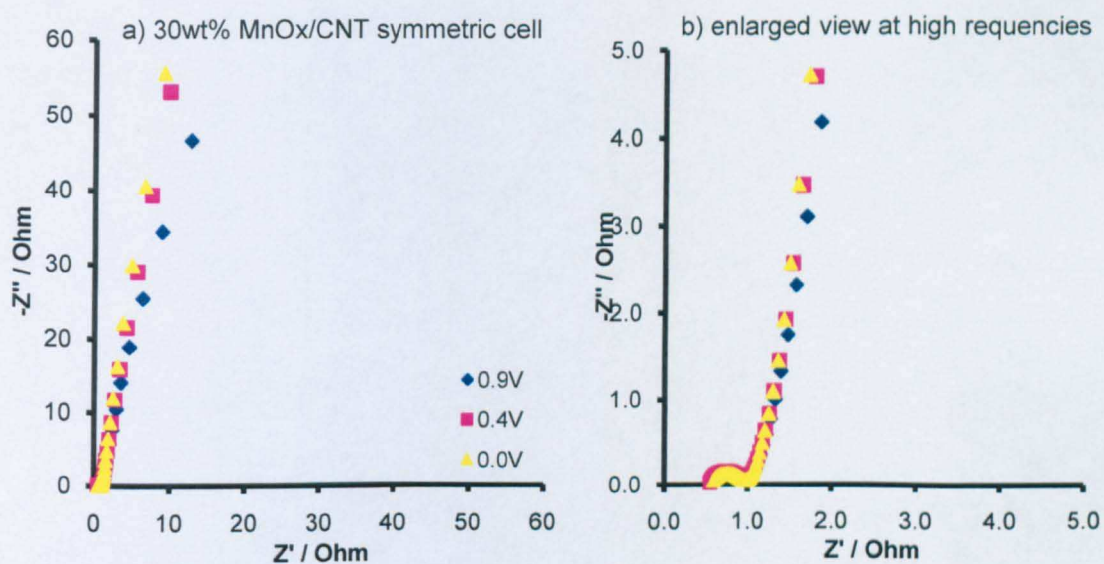
Fig. 8.8. AC Impedance of 30 wt% MnO_x/CNTs symmetrical cell in 2.0 M KCl

Current density	charge time (s)	discharge time (s)	cell C charge (mF)	cell C discharge (mF)	Specific C Charge (F/g)	Specific C discharge (F/g)	Coulombic efficiency
1 mA/cm^2	291.8	276.3	431.2	408.3	67.6	64.0	94.69 %
2 mA/cm^2	135.3	133	399.9	393.1	62.7	61.7	98.30 %
10 mA/cm^2	23.6	23.2	348.8	342.8	54.7	53.8	98.31 %
20 mA/cm^2	10.5	10	310.3	295.6	48.7	46.4	95.24 %

Table 8.5. Specific capacitance of 30 wt% MnO_x/CNTs from Galvanostatic
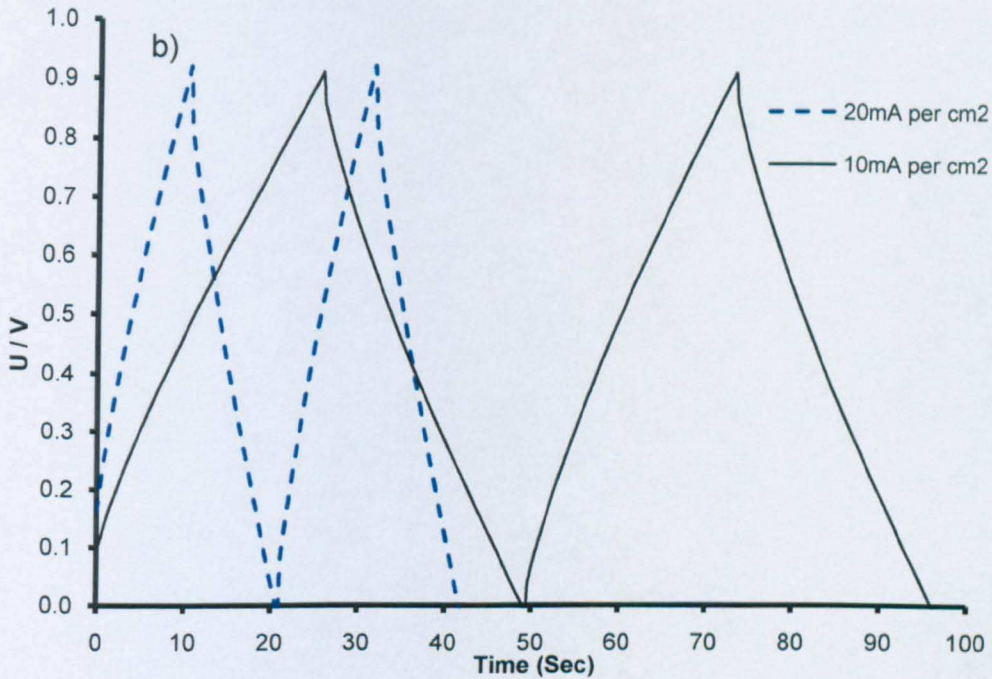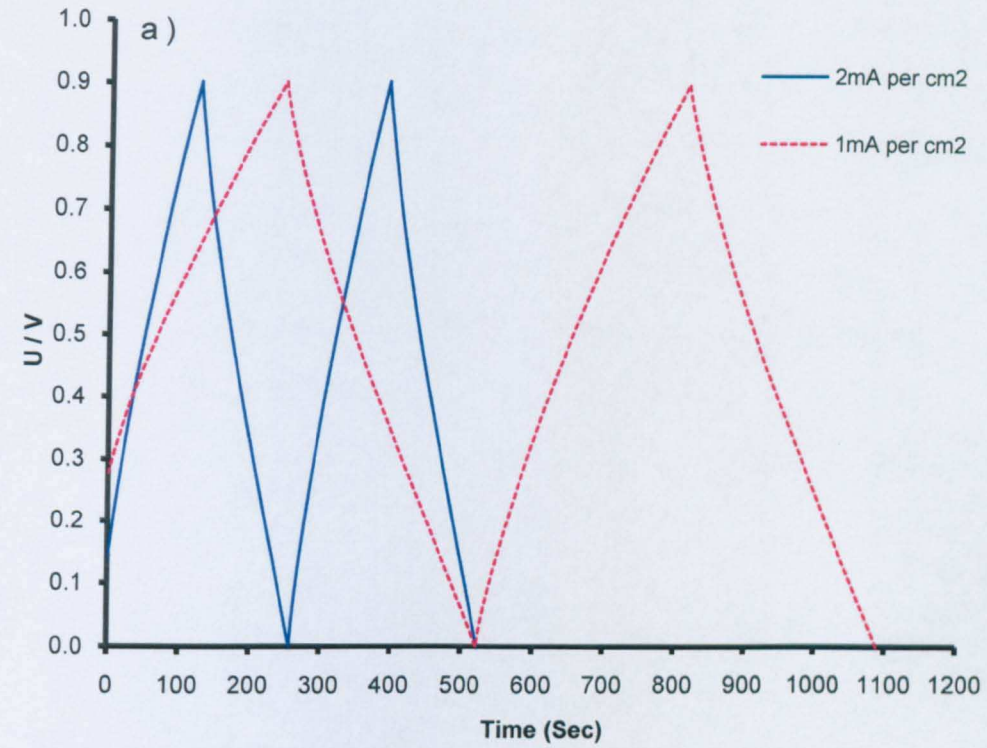
charge-discharge.

Fig. 8.9.Gavanostatic charge-discharge of 30 wt% MnOₓ/CNTs symmetrical

cell at different current density: 1-20 mA/cm².

In Fig. 8.9, sudden voltage drop, caused by the current passing through

resistance, can be observed. This potential drop is defined as the iR

drop. A small iR drop is genuinely desired as it is a direct indicator

of the cell resistance. The equivalent series resistance (ESR) of the cell, the proportion of iR drop in the cell voltage under different current densities are presented in Table 8.6. Consistent ESR values have been calculated for each cell under different current densities, which verifies the accuracy of iR drop recorded. Naturally, larger iR would be obtained under higher current density as iR drop is proportional to the current. At 20 mA/cm^2, the iR drop makes up more than 11.4 % of the whole cell voltage, suggesting significant energy loss due to the internal resistance.

current density	iR drop (V)	ESR (Ω)	% of total cell voltage
1 mA/cm^2	0.0049	1.84	0.54 %
2 mA/cm^2	0.0093	1.75	1.03 %
10 mA/cm^2	0.045	1.7	5.00 %
20 mA/cm^2	0.103	1.94	11.44 %

Table 8.6. The iR drop and ERS of the 30 wt% MnO$_x$/CNT symmetrical cells at different current densities.

Equivalent cell resistance (ERS), is a general term for resistive contributions rise from different aspects, including the resistance of electrolyte, the conductive diluents (carbon in this case) (Winter and Brodd, 2004), the contact resistance between the particles of active materials (Winter and Brodd, 2004), the contact resistance between the electrode and current collector (Burke, 2000) (Ng et al., 2009) and ion diffusion in the pores of the electrode materials (Burke, 2007). The resistance from ion diffusion within the electrode is approximated as (Burke, 2007):

$$R = \frac{2}{3}t \times \frac{r'}{A} \qquad \text{Eq. 8.11.}$$

where t is the electrode thickness, r' the resistivity of the electrolyte, and A the geometry area of the electrode. Therefore, it can be inferred

that significant reduction of this resistance can be achieved by reducing
the electrode thickness, increasing the electrolyte conductivity and
increasing the geometric area of the electrode.

4.1.3. 60 wt% MnO$_x$/CNTs Symmetrical Cell

The performance of the symmetrical cell 60 wt% MnO$_x$/CNTs is characterised
by CV, AC impedance and Gavanostatic charge-discharge techniques. The
results are presented in the Figures and Tables below. Detailed discussion
comparing the performance of different MnO$_x$/CNTs cells will be given in
Section 4.1.4.
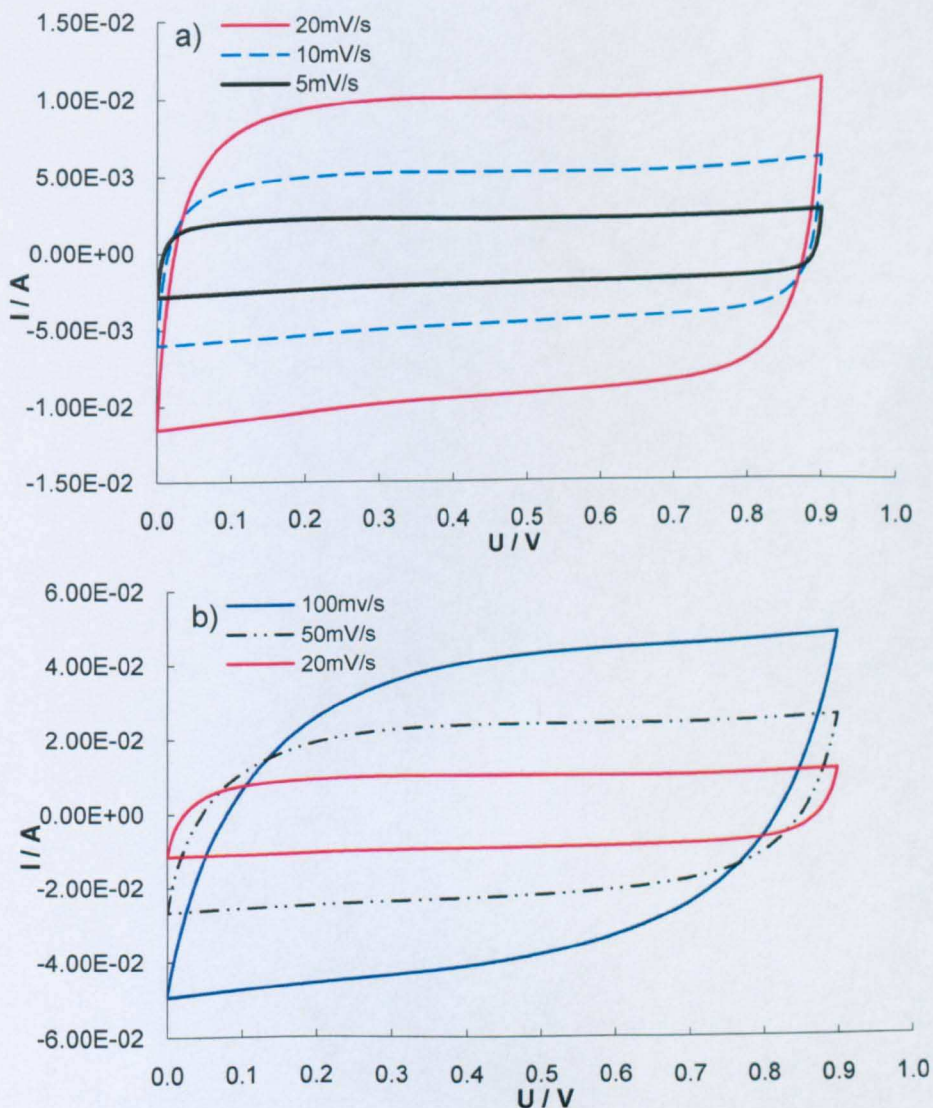
Fig. 8.10. Cyclic Voltammetry of 60 wt% MnO$_x$/CNTs symmetrical cell in
2.0 M KCl at various scan rates: 5 mV/s - 200 mV/s.

Scan rate	Cell capacitance (mF)	Specific capacitance (F/g)	Geometry capacitance (mF/cm^2)
5 mV/s	424	66.5	637.6
10 mV/s	496	77.8	745.9
20 mV/s	486	76.2	730.8
50mV/s	461	72.3	693.2
100mV/s	407	63.8	612.0

Table 8.7. Specific capacitance of 60 wt% MnO$_x$/CNTs from cyclic

voltammetry.
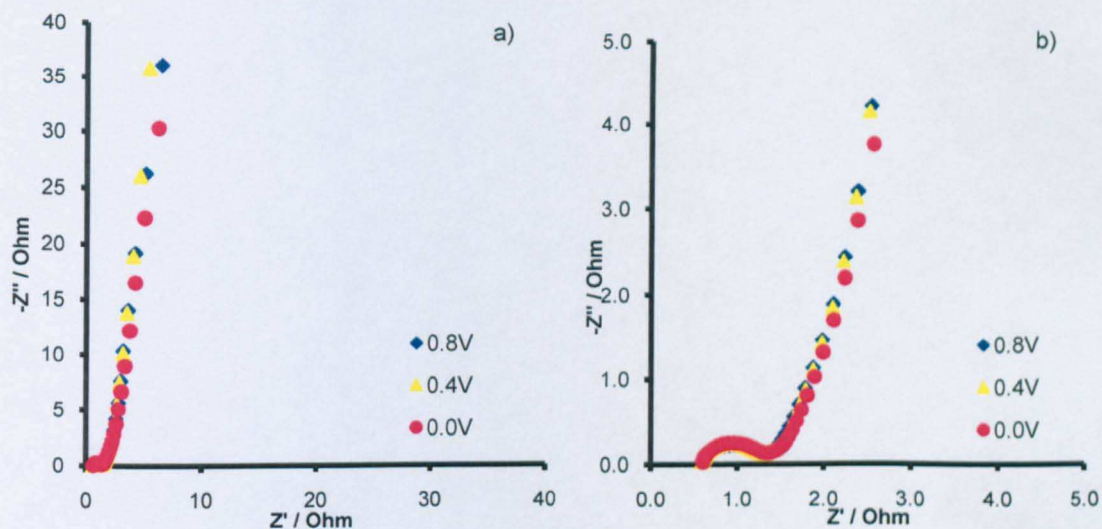
Fig. 8.11. AC Impedance of 60 wt% MnO$_x$/CNTs symmetrical cell in 2.0 M

KCl with enlarged view at high frequencies (b).

Current density	charge time (s)	discharge time (s)	Cell C charge (mF)	Cell C discharge (mF)	specific C charge (F/g)	Specific C discharge (F/g)	Coulombic efficiency
1 mA/cm^2	350.2	331.6	517.5	490.0	81.2	76.9	94.69 %
2 mA/cm^2	161.3	155.8	476.7	460.5	74.8	72.2	96.59 %
10 mA/cm^2	30.1	30.1	444.8	444.8	69.8	69.8	100.00 %
20 mA/cm^2	13.6	12.5	402.0	369.4	63.1	58.0	91.91 %

Table 8.8. Specific capacitance of 60 wt% MnO$_x$/CNTs from

Chronopotentiometry.
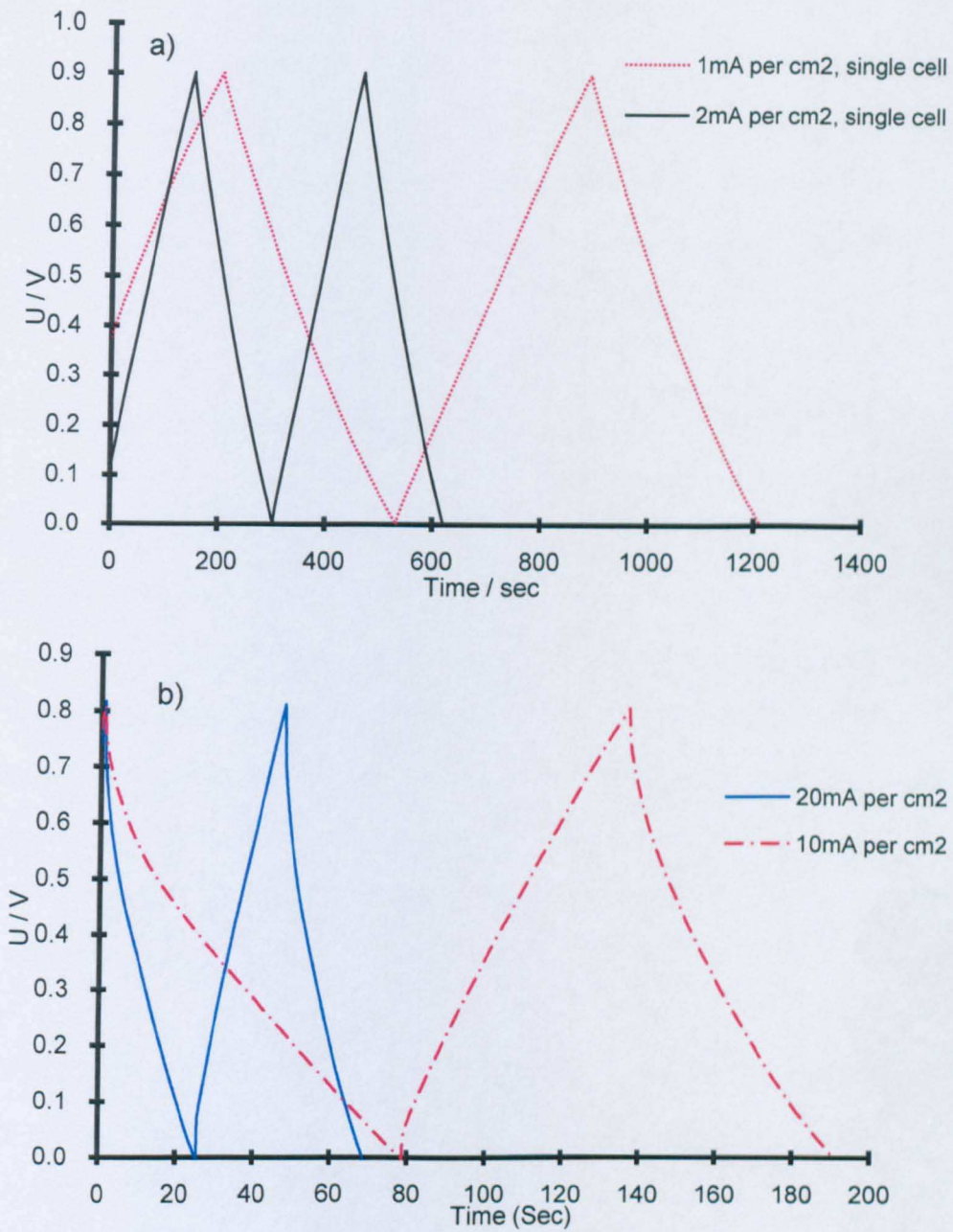
Fig. 8.12. Galvanostatic charge-discharge of 60 wt% MnO$_x$/CNTs symmetrical

cell at different current density: 1-20 mA/cm^2.

current density	iR drop (V)	ESR (Ω)	% of total cell voltage
1 mA/cm^2	0.0057	2.15	0.63 %
2 mA/cm^2	0.0109	2.05	1.21 %
10 mA/cm^2	0.0546	2.06	6.07 %
20 mA/cm^2	0.109	2.05	12.11 %

Table 8.9. The iR drop and ERS of the 60 wt% MnO$_x$/CNT symmetrical cells

at different current densities.

4.1.4. Symmetrical MnO_x/CNTs cells comparison

The capacitive properties of the 15 wt%, 30 wt% and 60 wt% MnO_x/CNTs symmetrical cells are compared in both CV (Fig. 8.13) and EIS (Fig. 8.14). The cell capacitance, specific capacitance, charge transfer resistance and cell Coulombic efficiency for the cells are listed in Table 8.10 and Table 8.11 for comparison.

Compared with the symmetrical cell fabricated with CNTs electrodes (Fig. 8.13), MnO_x/CNTs composites show significantly higher specific capacitance, due to the pseudocapacitive contribution from the redox reactions. Also, it is to be noted that the specific capacitance increases linearly with the increase of MnO_x content in the composites. For example, the capacitance of MnO_x/CNTs cell containing 60 wt% of manganese oxides is about 3.1 times the cell capacitance of a cell containing 15 wt% of manganese oxides, as measured by EIS at 0.0 V (Table 8.10). This result is confirmed by other measurements, i.e. CV and Galvanostatic charge-discharge (Table 8.11).

From Table 8.10, it is clear that the prototype cells showed comparable capacitance at 0.0 V and 0.4 V, indicating a constant capacitive behaviour within the operational voltage-range. The mass specific capacitance increases with the increase of manganese oxides content in the composites, with the 60 wt% MnO_x/CNT has a mass specific capacitance of 80.5 F/g (Table 8.10).
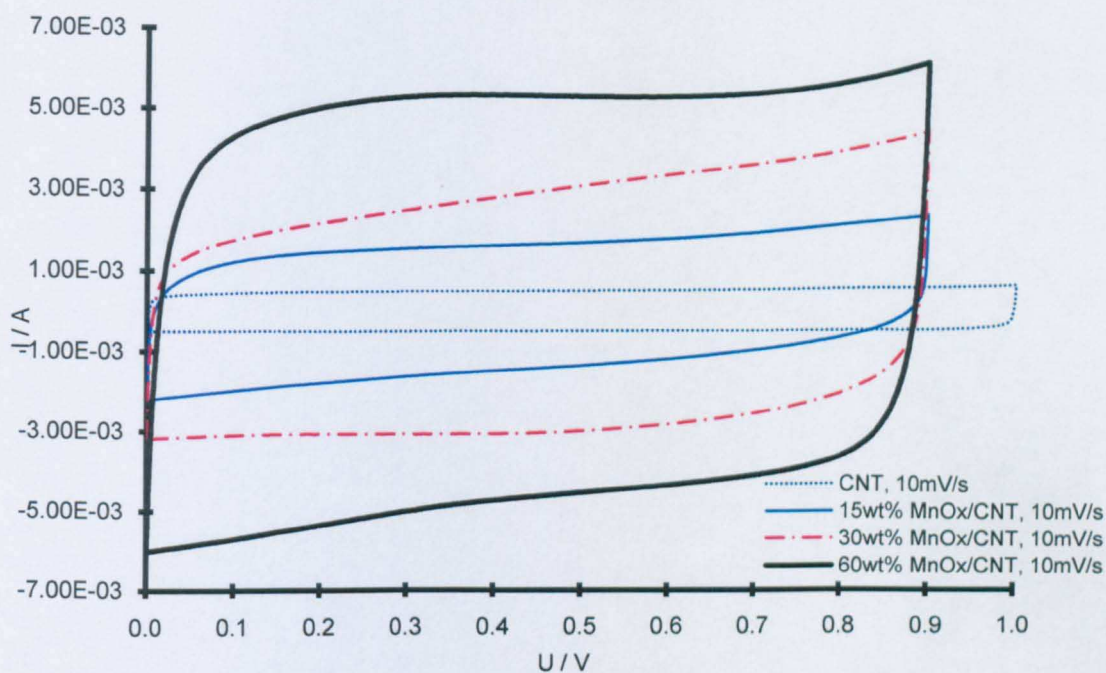
Fig. 8.13. CV comparison of capacitive behaviour of MnO$_x$/CNTs symmetrical

cells: 15 wt%, 30 wt% and 60 wt% MnO$_x$/CNTs (scan rate 10mV/s).
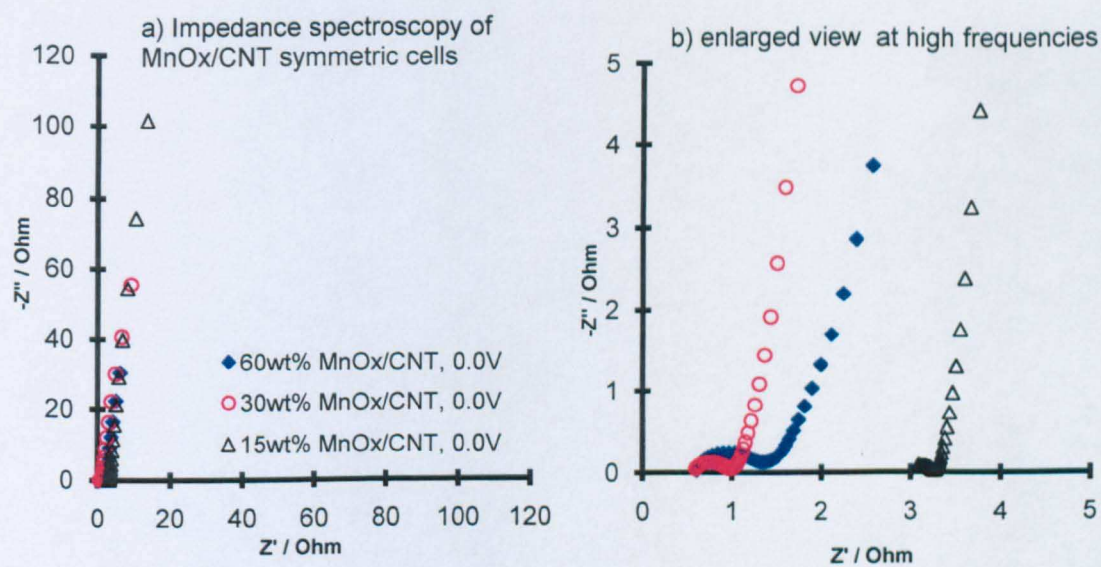
Fig. 8.14. Impedance comparison of capacitive behaviour of MnO$_x$/CNTs

symmetrical cells: 15 wt%, 30 wt% and 60 wt% MnO$_x$/CNTs at 0.0 V.

Symmetrical cells	15 wt% MnO$_x$/CNT	30 wt% MnO$_x$/CNT	60 wt% MnO$_x$/CNT
0.0 V			
cell capacitance (mF)	154	281	513
mass specific capacitance (F/g)	24.2	44.1	80.5
geo-specific capacitance (F/cm^2)	231.6	422.6	771.4
0.4 V			
cell capacitance (mF)	181	292	460
mass specific capacitance (F/g)	28.4	45.8	69
geo-specific capacitance (F/cm^2)	272.2	439.1	661.7

Table 8.10. Cell capacitance and specific capacitance from EIS characterisation of 15 wt% MnO$_x$/CNTs, 30 wt% MnO$_x$/CNTs and 60 wt% MnO$_x$/CNTs symmetrical cells.

MnO$_x$/CNTs symmetrical Cell	Cell capacitance CV at 20 mV/s	Cell capacitance EIS at 0 V	Cell capacitance, charge-discharge at 2 mA/cm^2	R$_{ct}$	Coulombic efficiency
15 wt% MnO$_x$/CNTs cell	179.8 mF	154 mF	190.9 mF	0.3 Ω	95.28 %
30 wt% MnO$_x$/CNTs cell	317.5 mF	422.6 mF	393.1 mF	0.5 Ω	98.30 %
60 wt% MnO$_x$/CNTs cell	486 mF	513 mF	460.5 mF	0.8 Ω	96.59 %

Table 8.11. Comparison of cell capacitance, charge resistance and coulombic efficiency of 15 wt% MnO$_x$/CNTs, 30 wt% MnO$_x$/CNTs and 60 wt% MnO$_x$/CNTs single symmetrical cells.

The semicircles observed in the impedance complex plane (Fig. 8.14) is characteristic for activation polarisation, the kinetics of redox reactions at electrode | electrolyte interface. Only one semicircle can

be observed for each cell, indicating the existence of only one relaxation process. Therefore, only one relaxation time, τ, is identified for the positive and negative electrodes of each cell.

$$\tau = \frac{1}{f_m} \qquad \text{Eq. 8.10}$$

where fm is the frequency at which the semicircle reaches maximum

The relaxation times for these three MnO_x/CNTs symmetrical cells at 0.0 V are: 0.075×10^{-3} second, 0.10×10^{-3} second and 0.193×10^{-3} second for 15 wt% MnO_x/CNTs, 30 wt% MnO_x/CNTs and 60 wt% MnO_x/CNTs cells respectively. These figures are in the lower limit of the 10^{-2} -10^{-4} second range for charge-transfer processes, suggesting rapid kinetics for activation polarisation at the interface.

Charge transfer resistance, R_{ct}, can be derived from the diameter of this semicircle. As listed in Table 8.11, R_{ct} increases with the increase of manganese content in the composites. This is due to the fact that manganese oxides are more resistive than carbon materials. Higher content of manganese oxides slow down the charge transfer process within the electrode and hence slows down the reaction.

However, contact resistance plays a significant part in R_{ct}. As shown in Fig. 8.15, different R_{ct} , i.e. 4.6 Ω, 8.2 Ω and 34.8 Ω, can be derived from data 1, data 2 and data 3. All these three electrochemical impedance spectra are based on the same prototype cell. The variation of R_{ct} is, in fact, caused by the different pressure applied to the cell between the two end plates, leading to different contact resistance. Therefore, the analysis of R_{ct} can only be validated when the pressure applied is controllable and the contact resistance is eliminated.
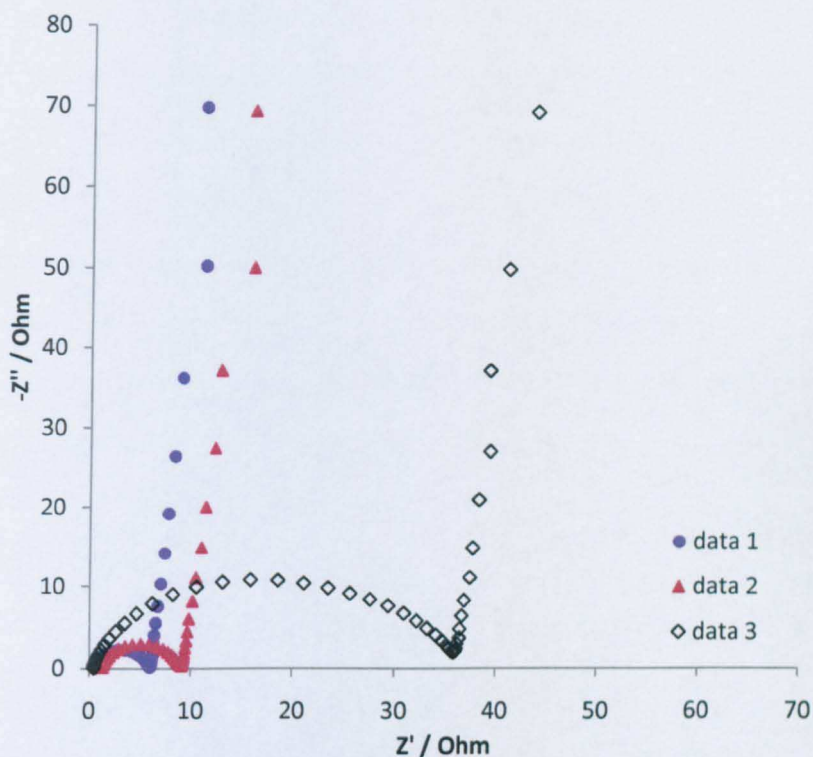
Fig. 8.15. **The variation of R_{ct} of a prototype cell under different clamp**

pressure.

To conclude, despite of some minor inferior properties, the 60 wt%

MnO_x/CNTs symmetrical cell boasts the highest capacitance among the three

MnO_x/CNTs composites investigated in this study. Thus, 60 wt% MnO_x/CNTs

is selected to represent MnO_x/CNTs composite for further investigation

in the cell structure, i.e. asymmetrical cells and cell stacks.

4.2. PAni/CNTs Symmetrical Cell

Symmetrical cells were fabricated with the PAni/CNTs composite with 80

wt% PAni. Each electrode contained 12.75 mg composite and 2.25 mg aligned

CNTs as the conducting additive. The mixture was pressed under 1 Ton into

a pellet with diameter of 13 mm (cross section area of 1.327 cm^2). 1 M

H_2SO_4 aqueous solution was applied as the electrolyte.

The cell was first characterised by cyclic voltammetry at various scan

rates between 0 - 0.5 V (Fig. 8.16). At scan rates higher than 20 mV/s,

an olive-shaped CV started to appear, suggesting that it would be difficult for redox reactions to proceed at higher scan rate. Nevertheless, the cell capacitance and specific capacitance calculated from CV are presented in Table 8.12. Compared with the figures calculated for MnO_x/CNTs composites, the PAni/CNTs composite has noticeably higher capacitance. A geometric capacitance of 1.2 F/cm^2 was achieved at 10 mV/s with this PAni/CNTs symmetrical cell. However, considerable decline in cell capacitance was recorded at scan rate above 30 mV/s (Table 8.12): 9 % decrease once scan rate reached 50 mV/s and 20.9 % decrease at the scan rate of 100 mV/s. However, the critical drawback for conducting polymers, compared with transition metal oxides and carbon materials, is their limited cell voltage. As an energy storage device, a limited cell voltage lowers the value in both energy and power densities (Eq. 8.2 and Eq. 8.3). Therefore, the applications of PAni are considerably limited.
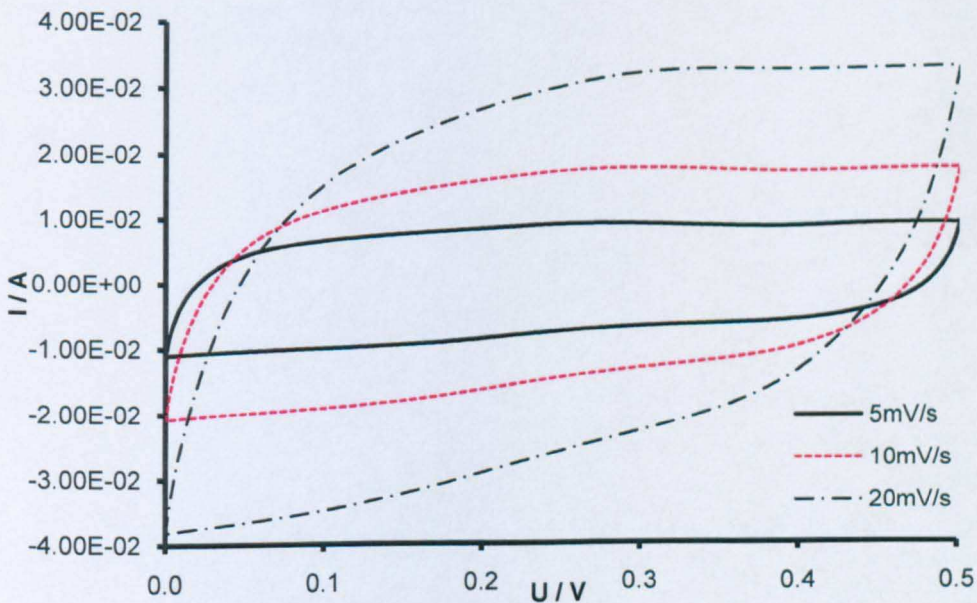
Fig. 8.16. CV of symmetrical Cell PAni/CNTs cell under different scan rate.

Scanrate	Cell capacitance (mF)	Specific capacitance (F/g)	Geometry capacitance mF/cm^2
5 mV/s	777	121.9	1168.4
10 mv/s	791	124.1	1189.4
20 mv/s	785	123.3	1180.4
30 mV/s	783	127.8	1177.4
40 mV/s	735	115.3	1105.2
50 mV/s	714	112.0	1073.6
100 mv/s	621	97.4	933.8

Table 8.12.Capacitance of symmetrical PAni/CNTs cell at different scan rates.

This PAni/CNTs symmetrical cell was also characterised with EIS. The results were presented in impedance complex-plane in Fig. 8.16. The capacitance values calculated from EIS (Table 8.14) are well in accordance to those obtained from CV characterisations. The charge transfer resistance, R_{ct}, for this PAni/CNTs symmetrical cell was 0.42 Ω. The cell performance will be further commented in Section 4.3 in comparison with the polypyrrole/CNTs symmetrical cell.
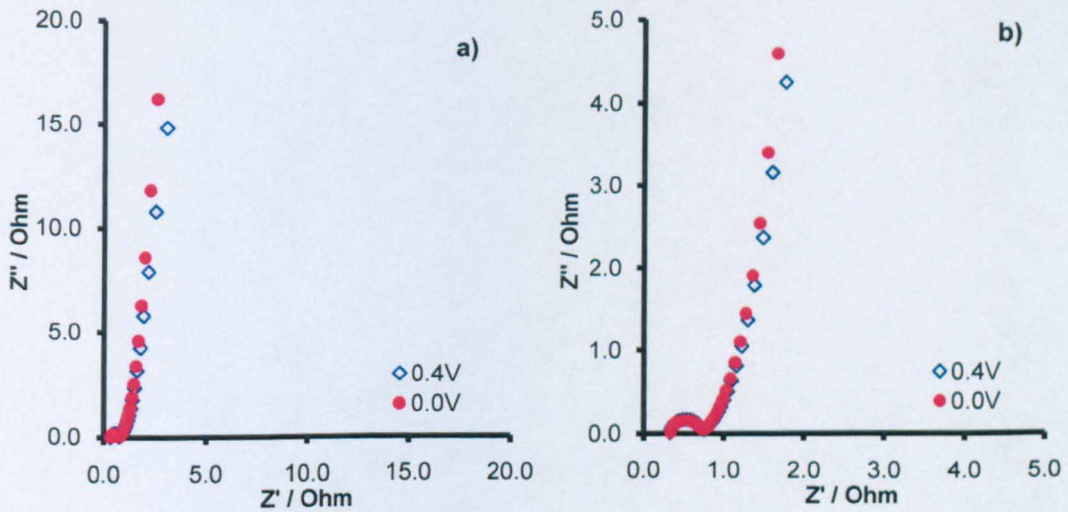
Fig. 8.17. Impedance of PAni/CNTs symmetrical cell in 1 M H_2SO_4 with enlarged view at high frequencies.

4.3. PPy/CNTs Symmetrical Cell

Symmetrical cells with 80 wt% PPy/CNTs composites with 80 wt% of PPy as electrode material are fabricated. Each electrode containing 12.75 mg composite and 2.25 mg aligned CNTs as conducting additive. The mixture was pressed under 1 Ton into pellet with 13 mm diameter (cross-section area of 1.327 cm^2). The 2 M KCl aqueous solution was applied as electrolyte.

The cell was first characterised by cyclic voltammetry at various scan rates between 5 – 50 mV/s (Fig. 8.18). Similar to the PAni/CNTs cell, the cell voltage was limited to a narrow range of 0 – 0.6 V. At scan rates higher than 50 mV/s, an olive-shaped CV started to appear (Fig. 8.18 b), suggesting that it would be difficult for reactions to proceed at higher scan rate due to the kinetic reasons. This upper limiting scan rate is higher than that of 20 mV/s for the PAni/CNTs symmetrical cell. Cell capacitance and specific capacitance calculated from CVs are presented in Table 8.13.
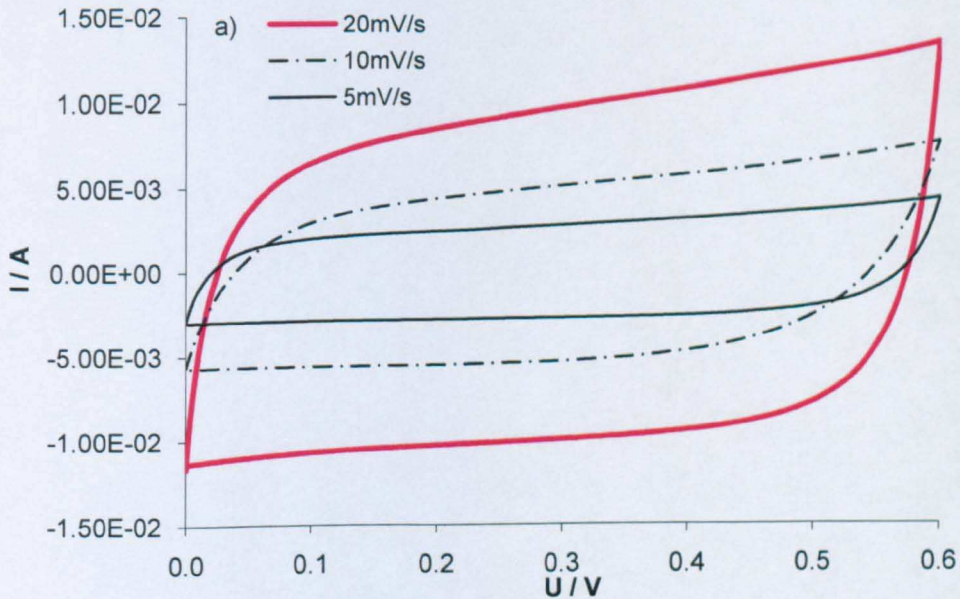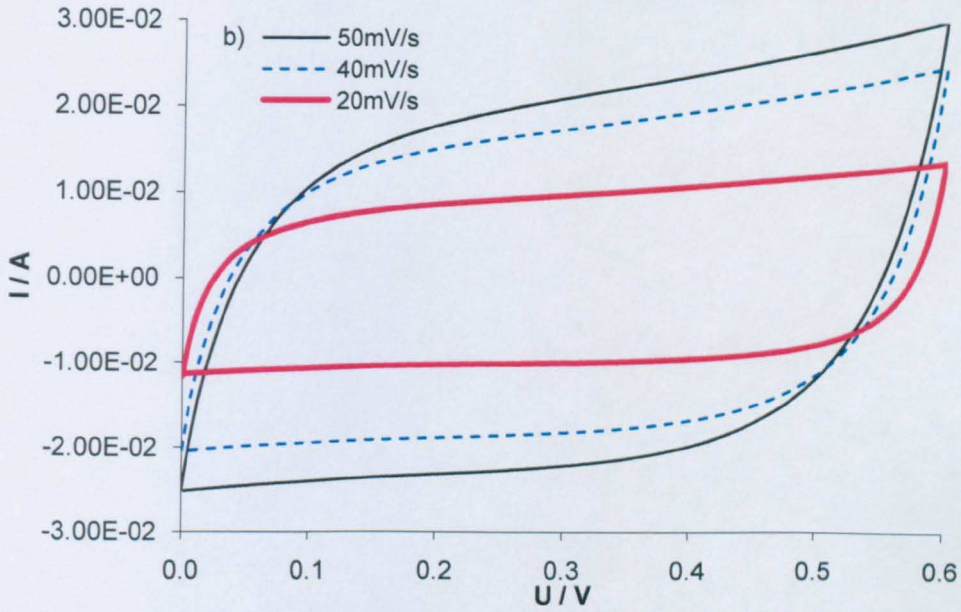
Fig. 8.18. CV of symmetrical Cell PPy/CNTs cell under different scan rate.

Scanrate	Cell capacitance (mF)	Specific C (F/g)	Geometry C (mF/cm^2)
5 mV/s	551	86.4	828.6
10 mV/s	519.5	81.5	781.2
20 mV/s	489.5	76.8	736.1
40 mV/s	443.8	69.6	667.4
50 mV/s	422	66.2	634.6
100 mV/s	352.5	55.3	530.1

Table 8.13. Capacitance of symmetrical PPy/CNTs cell at different scan rates.

The impedance data of the symmetrical PPy/CNTs cell are presented in Fig. 8.19, with specific capacitance calculated in Table 8.14. Charge transfer resistance of this PPy/CNTs symmetrical cell under study is 0.5 Ω.

The galvanostatic charge-discharge tests of the PPy/CNTs symmetrical cell were performed under different current densities. The results are presented in Fig. 8.20. Table 8.15 lists the specific value of capacitance and the Coulombic efficiency of the cell under different current densities. IR drops and equivalent series resistance of the cell under different current densities are presented in Table 8.16.
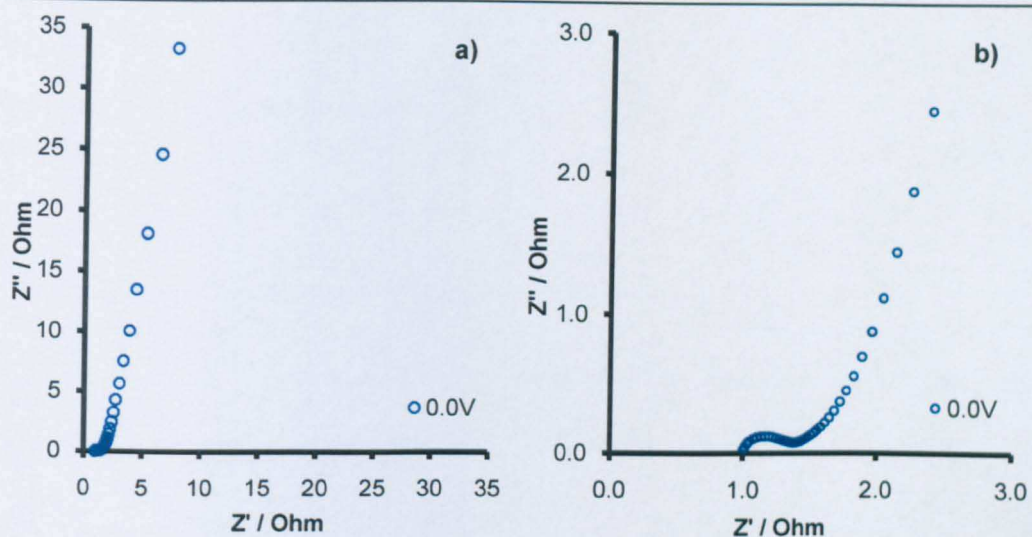
Fig. 8.19. Impedance of PPy/CNTs symmetrical cell in 2 M KCl with enlarged view at high frequencies (b).

Conducting polymer Symmetrical	Equilibrium Potential	Cell capacitance (mF)	Specific capacitance (F/g)	Geometry capacitance (mF/cm^2)
PPy/CNTs	0.0 V	466	73.1	700.8
Cell	0.4 V	489	76.7	735.3
PAni/CNTs	0V	970	152.2	1458.6
Cell	0.4V	1060	166.3	1594.0

Table 8.14. Specific capacitance of PPy/CNTs and PAni/CNTs symmetrical cell by impedance spectroscopy.
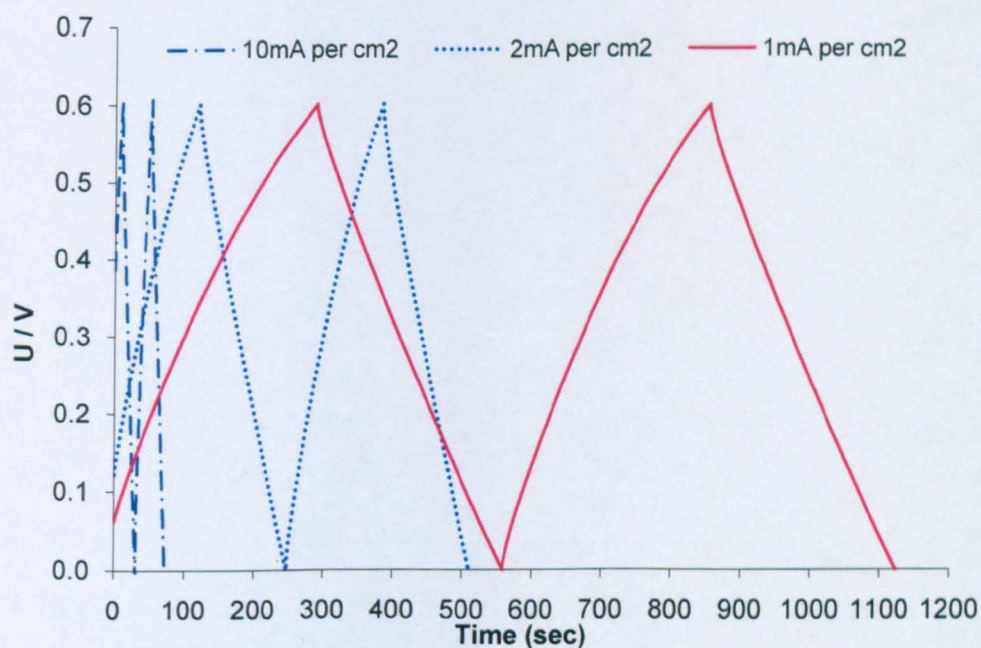
Fig. 8.20. Galvanostatic charge-discharge of PPy/CNTs symmetrical cell at various current densities: 1-10 mA/cm^2.

Current density	charge time (s)	discharge time (s)	Cell C charge (mF)	Cell C discharge (mF)	specific C charge (F/g)	Specific C discharge (F/g)	Coulombic efficiency
1 mA/cm²	296.1	269.4	656.4	597.2	103.0	93.7	90.98 %
2 mA/cm²	135.9	127	602.5	563.0	94.5	88.3	93.45 %
10 mA/cm²	21.9	20.4	485.5	452.2	76.1	70.9	93.15 %
20 mA/cm²	9.3	8.7	412.3	385.7	64.7	60.5	93.55 %

Table 8.15. Specific capacitance of 80 wt% PPy/CNTs symmetrical cell from Galvanostatic charge-discharge.

current density	iR drop (V)	ESR (Ω)	% of total cell voltage
1 mA/cm²	0.005	1.88	0.83 %
2 mA/cm²	0.011	2.07	1.83 %
10 mA/cm²	0.053	1.98	8.83 %

Table 8.16. iR drop and equivalent cell resistance of 80 wt% PPy/CNTs symmetrical cell.

It is to be noted that conducting polymers are more conducting in nature than manganese oxides. Therefore, cells constructed with conducting polymers have smaller iR drop, and smaller ESR, compared with MnO_x/CNTs cells. Moreover, cells constructed with conducting polymers have higher specific capacitance than MnO_x/CNTs cells. A relatively small cell voltage is a critical drawback for conducting polymers. A cell voltage of 0.5 V or 0.6 V seems to be rather limiting for practical applications. However, considering an operational voltage of an average fuel cell, of about 0.6 V (Larminie and Dicks, 2003), the cell voltage of conducting-polymer-supercapacitor is not that disappointing after all. Besides, higher cell voltage can be achieved by connecting cells in series. Therefore, further investigations are conducted to seek solution in expanding the cell

operational voltage in Section 5.

5. Asymmetrical Cells

Carbon materials, with their well known advantages of high overpotential

for hydrogen evolution, good double layer capacitive behaviour, excellent

cycling stability and electrical conductivity are undoubtedly a favorable

choice for asymmetrical cells. In this study, asymmetrical cells with

carbon material as the negative electrode and $MnO_x/CNTs$, $PAni/CNTs$ or

$PPy/CNTs$ as the positive electrode have been constructed to demonstrate

the improvement from an asymmetrical cell structure. The activate carbon,

Monarch 1300, is selected as the negative electrode material.

5.1. $MnO_x/CNTs$ and M1300 Asymmetrical Cell

Positive electrodes, identical to those in the symmetrical cell, were

fabricated with 12.75 mg of 60 wt% $MnO_x/CNTs$ with 2.25 mg aligned CNTs.

Negative electrode is built with 30 mg M1300, based on the specific

capacitance of M1300 calculated in Table 8.1. It is important that

positive and negative electrode have equal capacitance, since the cell

capacitance is determined by the smaller value of the two (Eq. 8.1). 2

M KCl is applied as the electrolyte in this investigation.

The capacitive performance of the $MnO_x/CNTs$ | M1300 asymmetrical cell

is first characterised by CV. As presented in Fig. 8.21, the asymmetrical

cell shows well defined capacitive behavior at scan rates between 10 and

100 mV/s. A cell voltage of 1.1 V has been achieved with this asymmetrical

structure, due to the high overpotential of hydrogen evolution on carbon

material. Gas evolution in this system starts at about 1.1 V. This is

signaled by the continuous increase of the current at voltage above 1.05

V, forming a 'tail' when voltage approaches 1.1 V (Fig. 8.21). With a

higher cell voltage and enhanced cell capacitance, CV characterizations

have demonstrated that the asymmetrical cell has better performance to
the symmetrical cell with MnO_x/CNTs electrode (Fig. 8.22). The cell
capacitance, specific capacitance for both positive and negative
electrodes materials of the asymmetrical cell at different scan rates
are calculated in Table 8.17. Compared with the values for symmetrical
cells listed in Table 8.7, the asymmetrical structure helps to achieve
much higher cell capacitance, particularly at scan rates above 50 mV/s.
Exceptional geometry capacitance of 0.96 F/cm^2 has been achieved with
this prototype cell, suggesting a good potential for industry
applications.
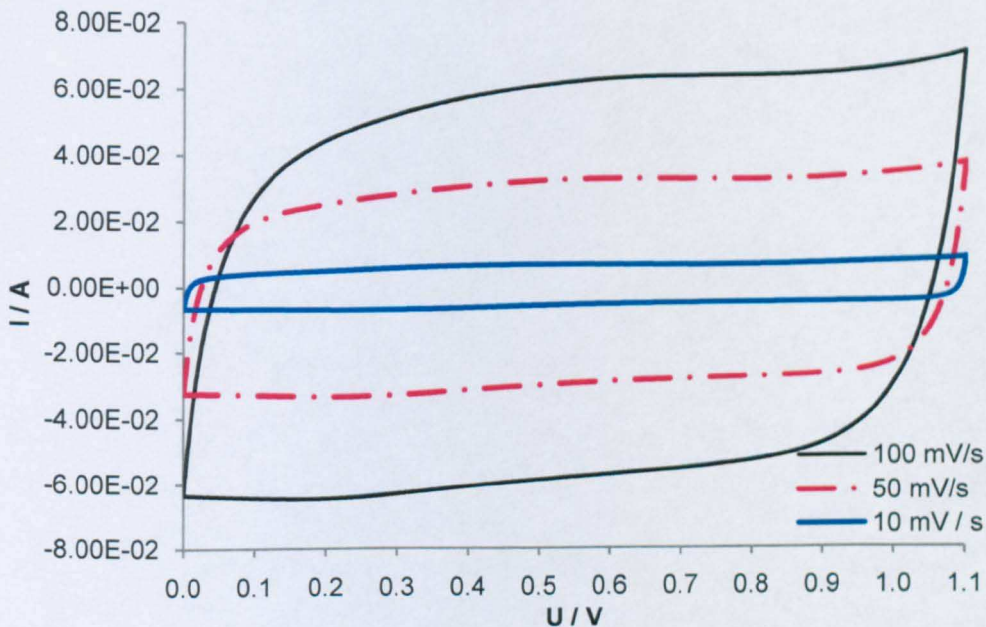
Fig. 8.21. CV of the asymmetrical 60 wt% MnO_x/CNTs | M1300 cell under
different scan rate: 10 - 100 mV/s in 2 M KCl.
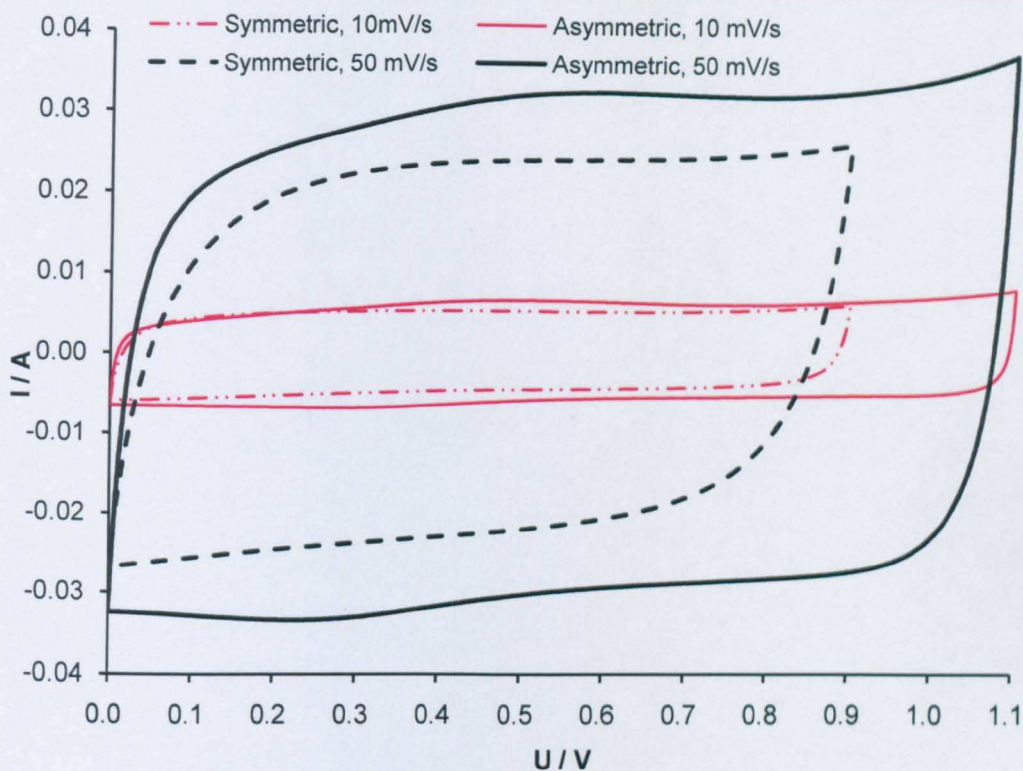
Fig. 8.22. CV comparison of capacitive behaviour of MnO_x/CNTs symmetrical

and asymmetrical cells.

Scanrate	Cell capacitance (mF)	Specific capacitance of MnO_x (F/g)	Specific capacitance of M1300 (F/g)	Geometry capacitance (mF/cm^2)
10 mV/s	606	95.1	40.4	911.3
20 mV/s	637.5	100.0	42.5	958.6
50 mV/s	620	97.3	41.3	932.3
100 mV/s	591	92.7	39.4	888.7
200 mV/s	528.1	82.8	35.2	794.1

Table 8.17. Capacitance of the asymmetrical cell with MnO_x/CNTs positive

electrode and M1300 negative electrode in 2.0 M KCl at different scan

rates.

In addition, the capacitive behaviour of the asymmetrical cell was

characterised with impedance technique (Fig. 8.23). Asymmetrical cell

has a much smaller charge transfer resistance of 0.28 Ω, a reduction of

65 % compared with the symmetrical MnO_x/CNTs cell.
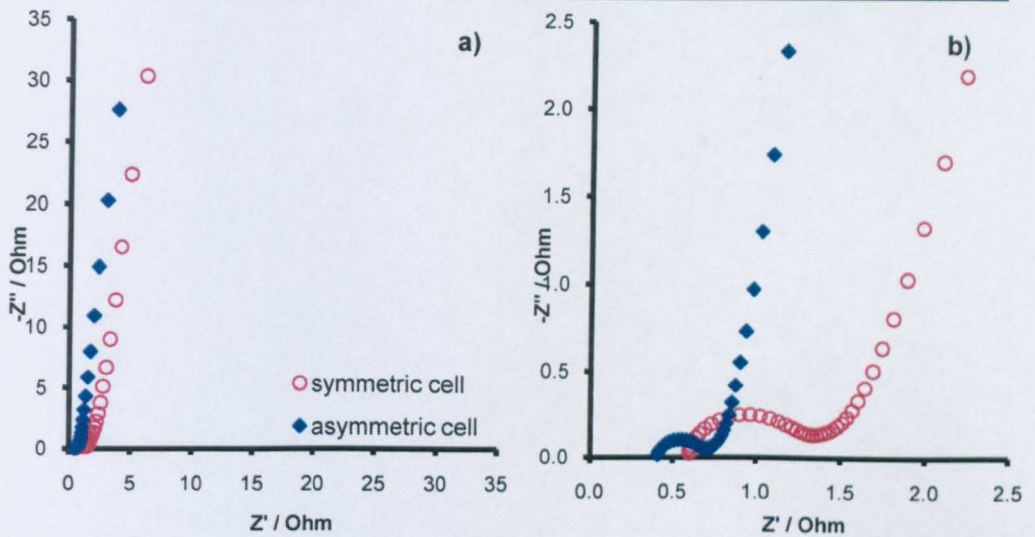
Fig. 8.23. Impedance comparison of capacitive behaviour of MnO_x/CNTs symmetrical and asymmetrical cells with enlarged view at high frequencies.

The charge transfer resistance, R_{ct}, associates with charge transfer barriers within the system, particularly the ion-injection from electrolyte to electrode surface (Niklasson et al., 2005). The barriers here include the electron transfer barrier between current-collector and electrode material, as well as the ion-transfer barrier between the electrode material and the electrolyte. Often, the ionic charge transfer barrier is significantly larger than the electronic charge transfer barrier (Chen, 1992). Under small voltage perturbations, R_{ct} is a useful indicator to describe the current-voltage relationship at the boundary.

In three electrode cell testing conditions, R_{ct} for a rate constant reaction across the electrode |electrolyte interface, O + ne = R, can be quantified at equilibrium potential E_r (net current is zero, and the concentration of oxidant and reductant in the electrode equals their bulk concentration) (Raistrict et al., 2005).

$$R_{ct} = \frac{RT}{nFi_0}$$ Eq. 8.12.

where i_0 is the exchange current density. This exchange current density

is defined by the current value at the equilibrium potential I_0, $I_0 = I_z$ = $-I_c$, divided by the electrode area: $i_0 = I_0 / A$. Through the Nernst-equation, i_0 is quantified as (Raistrict et al., 2005):

$$i_0 = nFk^0c_0^* \exp\left[\frac{-anF}{RT}(E_r - E^0)\right] \qquad \text{Eq. 8.13.}$$

where k^0 is the standard rate constant, C_0^* is the bulk concentration, α is the transfer coefficient and ($E_r - E^0$) is the over potential.

In two-electrode cell testing conditions, however, R_{ct} represents the sum of charge transfer barriers within the system. This includes the ionic interfacial barriers at the electrode | electrolyte interfaces on both positive and negative electrodes, and the ionic charge-transfer barrier within the separator. The contribution from each of these processes is, therefore, difficult to be quantified.

In principle, larger electrode surface area enhances the ion-accessibility and hence facilitates the ion-transfer. Activated carbon has significantly higher surface area, compared with nano-composites synthesised in this work. Therefore, when activated carbon is used as negative electrode for the asymmetrical cell, smaller R_{ct}, indicating smaller hindrance for charge-transfer, is achieved.

Interestingly, similar to the cases with symmetrical cells, only one semi-circle can be identified with the asymmetrical cell during EIS characterisation. This indicates that the two electrodes, although with different electrode materials, have similar RC constant (τ) responding to the input perturbations.

Galvanostatic charge-discharge tests of the asymmetrical cell confirmed reduced iR drop and improved ideal triangular charge-discharge (Fig.

8.24). The cell capacitance and the specific capacitance for positive and negative electrode materials are calculated in Table 8.18. These figures are well in accordance with the CV and EIS results. Coulombic efficiencies of the asymmetrical cell are listed in Table 8.19. Moreover, a comparison of the performance between symmetrical and asymmetrical cells at 10 mA/cm² is provided in Fig. 8.25, highlighting the improvements on the cell voltage, iR drop, Coulombic efficiency and cell capacitance. The iR drop and equivalent series resistance of this asymmetrical cell are presented in Table 8.20. Noticeably, at current density as high as 20 mA/cm², iR only takes up 4.93 % of the total cell voltage. This suggests that this asymmetrical cell is competent to perform at higher discharge rate. A comparison on general cell performance of the symmetrical and asymmetrical cell is presented in Table 8.21.
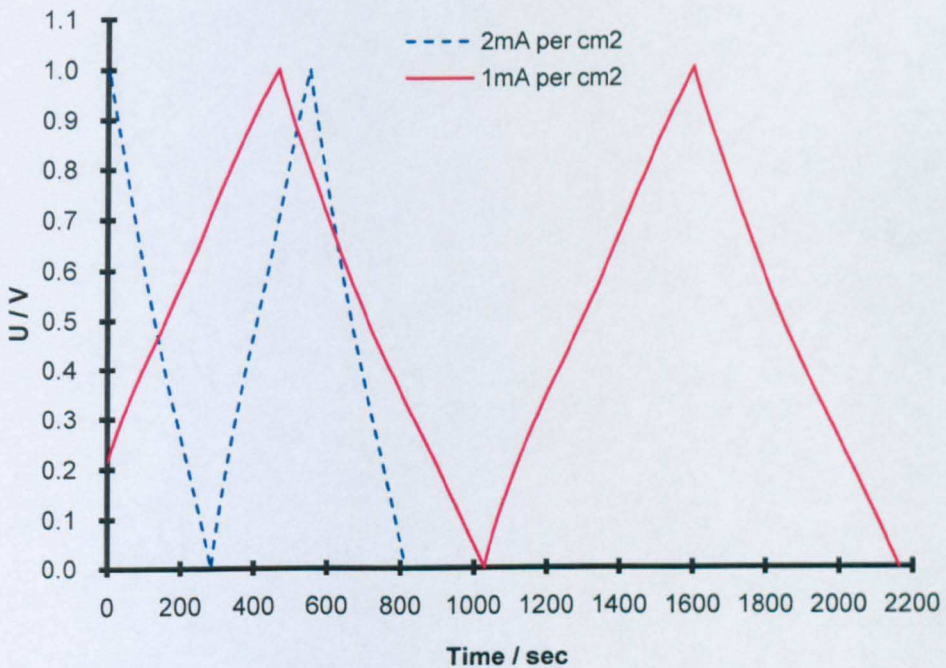
Fig. 8.24. Galvanostatic charge-discharge of MnOₓ/CNTs|M1300 asymmetrical cell.

Current density	current (mA)	charging time (s)	discharge time (s)	Cell C charge (mF)	Cell C discharge (mF)	Specific C (discharge) MnO$_x$ (F/g)	Specific C (discharge) M1300(F/g)
1 mA/cm^2	1.33	573.3	564.7	751.1	751.1	117.8	50.1
2 mA/cm^2	2.66	264.9	264.6	704.6	703.8	110.4	46.9
10 mA/cm^2	13.3	48.6	46.8	646.4	622.4	97.6	41.5
20 mA/cm^2	26.6	23.1	22	614.5	585.2	91.8	39.0

Table 8.18. Specific capacitance of MnOx/CNTs | M1300 asymmetrical cell

cell from Galvanostatic charge-discharge.

60 wt% MnO$_x$/CNTs asymmetrical cell		15mg per electrode (including 15 wt% ALCNTs) 2 M KCl 30mg M1300		
Current density	current (mA)	charging time (s)	discharge time (s)	Coulombic efficiency
1 mA/cm^2	1.33	573.3	564.7	98.50 %
2 mA/cm^2	2.66	264.9	264.6	99.89 %
10 mA/cm^2	13.3	48.6	46.8	96.30 %
20 mA/cm^2	26.6	23.1	22	95.24 %

Table 8.19. Coulombic efficiency of MnO$_x$/CNTs | M1300 asymmetrical cell

at different charge-discharge densities.
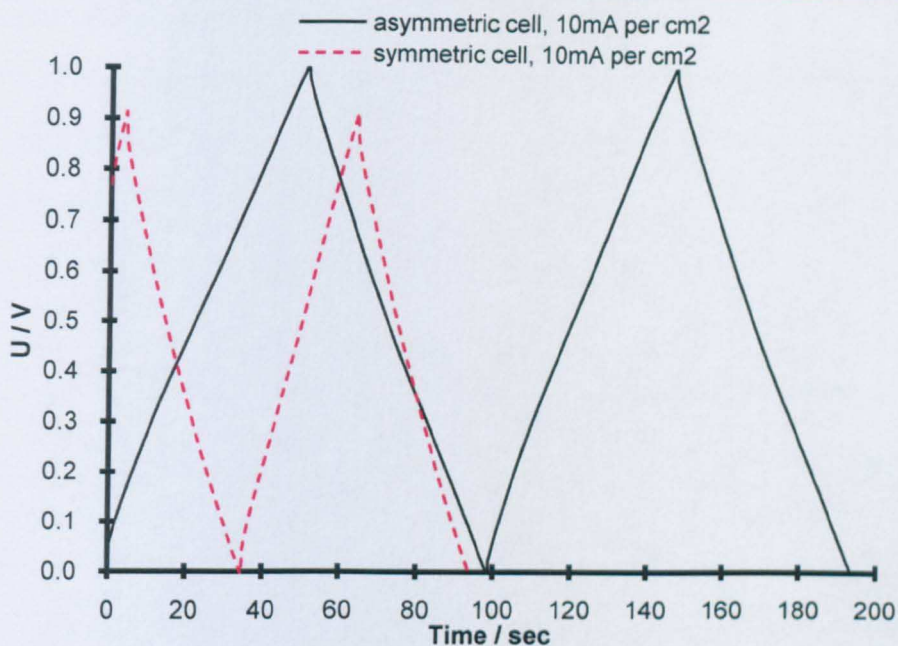
Fig. 8.25. Galvanostatic charge-discharge comparison of symmetrical and

asymmetrical cell of MnO$_x$/CNTs.

current density	iR drop (V)	ESR (Ω)	% of total cell voltage
1 mA/cm^2	0.0016	0.60	0.16 %
2 mA/cm^2	0.0043	0.81	0.43 %
10 mA/cm^2	0.023	0.86	2.30 %
20 mA/cm^2	0.04933	0.93	4.93 %

Table 8.20. iR drop and equivalent cell resistance of asymmetrical cell

with 60 wt% MnO$_x$/CNTs positive electrode and M1300 negative electrode.

60 wt% MnO$_x$/CNTs	symmetrical cell	asymmetrical cell
cell capacitance (CV at 10 mV/s)	0.496 F	0.606 F
cell capacitance (EIS at 0.0 V)	0.525 F	0.577 F
cell capacitance discharge (at 10 mA cm^{-2})	0.445 F	0.606 F
cell voltage	0.9 V	1.0 V
ESR (at 10 mA cm^{-2})	2.06 Ω	0.86 Ω
charge-transfer resistance	0.72 Ω	0.28 Ω
Coulombic efficiency (at 10 mA cm^{-2})	96.59 %	96.30 %

Table 8.21. Cell performance comparison of symmetrical and asymmetrical

cell with MnO$_x$/CNTs electrode.

5.2. PAni/CNTs and M1300 asymmetrical cell

With the encouraging results from the MnO_x/CNTs and carbon asymmetrical
cell, asymmetrical cells with polyaniline/CNTs composites as the positive
electrode and M1300 as the negative electrode were also fabricated. 1
M H_2SO_4 aqueous solution was applied as electrolyte.

However, compared with manganese oxides, the asymmetrical structure did
not lead to much improvement in the cell performance. As demonstrated in
Fig. 8.26, once the cell voltage was extended to 0.6 V, irregular shape
appeared in CV characterization. Therefore, the cell voltage of the
PAni/CNTs | M1300 cell was set to be 0.5 V, same as its PAni/CNTs symmetrical
equivalent. The upper limiting scan rate was 20 mV/s. Again, this value
is comparable with its symmetrical equivalent (comparing Fig. 8.27 with
Fig. 8.16). During the EIS characterisation, it was noted that the
asymmetrical cell structure was effective in reducing the charge transfer
resistance (Fig. 8.28). The charge transfer resistance of the symmetrical
cell is 0.42 Ω, while it is reduced to 0.10 Ω in the asymmetrical cell.
A comparison on the general cell performance of the symmetrical and
asymmetrical cell is presented in Table 8.22.
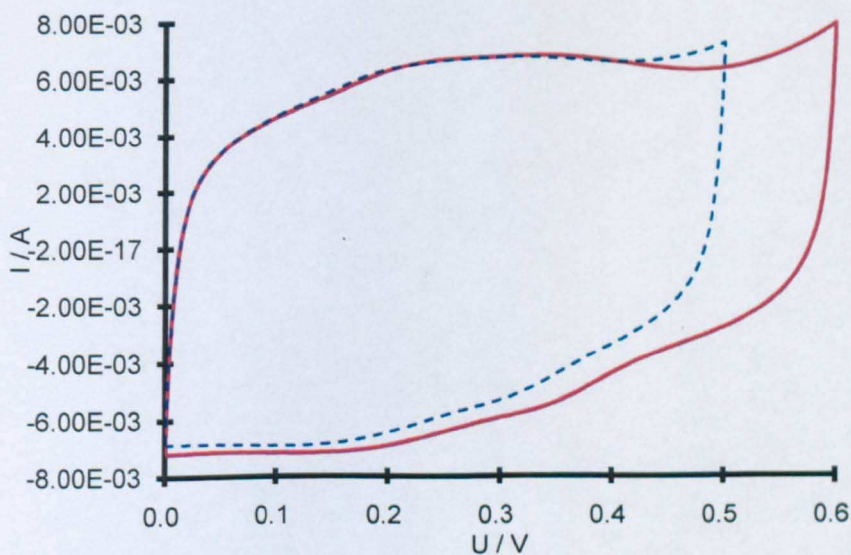
Fig. 8.26. Cell voltage of asymmetrical 80 wt% PAni/CNT | M1300 cell.
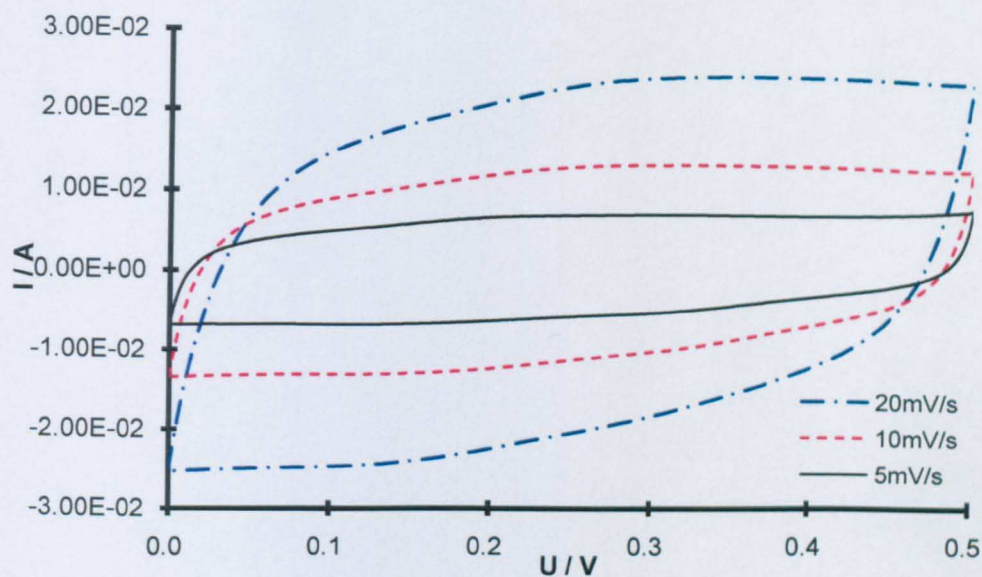
Fig. 8.27. CV of asymmetrical 80 wt% PAni/CNTs Vs M1300 cell under different scan rates: 5 - 20 mV/s.

scanrate	Cell capacitance (mF)	Specific capacitance of Pani/CNTs (F/g)	Geometry capacitance mF/cm^2
5 mV/s	1254	196.7	942.9
10 mV/s	1195	187.5	898.5
20 mV/s	1076	168.8	809.0

Table 8.22. Capacitance of asymmetrical cell with MnO$_x$/CNTs positive electrode and M1300 negative electrode in 2.0 M KCl at different scan rates.
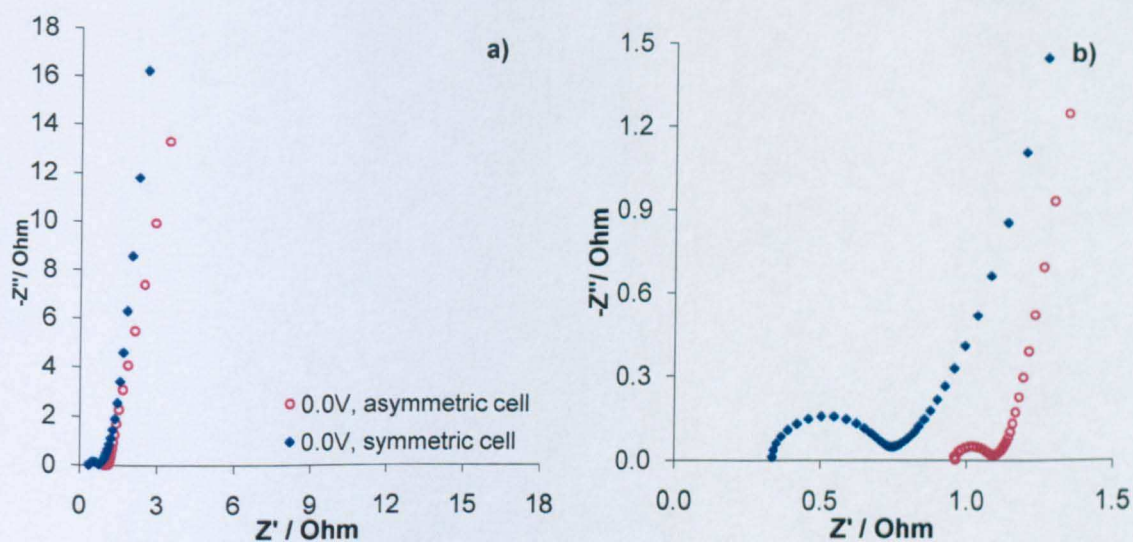
Fig. 8.28. Impedance comparison of capacitive behaviour of PAni/CNTs symmetrical and asymmetrical cells.
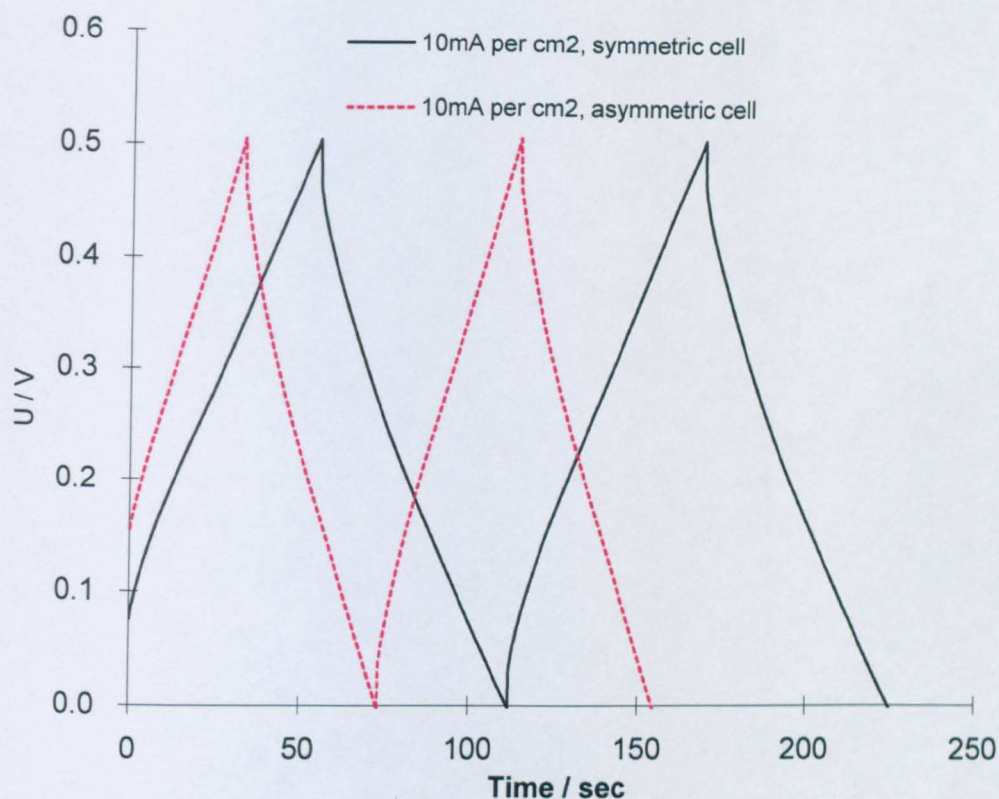
Fig. 8.29. Charge-discharge comparison of the symmetrical PAni/CNTs cell

and the asymmetrical PAni/CNTs | M1300 cell.

Current density	current (mA)	charging time (s)	discharge time (s)	Cell C charge (mF)	Cell C discharge (mF)	Specific discharge capacitance MnO$_x$ (F/g)	Specific discharge M1300 F/g
1 mA/cm^2	1.33	569.9	504.9	1515.9	1343.0	210.7	89.5
2 mA/cm^2	2.66	258.6	244.8	1375.8	1302.3	204.3	86.8
10 mA/cm^2	13.3	57.4	56	1526.8	1489.6	233.7	99.3
20 mA/cm^2	26.6	18.3	16.7	973.6	888.4	139.4	59.2

Table 8.23. Specific capacitance of PAni/CNTs | M1300 asymmetrical cell

from Galvanostatic charge-discharge.

PAni/CNTs | M1300 asymmetrical cell		15mg per electrode (including 15 wt% ALCNTs)1M H₂SO₄ 30 mg M1300		
Current density	current (mA)	charging time (s)	discharge time (s)	Coulombic efficiency
1 mA/cm²	1.33	569.9	504.9	88.59 %
2 mA/cm²	2.66	258.6	244.8	94.66 %
10 mA/cm²	13.3	57.4	56	97.56 %
20 mA/cm²	26.6	18.3	16.7	91.26 %

Table 8.24. Coulombic efficiency of PAni/CNTs \| M1300 asymmetrical cell

at different charge-discharge density.

current density	iR drop (V)	ESR (Ω)	% of total cell voltage
1 mA/cm²	0.0029	1.09	0.58 %
2 mA/cm²	0.0064	1.20	1.28 %
10 mA/cm²	0.034	1.28	6.80 %
20 mA/cm²	0.066	1.24	13.20 %

Table 8.25. iR drop and equivalent cell resistance of asymmetrical cell

with 80 wt% PAni/CNTs positive electrode and M1300 negative electrode.

80 wt% PAni/CNTs	symmetrical cell	asymmetrical cell
cell capacitance (CV at 10 mV/s)	1.575 F	1.195 F
cell capacitance (EIS at 0.0 V)	0.981 F	1.150 F
cell capacitance discharge (at 10 mA cm⁻²)	1.662 F	1.526 F
cell voltage	0.5 V	0.5 V
ESR (at 10 mA cm⁻²)	1.56 Ω	1.28 Ω
charge-transfer resistance	0.1 Ω	0.42 Ω
Coulombic efficiency (at 10 mA cm⁻²)	97.77 %	97.56 %

Table 8.26. Cell performance comparison of symmetrical and asymmetrical

cell with PAni/CNTs electrode

5.3. Summary on Asymmetrical Cell Structure

In general, asymmetrical cells with carbon negative electrode showed

reduced charge-transfer resistance, R_{ct}, compared with their symmetrical

equivalents. In addition, equivalent series resistance (ERS), quantified

from the iR drop observed during the galvanostatic charge-discharge is

noticeably improved with the asymmetrical cell structure. The reasons

behind these improvements will be discussed in Chapter 9, Prototype Cell

Modelling. On the other hand, only one semi-circle can be observed in

the EIS data for both the symmetrical and asymmetrical cells, indicating

the existence of only one RC constant. Also, asymmetrical cells and their

symmetrical equivalents have similar value in Coulombic efficiency.

Extended cell voltage was obtained with the asymmetrical structure for

MnO_x/CNTs cells, due to the higher overpotential on hydrogen evolution

of carbon materials. However, similar situation was not observed with

PAni/CNTs cells.

6. Cell Stacks with Bipolar Electrodes

6.1. Symmetrical Cell Stack

6.1.1. MnO_x/CNTs Stack

Symmetrical cell stack with 60 wt% MnO_x/CNTs as the electrode material

was constructed with a structure shown in Fig. 8.2. The composition and

mass of the electrode was in consistance with the single symmetrical cell,

as described in Section 4.1.3. 2.0 M KCl was applied as the aqueous

electrolyte for the cell stack.

The CV characterisation of this two cell stack, in comparison with the

single symmetrical 60 wt% MnO_x/CNTs cell, is presented in Fig. 8.30. The

voltage of the cell stack was successfully extended to 1.8 V, double that

of the single cell. Note that increased scan rates, e.g. 200 mV/s and

100 mV/s, were applied for stack characterisations, due to the fact that

voltage is divided among all the components in a series circuit. Excellent

capacitive behaviour was recorded with the cell stack, at scan rate up

to 200 mV/s. The stack capacitance and specific capacitance of the

electrode material are presented in Table 8.27. It is to be noted that although comparable values of specific capacitance and geometry capacitance are maintained, the overall stack capacitance is half the value of the single symmetrical cell (Table 8.27). This is due to the fact that when two capacitors are connected in series to form a stack, the overall stack capacitance follows the relation described in Eq.8.10:

$$\frac{1}{C_{stack}} = \frac{1}{C_{cell\,1}} + \frac{1}{C_{cell\,2}} + \frac{1}{C_{cell\,3}} + \cdots + \frac{1}{C_{cell\,n}}$$ Eq. 8.10.
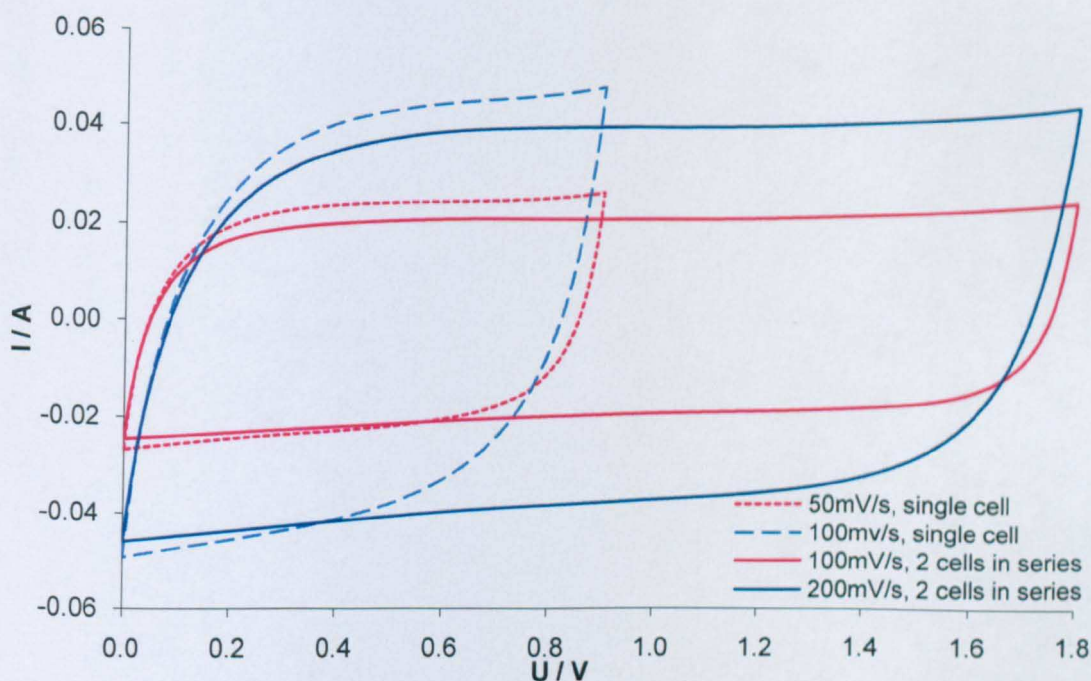
Fig. 8.30. CV comparison of capacitive behaviour of symmetrical MnO_x/CNTs single and stack cells at different scan rates.

60 wt% MnO_x/CNTs symmetrical	cell capacitance (mF)		specific capacitance (F/g)		geometry capacitance (mF /cm²)	
	single cell	two-cell stack	single cell	two-cell stack	single cell	two-cell stack
10 mV/s	519	248	81.5	77.8	781.2	745.9
20 mV/s	486	243	76.8	76.2	736.1	730.8
50 mV/s	461	209	72.3	65.4	693.2	627
100 mV/s	407	201	63.8	62.9	612	603

Table 8.27. Stack capacitance and specific capacitance of a 60 wt% MnO_x/CNTs symmetrical two-cell-stack in 2.0 M KCl at different scan rates, in comparison with a single cell.

The differences in electrochemical performance of the single and
two-cell-stack were also characterised with EIS to reveal more details
on the frequency-dependence of the prototype cells. The EIS data of the
two-cell-stack is presented in Fig. 8.31, in comparison with the single
cell. Specific capacitance and resistance values calculated from the EIS
data are presented in Table 8.28. It is noticed that the stack possessed
one half of the capacitance of a single cell, confirming the results
obtained from CV tests. The specific capacitance of the composite, however,
did not change much by the cell structure (Table 8.27). This
two-cell-stack showed twice the charge-transfer resistance (Table 8.28).

Fig. 8.31. EIS comparison of capacitive behaviour of asymmetrical
MnO_x/CNTs single cell and a two-cell stack; b) enlarged view at high
frequencies.

EIS at 0.0 V 60 wt% MnO_x/CNTs symmetrical cell	single cell	two-cell-stack
overall Capacitance	513 mF	236 mF
Specific capacitance of MnO_x/CNTs	80.5 F/g	74 F/g
electrode geometry capacitance	789.2 mF/cm^2	726.2 mF/cm^2
charge-transfer-resistance	0.72 Ω	1.4 Ω

Table 8.28. Comparison of cell performance by EIS: single and
two-cell-stack of MnO_x/CNTs prototype cells.

The charge-discharge at 2 mA/cm^2 of the two-cell stack is presented in Fig. 8.32, in comparison with the single cell. Linear and symmetrical charge-discharge process was retained in the cell-stack. The details of charge-discharge performance of this cell-stack are presented in Table 8.29. The equivalent series resistances of the stack at different current density, calculated from iR drop during charge-discharge tests, are listed in Table 8.30. It is interesting to note that the equivalent series resistance of this cell stack is about 2.7 Ω (Table 8.30). Since the individual cell has an equivalent series resistance of 2.06 Ω, the 2 cell stack is expected to have an ESR of 4.12 Ω. The test result, however, showed a much smaller value. This result suggests an encouraging fact that ESR is determined by many factors, e.g. contact resistance, and will not simply multiple in stacks.
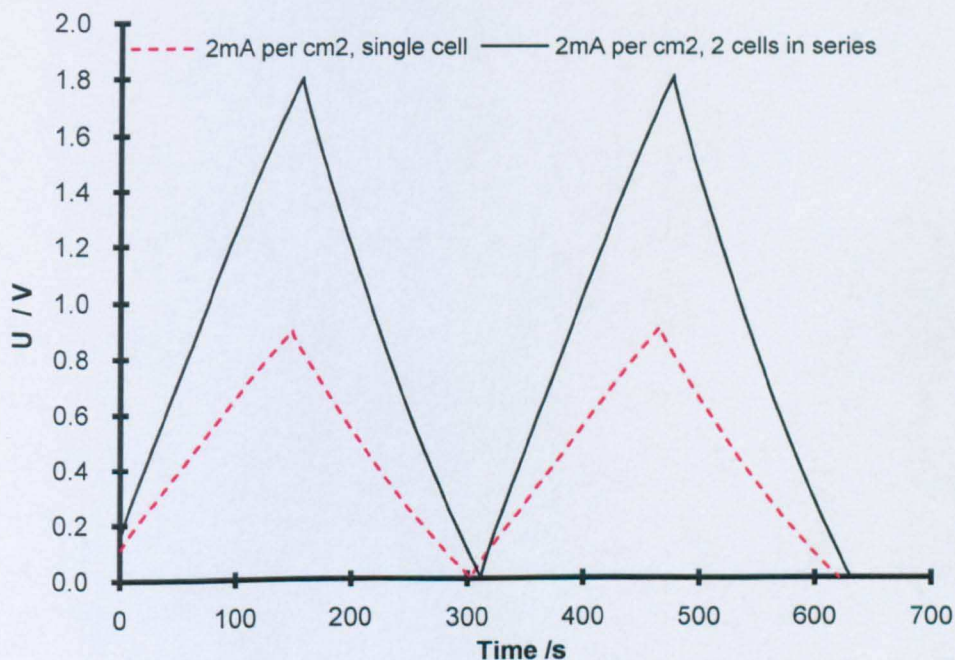
Fig. 8.32. Charge-discharge comparison of asymmetrical MnO$_x$/CNTs single cell and a two-cell stack.

A general comparison on the performance of single and two-cell stack is presented in Table 8.31. This two-cell-stack can achieve a cell voltage of 1.8 V, a doubled value of a single cell. The total capacitance of the

two-cell-stack is half the value of a single cell, since the two single

cells were connected in series. Naturally, charge-transfer-resistance

is doubled in the cell stack. On the other hand, the equivalent series

resistance of the stack is 131 % of value of the single cell. Single cell

and the stack have similar Coulombic efficiency during charge-discharge,

and similar specific capacitance value around 80 F/g.

MnO_x/CNTs 2-cell-stack	charge time (s)	discharge time (s)	charge C (mF)	discharge C (mF)	specific C (F/g)	Coulombic efficiency
1 mA/cm^2	340.9	319.6	251.9	236.1	74.1	93.75 %
2 mA/cm^2	163.6	155.9	241.8	230.4	72.3	95.29 %
10 mA/cm^2	29	27.8	214.3	205.4	64.4	95.86 %
20 mA/cm^2	13.8	12.1	203.9	178.8	56.1	87.68 %

Table 8.29. Capacitive behaviour of symmetrical 60 wt% MnO_x/CNTs

two-cell-stack at various current densities.

current density	iR drop (V)	ESR (Ω)	% of total cell voltage
1 mA/cm^2	0.0071	2.67	0.39 %
2 mA/cm^2	0.0134	2.12	0.74 %
10 mA/cm^2	0.0717	2.70	3.98 %
20 mA/cm^2	0.1495	2.81	8.31 %

Table 8.30. IR drop and equivalent cell resistance of two 60 wt% MnO_x/CNTs

symmetrical cell stack.

60 wt% MnO_x/CNTs	single cell	two-cell-stack
cell capacitance (CV at 10 mV/s)	0.496 F	0.210 F
cell capacitance (EIS at 0.0 V)	0.525 F	0.230 F
cell capacitance discharge (at 10 mA cm^{-2})	0.445 F	0.205 F
cell voltage	0.9 V	1.8 V
ESR (at 10 mA cm^{-2})	2.06 Ω	2.70 Ω
charge-transfer resistance	0.72 Ω	1.4 Ω
Coulombic efficiency (at 10 mA cm^{-2})	96.59 %	95.86 %

Table 8.31. General cell performance comparison on 60 wt% MnO_x/CNTs single

and two-cell-stack.

6.1.2. PPy/CNTs Two Cell Stack

PPy/CNTs stack is constructed with two identical symmetrical PPy/CNTs cells connected in series. The electrode is fabricated in the same method as described in Section 4.2. 1 M KCl is used as aqueous electrolyte in the stack.

The capacitive performance of a single cell and the two-cell-stack is compared in Fig. 8.33. As could be observed, the cell voltage is extended from 0.6 V to 1.1 V in the stack. Comparable capacitance is obtained in the stack and the single cell, as listed in Table 8.32.
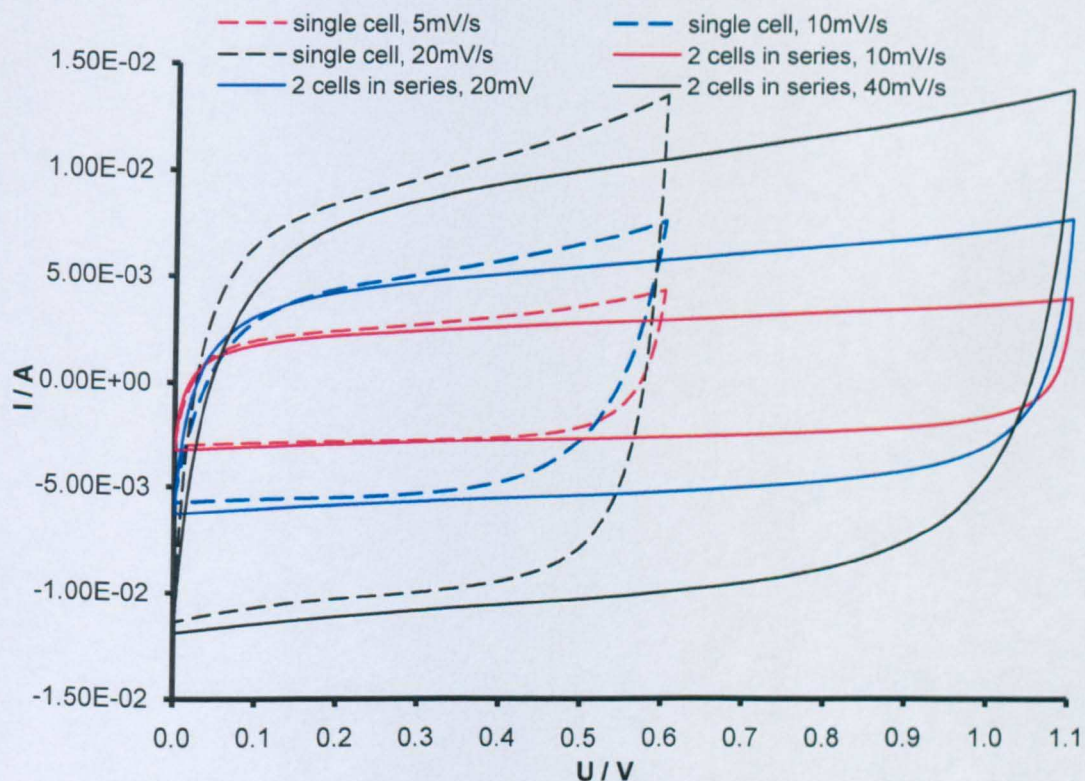
Fig. 8.33. CV comparison of capacitive behaviour of symmetrical PPy/CNTs single and stack cells at different scan rates.

PPy/CNTs symmetrical	cell capacitance (mF)		specific capacitance (F/g)		geometry capacitance (mF /cm²)	
	single cell	two-cell stack	single cell	two-cell stack	single cell	two-cell stack
5 mV/s	551	273	86.4	85.6	828.6	821
10 mV/s	519.5	273	81.5	85.6	781.2	821
20 mV/s	489.5	271.25	76.8	85.1	736.1	815.8
40 mV/s	443.8	253.8	69.6	79.6	667.4	763.4
50 mV/s	422	252	66.2	79.1	634.6	757.8
100 mV/s	352.5	209	55.3	65.6	530.1	628.6

Table 8. 32. Capacitance of symmetrical PPy/CNTs two-cell-stack in 1.0 M KCl at different scan rates, in comparison with single cell.

The capacitive performance of the cell stack is further investigated with EIS and the data is presented in Fig.8.34, in comparison with a single cell. Table 8.33 compares the specific values of a single cell and a two-cell-stack, calculated from EIS. Similar to the case of MnO_x/CNTs stack, PPy/CNTs stack has similar specific capacitance in single cell and cell stack. The stack has an overall capacitance half the value of a single cell and a R_{ct} twice the value of the single cell.
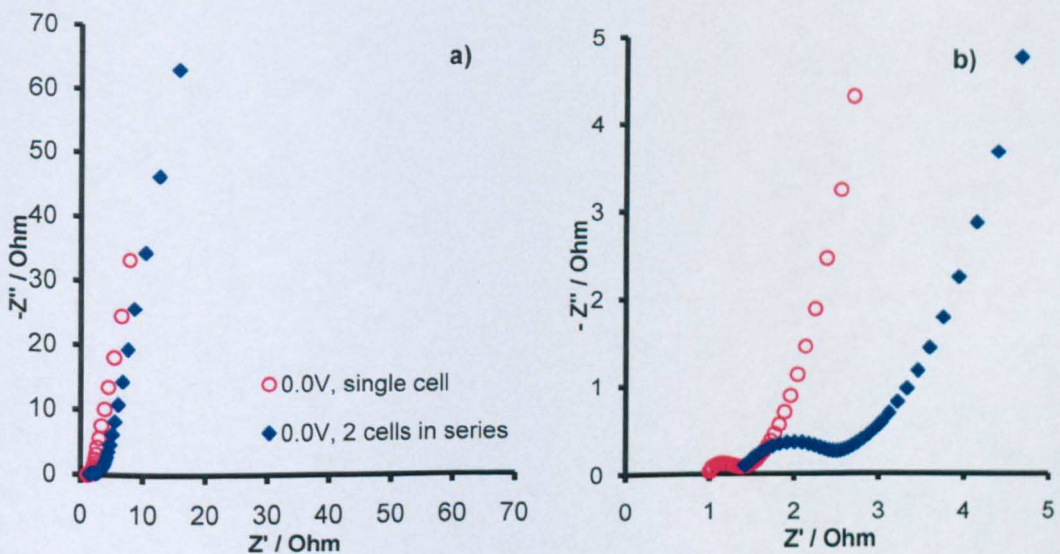
Fig. 8. 34. Impedance comparison of capacitive behaviour of symmetrical PPy/CNTs a single cell and a two-cell stack; b) enlarged view at high frequencies.

EIS at 0 V of symmetrical PPy/CNTs	Single cell	two-cell-stack
overall capacitance	466 mF	252 mF
Specific capacitance of PPy/CNTs	73.1 F/g	80.6 F/g
electrode geometry capacitance	700.8 mF/cm^2	773.1 mF/cm^2
charge-transfer-resistance	0.5 Ω	1.1 Ω

Table 8.33. Comparison of cell performance by EIS: single and

two-cell-stack of PPy/CNTs prototype cells.

Linear and symmetrical charge-discharges have been identified with PPy/CNTs two-cell stack at various current densities, as demonstrated in Fig. 8.35. The discharge capacitance and Coulombic efficiency of the stack at different current densities are presented in Table 8.34. Moreover, the equivalent series resistance of the stack, calculated from iR drop, are listed in Table 8.35. A comparison of the charge-discharge between a single cell and a two-cell stack at 2 mA/cm^2 is presented in Fig. 8.36. A more general comparison, highlighting the important parameters of the single cell and the two-cell stack, is presented in Table 8.36.
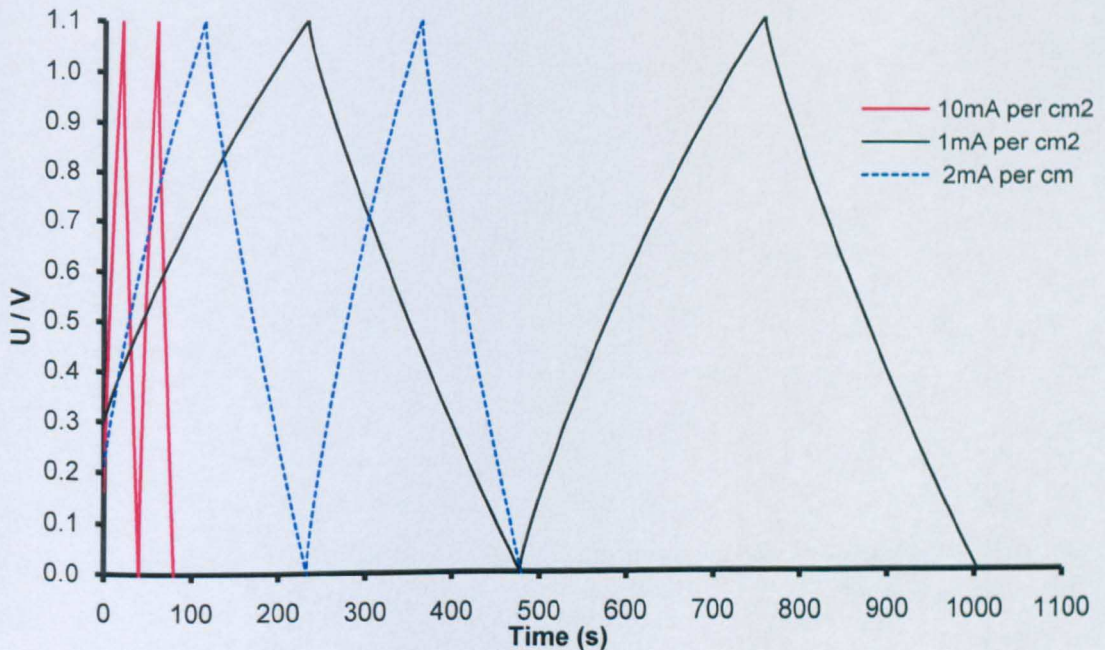
Fig. 8.35. Galvanostatic charge-discharge of PPy/CNTs symmetrical two

cell stack at various current densities.

PPy/CNTs symmetrical two cell stack	charge time (s)	discharge time (s)	discharge C (mF)	Discharge specific C (F/g)	Coulombic efficiency
20 mA/cm^2	8.5	8.1	195.9	61.5	96.94 %
10 mA/cm^2	19.8	19.3	233.4	73.2	97.47 %
2 mA/cm^2	129.5	117.6	284.4	89.2	90.81 %
1 mA/cm^2	279	247.2	298.9	93.8	88.60 %

Table 8.34. Capacitive behaviour of symmetrical PPy/CNTs two-cell-stack

at various current rates.

current density	iR drop (V)	ESR (Ω)	iR drop : total cell voltage (%)
1 mA/cm^2	0.01098	4.13	1.00 %
2 mA/cm^2	0.0197	3.71	1.79 %
10 mA/cm^2	0.108	4.06	9.82 %
20 mA/cm^2	0.1885	3.55	17.14 %

Table 8.35. ESR of symmetrical PPy/CNTs two-cell-stack.
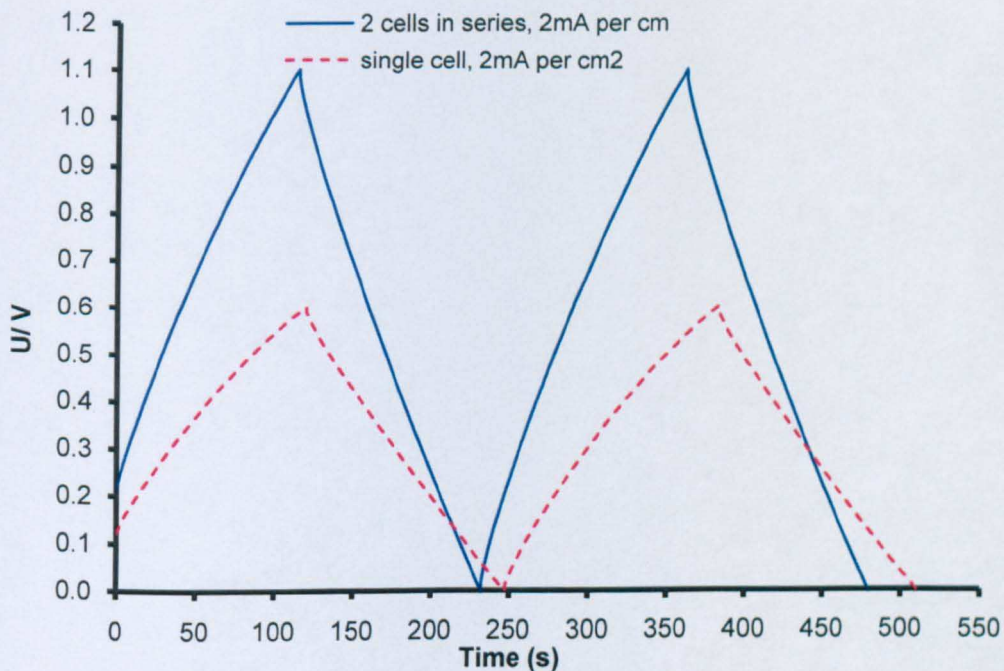
Fig. 8.36. Comparison of single and 2-cell PPy/CNTs symmetrical stack

charge-discharge performance.

PPy/CNTs symmetrical cell	single cell	2 cell stack
cell capacitance (CV at 10 mV/s)	0.519 F	0.273 F
cell capacitance (EIS at 0.0 V)	0.466 F	0.252 F
cell capacitance discharge (at 10 mA cm^{-2})	0.452 F	0.233 F
cell voltage	0.6 V	1.1 V
ESR (at 10 mA cm^{-2})	1.98 Ω	4.06 Ω
charge-transfer resistance	0.5 Ω	1.1 Ω
Coulombic efficiency (at 10 mA cm^{-2})	93.55 %	97.47 %

Table 8.36. General parameters of PPy/CNTs single cell and two-cell stack.

6.2. Asymmetrical Cell Stack

As discussed in Section 5, asymmetrical cell with carbon negative electrode is able to achieve higher cell voltage with a reduced charge-transfer resistance and ERS, particularly with MnO_x/CNTs cells. Therefore, cell-stack is also constructed with asymmetrical MnO_x/CNTs | M1300 cells.

This asymmetrical MnO_x/CNTs | M1300 two-cell-stack is characterised with CV, and the results are presented in Fig. 8.37 in comparison with the single asymmetrical cell. Capacitance and specific capacitance values calculated from CV are listed in Table 8.37, together with the values calculated from a single asymmetrical cell. The stack was able to operate over a voltage range of 0.0 – 1.9 V, 210 % of the single cell. As expected, the stack capacitance is 52.1 % of the value of a single cell. Moreover, the specific capacitance of MnO_x/CNTs composite has similar value in single cell and cell-stack, as showed in Table 8.37. This result confirms that the two asymmetrical cells connected in series in the stack functioned properly.
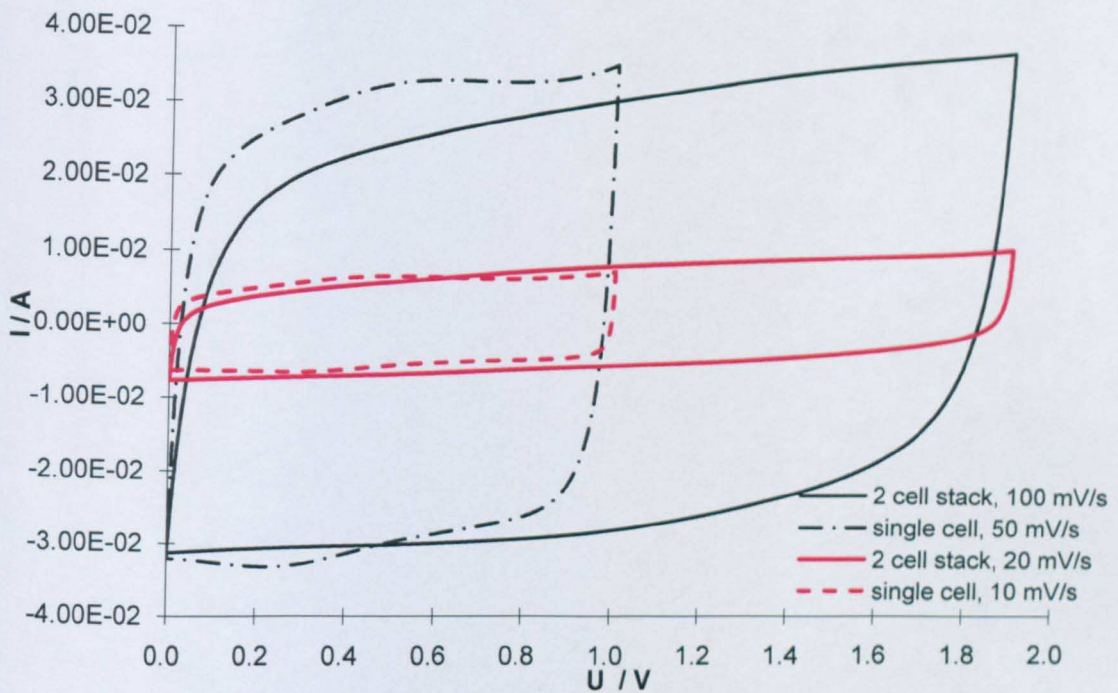
Fig. 8.37. CV of asymmetrical MnO_x/CNTs | M1300 two-cell stack in

comparison with a single cell.

MnO_x/CNTs | M1300 asymmetrical	cell capacitance (mF)		specific capacitance (F/g)		geometry capacitance (mF /cm^2)	
	single cell	two-cell stack	single cell	single cell	two-cell stack	single cell
10 mV/s	606	331.1	95.1	103.9	911.3	995.8
20 mV/s	637.5	332.1	100	104.2	958.6	998.8
50 mV/s	620	312	97.3	97.9	932.3	938.3
100 mV/s	591	289.3	92.7	90.8	888.7	870.1
200 mV/s	528.1	266.1	82.8	83.5	794.1	800.3

Table 8.37. Capacitance of asymmetrical MnO_x/CNTs | M1300 two-cell-stack

in 2.0 M KCl at different scan rates, in comparison with single cell

This asymmetrical two-cell-stack is then characterised with EIS and the

result is presented in Fig. 8.38 in comparison to the single cell. A more

detailed comparison in specific values is listed in Table 8.38. The

MnO_x/CNTs composite has very similar specific capacitance value in single

cell and cell stack, which is well in agreement with the results obtained
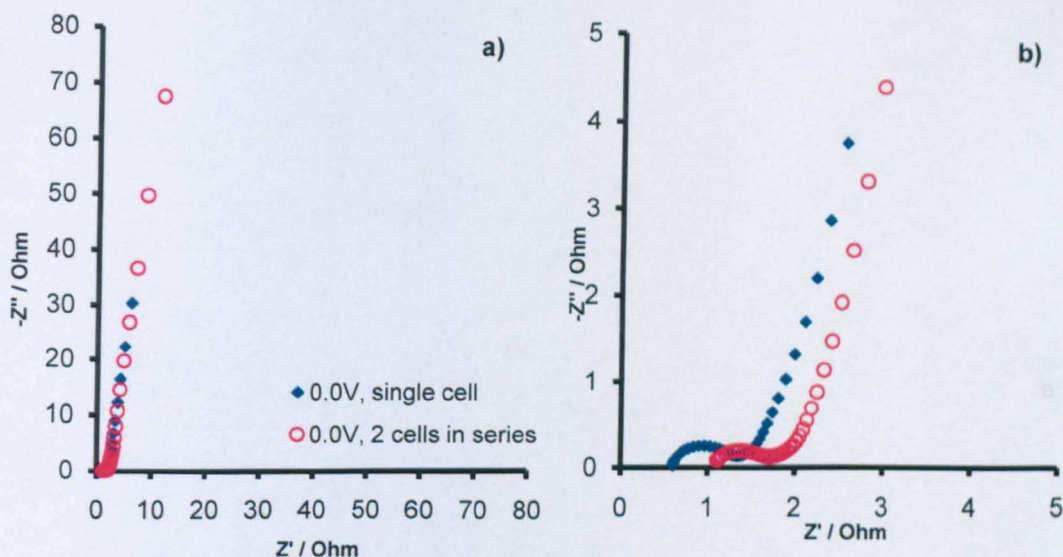
from CV tests (Table 8.38).
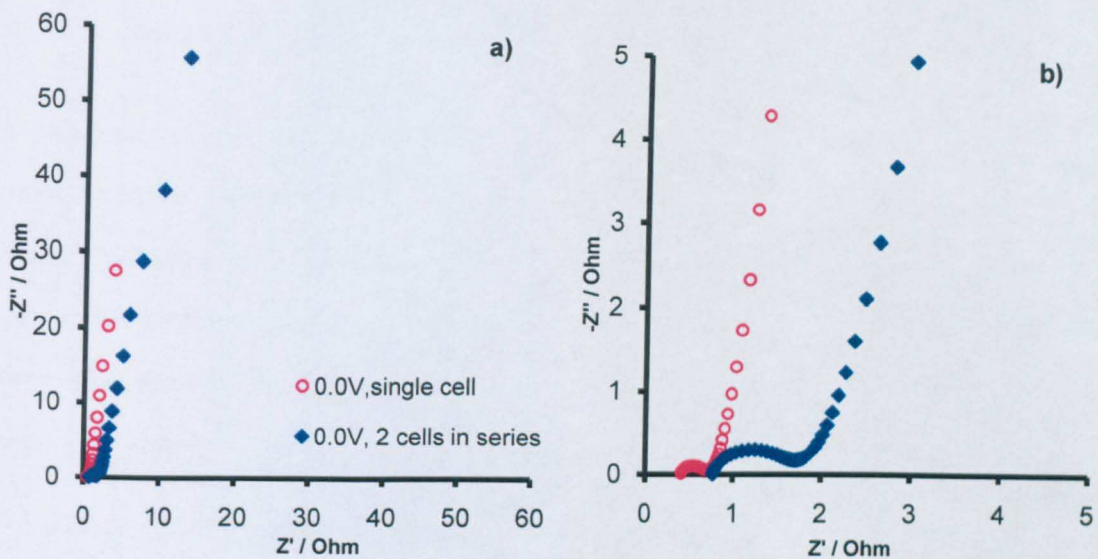
Fig. 8.38. EIS comparison of capacitive behaviour of an asymmetrical MnO$_x$/CNTs | M1300 single cell and a two-cell stack; b) enlarged view at high frequencies.

EIS at 0 V of asymmetrical MnO$_x$/CNTs | M1300	Single cell	two-cell-stack
overall capacitance	577 mF	285 mF
Specific capacitance of MnO$_x$/CNTs	92.3 F/g	91.2 F/g
electrode geometry capacitance	874.2 mF/cm^2	863.8 mF/cm^2
charge-transfer-resistance	0.35 Ω	0.92 Ω

Table 8.38. Comparison of cell performance by EIS: single and two-cell-stack of asymmetrical MnO$_x$/CNTs | M1300 prototype cells

The charge-discharge at 10 mA/cm^2 of the asymmetrical two-cell stack is presented in Fig. 8.39, in comparison with the corresponding single cell. Linear and symmetrical charge-discharge process was retained in the cell-stack. The details of charge-discharge performance of this cell-stack are presented in Table 8.39. The Coulombic efficiency, however, is rather low at the discharge density of 2 mA/cm^2, indicating of energy loss during charge-discharge process. The equivalent series resistances

of the stack at different current densities, calculated from iR drop
during charge-discharge tests, are listed in Table 8.40.

A general comparison on the performance of single and two-cell stack is
presented in Table 8.41. This asymmetrical two-cell-stack can achieve
a cell voltage of 1.9 V, 0.1 V higher than its corresponding symmetrical
cell-stack (Table 8.31). The capacitance of the two-cell-stack measured
by different methods, i.e. CV, EIS, charge-discharge, is in consistency,
and   is   half   the   value   of   the   asymmetrical   single   cell.
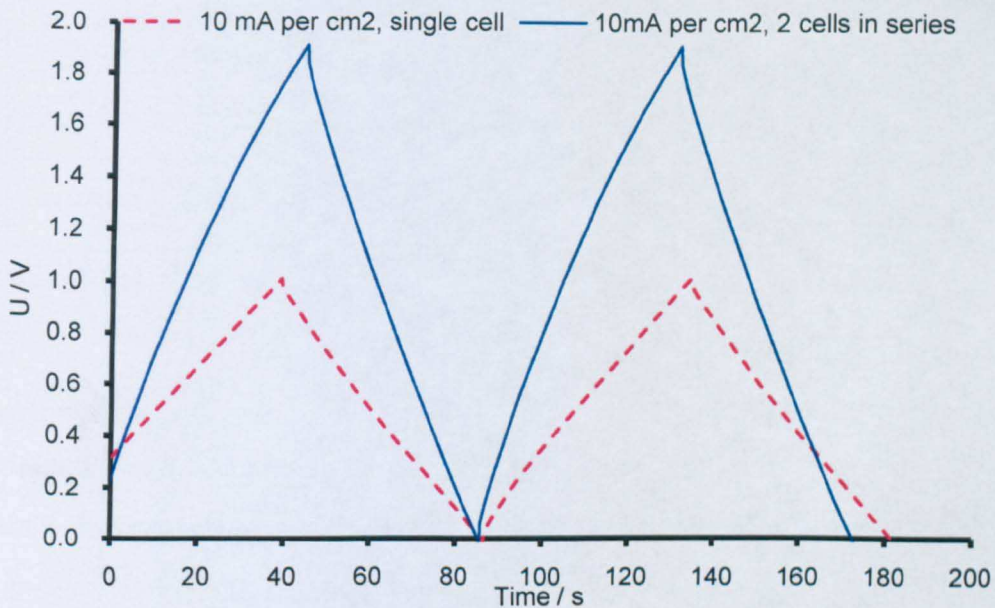
Fig. 8.39. Charge-discharge comparison of an asymmetrical $MnO_x/CNTs$ |
M1300 single cell and a two-cell stack.

Current density	charge time (s)	discharge time (s)	cell C charge (mF)	cell C discharge (mF)	Specific C of MnO_x (F/g)	Coulombic efficiency
2 mA/cm^2	335.4	236.7	469.6	331.4	104.0	70.57 %
10 mA/cm^2	46.4	40.6	324.8	284.2	89.2	87.50 %
20 mA/cm^2	21.4	18.9	299.6	264.6	83.0	88.32 %

Table 8.39. Specific capacitance of asymmetrical 60 wt% $MnO_x/CNTs$

two-cell-stack at various current densities

current density	iR drop (V)	ESR (Ω)	% of total cell voltage
2 mA/cm²	0.014	2.63	0.74 %
10 mA/cm²	0.061	2.28	3.21 %
20 mA/cm²	0.119	2.24	6.26 %

Table 8.40. iR drop and equivalent cell resistance of two 60 wt% MnO$_x$/CNTs symmetrical cell stack.

60 wt% MnO$_x$/CNTs | M1300	single cell	two-cell-stack
cell capacitance (CV at 10 mV/s)	0.606 F	0.210 F
cell capacitance (EIS at 0.0 V)	0.577 F	0.285 F
cell capacitance discharge (at 10 mA cm^{-2})	0.606 F	0.284 F
cell voltage	1.0 V	1.9 V
ESR (at 10 mA cm^{-2})	0.86 Ω	2.28 Ω
charge-transfer resistance	0.35 Ω	0.92 Ω
Coulombic efficiency (at 10 mA cm^{-2})	96.30 %	87.50 %

Table 8.41. General cell performance comparison of asymmetrical MnO$_x$/CNTs \| M1300 single and two-cell-stack.

6.3. Summary on Cell Stack

Both symmetrical and asymmetrical cells can be constructed into cell stacks, achieving a cell voltage twice the value of their single cell equivalent. The composites in cell stack retain their specific capacitance value as in a single cell. Also, cell stacks exhibit similar values in Coulombic efficiency with their corresponding single cells. These indicate that connecting two cells in series does not affect the electrochemical performance of the electrode materials. Generally, the cell stacks exhibit charge-transfer resistance twice the value of their single cell equivalent. On the other hand, equivalent series resistance of the cell stack is determined by various parameters, and therefore, does not multiply with the stacking.

It is noticed that with the two single capacitors connected in series, the capacitance of the stack is consequently half the value of each single capacitor. However, this reduction in capacitance can be compensated by connecting capacitors in parallel, e.g. increasing the size of each electrode. Hence, desirable voltage and capacitance can be achieved by connecting appropriate number of capacitors in series and in parallel.

1. Introductions

By modelling an electrochemical system with equivalent circuits, the individual processes can be distinguished. This made it possible to interpret and predict the behaviour of the electrochemical system, which is of significant importance in understanding and improving the systems. On the other hand, one of the most attractive aspects of EIS is that it allows researchers to investigate the direct connection between the behaviour of a real system and the idealised model circuits consisting of discrete electrical components (Raistrict et al., 2005). Therefore, EIS data of prototype cells were chosen to be fitted to exam the models proposed.

Simulation via an equivalent circuit, consisting of resistors and capacitors that pass current with the same amplitude and phase angle as the real system does, is one of the most commonly used methods in modeling (Bard and Faulkner, 2001). Equivalent circuit models are of particular interest in impedance spectroscopy as the frequency response behaviour of some basic electrical circuits is extensively studied and well understood (Raistrict et al., 2005). Therefore, it is regarded as an effective technique in discovering the frequency dependencies of the R and C elements in the system (Bard and Faulkner, 2001).

However, there are some limitations regarding simulation by equivalent circuits and this method should be handled with caution (Raistrict et al., 2005). First of all, equivalent circuits are not unique, i.e. several different circuits can have exactly the same, or very similar, impedance behaviour under investigation (Bard and Faulkner, 2001, Brett and Brett, 1993). Secondly, the effects of geometry on the current distribution are still to be thoroughly studied. Thirdly, some electrochemical properties

treated as frequency independent, e.g. conductivity, interface

capacitance, are actually frequency dependent. Thus, equivalent circuit

should only be used after a comprehensive understanding of the electrode

processes has been established (Raistrict et al., 2005).

2. Electrochemical Processes in Prototype Cells

Some explicit descriptions on the charge and discharge processes of an

electrochemical device and the mechanisms behind it have been given

(Barsoukov, 2005): the electric charge travels through an electronic

pathway from one active material to another, experiencing Ohmic

resistance; it passes between electronic and ionic conductive medium

interface through electrochemical reactions, suffering from energy-loss

based on the Butler-Volmer equation; it then journeys through the ionic

pathway in the electrolyte before reaching the counter electrode, often

through the electrolyte-filled porous separator, facing Ohmic resistance

(Barsoukov, 2005). All these processes impair the power and energy

performance of the electrochemical cell.

These processes in an electrode system mentioned above can be represented

as impedances (Bard and Faulkner, 2001), as demonstrated in Fig. 9.1.

Different steps are driven by different overpotentials, η: η_{mt} the

mass-transfer overpotential, η_{ct} the charge-transfer over potential, and

η_{rxn} the overpotential for a preceding reaction (Bard and Faulkner, 2001).
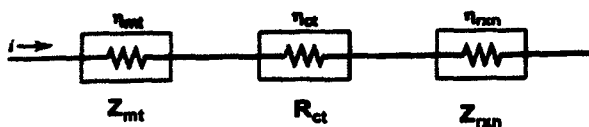
Fig.9.1. Schematic view of processes in an electrode reaction represented

as impedances (Bard and Faulkner, 2001).

Therefore, the elements in a single prototype cell can be represented

with the equivalent circuit in a similar manner (Fig. 9.2). In Fig. 9.2,

$\sum R_{Ohmic}$ is the overall Ohmic resistance of all elements, including electrolytic resistance, contact resistance, etc. $Z_{electrode1}$ and $Z_{electrode2}$ represent the impedance occurring at the two electrodes during the electrochemical processes. $R_{separator}$ is the ionic resistance when charges travel across the separator. R_1 and C_{dl1} stand for the interfacial resistance between current collector | positive electrode and the corresponding double layer capacitance; R_2 and C_{dl2} represent the interfacial resistance between positive electrode | electrolyte and its corresponding double layer capacitance. Meanwhile, R_3 and C_{dl3}, R_4 and C_{dl4} are the equivalent on the negative electrode.
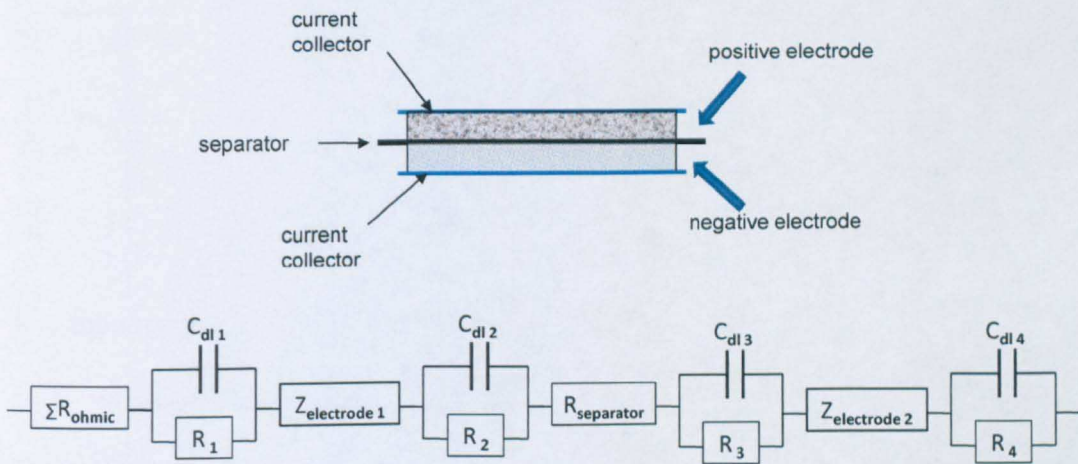
Fig. 9.2. A schematic illustration of electrochemical elements in a supercapacitor.

On the other hand, by analysing the EIS data, it is possible to distinguish processes with different kinetics and reconstruct the electrochemical processes within the supercapacitors. As shown in Fig. 9.3, a semicircle, representing the charge transfer resistance within the cell is followed by a transient diffusion region. At lower frequencies, this diffusion process gradually changes to a vertical line, indicating limited diffusion length and boundaries with limited thickness. It is also suggested that the importance of the resistive elements within the system can be quantified by their ratio (Barsoukov, 2005).
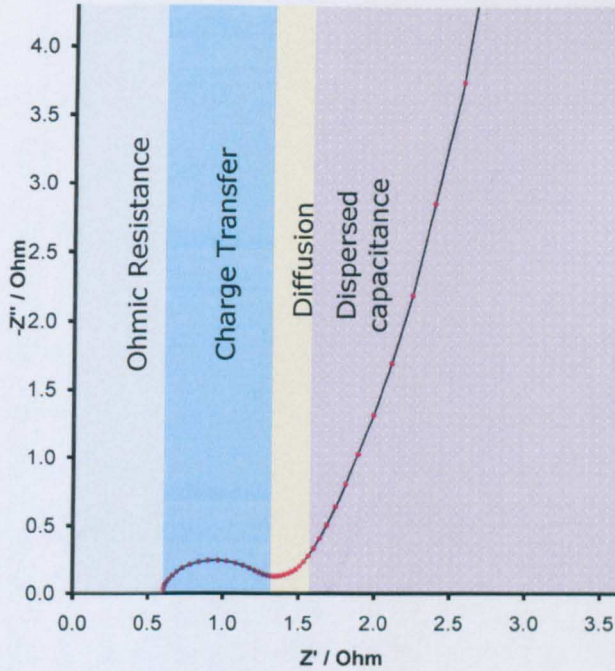
Fig. 9.3. General view of the kinetic steps of a prototype cell as interpreted by impedance spectroscopy.

3. Equivalent Circuits

3.1. Linear Systems

Localised processes, which occur in a specific volume and is negligible compared to the volume of the entire system, are described as linear systems (Barsoukov, 2005). The linear system can be represented by basic elements, e.g. resistors and capacitors, for its loss and storage (Barsoukov, 2005). In a linear system, the current response I(t) to an applied potential perturbation U(t) is determined by linear differential equations (Sluyters-Rehbach, 1994).

For a sinusoidal U(t):

$U(t) = \Delta U = U_m \sin(\omega t)$ Eq. 9.1.

$I(t) = \Delta I + I_m \sin(\omega t+\varphi) = I_m [\cos \varphi \sin\omega t + \sin \varphi \cos\omega t]$ Eq. 9.2.

Where φ is phase angle.

These linear systems show well defined behaviour. The fundamental

233

relationships for these systems with resistors, inductors and capacitors

are described below.

Resistor: $V(t) = R \cdot I(t)$ Eq. 9.3.

Inductor: $V(t) = L \cdot dI(t)/dt$ Eq. 9.4.

Capacitor: $C = dq(t)/dV(t)$ and $I(t) = C \cdot dV(t)/dt$ Eq. 9.5.

The Randles circuit, as presented in Fig. 9.4, is often used in

interpreting active electrode systems. In the Randles circuit, i_c of

interfacial double-layer charging is in parallel with i_f, which is

originated from faradaic processes. R_Ω is the Ohmic resistance, e.g.

electrolyte resistance. The faradaic processes, Z_f, can be subdivided

into series resistance R_s and pseudocapacitance C_s; or alternatively

charge-transfer resistance R_{ct} and the mass-transfer related Warburg

impedance Z_w (Bard and Faulkner, 2001).
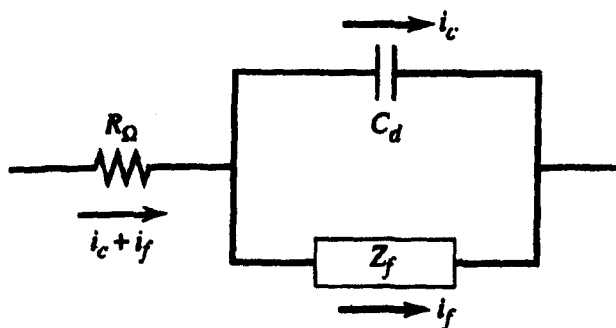
where Z_f can be further divided into:
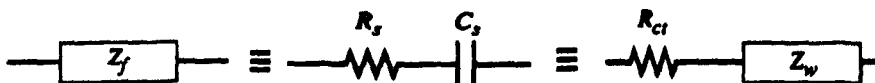
Fig. 9.4. The Randles circuit of a reactive system (Bard and Faulkner,
2001).

3.2. Kramers-Kronig Analysis

Although not all systems are linear, linear relationship is assumed

between the perturbation and response when small perturbation is applied

during EIS tests (Brett and Brett, 1993). In a linear system, dependence

between magnitude and phase, Z' and Z'' are expected. Hence, it is possible

234

to evaluate the quality of the EIS data by examining the dependence between Z' and Z''. The Kramers-Kronig analysis is such a method commonly employed to validate the quality of the data obtained from EIS.

According to the Kramers-Kronig transform, the real part of the impedance can be calculated from its corresponding imaginary part (Boukamp, 1995):

$$Z'(\omega) = R_\infty + \frac{2}{\pi} \int_0^\infty \frac{xZ''(x) - \omega Z''(\omega)}{x^2 - \omega^2} dx \qquad \text{Eq. 9.6.}$$

while the imaginary part of the impedance can be obtained in a similar manner (Boukamp, 1995):

$$Z''(\omega) = \frac{2\omega}{\pi} \int_0^\infty \frac{Z'(x) - Z'(\omega)}{x^2 - \omega^2} dx \qquad \text{Eq. 9.7.}$$

A pseudo chi-squared fit value, χ^2_{ps}, is used to quantify the 'fit' (Boukamp, 1995):

$$\chi^2_{ps} = \sum_{i=1}^N \omega_i \left([Z'_i - Z'(\omega_i)]^2 + [Z''_i - Z''(\omega_i)]^2 \right) \qquad \text{Eq. 9.8.}$$

In applications, the Kramer-Kronig analysis can be performed by direct integration of the equations, by experimental observation of linearity, by regression of specific electrical circuit models, and by regression of generalised measurement models (Orazem and Tribollet, 2008). In this thesis, the Kramer-Kronig analysis is carried out by fitting an equivalent circuit model to the data spectra, as proposed by Boukamp (Boukamp, 1995). Such a model consists of m serially connected Voigt elements, as shown in Fig. 9.5, to ensure its linearity.
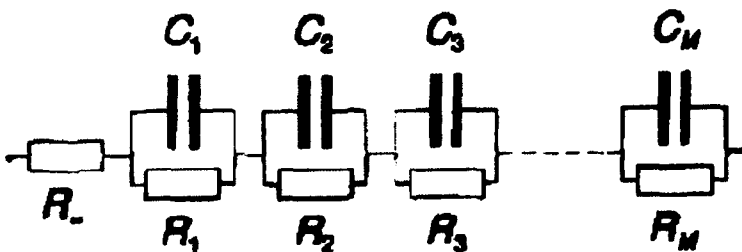
Fig. 9.5. Equivalent circuit model for the linear Kronig-Kramers transform test of data in the impedance representation (Boukamp, 1995).

If the Kramers-Kronig fit is poor, then the data spectrum is not

Kramer-Kronig transformable and therefore is non-linear. In such cases,

no suitable equivalent circuit models should be established since the

concept of equivalent circuit models are based on linear systems (Orazem

and Tribollet, 2008).

Kramers – Kronig tests were conducted on a Frequency Response Analyser

(Eco Chemie B.V) with all prototype cells in this work. The chi square

values for each cell were listed in Table 9.1. As shown, X_{ps}^2 values for

the prototype cells are generally smaller than 1.5E-05, indicating a

probability << 0.0015% of being non-linear. Therefore, the EIS data

obtained from the prototype cells are qualified to be modeled with

equivalent circuits.

MnO_x/CNTs Cells	potential	X_{ps}^2	X'_{ps}^2	X''_{ps}^2
symmetric single cell	0.0 V	4.82E-06	2.09E-06	2.73E-06
2 symmetric cells in series	0.0 V	1.57E-06	6.10E-07	9.59E-07
asymmetric single cell	0.0 V	4.60E-06	2.19E-06	2.41E-06
2 asymmetric cells in series	0.0 V	1.38E-05	6.79E-06	7.00E-06
PAni/CNTs cells symmetric single cell	0.0 V	3.12E-06	1.47E-06	1.65E-06
2 symmetric cells in series	0.0 V	7.36E-06	3.46E-06	3.90E-06
asymmetric single cell	0.0 V	6.05E-07	2.78E-07	3.27E-07

Table 9.1. Kramers – Kronig tests of prototype cells with different cell structures.

An obvious drawback of the Kramer-Kronig analysis is that it requires

the integration of the range of frequency from zero to infinite (Eq. 9.6

and Eq. 9.7), which is impossible in practice. Thus, the Kramer-Kronig

analysis carried out normally involves assumptions about the behaviour

of the system outside the frequency range tested. This might introduce

certain levels of inaccuracy (Orazem and Tribollet, 2008).

3.3. Distributed Elements

Due to the inhomogeneity of the electrodes and the existence of non-local processes, e.g. diffusion, nonlinearity is inevitable in reality (Raistrict et al., 2005). Therefore, distributed circuit elements are introduced into the equivalent circuits, in addition to linear elements, in an attempt to build more accurate models to resemble the electrochemical system.

Compared to the well-defined real elements, e.g. resistor and capacitor, the distributed elements are more abstract in nature (Macdonald and Johnson, 2005). They are related to the finite spatial extension of any real system and are essential in interpreting impedance spectra (Macdonald and Johnson, 2005). It usually takes two or more coordinates in defining a distributed process, e.g. time, space, frequency, etc (Barsoukov, 2005).

In analysing the prototype cell, it was found that a linear relation exist between $-Z''$ and $1/\omega$, as demonstrated in Fig. 9.6. For an ideal capacitor, the impedance, C, is: $Z_c = \frac{1}{2\pi f C} = \frac{1}{\omega C}$ (Eq. 8.7), with a zero real component. Therefore, the linear relation between $-Z''$ and $1/\omega$ of the prototype cell suggests a constant capacitance C at various frequencies. In other words, the total capacitance of the prototype cell is not dispersed with the frequencies. Hence, the distribution of the impedance of the cell is caused by the distributed resistive elements.
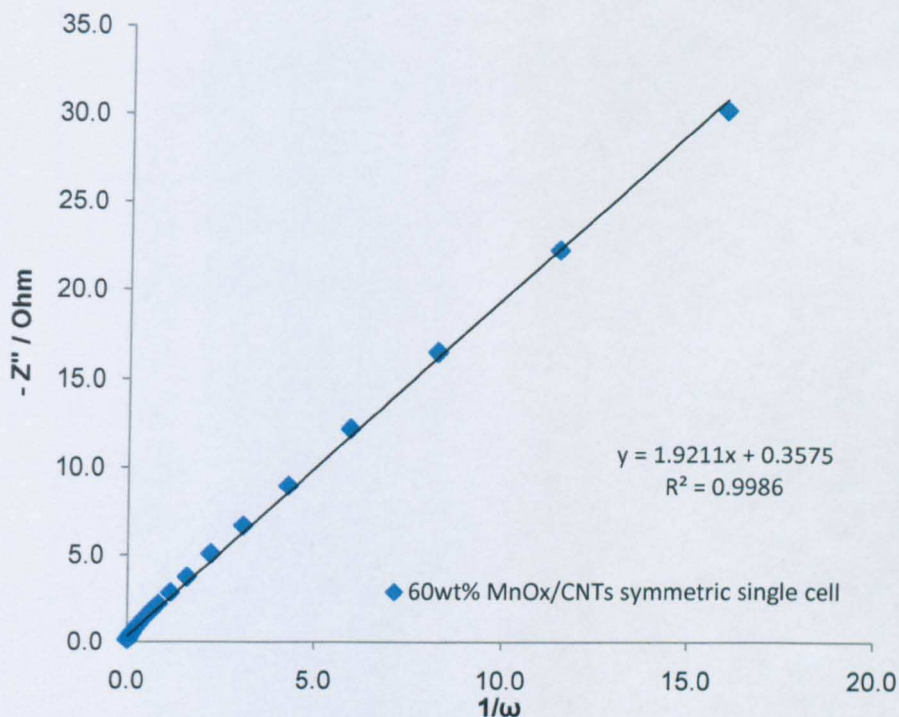
Fig. 9.6. A linear relation between $-Z''$ and $1/\omega$ of a symmetric 60wt% MnO_x/CNTs single cell.

Two techniques are commonly applied in interpreting the distributed elements: transmission line and constant phase element. These two models will be explained and fitted with EIS data of the prototype cell to exemplify their validity in Section 4 of this chapter.

4. Models for Distributed Elements

4.1. Transmission Line Model

The transmission line model (TLM) is a common approach to interpret the impedance data of distributed elements. The underlying principle of TLM is that the impedance at any frequency can be expressed as a series or parallel combinations of capacitance and resistance, as shown in Fig. 9.7 (Bard et al., 2008b). One of the advantages of TLM is that it can physically represent the porosity and inhomogeniety on the surface of an electrode with resistors and capacitors.
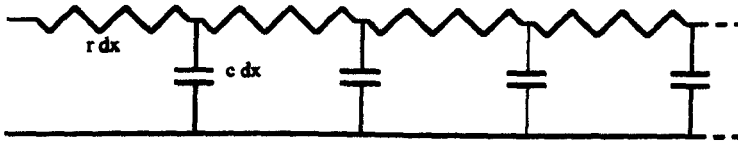
Fig. 9.7. A resistive-capacitive transmission line model for

semi-infinite diffusion (Raistrict et al., 2005).

An enhanced transmission line model, as shown in Fig. 9.8, with two rails

of resistance, has been developed by Albery and co-workers (Albery et

al., 1989) for a conducting polymer electrode system. In this model, C_Σ

is the distributed pseudocapacitance; while $R_\Sigma^{electron}$ and R_Σ^{ion} are the

distributed electronic and ionic resistance respectively.
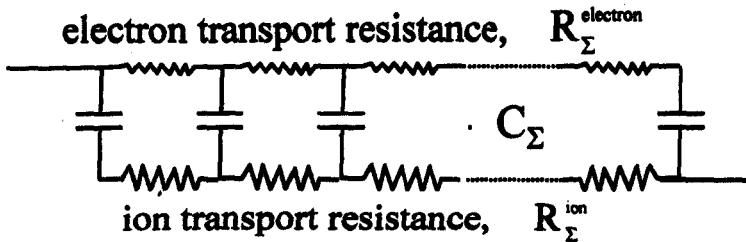
Fig. 9.8. A two-rail-transmission-line model with electron transport

resistance and ion transport resistance (Albery et al., 1989).

Based on the circuit shown in Fig. 9.2, a simplified equivalent circuit

with TLM has been proposed to represent the prototype cell (Chen, 1992).

As shown in Fig. 9.9, $\sum R_{Ohmic}$ is the total Ohmic resistance. C_{dl} is the

sum of two double-layer capacitance and R_{ct} is the sum of two interfacial

charge transfer resistance between electrode material and electrolyte

at both positive and negative electrodes. The double-layer capacitance

and charge transfer (electronic) resistance between current collector

and electrode are negligible, due to their insignificant value. The

details of the transmission line, Z_T, are presented in Fig. 9.8.
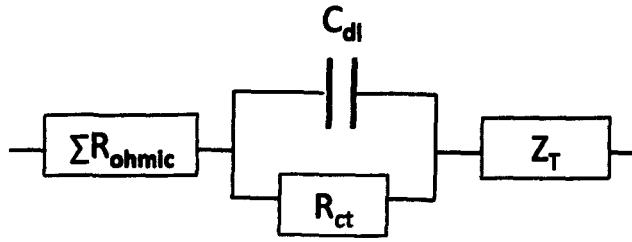
Fig. 9.9. Equivalent circuit of the prototype cell with transmission line.

The impedance of this transmission line, Z_T, can be calculated with the following equations (Chen, 1992):

$$Z_T = R_\Sigma \left[\frac{R_e R_i}{R_\Sigma^2} + 2\frac{R_e R_i}{R_\Sigma^2} \frac{1}{\sqrt{\omega j R_\Sigma C_\Sigma} \, Sinh\sqrt{\omega j R_\Sigma C_\Sigma}} + \left(1 - 2\frac{R_e R_i}{R_\Sigma^2}\right) \frac{1}{\sqrt{\omega j R_\Sigma C_\Sigma} \, tanh\sqrt{\omega j R_\Sigma C_\Sigma}} \right] \quad \text{Eq. 9.9.}$$

$$R_\Sigma = R_e + R_i \qquad\qquad \text{Eq. 9.10.}$$

$$R_\Sigma = 3(Z'_0 - R_{ohmic} - Z_{RC}') \qquad \text{Eq. 9.11.}$$

$$\frac{1}{Z'_\infty + R_{ohmic} + R_{ct}} = \frac{1}{R_e} + \frac{1}{R_i} \qquad \text{Eq. 9.12.}$$

$$C_\Sigma = \frac{1}{-\omega Z_0''} \qquad\qquad \text{Eq. 9.13.}$$

where ω is the angular frequency; Z'_0 and Z'_∞ are the real component of the impedance measured at the frequency $\to 0$ and frequency $\to \infty$, respectively. Z_0'' is the imaginary component of the impedance at frequency $\to 0$. R_Σ and C_Σ can be obtained from the experiment result and the value of R_e and R_i can be calculated thereafter. Z_T at different frequencies can thus be obtained.

Meanwhile, the total impedance of the system, represented by the circuit in Fig. 9.9, is the sum of Z_{ohmic}, Z_{RC} and Z_T:

$$Z = Z_{ohmic} + Z_T + Z_{RC} \qquad \text{Eq. 9.14.}$$

In Eq.9.14, Z_{ohmic} is the Ohmic resistance, available from EIS test result. Z_{RC}, a double capacitance (C_{dl}) and an interfacial resistance (R_{ct}) in parallel can also be calculated from EIS test result.

The EIS data of a symmetric prototype cell with 60wt% MnO_x/CNTs as

electrode material is fitted with TLM described above. The following

values are available from EIS experiment result: that $R_{ohmic} = 0.6\ \Omega$, R_{ct}

$= 0.72\ \Omega$, $R_{\Sigma} = 5.297\ \Omega$, $C_{dl} = 6.76E\text{-}05$ F, $C_{\Sigma} = 0.525$ F. Presumably, $R_{\Sigma}^{ion} >$

$R_{\Sigma}^{electron}$, then $R_i = 4.605\ \Omega$ and $R_e = 0.692\ \Omega$ (from Eq. 9.10 and Eq. 9.11).

The experimental data and the fitting result are presented in Fig. 9.9.

As shown in Fig. 9.10, the data obtained from experiment fits well into

this equivalent circuit at high frequencies (insert). At low frequencies,

however, the ideal capacitive region predicted by the simulation,

represented by a vertical line at low frequencies, does not match the

experimental result. Instead, a slope of 7.4 (Fig. 9.11) is observed with

Z' and $-Z''$ at frequencies below 0.19 Hz. This deviation from the vertical

line is regarded the results of dispersive effect at low frequencies.

As confirmed by Fig. 9.6, the overall capacitance of the prototype cell

is not dispersed with frequency. Therefore, this deviation has to be

attributed to the dispersion of resistive elements.
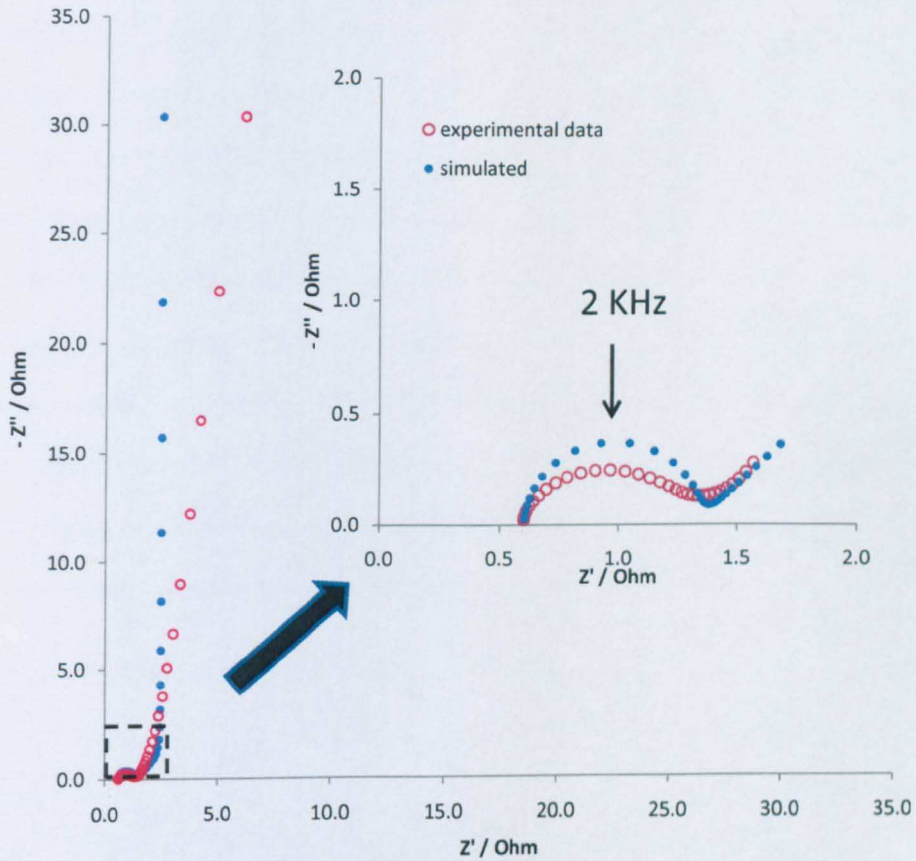
Fig. 9.10. Impedance of 60wt% MnO_x/CNTs symmetric cell fitted with Transmission line model, with enlarged view at high frequencies (hollow circle: experimental data, solid circle: simulation).
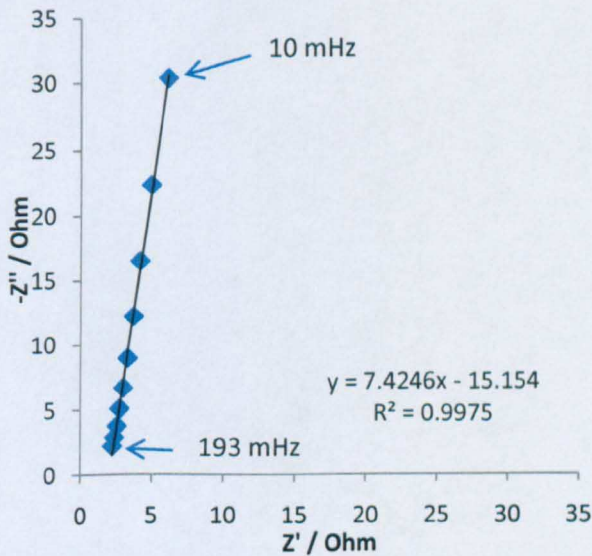
Fig. 9.11. Impedance of 60wt% MnO_x/CNTs symmetric cell at low frequencies (10 mHz – 193 mHz).

This deviation from a vertical line is commonly observed in the study
of electrochemical capacitors, particularly with porous electrode
materials, even in the absence of faradaic reaction. Many researchers
suggest that the major contribution towards this dispersion is the
penetrability of the pores (Song et al., 1999). Based on TLM, new
parameters, e.g. pore shape, pore depth, have been introduced to develop
enhanced models to represent this dispersion. For example, the ration
between penetration depth and penetrability, $\alpha_u = \lambda_u/l_p$, has been
identified to be a determinant of the deviation slope at low frequencies
(see Fig. 9.12) (Song et al., 1999).
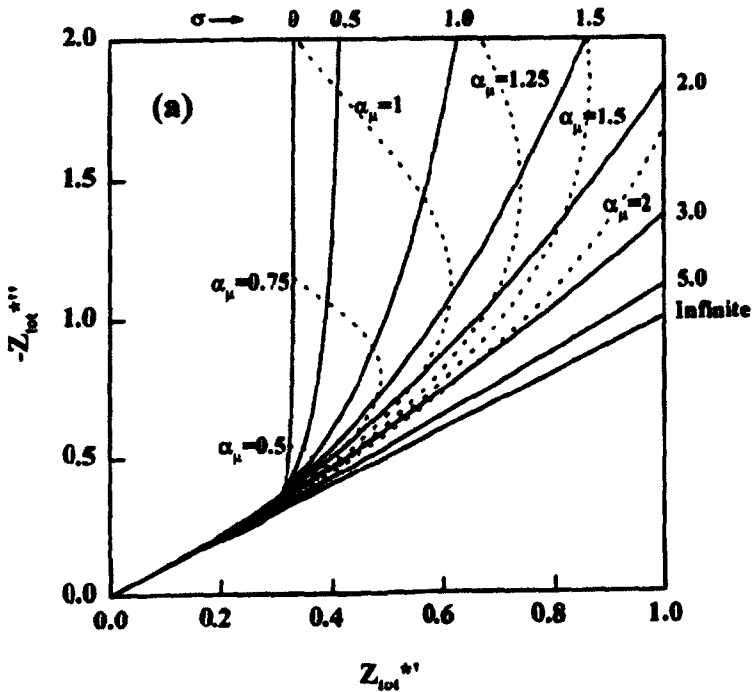
Fig. 9.12. Simulated impedances of porous materials with various pore
size distributions (Song et al., 1999).

On the other hand, the non-homogeneity of the electrodes also attributes
to the deviation. Essentially, the transmission line model is based on
the assumption that C, R_i and R_e in the circuit (Fig. 9.7) have constant
value per unit length. Besides, the porosity profile of the electrode
is presumed to be homogeneous, in terms of pore size, depth, slit direction,

etc. This idealised situation is next to impossible in the case of the prototype cell, whose electrodes were constructed by simply pressing the mixture of electrode material and conducting additive.

Moreover, C_Σ used in the simulation is an approximate value, obtained from the capacitance of the system at 10 mHz. In theory, C_Σ should be calculated with the following equation (Chen, 1992):

$$\frac{1}{C_\Sigma} = \frac{1}{C_p} + \frac{RT}{F^2 AL} \left(\frac{c}{a_0 b_0 n^2} + \frac{1}{x_0' m^2} \right) \qquad \text{Eq. 9.15.}$$

In Eq.9.15, A is the area of the electrode; L is the thickness of the electrode; a_0, b_0 and c are the concentration of reactant and resultant in the reversible electrochemical process; x_0 is the concentration of charge bearer; and m is the number of charges.

C_p is the Feldberg capacitance and is given by (Chen, 1992):

$$C_P = \frac{nbF \cdot AL}{\eta} \qquad \text{Eq. 9.16.}$$

In Eq.9.16, n is the number of electrons transferred between the oxidant and reductant; and η is the overpotential. In the electrochemical system of a prototype cell, some of the variables are difficult to obtain, e.g. the exact number of electrons transferred, the particular concentration of the reactants, etc. Hence, it is unlikely to acquire the accurate value of C_Σ.

To sum up, TLM can physically represent the inhomogeneity and porosity of the electrode and model the electrochemical behaviour of the prototype cells very well at high frequencies. Moreover, enhanced TLM with additional parameters, i.e. penetrability and pore shape, can represent the dispersion at low frequencies. However, homogeneity and pore-size distribution of the electrode materials are case dependent and should be re-fit for each cases. Alternatively, the concept of constant phase

element, as will be described in 4.2, provides a mathematical convenience in fitting the impedance data.

4.2. Constant Phase Element

As suggested by its title, constant phase element (CPE) is an electronic circuit element that is characterised by a constant phase angle between zero and $\pi/2$ (Bard et al., 2008a). CPE is frequently used to model the time-constant distribution due to the inhomogeneity of the electrodes. CPE is an empirical impedance that arises from various conditions, which includes the inhomogeneity of the electrodes: e.g. thickness, roughness and the porosity (Raistrict et al., 2005, Schiller and Strunz, 2001), the non-uniform current distribution (Jorcin et al., 2006), distribution of reaction rate (Kim et al., 2003) or even polycrystalline of the electrodes (Pajkossy, 2005). With the additional faradaic reactions, the non-uniform current distribution (Jorcin et al., 2006) and distribution of reaction rate (Kim et al., 2003) further complicate the situation.

To characterise the frequency dispersion of an element, e.g. capacitance, CPE is empirically defined as a power-law function of frequency (Pajkossy, 2005):

$$C(\omega) \propto (i\omega)^{\alpha-1} \qquad \text{Eq. 9.17.}$$

In Eq. 9.17, ω is the angular frequency and α is simply an index. For mathematical convenience, the impedance of the CPE is often expressed as (Boukamp, 1986):

$$Z_{CPE} = \frac{1}{Y} = \frac{1}{Q_0(i\omega)^n} \qquad \text{Eq. 9.18.}$$

where Q_0 has the numerical value of the admittance ($\frac{1}{|Z|}$) at $\omega = 1$ rad/s.

It is observed from Eq.9.18 that when n = 1, CPE is identical to a capacitor and when n = 0, CPE behaves like a resistor. For the situations in which $0 < n < 1$, CPE represents an electric element which is dispersed with

frequencies. Particularly, when n = 0.5, CPE represents the diffusion

process which is of significant importance in the electrochemical studies.

The impedance of CPE with n = 0.5 is termed as the Warburg impedance.

Warburg impedance, Z_w, represents the resistance of mass transfer (Bard

and Faulkner, 2001). It is originated from the diffusion of the

electroactive species over a finite length / thickness (Bard et al.,

2008c). Generally, it has a characteristic frequency dependence of $(i\omega)^{0.5}$

corresponding to the semi-infinite planar diffusion, where i is the

imaginary unit and ω is the angular frequency (Bard et al., 2008c). It

has become an important element in equivalent electric circuit. For

mathematical convenience, the Warburg impedance can be defined as

(Boukamp, 1986):

$$Z_w = \frac{1}{Y_0(i\omega)^{0.5}} \qquad \text{Eq. 9.19.}$$

The use of CPE usually leads to improved fit to experimental data. However,

the meaning of the electrochemical process behind the distributed

elements is often ambiguous (Orazem and Tribollet, 2008). The system does

not necessarily follow the specific distribution implied in the modelling.

Therefore, this constant phase element could only be exercised in

constructing equivalent circuit once some substantial understanding of

the electrochemical processes has been obtained. In this work, CPE is

applied to represent the dispersion of resistive elements at low

frequencies.

Based on the electrochemical processes presenting in prototype cells,

an equivalent circuit is proposed to represent the electrochemical system

(as shown in Fig. 9.13). In this equivalent circuit, $\sum R_{ohmic}$ is the sum

of all the Ohmic resistance in the system, including electrolyte

resistance, various contact resistance between the interfaces, etc. C_{dl}

is the double layer capacitance, concurrent with the Faradaic process

on the electrolyte | electrode interface. R_{ct}, C_{pseudo} and Z_w are the three

sequential steps in the Faradaic process, representing charge transfer

resistance, pseudocapacitance and Warburg mass transfer impedance

respectively.
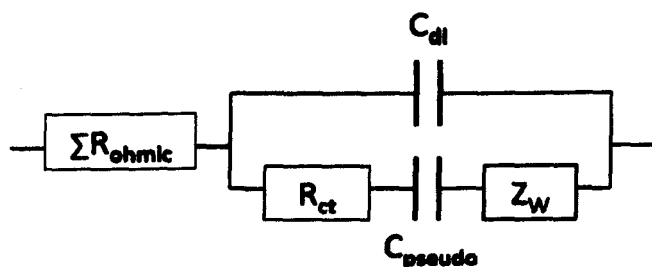
Fig. 9.13. An equivalent circuit constructed to fit the EIS data of

prototype cells.

The same symmetric MnO_x/CNTs prototype cell, as modelled with TLM in

section 9.4.1, is fitted with the equivalent circuit presented in Fig.

9.13 with Frequency Response Analyser (Eco Chemie B.V). The fitting

results are presented in Fig. 9.14. As demonstrated, the proposed

equivalent circuit produce an improved fit compared to TLM, especially

at low frequencies. However, at frequencies above 72 Hz, considerable

deviations of impedance (Fig.9.14 b), admittance (Fig.9.14 c) and phase

angle (Fig.9.14 d) occur.

Therefore, the dispersion of double-layer capacitance is considered. As

previously mentioned, this dispersion of capacitance is often observed

with rough, porous electrodes. With the indicator of a depressed

semi-circle at high frequencies (Fig. 9.14 b), constant phase angle, Q,

is considered to replace C_{dl} in the equivalent circuit to improve the fit.

Thereafter, equivalent circuit presented in Fig. 9.13 is employed in

fitting the EIS results of prototype cells with different structures:

symmetric, asymmetric, symmetric bipolar cell stack and asymmetric

bipolar cell stack.
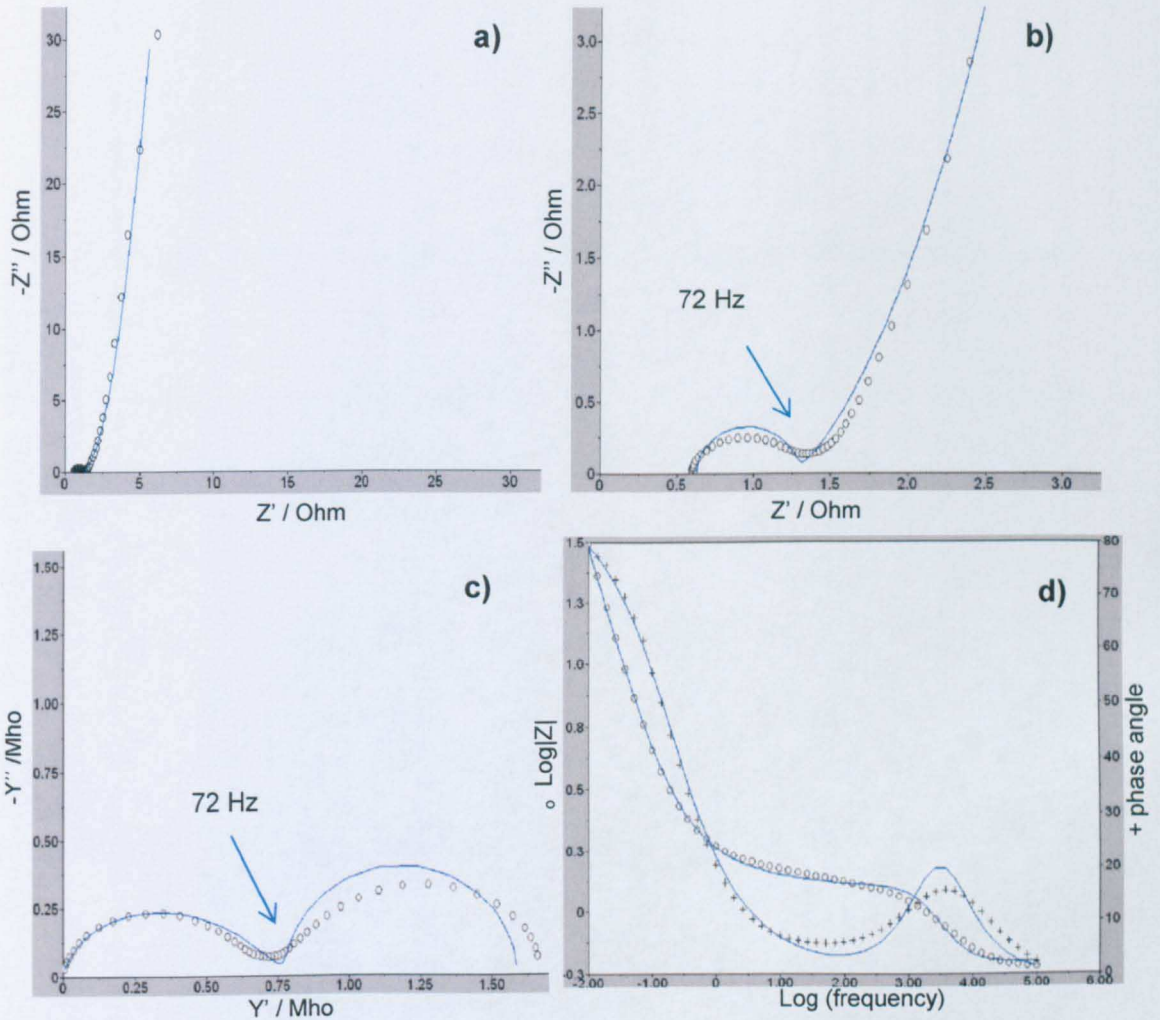
Fig. 9.14. EIS of 60wt% MnO_x/CNTs symmetric cell fitted with equivalent

circuit shown in Fig. 9.13. a) impedance complex plane; b) enlarged view

of a) at high frequencies; c) admittance; d) Bode plot. Hollow circle °

and cross + represent the EIS data while the solid line correspond to

the simulated result of the equivalent circuit.

The equivalent circuit with CPE is presented in Fig. 9.15, where constant

phase element Q replaces double-layer capacitance C_{dl} connected in

parallel to Faradaic processes. The mathematical value of Q is expressed

Eq. 9.10. The EIS data fitted to this equivalent circuit are presented

in Fig. 9.16. Improved fit for EIS data in impedance, admittance and phase

angle have been observed, particularly at high frequencies.
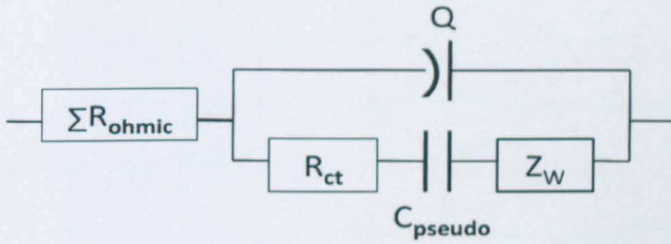
Fig. 9.15. An equivalent circuit with CPE to improve EIS data fitting.
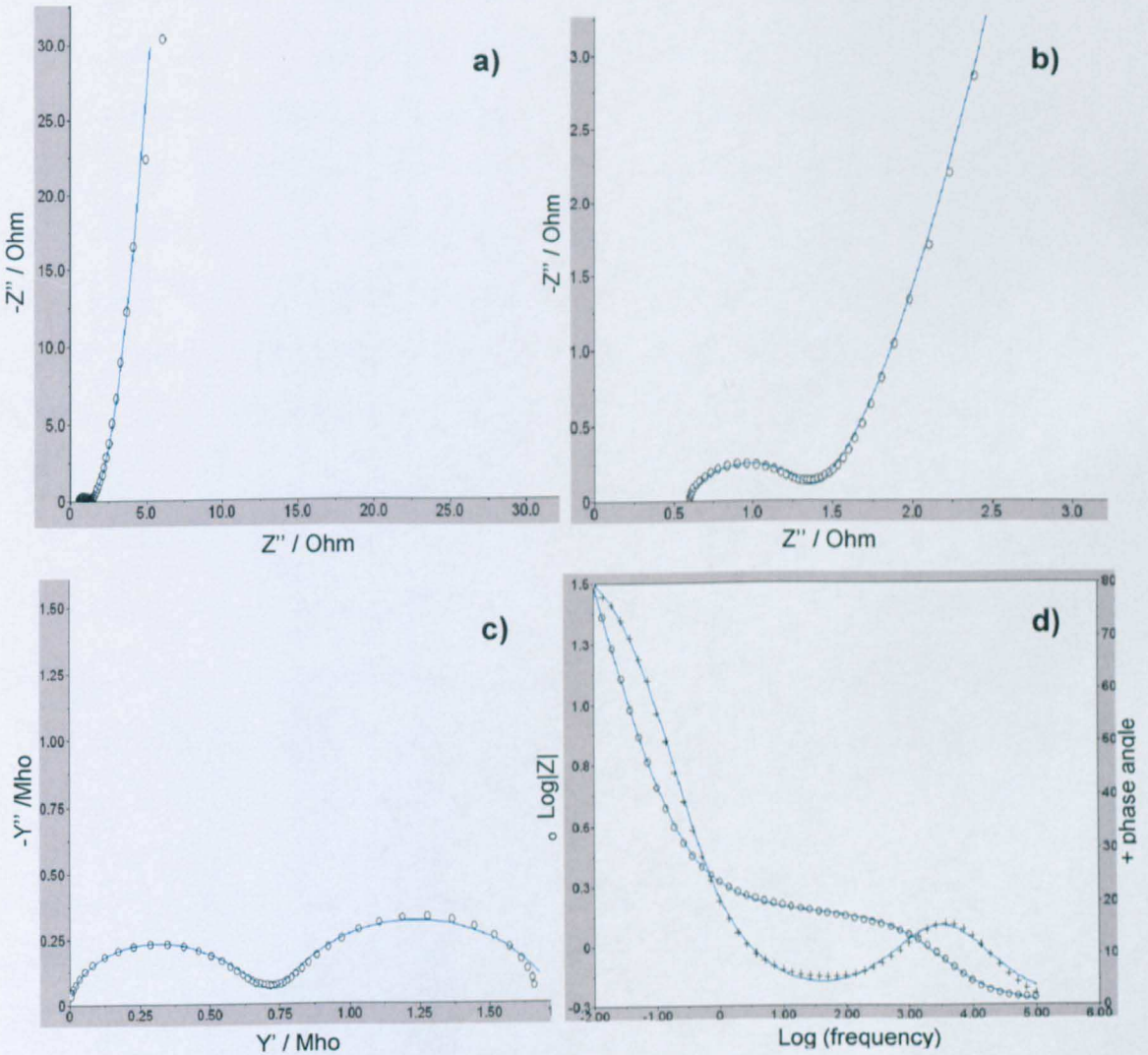
Fig. 9.16. EIS of 60wt% MnO$_x$/CNTs symmetric cell fitted with equivalent circuit shown in Fig. 9.15. a) impedance complex plane; b) enlarged view of a) at high frequencies; c) admittance; d) Bode plot. Hollow circle ^{o} and cross + represent the EIS data while the solid line correspond to the simulated result of the equivalent circuit.

5. Modelling of Prototype Cells

MnO_x/CNTs prototype cells are fitted with the equivalent circuit showed in Fig. 9.12. The simulated values for each element in the circuits are listed in Table 9.2 and Table 9.3. The estimated errors (%) of each simulation are also presented.

First of all, it is to be noted that the simulated value of pseudocapacitance, C_{pseudo}, for each cell is close to the cell capacitance calculated from CV, EIS and charge-discharge tests in Chapter 8. For electrochemical systems as presented in Fig. 9.13, in which double layer capacitance is connected in parallel with the faradaic process, C_{dl} is insignificant and thus negligible (Eq. 9.19). Hence, the overall cell capacitance is largely determined by the value of pseudocapacitance. Also, it is noticed that the capacitance of the bipolar cell-stacks, constructed with two identical capacitors, is half of value of its corresponding single cell, as predicted by Eq. 9.20.

Capacitance in parallel: $C_{total} = C_1 + C_2$ Eq. 9.19.

Capacitance in series: $\dfrac{1}{C_{total}} = \dfrac{1}{C_1} + \dfrac{1}{C_2}$ Eq. 9.20.

In addition, the simulated value of the overall Ohmic resistance ($\sum R_{ohmic}$) and charge transfer resistance (R_{ct}) confirm with the results calculated in Chapter 8. This verifies the validity of the simulation.

From the value obtained from the simulation, Warburg impedance can be calculated with Eq. 9.18 and the dispersion of $|Z_w|$ with frequency is presented in Fig. 9.17 and Fig. 9.18 to study the influence of cell construction on diffusion process, in which:

$$|Z_w| = \sqrt{Z_w(real)^2 + Z_w(imaginary)^2)}$$ Eq.9.19

From Fig. 9.17, it is observed that asymmetric structure helps to reduce the Warburg impedance with both MnO_x/CNTs and PAni/CNTs prototype cells.

Particularly, this tendency is manifested at the frequencies below 1 Hz, where the mass transfer is the limiting process for the electrochemical system. It could be explained that in cells with symmetric structure, mass transfer is required in both anode and cathode to precede the pseudocapacitive process. On the contrary, in asymmetric cells with carbon anodes, non-faradaic double-layer capacitive processes arise in response to charge and discharge. Only electron mobility is involved in situations like this.

Cell Construction	Element		Value	Error (%)
60wt% MnO_x/CNTs symmetric cell	$\sum R_{ohmic}$		0.572 Ohm	0.981
	Q (CPE)	Y_0	1.23E-04	1.900
		n	0.7098	3.370
	R_{ct}		0.789 Ohm	1.404
	C_{pseudo}		0.607 F	0.949
	Warburg (Y_0)		0.7275	1.730
60wt% MnO_x/CNTs symmetric cell 2 cells stack	$\sum R_{ohmic}$		0.973 Ohm	1.719
	Q (CPE)	Y_0	4.09E-05	11.600
		n	0.5045	2.237
	R_{ct}		0.883 Ohm	2.443
	C_{pseudo}		0.235 F	1.185
	Warburg (Y_0)		0.5707	2.436
60wt% MnO_x/CNTs asymmetric cell	$\sum R_{ohmic}$		0.405 Ohm	1.938
	Q (CPE)	Y_0	2.88E-04	12.094
		n	0.7956	5.917
	R_{ct}		0.299 Ohm	4.420
	C_{pseudo}		0.609 F	1.749
	Warburg (Y_0)		1.597	5.500
60wt% MnO_x/CNTs asymmetric cell 2 cells stack	$\sum R_{ohmic}$		0.748 Ohm	2.057
	Q (CPE)	Y_0	1.14E-04	7.943
		n	0.7198	4.572
	R_{ct}		0.945 Ohm	3.467
	C_{pseudo}		0.322 F	2.003
	Warburg (Y_0)		0.5353	4.327

Table 9.2 Fitted values of different elements in MnO_x/CNTs prototype cells

Cell	Element		Value	Error (%)
PAni/CNTs symmetric cell	R_{ohmic}		0.334 Ohm	2.245
	Q (CPE)	Y_0	1.20E-04	7.507
		n	0.8844	4.079
	R_{ct}		0.402 Ohm	3.105
	C_{pseudo}		1.180 F	2.461
	Warburg (Y_0)		1.433	4.593
PAni/CNTs asymmetric cell	R_{ohmic}		0.966 Ohm	1.399
	Q (CPE)	Y_0	2.34E-04	35.601
		n	0.9808	17.291
	R_{ct}		0.1076 Ohm	1.529
	C_{pseudo}		1.263 F	1.646
	Warburg (Y_0)		2.2327	5.144
PAni/CNTs symmetric 2 cells stack	R_{ohmic}		0.637 Ohm	2.049
	Q (CPE)	Y_0	4.77E-04	8.264
		n	0.7124	4.088
	R_{ct}		0.509 Ohm	3.272
	C_{pseudo}		0.741 F	1.128
	Warburg (Y_0)		1.144	2.611

Table 9.3 Fitted values of different element in PAni/CNTs prototype cells

Fig. 9.18 compares the dispersion of $|Z_w|$ against frequencies in single cell and bipolar two cell stack. As expected, the bipolar stack has higher $|Z_w|$ value compared to single cell, because extra diffusion processes are involved in bipolar cell stacks. However, no significant difference in Warburg Impedance between single cell and bipolar two-cell stack could be identified.
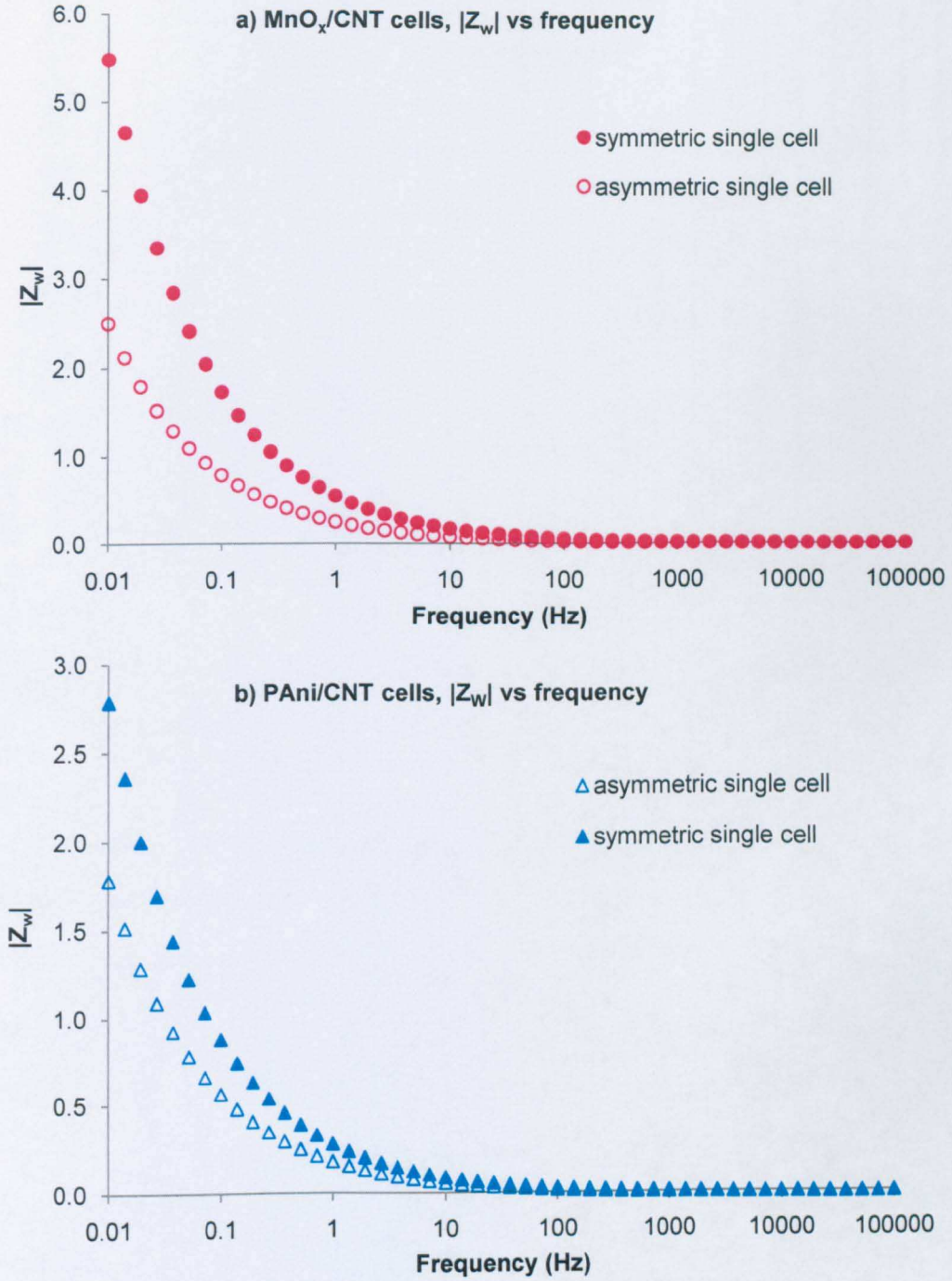
Fig. 9.17. Comparison of Warburg Impedance between symmetric and asymmetric cell structures: a) MnO_x/CNTs cells; b) PAni/CNTs cells.
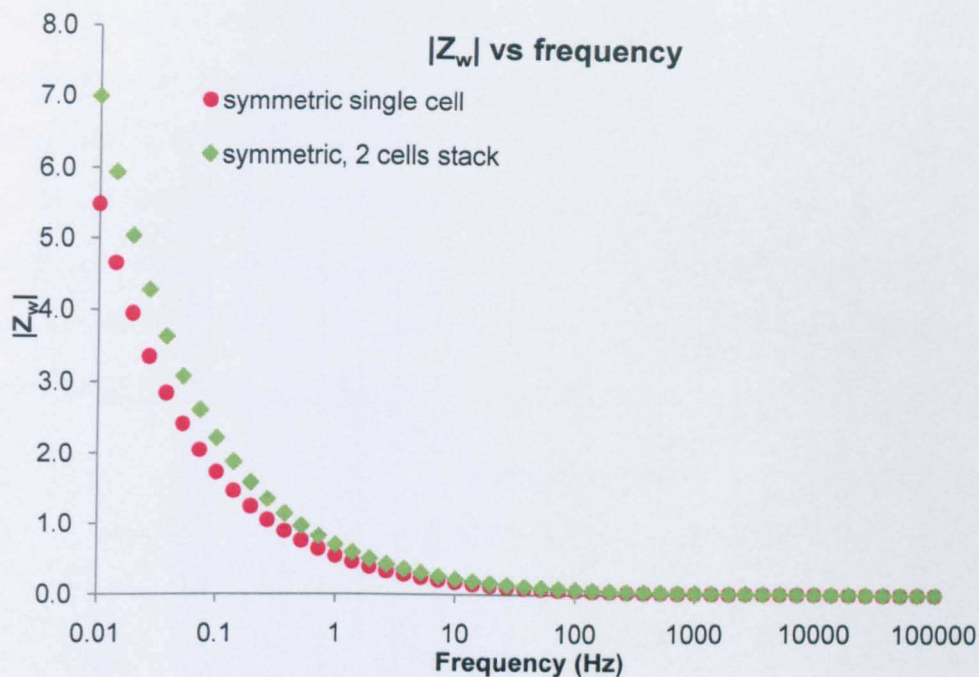
Fig. 9.18. Comparison of Warburg Impedance between single and 2-cell-stack of symmetric MnO_x/CNTs cells cell structures.

Furthermore, the importance of each resistive element in prototype cells can be determined by the ratio between these resistive elements (Barsoukov, 2005). Therefore, the ratio between the real component of Warburg impedance and charge transfer resistance, $\frac{Z_W{'}}{R_{ct}}$, indicates the contribution from the two resistive components at various frequencies.

Fig. 9.19 compares the importance of mass-transfer resistance and charge transfer resistance within MnO_x/CNTs cells with different cell structures. As illustrated, the diffusion processes are limited at high frequencies and charge transfer resistance plays a dominant role within the prototype cells. The influence of diffusion process begins to manifest at the frequencies below 1 Hz and become the dominant at frequencies lower than 0.1 Hz (Fig. 9.19). This tendency is observed with all prototype cells with different structures: symmetric and asymmetric single cells and bipolar cell stacks. It is thus confirmed that at low frequencies, at

which pseudocapacitive Faradaic processes occur, mass-transfer resistance is the principal resistance in the prototype cells. Lowering this diffusive resistance would be an effective way to improve the overall cell performance. Practical methods to reduce this diffusive resistance include: reducing the electrode thickness, enhancing the electron and ion accessibility, i.e. increasing the porosity of the electrode, and improving electron and ion mobility, etc.
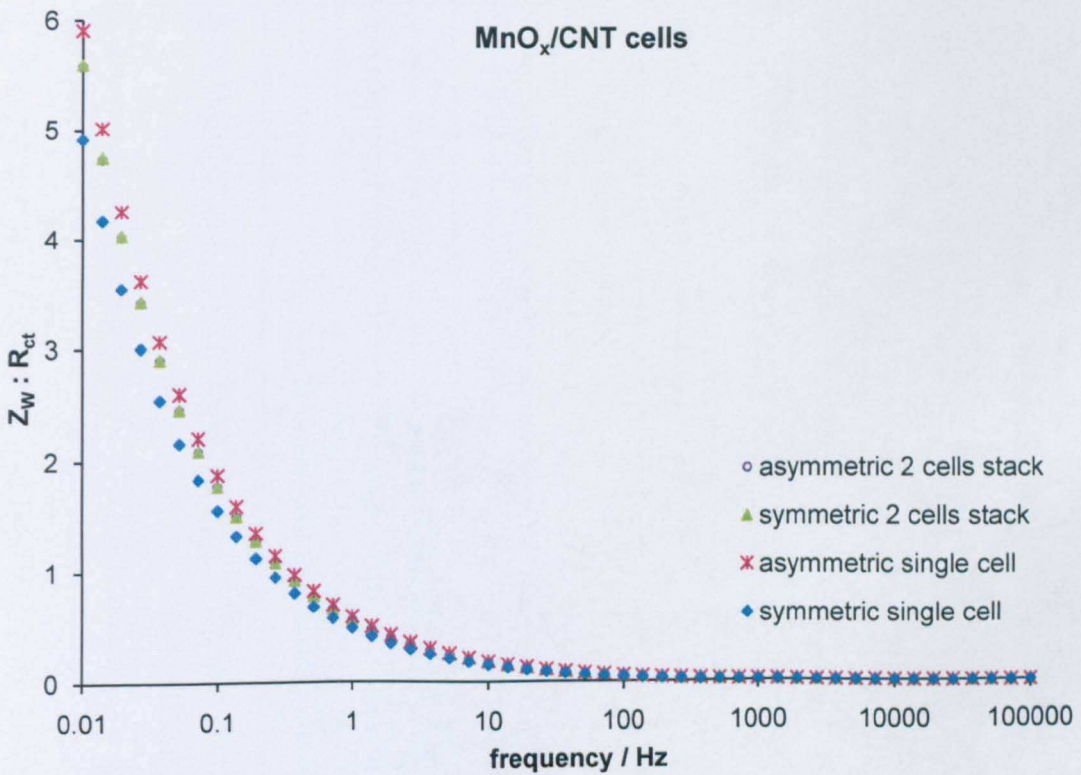
Fig. 9.19. Comparison of the importance of diffusion resistance and charge transfer resistance within prototype cells.

6. Summary

In this chapter, equivalent circuits were proposed for prototype cells based on the electrochemical processes presenting within the cell systems. Two models, transmission line model (TLM) and constant phase element (CPE) model, have been employed to interpret the distributed elements in cell systems. Upon fitting the EIS data with these two models, it was found

out that constant phase elements model could provide excellent fit. CPE model is then applied to analyse the value of individual elements within prototype cells of different structures: symmetric cell, symmetric bipolar cell stack, asymmetric cell and asymmetric bipolar cell stack. Diffusion resistance is identified as the dominant resistance at low frequency region, during which pseudocapacitive processes occur. Reducing this mass-transfer resistance will largely enhance the overall cell performance.

1. Chemical Redox Synthesis

Chemical redox reaction has been proven an effective method in synthesising nanocomposites containing carbon nanotubes. TEM results have confirmed that manganese oxides and conducting polymers, viz. polyaniline and polypyrrole, formed homogeneous coatings on the outer surface of individual carbon nanotubes. SEM results revealed that these nanocomposites form a coralloid 3-D structure, which is beneficial to the electron and ion transfer as an electrode material.

2. Properties of the Nanocomposites

BET adsorption results confirmed that these nanocomposites have moderate surface area, generally smaller than the acid treated carbon nanotubes, suggesting that the capacitance from these composites is pseudocapacitive in nature. From FT-IR results, it is verified that CNTs only provide mechanical support in these nanocomposites, without forming chemical bonding. Also, both polyaniline and polypyrrole exist in various oxidation states in the composites. Manganese oxides in the nanocomposites have been proven to be amorphous in nature with XRD. Manganese exists in both oxide and hydroxide forms in the composites as confirmed by XPS.

3. Electrochemistry of Nanocomposites

In the three-electrode electrochemical characterisation, the nanocomposites have exhibited promising capacitive performance in both cyclic voltammetry and electrochemical impedance spectroscopy. Desirable capacitive electrochemical behaviours with good reversibility can be obtained with these nanocomposites with appropriate operational potential window and scan rates. For each nanocomposites, different kinetics with different characteristic time frames, including Ohmic polarisation and concentration polarisation, have been revealed in

impedance complex-plane. Some characteristic parameters for charge-storage applications, i.e. knee frequency, f0, and T0, have been found to be strongly dependent on the electrolyte concentration. In general, electrolyte with higher concentration provides higher ion-mobility and accessibility which facilitates both diffusion and charge-transfer processes. Finally, excellent cyclic stability of the composites has been demonstrated. It is found out that CNTs act as backbone in the composites with conducting polymer and they significantly enhance the stability through cycling. Moreover, CNTs assist the electron and ion transfer within the electrode materials, thus level the current response and lead to a more desirable capacitive performance.

4. Prototype Cells

The nanocomposites can be easily fabricated into electrodes. By assembling the electrodes, prototype supercapacitor with different cell structures, viz. symmetrical, asymmetrical and bipolar stack, can be constructed. Electrochemical characterisations with the symmetrical prototype cells confirmed good capacitive performance of the nanocomposites, in accordance with the results obtained from the three-electrode tests. MnO_x/CNTs composite with 60wt% of manganese oxides is recognised as the optimal composites with highest capacitance of 82.4 F/g among all the MnO_x/CNTs composites synthesised in this work. The mass specific capacitance of PAni/CNTs and PPy/CNTs studied in this work are 127.8 F/g and 86.4 F/g correspondingly. The specific capacitance of M1300, the activated carbon used in this work, is 57 F/g, as measured in the similar conditions. Considering the loading and the size of the electrode, these figures are quite reasonable. Geometry capacitance of 0.99 mF/cm2, 0.83 F/cm2 and 1.19 mF/cm2 have been realised with MnO_x/CNTs, PPy/CNTs and PAni/CNTs cells correspondingly in their optimal conditions.

Asymmetrical cells with carbon negative electrodes are found to be

effective in extending the cell voltage, due to the higher oxygen evolution overpotential of carbon, particularly for the case of $MnO_x/CNTs$. Also, cells with asymmetrical structure shown reduced charge-transfer resistance compared with their symmetrical equivalents.

Both symmetrical and asymmetrical cells could be constructed into bipolar cell stacks, achieving a cell voltage twice the value of each individual single cell. Operational voltage of 1.8 V and 1.9 V have been realised with $MnO_x/CNTs$ symmetrical and asymmetrical two-cell-stacks respectively. The composites in cell stack retained their specific capacitance value as in a single cell. Moreover, cell stacks exhibited similar values in Coulombic efficiency with their corresponding single cells. These indicated that connecting two cells in series did not affect the electrochemical performance of the electrode materials. Generally, the cell stacks exhibited charge-transfer resistance twice the value of the corresponding single cells. On the other hand, equivalent series resistance of the cell stack is determined by various parameters, and therefore, does not multiply with the stacking.

5. Cell Modelling

Based on the existing electrochemical processes in the systems, equivalent circuits have been proposed for the prototype cells. Two models, the transmission line model (TLM) and the constant phase element (CPE) model, have been employed to interpret the distributed elements in cell systems. Upon fitting the EIS data with these two models, it was found out that the TLM can represent the electrochemical behaviour of the prototype cell well at high frequencies. At low frequencies, however, dispersion arises from the pore size distribution and other inhomogeneities on the electrode. Introducing a CPE model can provide an improved fit, nonetheless, it made the physical meaning and value of the element ambiguous. Therefore, the application of the CPE should be

restricted. The value of individual elements within prototype cells are thus analysed with the model. These values are compared among prototype cells of different structures: symmetrical cell, symmetrical bipolar cell stack, asymmetrical cell and asymmetrical bipolar cell stack. Diffusion resistance is identified as the dominant resistance at low frequency region, during which pseudocapacitive processes occur. Reducing this mass-transfer resistance will largely enhance the overall cell performance.

6. General Conclusions

Nanocomposites, viz. $MnO_x/CNTs$, PPy/CNTs and PAni/CNTs, can be synthesised through chemical redox reactions. CNTs function as the backbone in the nanocomposites to promote the mechanical strength, conductivity and porosity of the materials. The composites exhibited ideal capacitive behaviour with superior cycling stability. Moreover, the composites can be easily engineered into electrodes to build prototype cell. Prototype supercapacitors with different cell structures, viz. symmetrical and asymmetrical, have shown satisfactory performance during CV, EIS and galvanostatic charge-discharge characterisations. Bipolar connection of two prototype cells creates a stack. This process doubles the operational voltage but halves the capacitance as compared with each single cell, since stacking essentially connects two supercapacitors in series. However, this reduction in capacitance can be compensated by connecting capacitors in parallel, e.g. increasing the size of each electrode. Hence, desirable voltage and capacitance can be achieved by connecting appropriate number of capacitors in series and in parallel. Through modelling, diffusion resistance is identified as the dominant resistance at low frequency region. Reducing this diffusion resistance will significantly enhance the cell performance.

10.7. Future Work

Supercapacitors constructed with nanomaterials with pseudocapacitive behaviour provide a new area for significant development. From the material synthesis to the prototype construction, there are still several aspects to be addressed as avenues for future research.

Material Synthesis and Characterisation

The polymerisation of aniline and pyrrole, forming nanocomposites with CNTs, can be investigated in detail with in-situ technologies, e.g. nuclear magnetic resonance spectroscopy, to provide valuable information on the initiation and termination of the process. These results will reveal valuable information, including the function of radicals during the polymerisation and the chain-length of the products, providing possibility to optimise the process. In addition, properties of the polymers and the polymer nanocomposites, including glass transition temperature, Young's Modulus, crystallinity, can be investigated to provide a guideline for electrode construction.

On the other hand, other transition metal oxides could be good alternatives to MnO_x in forming nanocomposite with CNTs. Electrical conductivity within the electrode would be enhanced by this alteration. Moreover, electrode materials consist of more than one species of nanocomposite, e.g. Co_nMnO_x, $MnFe_2O_4$, could be another feasible approach to enhance the electrochemical performance of MnO_x.

Electrode Fabrication

Pressed electrodes, as applied in this work, are practical in constructing supercapacitor prototypes and stacks. However, its thickness hinders the charge-transfer and increases the resistance of the electrode. Inevitably, this design prevents the full utilisation of the pseudocapacitance of the electrode materials. New techniques to fabricate the electrodes, e.g.

261

spray, screen-printing, inkjet-printing, etc., should be explored to further develop the prototypes towards commercialisation.

Electrolyte

Aqueous electrolyte with neutral pH values have been applied in this work. Although this type of environmentally-friendly electrolyte can ensure low uncompensated resistance within the system, it causes some problems in operation, including metal-corrosion and limited operating voltage. Therefore, other types of electrolyte, i.e. organic solvent and ionic liquid are recommended for future study. These electrolytes will substantially increase the potential window and hence the power and energy profile of supercapacitor prototype.

Cell Design

Supercapacitor prototypes developed during this work are based on a stack design. In this pristine design, several issues, including sealing and scale-up, remain. More sophisticated designs, such as cylindrical type and pouch type electrode-separator assembly, have been proved successful in battery industry. Therefore, these designs could be applied in the prototype development for future investigations.

ADHIKARI, A. (2004) Conducting polyaniline and polypyrrole: studies of their catalytic properties. *Chemistry.* University of Pune.

ALBERY, W. J., CHEN, Z., HORROCKS, B. R., MOUNT, A. R., WILSON, P. J., BLOOR, D., MONKMAN, A. T. & ELLIOTT, C. M. (1989) Spectroscopic and Electrochemical Studies of Charge-Transfer in Modified Electrodes. *Faraday Discussions,* 88.

AN, K. H., JEON, K. K., HEO, J. K., LIM, S. C., BAE, D. J. & LEE, Y. H. (2002) High-Capacitance Supercapacitor Using a Nanocomposite Electrode of Single-Walled Carbon Nanotube and Polypyrrole. *Journal of The Electrochemical Society,* 149, A1058-A1062.

AN, K. H., KIM, W. S., PARK, Y. S., MOON, J. M., BAE, D. J., LIM, S. C., S., L. Y. & LEE, Y. H. (2001) Electrochemical Properties of High-Power Supercapacitors Using Single-Walled Carbon Nanotube Electrodes. *Advanced Functional Materials,* 11, 387-392.

ANDREAS, H. A. & CONWAY, B. E. (2006) Examination of the double-layer capacitance of an high specific-area C-cloth electrode as titrated from acidic to alkaline pHs *Electrochimica Acta* 51, 6510-6520.

ARMES, S. P. & MILLER, J. F. (1988) Optimum reaction conditions for the polymerization of aniline in aqueous solution by ammonium persulphate. *Synthetic Metals,* 22, 385-393.

ATHOUEL, L., MOSER, F., DUGAS, R., CROSNIER, O., BELANGER, D. & BROUSSE, T. (2008) Variation of the MnO2 Birnessite Structure upon Charge/Discharge in an Electrochemical Supercapacitor Electrode in Aqueous Na2SO4 Electrolyte. *J. Phys. Chem. C,* 112, 7270-7277.

AUDEBERT, P., & Miomandre, F. (2007) Electrochemistry of Conducting Polymers. IN SKOTHEIM, T. A. & REYNOLDS, J. R. (Eds.) *Handbook*

of *Conducting Polymers - Conjugated Polymers* CRC Press.

AYAD, M. M., SALAHUDDIN, N. & SHENASHIN, M. A. (2004) The optimum HCl concentration for the in situ polyaniline film formation. *Synthetic Metals*, 142, 101-106.

BACH, S., HENRY, M., BAFFIER, N. & LIVAGE, J. (1990) Sol-gel synthesis of manganese oxides. *Journal of Solid State Chemistry*, 88, 325-333.

BARD, A. J. & FAULKNER, L. R. (2001) *Electrochemical Methods: Fundamentals and Applications*, New York, John Wiley & Sons, Inc.

BARD, A. J., INZELT, G. & SCHOLZ, F. (2008a) Constant phase element. *Electrochemical Dictionary*. Berlin, Springer.

BARD, A. J., INZELT, G. & SCHOLZ, F. (2008b) Transmission Line. *Electrochemical Dictionary*. Berlin, Springer.

BARD, A. J., INZELT, G. & SCHOLZ, F. (2008c) Warburg Impedance. *Electrochemical Dictionary*. Berlin, Spinger.

BARSOUKOV, E. (2005) Special Aspects of Impedance Modeling of Power Sources. IN BARSOUKOV, E. & MACDONALD, J. R. (Eds.) *Impedance Spectroscopy - Theory, Experiment, and Applications*. 2nd ed., Wiley & Sons.

BECKER, H. E. (1957) U.S.Patent 2 800 616 (to General Electric)

BELANGER, D., REN, X., DAVEY, J., URIBE, F. & GOTTESFELD, S. (2000) Characterization and Long-Term Performance of Polyaniline-Based Electrochemical Capacitors. *Journal of The Electrochemical Society*, 147, 2923-2929.

BEXELL, U. (2003) Surface Characterisation Using ToF-SIMS, AES and XPS of Silane Films and Organic Coatings Deposited on Metal Substrates. *Department of Materials Science*. Uppsala University.

BLACKMAN, J. M. (2005) High Pressure Hydrogen Storage on Carbon

Materials for Mobile Applications. *Chemical and Environmental Engineering*. The University of Nottingham.

BLEDA-MARTÍNEZ, M. J., LOZANO-CASTELLÓ, D., MORALLÓN, E., CAZORLA-AMORÓS, D. & LINARES-SOLANO, A. (2006) Chemical and electrochemical characterization of porous carbon materials. *Carbon*, 44, 2642-2651.

BOTTOM, R. (2008) *Principles and Applications of Thermal Analysis*, Blackwell Publishing Ltd.

BOUKAMP, B. A. (1986) A package for impedance/admittance data analysis. *Solid State Ionics*, 18-19, 136-140.

BOUKAMP, B. A. (1995) A Linear Kronig-Kramers Transform Test for Immittance Data Validation. *Journal of The Electrochemical Society*, 142, 1885-1894.

BRETT, C. M. A. & BRETT, A. M. O. (1993) *Electrochemistry: Principles, Methods and Applications*, New York, Oxford University Press.

BRIGGS, D. & RIVIERE, J. C. (1990) Spectral Interpretation. IN BRIGGS, D. & SEAH, M. P. (Eds.) *Practical Surface Analysis*. 2nd ed., John Wiley & Sons, Inc.

BROCK, S. L., SANABRIA, M., SUIB, S. L., URBAN, V., THIYAGARAJAN, P. & POTTER, D. I. (1999) Particle Size Control and Self-Assembly Processes in Novel Colloids of Nanocrystalline Manganese Oxide. *J. Phys. Chem. B*, 103, 7416-7428.

BROUGHTON, J. N. & BRETT, M. J. (2004) Investigation of thin sputtered Mn films for electrochemical capacitors. *Electrochimica Acta*, 49, 4439-4446.

BROUGHTON, J. N. & BRETT, M. J. (2005) Variations in MnO2 electrodeposition for electrochemical capacitors. *Electrochimica Acta*, 50, 4814-4819.

BROUSSE, T. & BELANGER, D. (2003) A Hybrid Fe3O4-MnO2 Capacitor in

Mild Aqueous Electrolyte. *Electrochemical and Solid-State Letters*, 6, A244-A248.

BROUSSE, T., TOUPIN, M. & BELANGER, D. (2004) A Hybrid Activated Carbon-Manganese Dioxide Capacitor using a Mild Aqueous Electrolyte. *Journal of The Electrochemical Society*, 151, A614-A622.

BROUSSE, T., TOUPIN, M., DUGAS, R., ATHOUEL, L., CROSNIER, O. & BELANGER, D. (2006) Crystalline MnO_2 as Possible Alternatives to Amorphous Compounds in Electrochemical Supercapacitors. *Journal of The Electrochemical Society*, 153, A2171-A2180.

BRUNAUER, S., EMMETT, P. H. & TELLER, E. (1938) Adsorption of Gases in Multimolecular Layers. *J. Am. Chem. Soc.*, 60, 309-319.

BURKE, A. (2000) Ultracapacitors: why, how, and where is the technology. *Journal of Power Sources*, 91, 37-50.

BURKE, A. (2007) R&D considerations for the performance and application of electrochemical capacitors. *Electrochimica Acta*, 53, 1083-1091.

CAO, Y., ANDREATTA, A., HEEGER, A. J. & SMITH, P. (1989) Influence of chemical polymerization conditions on the properties of polyaniline. *Polymer*, 30, 2305-2311.

CASCALES, J. J. L. & OTERO, T. F. (2004) Molecular dynamic simulation of the hydration and diffusion of chloride ions from bulk water to polypyrrole matrix. *The Journal of Chemical Physics*, 120, 1951-1957.

CHANG, J.-K., CHEN, Y.-L. & TSAI, W.-T. (2004a) Effect of heat treatment on material characteristics and pseudo-capacitive properties of manganese oxide prepared by anodic deposition. *Journal of Power Sources*, 135, 344-353.

CHANG, J.-K., LEE, M.-T. & TSAI, W.-T. (2007) In situ Mn K-edge X-ray absorption spectroscopic studies of anodically deposited

manganese oxide with relevance to supercapacitor applications. *Journal of Power Sources,* 166, 590-594.

CHANG, J.-K., LIN, C.-T. & TSAI, W.-T. (2004b) Manganese oxide/carbon composite electrodes for electrochemical capacitors. *Electrochemistry Communications,* 6, 666-671.

CHANG, J.-K. & TSAI, W.-T. (2003) Material Characterization and Electrochemical Performance of Hydrous Manganese Oxide Electrodes for Use in Electrochemical Pseudocapacitors. *Journal of The Electrochemical Society,* 150, A1333-A1338.

CHANG, J.-K. & TSAI, W.-T. (2005) Microstructure and Pseudocapacitive Performance of Anodically Deposited Manganese Oxide with Various Heat-Treatments. *Journal of The Electrochemical Society,* 152, A2063-A2068.

CHEN, C.-Y., LYU, Y.-R., SU, C.-Y., LIN, H.-M. & LIN, C.-K. (2007) Characterization of spray pyrolyzed manganese oxide powders deposited by electrophoretic deposition technique. *Surface and Coatings Technology,* 202, 1277-1281.

CHEN, G. Z., SHAFFER, M. S. P., COLEBY, D., DIXON, G., ZHOU, W., FRAY, D. J. & WINDLE, A. H. (2000) Carbon Nanotube and Polypyrrole Composites: Coating and Doping. *Advanced Materials,* 12, 522 - 526.

CHEN, J. H., LI, W. Z., WANG, D. Z., YANG, S. X., WEN, J. G. & REN, Z. F. (2002) Electrochemical characterization of carbon nanotubes as electrode in electrochemical double-layer capacitors. *Carbon,* 40, 1193-1197.

CHEN, Y.-S., HU, C.-C. & WU, Y.-T. (2004) Capacitive and textural characteristics of manganese oxide prepared by anodic deposition: effects of manganese precursors and oxide thickness *Journal of Solid State Electrochemistry,* 8, 467-473.

CHEN, Z. (1992) Studies of Polymer Modified Electrodes. *Department*

of Chemistry. London, Imperial College of Science, Technology and Medicine.

CHIGANE, M. & ISHIKAWA, M. (2000) Manganese Oxide Thin Film Preparation by Potentiostatic Electrolyses and Electrochromism. *Journal of The Electrochemical Society,* 147, 2246-2251.

CHIN, S.-F., PANG, S.-C. & ANDERSON, M. A. (2002) Material and Electrochemical Characterization of Tetrapropylammonium Manganese Oxide Thin Films as Novel Electrode Materials for Electrochemical Capacitors. *Journal of The Electrochemical Society,* 149, A379-A384.

CHO, G., FUNG, B. M., GLATZHOFER, D. T., LEE, J.-S. & SHUL, Y.-G. (2001) Preparation and Characterization of Polypyrrole-Coated Nanosized Novel Ceramics. *Langmuir,* 17, 456-461.

CHO, S. H., SONG, K. T. & LEE, J. Y. (2007) Recent Advances in Polypyrrole. IN SKOTHEIM, T. A. & REYNOLDS, J. R. (Eds.) *Handbook of Conducting Polymers - Conjugated Polymers.* CRC Press.

CHRISTENSE, P. A. & HAMNETT, A. (1994) *Techniques and Mechanisms in Electrochemicstry,* Chapman & Hall.

CHRISTENSEN, J., SRINIVASAN, V. & NEWMAN, J. (2006) Optimization of Lithium Titanate Electrodes for High-Power Cells. *Journal of The Electrochemical Society,* 153, A560-A565.

CLARKE, C. J., BROWNING, G. J. & DONNE, S. W. (2006) An RDE and RRDE study into the electrodeposition of manganese dioxide. *Electrochimica Acta,* 51, 5773-5784.

COMPTON, R. G. & BANKS, C. E. (2007) *Understanding Voltammetry,* World Scientific Publishing Co. Pte. Ltd.

CONDON, J. B. (2006) *Surface Area and Porosity Determinations by Physisorption, Measurements and Theory,* Elsevier.

CONWAY, B. E. (1999) *Electrochemical Supercapacitors: Scientific fundamentals and technological applications,* New York, Kluwer Academic/ Plenum Publishers.

CONWAY, B. E. (2005) Impedance Behavior of Electrochemical Supercapacitors and Porous Electrodes. IN BARSOUKOV, E. (Ed.) *Impedance Spectroscopy: Theory, Experiment and Application.* 2nd ed., John Wiley & Sons, Inc.

CONWAY, B. E., BIRSS, V. & WOJTOWICZ, J. (1997) The role and utilization of pseudocapacitance for energy storage by supercapacitors. *Journal of Power Sources,* 66, 1 - 14.

COTTINEAU, T., TOUPIN, M., DELAHAYE, T., BROUSSE, T. & BÉLANGER, D. (2006) Nanostructured transition metal oxides for aqueous hybrid electrochemical supercapacitors. *Applied Physics A: Materials Science & Processing,* 82, 599-606.

CULLITY, B. D. & STOCK, S. R. (2001) *Elements of X-ray Diffraction,* Prentice Hall, Inc.

DAI, Y., WANG, K. & XIE, J. (2007) From spinel Mn_3O_4 to layered nanoarchitectures using electrochemical cycling and the distinctive pseudocapacitive behavior. *Applied Physics Letters,* 90, 104102-3.

DAWN, C. & GOODHEW, P. J. (1990) *The Operation of Transmission and Scanning Electron Microscopes,* Oxford University Press.

DE LEVIE, R. (1963) On porous electrodes in electrolyte solutions : I. Capacitance effects. *Electrochimica Acta,* 8, 751-780.

DE LEVIE, R. (1965) The influence of surface roughness of solid electrodes on electrochemical measurements. *Electrochimica Acta,* 10, 113-130.

DEVARAJ, S. & MUNICHANDRAIAH, N. (2005a) High Capacitance of Electrodeposited MnO_2 by the Effect of a Surface-Active Agent. *Electrochemical and Solid-State Letters,* 8, A373-A377.

DEVARAJ, S. & MUNICHANDRAIAH, N. (2005b) High Capacitance of Electrodeposited MnO[sub 2] by the Effect of a Surface-Active Agent. *Electrochemical and Solid-State Letters,* 8, A373-A377.

DEVARAJ, S. & MUNICHANDRAIAH, N. (2007a) The Effect of Nonionic Surfactant Triton X-100 during Electrochemical Deposition of MnO[sub 2] on Its Capacitance Properties. *Journal of The Electrochemical Society,* 154, A901-A909.

DEVARAJ, S. & MUNICHANDRAIAH, N. (2007b) Electrochemical Supercapacitor Studies of Nanostructured alpha-MnO[sub 2] Synthesized by Microemulsion Method and the Effect of Annealing. *Journal of The Electrochemical Society,* 154, A80-A88.

DJURFORS, B., BROUGHTON, J. N., BRETT, M. J. & IVEY, D. G. (2003) Microstructural characterization of porous manganese thin films for electrochemical supercapacitor applications. *Journal of Materials Science,* 38, 4817-4830.

DJURFORS, B., BROUGHTON, J. N., BRETT, M. J. & IVEY, D. G. (2005) Electrochemical oxidation of Mn/MnO films: formation of an electrochemical capacitor. *Acta Materialia,* 53, 957-965.

DIT (Department of Trade and Industry, UK) (2006 a) The Energy Challenge - Energy Review Report 2006.

DIT (Department of Trade and Industry, UK) (2006 b) Power from the people - Microgeneration Strategy.

DIT (Department of Trade and Industry, UK) (2007) Meeting the Energy Challenge - A white Paper on Energy.

DU, C., YEH, J. & PA, N. (2005) Carbon nanotube thin films with ordered structures. *Journal of Materials Chemistry,* 15, 548-550.

EIA (Energy Information Administration, US Department of Energy) (2008) International Energy Outlook.

EMMENEGGER, C., MAURON, P., ZUTTEL, A., NUTZENADEL, C., SCHNEUWLY, A., GALLAY, R. & SCHLAPBACH, L. (2000) Carbon nanotube synthesized on metallic substrates. *Applied Surface Science*, 162-163, 452-456.

ENDO, M., MAEDA, T., TAKEDA, T., KIM, Y. J., KOSHIBA, K., HARA, H. & DRESSELHAUS, M. S. (2001) Capacitance and pore-size distribution in aqueous and nonaqueous electrolytes using various activated carbon electrodes. *Journal of the Electrochemical Society*, 148, A910-A914.

ESUMIM, K., NAKAJIMA, K., AWADA, S. & HONDA, H. (1996) Chemical treatment of carbon nanotubes. *Carbon*, 34, 279.

FAN, L.-Z. & MAIER, J. (2006) High performance polypyrrole electrode materials for redox supercapacitors. *Electrochemistry Communications* 8, 937-940.

FAN, Z., CHEN, J., WANG, M., CUI, K., ZHOU, H. & KUANG, Y. (2006) Preparation and characterization of manganese oxide/CNT composites as supercapacitive materials. *Diamond & Related Materials*, 15, 1478-1483.

FEAST, W. J. (1986) *Synthesis of conducting polymers*, Marcel Dekker Inc.

FELDBERG, S. W. (1984) Reinterpretation of polypyrrole electrochemistry. Consideration of capacitive currents in redox switching of conducting polymers. *J. Am. Chem. Soc.*, 106, 4671-4674.

FELDMAN, B. J., BURGMAYER, P. & MURRAY, R. W. (1985) The potential dependence of electrical conductivity and chemical charge storage of poly(pyrrole) films on electrodes. *Journal of the American Chemical Society* 107, 872-878.

FENG, Q., YANAGISAWA, K. & YAMASAKI, N. (1998) Hydrothermal Soft Chemical Process for Synthesis of Manganese Oxides with Tunnel

Structures. *Journal of Porous Materials,* 5, 153-162.

FISCHER, U., SALIGER, R., BOCK, V., PETRICEVIC, R. & FRICKE, J. (1997) Carbon Aerogels as Electrode Material in Supercapacitors. *Journal of Porous Materials,* 4, 281-285.

FISHER, A. C. (1996) *Electrode Dynamics,* Oxford University Press.

FOORD, J. S., JACKMAN, R. B. & ALLEN, G. C. (1984) An X-ray photoelectron spectroscopic investigation of the oxidation of manganese. *Philosophical Magazine A,* 49, 657 - 663.

FRACKOWIAK, E. (2007) Carbon materials for supercapacitor application. *Physical Chemistry Chemical Physics,* 1774 - 1785.

FRACKOWIAK, E. & BEGUIN, F. (2001) Carbon materials for the electrochemical storage of energy in capacitors. *Carbon,* 39, 937-950.

FRACKOWIAK, E., DELPEUX, S., JUREWICZ, K., SZOSTAK, K., CAZORLA-AMOROS, D. & BEGUIN, F. (2002) Enhanced capacitance of carbon nanotubes through chemical activation. *Chemical Physics Letters,* 361, 35-41.

FRACKOWIAK, E., KHOMENKO, V., JUREWICZ, K., LOTA, K. & BEGUIN, F. (2006) Supercapacitors based on conducting polymers/nanotubes composites. *Journal of Power Sources,* 153, 413-418.

FRANGER, S., BACH, S., FARCY, J., PEREIRA-RAMOS, J. P. & BAFFIER, N. (2002) Synthesis, structural and electrochemical characterizations of the sol-gel birnessite $MnO1.84 \cdot 0.6H2O$. *Journal of Power Sources,* 109, 262-275.

FU, Y. & ELSENBAUMER, R. L. (1994) Thermochemistry and Kinetics of Chemical Polymerization of Aniline Determined by Solution Calorimetry. *Chemical Materials,* 6, 671 - 677.

FUERTES, A. B., PICO, F. & ROJO, J. M. (2004) Influence of pore structure on electric double-layer capacitance of template mesoporous carbons. *Journal of Power Sources,* 133, 329-336.

GAILLOT, A. C., LANSON, B. & DRITS, V. A. (2005) Structure of birnessite obtained from decomposition of permanganate under soft hydrothermal conditions.

1. Chemical and structural evolution as a function of temperature. *Chemical Materials*, 17, 2959.

GAO, M., HUANG, S., DAI, L., WALLACE, G., GAO, R. & WANG, Z. (2000) *Angewandte Chemie*, 39, 3664 - 3667.

GRIFFITHS, P. R. & DE HASETH, J. A. (2007) *Fourier transform infrared spectrometry*, Springer Berlin / Heidelberg.

HALL, P. J. (2008) Energy Storage: The route to liberation from the fossil fuel economy. *Energy Policy*, 36, 4363 - 4367.

HAMANN, C. H. & VIELSTICH, W. (1998) *Electrochemistry*, Wiley-VCH.

HARDAKER, S. S. & GREGORY, R. V. (1999) Polyaniline. IN MARK, J., E. (Ed.) *Polymer Data Handbook*. Oxford University Press.

HAYAT, M. A. (1973) *Principles and Techniques of Electron Microscopy - 3 Biological Applications*, Van Nost. Reinhold.

HO, C., RAISTRICK, I. D. & HUGGINS, R. A. (1980) Application of A-C Techniques to the Study of Lithium Diffusion in Tungsten Trioxide Thin Films. *Journal of The Electrochemical Society*, 127, 343-350.

HONDA, Y., HARAMOTO, T., TAKESHIGE, M., SHIOZAKI, H., KITAMURA, T. & ISHIKAWA, M. (2007) Aligned MWCNT Sheet Electrodes Prepared by Transfer Methodology Providing High-Power Capacitor Performance. *Electrochemical and Solid-State Letters*, 10, A106-A110.

HONG, M. S., LEE, S. H. & KIM, S. W. (2002) Use of KCl Aqueous Electrolyte for 2 V Manganese Oxide/Activated Carbon Hybrid Capacitor. *Electrochemical and Solid-State Letters*, 5, A227-A230.

HSIEH, C.-T. & TENG, H. (2002) Influence of oxygen treatment on

electric double-layer capacitance of activated carbon fabrics. *Carbon*, 40, 667 - 674.

HSING, C. F., KOVACIC, P. & KHOURY, I. A. (1983) *J. Polym. Sci., Polym. Chem.*, 21, 457.

HU, C.-C. & TSOU, T.-W. (2002a) Capacitive and textural characteristics of hydrous manganese oxide prepared by anodic deposition. *Electrochimica Acta*, 47, 3523-3532.

HU, C.-C. & TSOU, T.-W. (2002b) Ideal capacitive behavior of hydrous manganese oxide prepared by anodic deposition. *Electrochemistry Communications*, 4, 105-109.

HU, C.-C., WU, Y.-T. & CHANG, K.-H. (2008) Low-Temperature Hydrothermal Synthesis of Mn3O4 and MnOOH Single Crystals: Determinant Influence of Oxidants. *Chem. Mater.*, 20, 2890-2894.

HUANG, W. S., HUMPHREY, B. D. & MACDIARMID, A. G. (1986) Polyaniline, a novel conducting polymer. Morphology and chemistry of its oxidation and reduction in aqueous electrolytes. *Journal of the Chemical Society, Faraday Transactions 1*, 82, 2385-2400.

HUANG, X., YUE, H., ATTIA, A. & YANG, Y. (2007) Preparation and Properties of Manganese Oxide/Carbon Composites by Reduction of Potassium Permanganate with Acetylene Black. *Journal of The Electrochemical Society*, 154, A26-A33.

HUGHES, M., CHEN, G. Z., SHAFFER, M. S. P., FRAY, D. J. & WINDLE, A. H. (2002) Electrochemical Capacitance of a Nanoporous Composite of Carbon Nanotubes and Polypyrrole. *Chem. Mater.*, 14, 1610-1613.

IM, D. & MANTHIRAM, A. (2002) Nanostructured Lithium Manganese Oxide Cathodes Obtained by Reducing Lithium Permanganate with Methanol. *Journal of The Electrochemical Society*, 149, A1001-

A1007.

IOWA, T. U. O. (2008a) Methodology of Scanning Electron Microscopy.

IOWA, T. U. O. (2008b) Methodology of Transmission Electron Microscopy.

IRVIN, J. A., IRVIN, D. J. & STENGER-SMITH, J. D. (2007) Electroactive Polymers for Batteries and Supercapacitors. IN SKOTHEIM, T. A. & REYNOLDS, J. R. (Eds.) *Handbook of Conducting Polymers - Conjugated Polymers*. CRC Press.

JANG, J. H., HAN, S., HYEON, T. & OH, S. M. (2003) Electrochemical capacitor performance of hydrous ruthenium oxide/mesoporous carbon composite electrodes. *Journal of Power Sources*, 123, 79-85.

JEONG, Y. U. & MANTHIRAM, A. (2002) Nanocrystalline Manganese Oxides for Electrochemical Capacitors with Neutral Electrolytes. *Journal of The Electrochemical Society*, 149, A1419-A1422.

JIANG, J. H. & KUCERNAK, A. (2002) Electrochemical supercapacitor material based on manganese oxide: preparation and characterization. *Electrochimica Acta*, 47, 2381-2386.

JIANG, Q., QU, M. Z., ZHOU, G. M., ZHANG, B. L. & YU, Z. L. (2002) A study of activated carbon nanotubes as electrochemical super capacitors electrode materials. *Materials Letters*, 57, 988-991.

JIN, X.B, ZHOU, W., ZHANG, S. & CHEN, GEORGE Z. (2007) Nanoscale Microelectrochemical Cells on Carbon Nanotubes. *Small*, 3, 1513-1517.

JORCIN, J.-B., ORAZEM, M. E., PEBERE, N. & TRIBOLLET, B. (2006) CPE analysis by local electrochemical impedance spectroscopy. *Electrochimica Acta*, 51, 1473-1479.

KARAUSE, S. (2003) Impedance Methods. IN BARD, A., STRATMANN, M. & UNWIN, P. R. (Eds.) *Instrumentation and Electroanalytical*

Chemistry. Wiley.

KASTENING, B., HAHN, M., RABANUS, B., HEINS, M. & ZUM FELDE, U. (1997) Electronic properties and double layer of activated carbon. *Electrochimica Acta,* 42, 2789-2799.

KHALFAOUI, M., KNANI, S., HACHICHA, M. A. & LAMINE, A. B. (2003) New theoretical expressions for the five adsorption type isotherms classified by BET based on statistical physics treatment. *Journal of Colloid and Interface Science,* 263, 350-356.

KHOMENKO, V., RAYMUNDO-PINERO, E. & BEGUIN, F. (2006a) Optimisation of an asymmetric manganese oxide/activated carbon capacitor working at 2 V in aqueous medium. *Journal of Power Sources,* 153, 183-190.

KHOMENKO, V., RAYMUNDO-PINERO, E., FRACKOWIAK, E. & BEGUIN, F. (2006b) High-voltage asymmetric supercapacitors operating in aqueous electrolyte. *Applied Physics a-Materials Science & Processing,* 82, 567-573.

KIM, C.-H., PYUN, S.-I. & KIM, J.-H. (2003) An investigation of the capacitance dispersion on the fractal carbon electrode with edge and basal orientations. *Electrochimica Acta,* 48, 3455-3463.

KIM, H. & POPOV, B. N. (2003) Synthesis and Characterization of MnO_2-Based Mixed Oxides as Supercapacitors. *Journal of The Electrochemical Society,* 150, D56-D62.

KONG, H., GAO, C. & YAN, D. (2004) Controlled functionalization multiwalled carbon nanotubes by in situ atom transfer radical polymerization. *Journal of American Chemical Society,* 126, 412.

KONYUSHENKO, E. N., STEJSKAL, J., TRCHOV, M., HRADIL, J., KOVÁŘOV, J., PROKES, J., CIESLAR, M., HWANG, J.-Y., CHEN, K.-H. & SAPURINA, I. (2006) Multi-wall carbon nanotubes coated with

polyaniline. *Polymer*, 47, 5715-5723.

KÖTZ, R. & CARLEN, M. (2000) Principles and applications of electrochemical capacitors. *Electrochimica Acta*, 45, 2483-2498.

LAFORGUE, A., SIMON, P., FAUVARQUE, J. F., SARRAU, J. F. & LAILLER, P. (2001) Hybrid Supercapacitors Based on Activated Carbons and Conducting Polymers. *Journal of The Electrochemical Society*, 148, A1130.

LAM, L. T. & LOUEY, R. (2006) Development of ultra-battery for hybrid-electric vehicle applications. *Journal of Power Sources*, 158, 1140-1148.

LARGEOT, C., PORTET, C., CHMIOLA, J., TABERNA, P.-L., GOGOTSI, Y. & SIMON, P. (2008) Relation between the Ion Size and Pore Size for an Electric Double-Layer Capacitor. *J. Am. Chem. Soc.*, 130, 2730-2731.

LARMINIE, J. & DICKS, A. (2003) *Fuel Cell Systems Explained*, John Wiley & Sons Ltd.

LEE, H. Y. & GOODENOUGH, J. B. (1999) Supercapacitor Behavior with KCl Electrolyte. *Journal of Solid State Chemistry*, 144, 220-223.

LEE, H. Y., KIM, S. W. & LEE, H. Y. (2001) Expansion of Active Site Area and Improvement of Kinetic Reversibility in Electrochemical Pseudocapacitor Electrode. *Electrochemical and Solid-State Letters*, 4, A19-A22.

LEE, K.-T. & WU, N.-L. (2008) Manganese oxide electrochemical capacitor with potassium poly(acrylate) hydrogel electrolyte. *Journal of Power Sources*, 179, 430-434.

LEFRANT, S., BUISSON, J. P., SCHREIBER, J., CHAUVET, O., BAIBARAC, M. & BALTOG, I. (2003) Study of interactions in carbon nanotubes systems by using Raman and SERS spectroscopy.

Synthetic Metals, 139, 783-785.

LI, C., WANG, D., LIANG, T., WANG, X. & JI, L. (2004) A study of activated carbon nanotubes as double-layer capacitors electrode materials. *Materials Letters,* 58, 3774-3777.

LI, J. & ZHITOMIRSKY, I. (2008) Electrophoretic deposition of manganese dioxide -carbon nanotube composites. *Journal of Materials Processing Technology,* In Press, Accepted Manuscript.

LI, W., REICHENAUER, G. & FRICKE, J. (2002) Carbon aerogels derived from cresol-resorcinol-formaldehyde for supercapacitors. *Carbon,* 40, 2955-2959.

LI, Y. & QIAN, R. (2000) Electrochemical overoxidation of conducting polypyrrole nitrate film in aqueous solutions. *Electrochimica Acta,* 45, 1727-1731.

LIN, C., RITTER, J. A. & POPOV, B. N. (1999) Development of carbon-metal oxide supercapacitors from sol-gel derived carbon-ruthenium xerogels. *Journal of the Electrochemical Society,* 146, 3155-3160.

LIN, R., TABERNA, P. L., CHMIOLA, J., GUAY, D., GOGOTSI, Y. & SIMON, P. (2009) Microelectrode Study of Pore Size, Ion Size, and Solvent Effects on the Charge/Discharge Behavior of Microporous Carbons for Electrical Double-Layer Capacitors. *Journal of The Electrochemical Society,* 156, A7-A12.

LONG, J. W., SWIDER-LYONS, K. E., STROUD, R. M. & ROLISON, D. R. (2000) Design of Pore and Matter Architectures in Manganese Oxide Charge-Storage Materials. *Electrochemical and Solid-State Letters,* 3, 453-456.

LONG, J. W., YOUNG, A. L. & ROLISON, D. R. (2003) Spectroelectrochemical Characterization of Nanostructured, Mesoporous Manganese Oxide in Aqueous Electrolytes. *Journal of*

The Electrochemical Society, 150, A1161-A1165.

LUFRANO, F. & STAITI, P. (2004) Conductivity and capacitance properties of a supercapacitor based on Nafion electrolyte in a nonaqueous system. *Electrochemical and Solid State Letters,* 7, A447-A450.

LUFRANO, F., STAITI, P. & MINUTOLI, M. (2003) Evaluation of nafion based double layer capacitors by electrochemical impedance spectroscopy. *Journal of Power Sources,* 124, 314-320.

LUIZ, C. A. O., SILVA, C. N., YOSHIDA, M. I. & LAGO, R. M. (2004) *Carbon,* 42, 2279 - 2284.

LUO, J.-Y. & XIA, Y.-Y. (2007) Effect of Pore Structure on the Electrochemical Capacitive Performance of MnO_2. *Journal of The Electrochemical Society,* 154, A987-A992.

MA, S.-B., AHN, K.-Y., LEE, E.-S., OH, K.-H. & KIM, K.-B. (2007a) Synthesis and characterization of manganese dioxide spontaneously coated on carbon nanotubes. *Carbon,* 45, 375-382.

MA, S.-B., LEE, Y.-H., AHN, K.-Y., KIM, C.-M., OH, K.-H. & KIM, K.-B. (2006) Spontaneously Deposited Manganese Oxide on Acetylene Black in an Aqueous Potassium Permanganate Solution. *Journal of The Electrochemical Society,* 153, C27-C32.

MA, S.-B., NAM, K.-W., YOON, W.-S., YANG, X.-Q., AHN, K.-Y., OH, K.-H. & KIM, K.-B. (2007b) A novel concept of hybrid capacitor based on manganese oxide materials. *Electrochemistry Communications,* 9, 2807-2811.

MACDONALD, J. R. & JOHNSON, W. B. (2005) Fundamentals of Impedance Spectroscopy. IN BARSOUKOV, E. (Ed.) *Impedance Spectroscopy: Theory, Experimental and Applications.* 2nd ed., John Wiley & Sons, Inc.

MALINAUSKAS, A. (2001) Chemical deposition of conducting polymers. *Polymer,* 42, 3957-3972.

MASAYA, C. & MASAMI, I. (2000) Manganese Oxide Thin Film Preparation by Potentiostatic Electrolyses and Electrochromism. *Journal of The Electrochemical Society,* 147, 2246-2251.

MAYER, S. T., PEKALA, R. W. & KASCHMITTER, J. L. (1993) The Aerocapacitor: An Electrochemical Double-Layer Energy-Storage Device. *Journal of The Electrochemical Society,* 140, 446-451.

MCKEOWN, D. A., HAGANS, P. L., CARETTE, L. P. L., RUSSELL, A. E., SWIDER, K. E. & ROLISON, D. R. (1999) Structure of Hydrous Ruthenium Oxides: Implications for Charge Storage. *J. Phys. Chem. B,* 103, 4825-4832.

MESSAOUDI, B., JOIRET, S., KEDDAM, M. & TAKENOUTI, H. (2001) Anodic behaviour of manganese in alkaline medium. *Electrochimica Acta,* 46, 2487-2498.

MILLER, J. M., DUNN, B., TRAN, T. D. & PEKALA, R. W. (1997) Deposition of Ruthenium Nanoparticles on Carbon Aerogels for High Energy Density Supercapacitor Electrodes. *Journal of The Electrochemical Society,* 144, L309-L311.

MINDT, W. (1971) Electroless Deposition of Certain Metal Oxides. *Journal of The Electrochemical Society,* 118, 93-95.

MINTMIRE, J. W., DUNLAP, B. I. & WHITE, C. T. (1992) Are Fullerene Tubules Metallic. *Physical Review Letters,* 68, 631-634.

MOMMA, T., LIU, X. J., OSAKA, T., USHIO, Y. & SAWADA, Y. (1996) Electrochemical modification of active carbon fiber electrode and its application to double-layer capacitor. *Journal of Power Sources,* 60, 249-253.

MOTTAGHITALAB, V. (2006) Development and Characterisation of Polyaniline-Carbon Nanotube Conducting Composite Fibres. *School of Material, Mechanical and Mechatronic Engineering.* Wollongong, University of Wollongong.

MULVANEY, P., COOPER, R., GRIESER, F. & MEISEL, D. (1990) Kinetics

of reductive dissolution of colloidal manganese dioxide. 94, 8339-8345.

NAJAFI, E., KIM, J.-Y., HAN, S.-H. & SHIN, K. (2006) UV-ozone treatment of multi-walled carbon nanotubes for enhanced organic solvent dispersion. *Colloids and Surfaces A: Physicochemical and Engineering Aspects*, 284-285, 373-378.

NAKAYAMA, M., TANAKA, A., KONISHI, S. & OGURA, K. (2004) Effects of heat-treatment on the spectroscopic and electrochemical properties of a mixed manganese/vanadium oxide film prepared by electrodeposition. *J. Mater. Res.* , 19, 1509-1515.

NALAWA, H. S., DALTON, L. R., SCHMIDT, W. F. & REBE, J. G. (1985) Conducting Polyaniline and polypyrrole: studies of their catalytic properties. *Polymer Communications* 27.

NAM, K.-W. & KIM, K.-B. (2006) Manganese Oxide Film Electrodes Prepared by Electrostatic Spray Deposition for Electrochemical Capacitors. *Journal of The Electrochemical Society*, 153, A81-A88.

NAOI, K., OGIHARA, N., IGARASHI, Y., KAMAKURA, A., KUSACHI, Y. & UTSUGI, K. (2005) Disordered Carbon Anode for Lithium-Ion Battery. *Journal of The Electrochemical Society*, 152, A1047-A1053.

NARITA, E. & OKABE, T. (1980) The Formation and Some Properties of Hydrous Manganese (IV) Oxide. *The Chemical Society of Japan*, 53, 525-532.

NG, K. C., ZHANG, S. & CHEN, G. Z. (2008a) An asymmetrical supercapacitor based on CNTs/SnO2 and CNTs/MnO2 nanocomposites working at 1.7 V in aqueous electrolyte. *Electrochemical Capacitors and Hybrid Power Sources, 214th ECS Annual Meeting (PRiME 2008)*. Hawaii, The Electrochemical Society.

NG, K. C., ZHANG, S. & CHEN, G. Z. (2008b) An asymmetrical

supercapacitor based on CNTs/SnO2 and CNTs/MnO2 nanocomposites working at 1.7 V in aqueous electrolyte. *ECS Trans. 214th ECS Annual Meeting,* 16, 153-162.

NG, K. C., ZHANG, S., PENG, C. & CHEN, G. Z. (2009) Individual and Bipolarly Stacked Asymmetrical Aqueous Supercapacitors of CNTs/SnO2 and CNTs/MnO2 Nanocomposites. *Journal of the Electrochemical Society.*

NICHOLSON, R. S. & SHAIN, I. (1964) Theory of Stationary Electrode Polarography-Single Scan and Cyclic Methods Applied to Reversible,Irreversible, and Kinetic Systems. *Analytical Chemistry* 36, 706-723.

NIKLASSON, G. A., JOHSSON, A. K. & STROMME, M. (2005) Impedance Response of Electrochromic Materials and Devices. IN BARSOUKOV, E. & MACDONALD, J. R. (Eds.) *Impedance Spectroscopy - Theory, Experiment, and Applications.* 2nd ed.

NIU, C., SICHEL, E. K., HOCH, R., MOY, D. & TENNENT, H. (1997) High power electrochemical capacitors based on carbon nanotube electrodes. *Applied Physics Letters,* 70, 1480-1482.

NOVA´K, P., MULLER, K., SANTHANAM, K. S. V. & HAAS, O. (1997) Electrochemically Active Polymers for Rechargeable Batteries. *Chem. Rev.,* 97, 207-281.

ORATA, D. & BUTTRY, D. A. (1987) Determination of ion populations and solvent content as functions of redox state and pH in polyaniline. 109, 3574-3581.

ORAZEM, M. E. & TRIBOLLET, B. (2008) *Electrochemical Impedance Spectroscopy,* Wiley & Sons, Inc.

OVEJERO, G., SOTELO, J. L., ROMERO, M. D., RODRIGUEZ, A., OCANA, M. A., RODRIGUEZ, G. & GARCIA, J. (2006) Multiwalled carbon nanotubes for liquid-phase oxidation. Functionalization, characterization, and catalytic activity. *Industrial &*

Engineering Chemistry Research, 45, 2206-2212.

OZAKI, Y., MORITA, S. & DU, Y. (2007) Spectral Analysis. IN OZAKI, Y., MCCLURE, W. F. & CHRISTY, A. A. (Eds.) *Near-Infrared Spectroscopy in Food Science and Technology*. John Wiley & Sons, Inc.

PAJKOSSY, T. (2005) Impedance spectroscopy at interfaces of metals and aqueous solutions - Surface roughness, CPE and related issues. *Solid State Ionics*, 176, 1997-2003.

PANDOLFO, A. G. & HOLLENKAMP, A. F. (2006) Carbon properties and their role in supercapacitors. *Journal of Power Sources*, 157, 11-27.

PANDOLFO, A. G., VASALLO, A. M. & PAUL, G. L. (1997) *Proceedings of The 7th International Seminar on Double Layer Capacitors and Similar Energy Storage Devices*. Florida Educational Seminar.

PANG, S.-C., ANDERSON, M. A. & CHAPMAN, T. W. (2000) Novel Electrode Materials for Thin-Film Ultracapacitors: Comparison of Electrochemical Properties of Sol-Gel-Derived and Electrodeposited Manganese Dioxide. *Journal of The Electrochemical Society*, 147, 444-450.

PARK, J. H. & PARK, O. O. (2002) Hybrid electrochemical capacitors based on polyaniline and activated carbon electrodes. *Journal of Power Sources*, 111, 185-190.

PASQUIER, A. D., PLITZ, I., GURAL, J., BADWAY, F. & AMATUCCI, G. G. (2004) Power-ion battery: bridging the gap between Li-ion and supercapacitor chemistries. *Journal of Power Sources*, 136, 160-170.

PAUL, E. W., RICCO, A. J. & WRIGHTON, M. S. (1985) Resistance of polyaniline films as a function of electrochemical potential and the fabrication of polyaniline-based microelectronic devices. *The Journal of Physical Chemistry*, 89, 1441-1447.

PENG, C. (2007) Electrochemical Synthesis of Composites of Conducting Polymers and Carbon Nanotubes for Supercapacitors. *Department of Chemical and Environmental Engineering.* Nottingham, The University of Nottingham.

PENG, C., JIN, J. & CHEN, G. Z. (2007a) A comparative study on electrochemical co-deposition and capacitance of composite films of conducting polymers and carbon nanotubes. *Electrochimica Acta,* Article in Press.

PENG, C., ZHANG, S., JEWELL, D. & CHEN, G. Z. (2007b) **Carbon Nanotube and Conducting Polymer Composites for Supercapacitors.** *Paper in process.*

PENG, C., ZHANG, S., JEWELL, D. & CHEN, G. Z. (2008) **Carbon nanotube and conducting polymer composites for supercapacitors.** *Progress in Natural Science,* 18, 777-788.

PHILLIPS, J., XIA, B. & MENEÂNDEZ, J. A. (1998) *Thermochimica Acta,* 312, 87 - 93.

PLETCHER, D., GREEF, R., PEAT, R., PETER, L. M. & ROBINSON, J. (2001) *Instrumental Methods in Electrochemistry* Horwood Publishing.

PORRO, S., MUSSO, S., VINANTE, M., VANZETTI, L., **ANDERLE, M.,** TROTTA, F. & TAGLIAFERRO, A. (2007) Purification of carbon nanotubes grown by thermal CVD. *Physica E: Low-dimensional Systems and Nanostructures,* 37, 58-61.

POST (Parliament Office of Science and Technology, UK), Electricity Storage (2008).

POTTER, R. M. & ROSSMAN, G. R. (1979) The tetravalent **manganese** oxides: identification, hydration, and **structural** relationships by infrared spectroscopy *American Mineralogist,* 64, 1199.

POURBAIX, M. (1966) *Atlas of Electrochemical Equilibria in Aqueous*

Solutions, Centre belge d'étude de la corrosion

PRICE, A. (2005) Electrical energy storage—a review of technology options. *Proceedings of ICE*, 158, 52-58.

PRÖBSTLE, H., WIENER, M. & FRICKE, J. (2003) Carbon Aerogels for Electrochemical Double Layer Capacitors. *Journal of Porous Materials*, 10, 213-222.

RAISTRICT, I. D., FRANCESCHETTI, D. R. & MACDONALD, J. R. (2005) Theory of Impedance Spectroscopy. IN BARSOUKOV, E. & MACDONALD, J. R. (Eds.) *Impedance Spectroscopy: Theory, Experiment and Applications.* 2nd ed., John Wiley & Sons, Inc.

RAJENDRA PRASAD, K. & MIURA, N. (2004) Electrochemically synthesized MnO2-based mixed oxides for high performance redox supercapacitors. *Electrochemistry Communications*, 6, 1004-1008.

RASMUSSEN, S. C. & POMERANTZ, M. (2007) Low Bandgap Conducting Polymers. IN SKOTHEIM, T. A. & REYNOLDS, J. R. (Eds.) *Handbook of Conducting Polymers* 3rd ed., CRC Press.

RAYMUNDO-PINERO, E., KHOMENKO, V., FRACKOWIAK, E. & BEGUIN, F. (2005) Performance of Manganese Oxide/CNTs Composites as Electrode Materials for Electrochemical Capacitors. *Journal of The Electrochemical Society*, 152, A229-A235.

REDDY, R. N. & REDDY, R. G. (2003) Sol-gel MnO2 as an electrode material for electrochemical capacitors. *Journal of Power Sources*, 124, 330-337.

REDDY, R. N. & REDDY, R. G. (2004) Synthesis and electrochemical characterization of amorphous MnO2 electrochemical capacitor electrode material. *Journal of Power Sources*, 132, 315-320.

REED, S. J. B. (2005) *Electron Microprobe Analysis and Scanning Electron Microscopy in Geology*, Cambridge University Press.

ROS, T. G., VAN DILLEN, A. J., GEUS, J. W. & KONINGSBERGER, D. C.

(2002) Surface Oxidation of Carbon Nanofibres. *Chemistry - A European Journal*, 8, 1151-1162.

RUCH, P. W., KOTZ, R. & WOKAUN, A. (2009) Electrochemical characterization of single-walled carbon nanotubes for electrochemical double layer capacitors using non-aqueous electrolyte. *Electrochimica Acta*, 54, 4451-4458.

RUDGE, A., DAVEY, J. & GOTTESFELD S. (1994a) Conducting polymers as active materials in electrochemical capacitors. *Journal of Power Sources*, 47, 89-107.

RUDGE, A., RAISTRICK, I., GOTTESFELD, S. & FERRARIS, J. P. (1994b) A study of the electrochemical properties of conducting polymers for application in electrochemical capacitors. *Electrochimica Acta*, 39, 273 - 287.

SALANECK, W. R., STAFSTROM, S. & BREDAS, J. L. (1996) *Conjugated Polymer Surfaces and Interfaces*, Cambridge university Press.

SARANGAPANI, S., TILAK, B. V. & CHEN, C. P. (1996) Materials for electrochemical capacitors - Theoretical and experimental constraints. *Journal of the Electrochemical Society*, 143, 3791-3799.

SCHILLER, C. A. & STRUNZ, W. (2001) The evaluation of experimental dielectric data of barrier coatings by means of different models. *Electrochimica Acta*, 46, 3619-3625.

SCHOLZ, F. & BOND, A. M. (2005) *Electroanalytical Methods: Guide to Experiments and Applications*, Springer.

SHAFFER, M. S. P., FAN, X. & WINDLE, A. H. (1998) Dispersion and packing of carbon nanotubes. *Carbon*, 36, 1603-1612.

SHANMUGAM, S. & GEDANKEN, A. (2006) Generation of Hydrophilic, Bamboo-Shaped Multiwalled Carbon Nanotubes by Solid-State Pyrolysis and Its Electrochemical Studies. *J. Phys. Chem. B*, 110, 2037-2044.

SHANMUGHARAJ, A. M., BAE, J. H., LEE, K. Y., NOH, W. H., LEE, S. H. & RYU, S. H. (2007) Physical and chemical characteristics of multiwalled carbon nanotubes functionalized with aminosilane and its influence on the properties of natural rubber composites. *Composites Science and Technology*, 67, 1813-1822.

SHERWOOD, P. M. A. (1990) Data Analysis in XPS and AES. IN BRIGGS, D. & SEAH, M. P. (Eds.) *Practical Surface Analysis*. 2nd ed., John Wiley & Sons, Inc.

SIMON, P. & GOGOTSI, Y. (2008) Materials for electrochemical capacitors. *Nature Materials*, 7, 845-854.

SING, K. S. W., EVERETT, D. H., PIEROTTI, R. A., JOUQUEROL, J. & SIEMIENIEWSKA, T. (1985) Reporting Physisorption Data for Gas/Solid Systems with Special Reference to the Determination of Surface Area and Porosity. *Pure & Appl. Chem.*, 57, 603-619.

SIVAKKUMAR, S. R., KO, J. M., KIM, D. Y., KIM, B. C. & WALLACE, G. G. (2007) Performance evaluation of CNT/polypyrrole/MnO2 composite electrodes for electrochemical capacitors. *Electrochimica Acta*, 52, 7377-7385.

SLUYTERS-REHBACH, M. (1994) Impedances of electrochemical systems: Terminology, nomenclature and representation - Part 1: Cells with metal electrodes and liquid solutions. *Pure and Applied Chemistry*, 66, 1831-1891.

SMELA, E. (2003) Conjugated Polymer Actuators for Biomedical Applications. *Advanced Materials*, 15, 481-494.

SONG, H.-K., HWANG, H.-Y., LEE, K.-H. & DAO, L. H. (2000) The effect of pore size distribution on the frequency dispersion of porous electrodes. *Electrochimica Acta*, 45, 2241-2257.

SONG, H.-K., JUNG, Y.-H., LEE, K.-H. & DAO, L. H. (1999) Electrochemical impedance spectroscopy of porous electrodes: the effect of pore size distribution. *Electrochimica Acta*, 44,

3513-3519.

SPEISER, B. (2002) Linear Sweep and Cyclic Voltammetry. IN BARD, A. & STRATMANN, M. (Eds.) *Introduction to Electroanalytical Techniques and Instrumentation, Volume 3 of Encyclopedia of Electrochemistry* Wiley-VCH.

SPENCE, J. C. H. (2003) *High-Resolution Electron Microscopy*, New York, Oxford University Press.

STADNIYCHUK, H. P., ANDERSON, M. A. & CHAPMAN, T. W. (1996) Sol-Gel-Derived Thin-Film Manganese Dioxide Cathodes. *Journal of The Electrochemical Society,* 143, 1629-1632.

STUART, B. H. (2004) *Infrared Spectroscopy : Fundamentals and Applications,* Sidney, John Wiley & Sons.

SUBRAMANIAN, V., ZHU, H., VAJTAI, R., AJAYAN, P. M. & WEI, B. (2005) Hydrothermal Synthesis and Pseudocapacitance Properties of MnO2 Nanostructures. *The Journal of Physical Chemistry B,* 109, 20207-20214.

SUBRAMANIAN, V., ZHU, H. & WEI, B. (2006) Synthesis and electrochemical characterizations of amorphous manganese oxide and single walled carbon nanotube composites as supercapacitor electrode materials. *Electrochemistry Communications,* 8, 827-832.

SUGIMOTO, W., IWATA, H., YOKOSHIMA, K., MURAKAMI, Y. & TAKASU, Y. (2005) Proton and Electron Conductivity in Hydrous Ruthenium Oxides Evaluated by Electrochemical Impedance Spectroscopy: The Origin of Large Capacitance. *J. Phys. Chem. B,* 109, 7330-7338.

SUGIMOTO, W., KIZAKI, T., YOKOSHIMA, K., MURAKAMI, Y. & TAKASU, Y. (2004) Evaluation of the pseudocapacitance in RuO2 with a RuO2/GC thin film electrode. *Electrochimica Acta,* 49, 313-320.

SWANBARTON (2004) Status of Electrical Energy Storage Systems. IN

INDUSTRY, D. O. T. A. (Ed.), Crown.

TABERNA, P. L., SIMON, P. & FAUVARQUE, J. F. (2003) Electrochemical characteristics and impedance spectroscopy studies of carbon-carbon supercapacitors. *Journal of the Electrochemical Society*, 150, A292-A300.

TAGUCHI, A., INOUE, S., AKAMARU, S., HARA, M., WATANABE, K. & ABE, T. (2006) Phase transition and electrochemical capacitance of mechanically treated manganese oxides. *Journal of Alloys and Compounds*, 414, 137-141.

TIAN, B. & ZERBI, G. (1990) Lattice dynamics and vibrational spectra of polypyrrole. *Journal of Chemical Physics*, 92, 3886-3891.

TOUPIN, M., BROUSSE, T. & BELANGER, D. (2002a) Influence of Microstucture on the Charge Storage Properties of Chemically Synthesized Manganese Dioxide. *Chem. Mater.*, 14, 3946-3952.

TOUPIN, M., BROUSSE, T. & BELANGER, D. (2002b) Influence of Microstucture on the Charge Storage Properties of Chemically Synthesized Manganese Dioxide. *Chem. Mater.*, 14, 3946-3952.

TOUPIN, M., BROUSSE, T. & BELANGER, D. (2004) Charge Storage Mechanism of MnO2 Electrode Used in Aqueous Electrochemical Capacitor. *Chem. Mater.*, 16, 3184-3190.

TRCHOV, M., SEDENKOV, I. & STEJSKAL, J. (2005) In-situ polymerized polyaniline films 6. FTIR spectroscopic study of aniline polymerisation. *Synthetic Metals*, 154, 1-4.

UN (United Nations) Report of the Conference of the Parties on its 13th session: Framework Convention on Climate Change (2007).

UNUMA, H., KANEHAMA, T., YAMAMOTO, K., WATANABE, K., OGATA, T. & SUGAWARA, M. (2003) Preparation of thin films of MnO2 and CeO2 by a modified chemical bath (oxidative-soak-coating) method. *Journal of Materials Science*, 38, 255-259.

VIX-GUTERL, C., FRACKOWIAK, E., JUREWICZ, K., FRIEBE, M.,

PARMENTIER, J. & BEGUIN, F. (2005) *Carbon*, 43, 1293.

WAGNER, C. D. (1994) Photoelectron and Auger Energies and the Auger Parameter: A Data Set. IN BRIGGS, D. & SEAH, M. P. (Eds.) *Practical Surface Analysis: Auger and X-Ray Photoelectron Spectroscopy* 2nd ed., John Wiley & Sons Ltd

WAN, C., AZUMI, K. & KONNO, H. (2007) Hydrated Mn(IV) oxide-exfoliated graphite composites for electrochemical capacitor. *Electrochimica Acta*, 52, 3061-3066.

WANG, G.-X., ZHANG, B.-L., YU, Z.-L. & QU, M.-Z. (2005) Manganese oxide/MWNTs composite electrodes for supercapacitors. *Solid State Ionics*, 176, 1169-1174.

WARREN, M. (2005) Electronic and Structural Effects on the Electrochemistry of Polypyrrole. *Physics*. The University of British Columbia.

WEI, J., NAGARAJAN, N. & ZHITOMIRSKY, I. (2007) Manganese oxide films for electrochemical supercapacitors. *Journal of Materials Processing Technology*, 186, 356-361.

WINTER, M. & BRODD, R. J. (2004) What are batteries, fuel cells and supercapacitors? *Chem. Rev.,*, 104, 4245-4270.

WU, M.-S. (2005) Electrochemical capacitance from manganese oxide nanowire structure synthesized by cyclic voltammetric electrodeposition. *Applied Physics Letters*, 87, 153102-3.

WU, M.-S. & CHIANG, P.-C. J. (2004) Fabrication of Nanostructured Manganese Oxide Electrodes for Electrochemical Capacitors. *Electrochemical and Solid-State Letters*, 7, A123-A126.

WU, M., SNOOK, G. A., CHEN, G. Z. & FRAY, D. J. (2004a) Redox deposition of manganese oxide on graphite for supercapacitors. *Electrochemistry Communications*, 6, 499-503.

WU, M., SNOOK, G. A., GUPTA, V., SHAFFER, M., FRAY, D. J. & CHEN, G. Z. (2005a) Electrochemical fabrication and capacitance of

composite films of carbon nanotubes and polyaniline. *Journal of Materials Chemistry*, 15, 2297 - 2303.

WU, M. S., LEE, J. T., WANG, Y. Y. & WAN, C. C. (2004b) Field Emission from Manganese Oxide Nanotubes Synthesized by Cyclic Voltammetric Electrodeposition. *J. Phys. Chem. B*, 108, 16331-16333.

WU, T.-M., LIN, Y.-W. & LIAO, C.-S. (2005b) Preparation and characterization of polyaniline/multi-walled carbon nanotube composites. *Carbon*, 43, 734-740.

XU, J. J., KINSER, A. J., OWENS, B. B. & SMYRL, W. H. (1998) Amorphous Manganese Dioxide: A High Capacity Lithium Intercalation Host. *Electrochemical and Solid-State Letters*, 1, 1-3.

YANG, X., MAKITA, Y., LIU, Z. H., SAKANE, K. & OOI, K. (2004) Structural Characterization of Self-Assembled MnO2 Nanosheets from Birnessite Manganese Oxide Single Crystals. *Chem. Mater.*, 16, 5581-5588.

YBARRA, G., MOINA, C., FLORIT, M. I. & POSADAS, D. (2000) Proton Exchange during the Redox Switching of Polyaniline Film Electrodes. *Electrochemical and Solid-State Letters*, 3, 330-332.

YUAN, A. & ZHANG, Q. (2006) A novel hybrid manganese dioxide/activated carbon supercapacitor using lithium hydroxide electrolyte. *Electrochemistry Communications*, 8, 1173-1178.

ZHANG, S. & CHEN, Z. G. (2009) Manganese Oxide based Materials for Supercapacitors *Energy Materials*.

ZHENG, J. P. (2003) The limitations of energy density of battery/double-layer capacitor asymmetric cells. *Journal of the Electrochemical Society*, 150, A484-A492.

ZHOU, Y. K., TOUPIN, M., BÉLANGER, D., BROUSSE, T. & FAVIER, F. (2006) Electrochemical preparation and characterization of Birnessite-type layered manganese oxide films. *Journal of Physics and Chemistry of Solids,* 67, 1351-1354.

ZOTTI, G., ZECCHIN, S., SCHIAVON, G., VERCELLI, B., BERLIN, A. & DALCANALE, E. (2003) Potential-Driven Conductivity of Polypyrroles, Poly-N-Alkylpyrroles, and Polythiophenes: Role of the Pyrrole NH Moiety in the Doping-Charge Dependence of Conductivity. *Chemistry of Materials* 15, 4642-4650.